申报	系列：教学科研并重型
	专业：农业电气化与自动化
	职称：教授

业绩成果材料

（申报人的业绩成果材料包括论文、科研项目、获奖以及其他成果等）

单　位（二级单位）　工程学院

姓　名　　汪　沛

材料核对人:　　单位盖章:

核对时间:

华南农业大学制

目　录

一、教学研究业绩

1.教学研究项目

2.教学成果

二、科研项目

1.主持

三、论文、著作等

四、科研成果

五、其他业绩

教育部学位与研究生教育发展中心

学位中心函〔2024〕8号

关于反馈2023年度主题案例立项结果的函

华南农业大学:

2023年12月，教育部学位与研究生教育发展中心面向全国研究生培养单位开展主题案例征集工作，扎根中国大地，聚焦时代热点，汇聚各方力量，开发具有时代性、引领性、学理性、创新性的高质量案例。经过“单位审核推荐”“专家分组评议”“案例专家委审核”三级评议审核及结果公示，你校共有3项选题入围，其中“大国智造”主题2项，“区域协调发展”主题1项，详细清单附后。

项目将于2024年7月开展中期交流，10月启动结项验收，具体安排另行通知。请组织并支持各首席专家团队推动项目实施，产出高质量案例成果。

感谢对中国专业学位案例建设事业的支持!

附件：2023年度主题案例立项结果清单

教育部学位与研究生教育发展中心

2024年3月25日

附件

2023年度主题案例立项结果清单

（按主题方向及首席专家姓氏笔画排序）

单位名称：华南农业大学

序号	项目编号	首席专家	主题方向	选题名称
1	ZT-231056410	胡炼	大国智造	智能农机实现无人化智慧农场的探索与实践——以广东万绿智慧无人农场为例
2	ZT-231056407	谭成全	大国智造	高产母猪精准营养与智慧养殖
3	ZT-231056408	陈灿	区域协调发展	农业集群品牌价值共创研究——以“万绿河源”为例

结项证书

CERTIFICATE OF COMPLETION

项目类别：　中国专业学位案例中心 2023 年度主题案例

项目编号：　ZT-231056410

项目名称：　智能农机实现无人化智慧农场的探索与实践——以广东万绿智慧无人农场为例

首席专家：　胡炼

团队成员：　何杰,汪沛,黄培奎,赵润茂,高锐涛

本项目经审核准予结项，特发此证。

教育部学位与研究生教育发展中心

2025 年 08 月

华南农业大学文件

华南农教〔2025〕57号

关于公布华南农业大学2025年度校级本科教学质量与教学改革工程项目立项名单的通知

各学院、部处、各单位:

根据《关于开展2025年度校级本科教学质量与教学改革工程项目申报工作的通知》精神,经项目负责人申请、所在单位推荐、本科生院审核、学校组织专家评审和公示(无异议)等程序,决定立项“善境伦理学与风景园林专业实践教学深度融合的探索与实践”等127个项目为2025年度校级本科教学改革项目,立项“筑基·焕新·赋能:食品质量与安全专业‘新工科’建设暨工程教育认证提质创新工程”等52个项目为2025年度校级本科质量工程项目。具体名单见附件。

请各项目负责人按照项目建设任务及要求,及时开展各项改

革工作; 各单位要切实履行项目建设主体责任，加强对项目建设的督促、指导，以确保项目建设任务高质量完成。

特此通知。

附件：1. 2025 年度校级本科教学改革项目立项名单

2. 2025 年度校级本科质量工程项目立项名单

华南农业大学

2025 年 10 月 14 日

（联系人：孙齐胜；电　话：85288020）

公开方式：主动公开

华南农业大学党政办公室　　2025 年 10 月 15 日印发

2025年度校级本科教学改革项目立项名单

序号	项目编号	项目名称	级别	所在单位	项目负责人	项目组成员
1	JG2025001	善境伦理学与风景园林专业实践教学深度融合的探索与实践	重点	林学与风景园林学院	翁殊斐	高伟、李自若、李剑、冼丽铧
2	JG2025002	基于“AI赋能·科创融合”《中药鉴定学》教学改革探索与实践	重点	林学与风景园林学院	李雁群	白玫、谭建文、何韩军、李镇魁
3	JG2025003	基于OBE理念的“数字赋能、思政融合、产教协同”的《制药设备与工艺设计》课程育人模式研究与实践	重点	材料与能源学院	林雅铃	宋高鹏，聂燕芳，霍理坚
4	JG2025004	面向智慧国土空间规划的《区域规划》 数智化教学改革	重点	公共管理学院	李玮	高艳梅、孙传谆、武侠、刘卓君
5	JG2025005	基于批判性思维培养的公共管理类专业课“GenAI+”教学模式探索——以投资学课程为例	重点	公共管理学院	李韵婷	贾海薇、段 静、周丽云、杨明旭
6	JG2025006	“AI赋能-人机协同”课堂互动重构研究—以C语言课程为例	重点	数学与信息学院、软件学院	彭利民	李双娟，杨磊，吴理华，司国东
7	JG2025007	思政引领和业财融合导向的《中级财务会计》智慧教学改革与实践	重点	经济管理学院	陈晓敏	陈艳艳，牟小容，何艳玲
8	JG2025008	基于智能设备与线上平台的HIIT混合式体育教学创新设计与实践	重点	体育教学研究部	单宇	麦粤徽、张波、吕立、张晓萍
9	JG2025009	“AI+专业知识库”驱动的生态学实验创新设计教学：批判思维培养与实践范式应用	重点	资源环境学院	赵本良	章家恩、余光伟、危晖、李荣华
10	JG2025010	数字孪生与AI融合的《动物组织学与胚胎学》课程体系数智化升级与实践	重点	兽医学院	梁晓欢	马勇江、张媛、叶亚琼、李冰心
11	JG2025011	融合科学家精神与科研思维的《细胞生物学》“双核育人”改革与实践	重点	动物科学学院	冯敏	邓小娟、杨婉莹、胡豆豆、易辉玉
12	JG2025012	《食品标准与法规》创新能力培养体系的构建与应用研究	重点	食品学院	林晓蓉	郑倩望、李梦婷
13	JG2025013	轻量化AI驱动大学英语听说教改：POA-SOLO双轨分级训练模式	重点	外国语学院	王莹	钟志英、苏君、黄净、王世龙
14	JG2025014	基于深度学习的大学生高阶思维能力培养的教学模式改革与实践研究—以《作物育种学》为例	重点	农学院	陈婷婷	马启彬、张雷、黄君、夏辉
15	JG2025015	数智AI赋能高校形象设计教学“三化五全”育人模式的探索	重点	艺术学院	郑丽娜	王羊羊、郝丽、米平平、李若衡
16	JG2025016	《车用电机及控制技术》课程“仿真驱动-问题探究”教学模式改革与实践	重点	工程学院	吴双龙	李庆、林彩霞、肖博一
17	JG2025017	数智化转型中《无机及分析化学》课程思政与 AI 赋能教学融合路径探索	重点	材料与能源学院	高琼芝	高琼芝，刘英菊，刘海峰，张声森，杨思源
18	JG2025018	校地协同视域下环境工程本科人才实践能力培养路径优化	重点	资源环境学院	林云琴	陈杨梅 梁瑜海 郑芊 赖文威
19	JG2025019	“产教+科教”双融合下设计类专业创新型复合人才培养模式探索	重点	艺术学院	陈薇薇	黄鑫、冯悦、杨翠钰、李春阳
20	JG2025020	AI赋能高校精准化学业指导路径研究	重点	本科生院	倪妙珊	吴银宝、王金凤、李晨光、张佳琛
21	JG2025021	智慧教学背景下OBE导向的英语专业实践类课程的转型与重构	重点	外国语学院	朱婕	严晓蓉、苏君、林绿、杨敏
22	JG2025022	与极飞科技产教融合的人工智能人才培养探索	重点	电子工程学院（人工智能学院）	熊万杰	邓小玲、徐海涛、刘景峰、董昕

23	JG2025023	聚焦机器视觉课程改革—基于产教融合、科教融汇的卓越应用型人才培养路径探索	重点	电子工程学院（人工智能学院）	杨意	刘金龙，马稚昱，刘勇，牟英辉
24	JG2025024	AI赋能学生论文写作的教学改革与实践——基于学生认知视角	重点	经济管理学院	石敏	贺梅英、谭莹
25	JG2025025	英国文学史课程的AI知识图谱构建及数智化教学实践研究	重点	外国语学院	李良博	吕靖、张丁元、侯金萍、袁庆锋
26	JG2025026	AI赋能《数学分析》一流课程建设的改革与实践研究	重点	数学与信息学院、软件学院	金玲玉	金玲玉、房少梅、杨德贵、雷春林、危苏婷
27	JG2025027	AI背景下面向农经专业本科生的《大数据 分析与挖掘》课程体系建设与教学模式优化	重点	经济管理学院	文乐	李琴、陈有华、谭莹、伍敬文
28	JG2025028	基于大模型辅助的软件体系结构课程生成式编程教学改革与实践	重点	数学与信息学院、软件学院	林毅申	林毅申、曹维、周运华、梁早清
29	JG2025029	《种子加工与贮藏学》“理论-实践-实习”三位一体教学的探索和实践	重点	农学院	张亚锋	徐振江、邓婧、江院、张慧
30	JG2025030	中华优秀传统文化融入高校思政课程的路径研究——聚焦《马克思主义基本原理》课程	重点	马克思主义学院	禹规娥	何艳玲、王竹波、蒋正峰、谢翾
31	JG2025031	新时代应用型人才培养模式创新改革与实践研究——以环境工程专业为例	重点	资源环境学院	陈烁娜	方秋中、卫泽斌、黄柱坚、钟媛卿
32	JG2025032	产教融合视域下《家具定制技术》课程“三融四阶五维”教学模式创新与实践	重点	材料与能源学院	郭琼	宋杰、欧荣贤、涂登云，徐宁
33	JG2025033	面向AI赋能的《机械设计基础》“1+1+1+N”混合式教学方法	重点	工程学院	王慰祖	夏红梅、甄文斌、卢家欢、程碧懿
34	JG2025034	“科研-竞赛-创新”协同融合培养智慧农业拔尖人才探索与实践	重点	工程学院	何杰	何杰，汪沛，胡炼，高锐涛，赵润茂
35	JG2025035	基于RAMP原则的“学科——安全” 化学实验双线融合教育体系构建与实践	重点	基础实验与实践训练中心	林碧敏	郑明轩，肖勇，刘维，刘小波
36	JG2025036	基于人工智能与虚拟仿真融合的《分子生物学》智慧课程体系建设与教学模式改革	重点	食品学院	叶志伟	赵雷、黎攀、邹苑
37	JG2025037	产科教融合视角下茶学专业课程体系优化与实践——以《茶树栽培学》为例	重点	园艺学院	郑鹏	孙彬妹、曹藩荣、刘少群、晏嫦妤
38	JG2025038	生成式AI驱动农林院校“新文科”教学模式创新 —《应急管理概论》智慧课程的建设实践	重点	公共管理学院	游艳玲	刘志明、赵国洪、马启彬、张建桃
39	JG2025039	面向实践能力提升的新文科（管理学类）AI课堂：数据分析可视化的“教-学-练-评”闭环体系构建	重点	数学与信息学院、软件学院	古万荣	唐德玉，余平祥，韦婷婷，毛宜军
40	JG2025040	基于“课程思政+产教融合”双驱动的茶叶审评与检验实习课程创新实践	重点	园艺学院	孟慧	谭新东、孙彬妹、张凌云、周仁杰
41	JG2025041	基于智能网络的生物化学全英课程改革与实践	重点	生命科学学院	洪梅	朱国辉、母培强、张智胜
42	JG2025042	植物病理学课程思政教育的创新与实践	自筹	植物保护学院	司徒俊键	孔广辉；习平根；李敏慧；姜子德
43	JG2025043	三全育人视域下的《病媒生物》思政教学探索与实践	自筹	植物保护学院	王德森	王磊、黄嘉

华南农业大学教育教学研究和改革项目

申　报　书

项目类别　2025 年度教育教学改革项目重 点项目

项目名称　“科研-竞赛-创新”协同融合培养智慧农业拔尖人才探索与实践

项目负责人　何　杰

职　　称　副教授

手机号码　

所在单位　工程学院（公章）

申报日期　2025.6.15

华南农业大学 本科生院　制

二 〇 二 五 年　五 月

一、项目及项目负责人、项目组简况

<table>
<tr><td rowspan="3">项目简况</td><td>项目名称</td><td colspan="6">“科研-竞赛-创新”协同融合培养智慧农业拔尖人才探索与实践</td></tr>
<tr><td>项目类别</td><td colspan="6">■1.重点项目　　□2.自筹项目</td></tr>
<tr><td>起止年月</td><td colspan="6">2026 年 1 月-2027 年 12 月</td></tr>
<tr><td rowspan="12">项目申请人</td><td>姓名</td><td colspan="2">何杰</td><td>性别</td><td>男</td><td>出生年月</td><td></td></tr>
<tr><td colspan="2">专业技术职务/
行政职务</td><td colspan="2">副教授/无</td><td colspan="2">最终学位/授予国家</td><td>博士/中国</td></tr>
<tr><td rowspan="2">所在单位及联系方式</td><td>单位名称</td><td colspan="3">工程学院</td><td>手机号码</td><td></td></tr>
<tr><td>电子邮箱</td><td colspan="5">hooget@scau.edu.cn</td></tr>
<tr><td rowspan="10">主要教学工作简历</td><td>时间</td><td>课程名称</td><td colspan="2">授课对象</td><td>学时</td><td>所在单位</td></tr>
<tr><td>2023-2025</td><td>电路与模拟电子技术</td><td colspan="2">2022-2023 车辆工程 本科</td><td>128</td><td>工程学院</td></tr>
<tr><td>2024-2025</td><td>数字电子技术</td><td colspan="2">2022-2023 车辆工程 本科</td><td>64</td><td>工程学院</td></tr>
<tr><td>2018-2023</td><td>自动控制理论实验</td><td colspan="2">2015-2021 自动化、电气工程及其自动化本科</td><td>16</td><td>工程学院</td></tr>
<tr><td>2018-2023</td><td>PLC 实验</td><td colspan="2">2015-2021 自动化、电气工程及其自动化本科</td><td>16</td><td>工程学院</td></tr>
<tr><td>2018-2023</td><td>传感器与检测实验</td><td colspan="2">2015-2022 自动化、电气工程及其自动化、机器人工程本科</td><td>16</td><td>工程学院</td></tr>
<tr><td>2018-2023</td><td>计算机控制技术实验</td><td colspan="2">2015-2021 自动化、电气工程及其自动化本科</td><td>16</td><td>工程学院</td></tr>
<tr><td>2019-2023</td><td>智能农机装备</td><td colspan="2">2019-2022 工程研究生</td><td>8</td><td>工程学院</td></tr>
<tr><td>2025</td><td>智慧农业</td><td colspan="2">2024 工程研究生</td><td>16</td><td>工程学院</td></tr>
<tr><td>主要教学</td><td>时间</td><td colspan="4">项目名称</td><td>获奖情况</td></tr>
</table>

<table>
<tr><td rowspan="4"></td><td rowspan="3">改革和科学研究工作简历</td><td>2022</td><td colspan="4">科教融合的智慧农业创新人才培养模式探索与实践</td><td></td></tr>
<tr><td>2020</td><td colspan="4">《农业机器人》教学模式与创新实践</td><td></td></tr>
<tr><td></td><td colspan="4"></td><td></td></tr>
<tr><td rowspan="8">项目组</td><td rowspan="2">总人数</td><td colspan="3">职称</td><td colspan="3">学位</td><td></td></tr>
<tr><td>高级</td><td>中级</td><td>初级</td><td>博士后</td><td>博士</td><td>硕士</td><td>参加单位数</td></tr>
<tr><td>6</td><td>6</td><td>0</td><td>0</td><td>1</td><td>1</td><td>2</td><td>1</td></tr>
<tr><td rowspan="6">主要成员（不含申请者）</td><td>姓名</td><td>性别</td><td>出生年月</td><td>职称</td><td>工作单位</td><td>分工</td><td>签名[2]</td></tr>
<tr><td>汪沛</td><td>女</td><td></td><td>副教授</td><td>工程学院</td><td>教学研究</td><td></td></tr>
<tr><td>胡炼</td><td>男</td><td></td><td>研究员</td><td>工程学院</td><td>教学研究</td><td></td></tr>
<tr><td>高锐涛</td><td>男</td><td></td><td>教授</td><td>工程学院</td><td>教学研究</td><td></td></tr>
<tr><td>黄培奎</td><td>男</td><td></td><td>高级工程师</td><td>工程学院</td><td>教学研究</td><td></td></tr>
<tr><td>赵润茂</td><td>男</td><td></td><td>副教授</td><td>工程学院</td><td>教学研究</td><td></td></tr>
</table>

[2]此页须成员手写签字后扫描成 PDF 电子版。

六、单位意见

所在单位意见：

（公章）

单位负责人签字：

2025 年 6 月 20 日

第十三届“挑战杯”
中国大学生创业计划竞赛

获奖证书

邹佳蕊 黄辉 林蔚楠 李婧涵 王浩嘉 张颖兴 冯达文 李明锦 许晓媛 徐耿坚 岳孟东
陈高隆 黄钰峰 田力 张强志 同学

你（们）的项目《 无人化托管——水稻智慧生产新引擎 》

在第十三届“挑战杯”中国大学生创业计划竞赛中荣获

银 奖

指导老师： 汪沛 胡炼 林伟波 何杰 高锐涛

特颁此证，以资鼓励。

主办单位：共青团中央、教育部、人力资源社会保障部、中国科协、全国学联、北京市人民政府
承办单位：北京理工大学、共青团北京市委、北京市房山区人民政府
协办单位：中国社会科学院大学、首都师范大学、北京工商大学、北京中医药大学
合作单位：海松资本有限公司、深圳市腾讯计算机系统有限公司、阿里云计算有限公司、北京快手科技有限公司

第十三届“挑战杯”中国大学生创业计划竞赛全国组织委员会
全国组织委员会
三月
（2022.05.05-2023.03.19）
1101081045166?

广东省人力资源和社会保障厅
广 东 省 教 育 厅 文件

粤人社发〔2025〕47号

广东省人力资源和社会保障厅 广东省教育厅关于表彰全省学校（高等教育）优秀教学成果奖的决定

各地级以上市教育局、人力资源和社会保障局，各高等学校，省直有关单位：

近年来，全省高校深入学习贯彻习近平新时代中国特色社会主义思想，全面落实立德树人根本任务，牢记为党育人、为国育才初心使命，在推进教育强省、科技创新强省、人才强省建设中，

凝练出一批提高人才培养质量的优秀成果。

在各高校推荐基础上，经有关程序，决定授予819项优秀教学成果为2025年全省学校（高等教育）优秀教学成果奖。其中：本科类优秀教学成果奖640项（含特等奖40项、一等奖200项、二等奖400项），研究生类优秀教学成果奖179项（含特等奖10项、一等奖49项、二等奖120项）。

希望各高校和教育工作者深入贯彻党的二十大和二十届历次全会精神，深入贯彻习近平总书记对广东系列重要讲话和重要指示精神，再接再厉，开拓创新，进一步加强高等教育教学研究和改革工作，大力弘扬教育家精神，提升教书育人本领，为加快建设教育强省、推动广东在推进中国式现代化建设中走在前列作出新的贡献。

附件：2025年全省学校（高等教育）优秀教学成果奖获奖成果名单

广东省人力资源和社会保障厅　　广东省教育厅

2025年12月25日

公开方式：主动公开

附件

2025年全省学校（高等教育）优秀教学成果奖获奖成果名单

一、2025年全省学校（高等教育）优秀教学成果奖（本科类）获奖成果名单

特等奖（40项）

序号	成果名称	完成人	牵头完成单位
1	通专融合，提升学习力思想力行动力--创造性人才培养体系构建与实践	高松、王博、李正、谢澜、王彩萍、傅绥燕、项聪、张雁、裴坚、秦昕、刘建波、金顶兵、靳祥鹏、欧阳钢锋、杨小柳	中山大学
2	四维协同，战略新兴领域生物医学教材体系的构建与创新	张雁、王世强、贺雄雷、刘杰、黄燕、吴雪梅、靳然、贺竹梅、卢湘婉	中山大学
3	超算筑基·AI深嵌·产教共研—创新型计算机人才培养探索与实践	吴迪、陈志广、张献伟、黄聃、胡淼、周知、陈刚、陈鹏飞、沈明华、卢宇彤	中山大学
4	铸魂·重构·创新：“口腔医学+”复合型人才培养新体系的创立与实践	陈莉莉、程斌、林正梅、陈泽涛、王焱、洪筠、李晓岚、黎琳、李蜀鄂、王茜、赵川江、侯劲松、杨博、施松涛、陈冬茹	中山大学
5	湾区引领·四维融通·实践赋能：中文拔尖人才培养体系的探索与创新	彭玉平、张均、吴承学、黄仕忠、谢有顺、范常喜、张奕琳、赵宏祥、宋俊华、洪炜	中山大学
6	聚焦在地国际化的新工科拔尖创新人才培养模式探索与实践	章熙春、李正、文宏、程正迪、李卫青、项聪、吴福胜、李慧龙	华南理工大学
7	“思政引领、科研赋能、竞赛驱动、校企协同”机械类人才培养模式探索与实践	李巍华、黄沿江、雷育胜、肖刚锋、杨丽新、宋长辉、李旻、张宪民、李琳、黄平	华南理工大学
8	思政铸魂 四维聚力：港澳台侨学生实战化全场景育人体系创建与实践	邢锋、张小欣、刘涛、颜海波、孙建莉、何清文、陈晓明、张沫、伍秀君、易晖、谢舒潇、杨泽铭、邓启东、林焕楠、陈璐莹	暨南大学
9	场景锚定 数智引擎：创新创业驱动大湾区新闻传播人才培养改革的新文科实践	刘涛、支庭荣、罗昕、林小榆、方惠、张建敏、谷虹、张潇潇、赵甜芳、蔡心仪	暨南大学
10	文化浸润 绿智赋能：中国特色管理理论引领下的一流商科人才培养改革与实践	黎文靖、欧锦文、谭有超、齐珺、谭小平、王斌会、王春刚	暨南大学
11	开创专业，打造标准，全球华文教育人才三融三通培养体系创建与实践	蔡丽、侯兴泉、金颖、曾毅平、王汉卫、刘潇潇、熊玉珍	暨南大学
12	新农科背景下“四维一体”农业生物学创新人才培养模式的构建与实践	刘耀光、朱国辉、陈乐天、文继开、安娜、王应祥、梁春江、方媛媛、陈超、谢勇尧	华南农业大学
13	"一核两翼·三擎导向·四维融合"卓越临床药学人才培养改革探索与实践	毕惠娣、吴少瑜、王文雅、陈金香、吕琳、李亦蕾、陈文琪、许重远、王巨旦、马豫峰	南方医科大学
14	建好人才培养主阵地：卓越医学人才培养改革二十年创新实践	郭洪波、谢小燕、王晶、夏欧东、田京、李晓丹、李乐平、王雪	南方医科大学
15	聚焦三力 构建三系：港澳中医药人才培养45年创新实践	陈文锋、游江、许能贵、张忠德、邝卫红、宋君玲、盛楠、冼冠儒、苗青、肖建喜	广州中医药大学
16	广东“新师范”新机制 新模式 新技术创建“六位一体”自主卓越师范生培养体系	赵艺、陈文海、阳成伟、金义富、郑耿忠、张学波、周立群、袁德辉、乐琦、连泽纯、郑凯、彭上观、李霓虹、郭连华	华南师范大学
17	指向知识创造的小学教育专业教师教育课程体系建构与实践	曾文婕、黄甫全、蒋慧芳、潘蕾琼、孙福海、尹睿、王文岚、董娜、陈思宇、陈志辉	华南师范大学
18	“科教融合·三阶跃升·四系融通”物理学拔尖创新人才培养体系的构建与实践	薛正远、朱诗亮、郭绮琪、周少娜、王振宇、李志、周旭、邓明勋、张丹伟、王丰	华南师范大学

序号	成果名称	完成人	牵头完成单位
396	身心互哺 分类分层 数字赋能：大学“体心融合”课程改革与实践	陈赛红、蒋街良、蔡煜浩、陈佳、梁艳、刘亮、谭智斌、赵可意、唐伊美、胡敏蕊	广州理工学院
397	民办高校“一体两翼三协同”外语专业人才培养模式创新与实践	章美芳、冯军霞、邓博文、刘香萍、马郁、廖益清、郭遂红、蔡俊、冉海涛、吕丽红、周杨、申丹、徐付娟、李欣	广州理工学院
398	面向中小型企业的“四融双驱式”智能制造类应用型人才培养探索与实践	朱亚峰、李玉忠、张德福、王如意、袁洁贞、陈婵媛、贾林锋、文龙振、庞姗	广州理工学院
399	诗词弦歌：工科大学四场域、五融合、六举措一体化美育新模式	张强、张海鸥、张明军、谢丽娜、黄牧乾	广州软件学院
400	数智物流“π型”人才培养模式的创新与实践	刘保庵、胥爱霞、刘瀛寰、许晓君、钱可欣、徐辉、李文娟、林育焜、卢逸璇、赵沅君	广州软件学院

二、2025年全省学校（高等教育）优秀教学成果奖（研究生类）获奖成果名单

特等奖（10项）

序号	成果名称	完成人	牵头完成单位
1	“从阿者科出发”：深入中国田野的研究性教学与实践	保继刚、杨兵、刘逸、翁时秀、左冰、梁增贤、黄琢玮、张骁鸣、何莽、陈钢华	中山大学
2	有机光电材料研究生“四统一”创新人才培养模式探索与实践	马於光、曹镛、黄飞、刘琳琳、苏仕健、彭俊彪、王丹、陈军武、兰林锋、孟勋	华南理工大学
3	研究生思政共同体“一·九·零·六”育人模式的构建与实践	孙彧、李朋军、程京武、吴昱、韩刚、戴玉洁、邓双全、周楠楠	暨南大学
4	“情怀引领、创新赋能、实践强基”现代农机类研究生培养模式构建与应用	罗锡文、胡炼、汪沛、林佩云、何杰、钱立雄、臧英、邱亚龙、李君、王红军	华南农业大学
5	“十大十制”基础医学拔尖人才培养创新模式的构建与实践	高天明、黎孟枫、马骊、刘叔文、吴砂、白晓春、钟世镇、赵小阳、姚开泰、黄文华、罗深秋、赵克森、丁彦青、黄巧冰、曹雄、徐湘民、夏来新、张琳、赵亮、董为人、梁莉、邱钰晖	南方医科大学
6	“理论-方法-应用”三元融合：面向人工智能时代的“法商融合”研究生课程体系改革与实践	鲁晓明、姚志伟、张肇廷、耿颖、刘薇、王海洋、黄伟文	广东财经大学
7	基于乡村振兴视野下的工艺美术研究生人才培养模式构建	林蓝、齐喆、余潮松、韦潞、罗保权、庞国华、谭红宇、金生花、杜沁芬、苏若山	广州美术学院
8	双核定向、双擎驱动、双重赋能：职业技术教育硕士研究生培养模式创新与实践	邓文新、陈泳竹、陈伟、刘海兰、杨蕾、郭腾飞、兰金林、蒋凡、杨勇、王敏、单纯、徐伟、邓兰、巫兴宏、尧勇	广东技术师范大学
9	网络强国战略下实战创新型网安人才“三段三融合”培养模式的“方班”实践	方滨兴、田志宏、王乐、鲁辉、许嘉、唐可可、张帆、张怡凯、齐佳音、徐国爱、蒋琳、陈艳利、廖清	广州大学
10	面向国家战略定制化培养卓越工程人才—南方科技大学产教融合培养实践与探索	薛其坤、方红卫、汪宏、叶飞、程鑫、张建明、唐瑜、潘权、余浩、孙大陟、万玉喜、张程程、梁佳惠、叶田田	南方科技大学

一等奖（49项）

序号	成果名称	完成人	牵头完成单位
1	面向健康中国战略的医学研究生“胜任力导向型”分类培养体系创新与实践	匡铭、肖莉华、李辉雁、戴国琳、胡文杰、陈崴、王骥、谭进富、刘晨、尹军强	中山大学
2	"并行计算•AI+”创新型计算机研究生培养体系建设与实践	肖侬、吴维刚、陈志广、杨跃东、江颖、张献伟、李冠彬、谭宁、黄凯、颜晓辉	中山大学

華南農業大學

研究生教学成果奖

获奖证书

获奖成果：“情怀引领、创新赋能、实践强基”现代农机类研究生培养模式构建与应用

获 奖 者：罗锡文、胡　炼、汪　沛、林佩云、何　杰、钱立雄、臧　英、邱亚龙、李　君、王红军

获奖等级：特等奖

证书编号：YJSJXCG25001

2025年9月9日

華南農業大學

本科教学成果奖

获奖证书

获奖成果：“一库两基地”产科教汇融平台赋能智能农机类拔尖人才培养模式的探索与实践

获 奖 者：胡　炼、何　杰、赵润茂、汪　沛、罗锡文、许细薇、王红军

获奖等级：一等奖

证书编号：JXCG24015

2025年9月9日

荣誉证书

HONORARY CREDENTIAL

汪 沛 老 师：

在华南农业大学 2022-2023 学年青年教师教学优秀奖评选中荣获

三等奖

特发此证，以资证明！

华 南 农 业 大 学

2024 年 1 月 4 日

课题编号：2025YFD2300404　　**密　级：公开**

国家重点研发计划
课题任务书

课题名称：	面向东北水田（水稻）的边缘智能技术开发及精准作业装备创制
所属项目：	东北地区规模化粮食作物智慧农场构建技术
所属专项：	主要作物丰产增效科技创新工程
项目牵头承担单位：	潍柴雷沃智慧农业科技股份有限公司
课题承担单位：	华南农业大学
课题负责人：	汪沛
执行期限：	2025 年 12 月 至 2028 年 11 月

中华人民共和国科学技术部制

2026 年 01 月 06 日

0003YF 2025YFD2300404 2026-01-06 17:59:53

课题基本信息表

<table>
<tr><td>课题名称</td><td colspan="5">面向东北水田（水稻）的边缘智能技术开发及精准作业装备创制</td></tr>
<tr><td>课题编号</td><td colspan="5">2025YFD2300404</td></tr>
<tr><td>所属项目</td><td colspan="5">东北地区规模化粮食作物智慧农场构建技术</td></tr>
<tr><td>所属专项</td><td colspan="5">主要作物丰产增效科技创新工程</td></tr>
<tr><td>密级</td><td colspan="2">■公开 □秘密 □机密</td><td>单位总数</td><td colspan="2">3</td></tr>
<tr><td>课题类型</td><td colspan="5">□基础前沿□重大共性关键技术■应用示范研究□其他</td></tr>
<tr><td>课题活动类型</td><td colspan="5">□基础前沿■应用研究□试验发展</td></tr>
<tr><td>课题研究
所属学科</td><td colspan="5">自然科学相关工程与技术
农业工程</td></tr>
<tr><td>课题成果应
用的主要国
民经济行业</td><td colspan="5">农、林、牧、渔业
农业
谷物种植
稻谷种植</td></tr>
<tr><td>课题的社会
经济目标</td><td colspan="5">农林牧渔业发展
农林牧渔业发展一般问题</td></tr>
<tr><td>经费预算</td><td colspan="5">总需求 405.00 万元，其中中央财政专项资金需求 205.00 万元</td></tr>
<tr><td rowspan="2">课题周期节点</td><td>起始时间</td><td>2025 年 12 月</td><td>结束时间</td><td colspan="2">2028 年 11 月</td></tr>
<tr><td>实施周期</td><td>共 36 个月</td><td>预计中期时间点</td><td colspan="2">2027 年 06 月</td></tr>
<tr><td rowspan="8">课题
承担
单位</td><td>单位名称</td><td colspan="2">华南农业大学</td><td>单位法定
代表人姓名</td><td>薛红卫</td></tr>
<tr><td>单位性质</td><td colspan="2">大专院校</td><td>组织机构代码</td><td>124400004554165634</td></tr>
<tr><td>单位主管部门</td><td colspan="2"></td><td>隶属关系</td><td>地方</td></tr>
<tr><td>单位所属地区</td><td colspan="2">广东省</td><td>地市（市、自
治州、盟）</td><td>广州市　天河区</td></tr>
<tr><td>通信地址</td><td colspan="2">广州市天河区五山路 483 号</td><td>邮政编码</td><td>510642</td></tr>
<tr><td>单位开户名称</td><td colspan="4">华南农业大学</td></tr>
<tr><td>开户银行
（全称）</td><td colspan="2">中国工商银行股份有限公司
广州五山支行</td><td>汇入地点</td><td>广东省　广州
市</td></tr>
</table>

<table>
<tr><td></td><td>银行账号</td><td colspan="3">36020026090000310520</td><td>银行机构代码</td><td colspan="2">102581000546</td></tr>
<tr><td rowspan="6">课题负责人</td><td>姓 名</td><td>汪沛</td><td>性 别</td><td>□男 ■女</td><td>出生日期</td><td colspan="2"></td></tr>
<tr><td>证件类型</td><td>身份证</td><td>证件号码</td><td colspan="4"></td></tr>
<tr><td>所在单位</td><td colspan="6">华南农业大学</td></tr>
<tr><td>最高学位</td><td colspan="6">■博士□硕士□学士□其他</td></tr>
<tr><td>职 称</td><td colspan="3">□正高级■副高级□中级□初级□其他</td><td>职 务</td><td colspan="2">无</td></tr>
<tr><td>电子邮箱</td><td colspan="2">wangpei@scau.edu.cn</td><td>移动电话</td><td colspan="3"></td></tr>
<tr><td rowspan="3">课题联系人</td><td>姓 名</td><td>赵润茂</td><td>电子邮箱</td><td colspan="4">rmzhao@scau.edu.cn</td></tr>
<tr><td>固定电话</td><td>020-38676975</td><td>移动电话</td><td colspan="4"></td></tr>
<tr><td>证件类型</td><td>身份证</td><td>证件号码</td><td colspan="4"></td></tr>
<tr><td rowspan="3">课题财务负责人</td><td>姓 名</td><td>肖斐</td><td>电子邮箱</td><td colspan="4">37115980@qq.com</td></tr>
<tr><td>固定电话</td><td>020-85288032</td><td>移动电话</td><td colspan="4"></td></tr>
<tr><td>证件类型</td><td>身份证</td><td>证件号码</td><td colspan="4"></td></tr>
<tr><td rowspan="3">其他参与单位</td><td>序号</td><td colspan="2">单位名称</td><td colspan="2">单位性质</td><td colspan="2">组织机构代码</td></tr>
<tr><td>1</td><td colspan="2">潍柴雷沃智慧农业科技股份有限公司</td><td colspan="2">国有企业</td><td colspan="2">91370000766689139Q</td></tr>
<tr><td>2</td><td colspan="2">东北农业大学</td><td colspan="2">大专院校</td><td colspan="2">122300004140017248</td></tr>
<tr><td rowspan="2">课题参加人数</td><td rowspan="2">34 人。其中：</td><td colspan="6">高级职称 3 人，中级职称 6 人，初级职称 1 人，其他 24 人；</td></tr>
<tr><td colspan="6">博士学位 2 人，硕士学位 15 人，学士学位 15 人，其他 2 人。</td></tr>
<tr><td>课题简介(限 500 字以内)</td><td colspan="7">以东北水稻生产全流程处方决策为基础，以“实时感知-边缘决策-精准执行”为核心技术主线，重点突破旋耕起浆深度实时感知与抗扰精准控制，漏插识别、施肥闭环调控与插植部独立线控，多维融合感知与主动抑飘技术，收获自主配速割台调高与实时测产技术。集成创制耕深自保持智能旋耕起浆机，漏插监测-同步变量闭环施肥-分区插植的智能移栽机，精准对靶-主动抑飘喷施无人飞机，配速调高-测产一体的大喂入量智能收获机，解决传统规模作业模式粗放、植保产品利用率低、收获损失高的难题，通过执行效果评估，为下一季生产方案提供决策依据。课题解决关键技术问题包括：1. 水田复杂动态环境下多源信息融合与协同控制技术；2. 水田复杂动态环境下高精度执行机构与智能控制技术。针对关键技术问题</td></tr>
</table>

九、课题参加人员基本情况表

填表说明： 1.专业技术职称：A、正高级　B、副高级　C、中级　D、初级　E、其他；
2.投入本课题的全时工作时间（人月）是指在课题实施期间该人总共为课题工作的满月度工作量；累计是指课题组所有人员投入人月之和；
3.课题固定研究人员需填写人员明细；
4.是否有工资性收入：Y、是　N、否；
5.人员分类代码：B、课题负责人　C、项目/课题骨干　D、其他研究人员；
6.工作单位：填写单位全称，其中高校要具体填写到所在院系。

序号	姓名	性别	出生日期	证件类型	证件号码	专业技术职称	职务	最高学位	专业	投入本课题的全时工作时间（人月）	人员分类代码	在课题中分担的任务	是否有工资性收入	工作单位
1	汪沛	女		身份证		副高级	无	博士	农业电气化与自动化	18	课题负责人	课题负责人	是	华南农业大学工程学院
2	王朔	男		身份证		其他	软件开发工程师	学士	自动化	6	课题骨干	软件开发	是	潍柴雷沃智慧农业科技股份有限公司
3	王立军	女		身份证		正高级	无	博士	农业机械化工程	6	课题骨干	总体方案设计	是	东北农业大学工程学院
4	张盟	男		身份证		其他	决策子模块主管工程师	硕士	农业机械化工程	2	课题骨干	系统开发	是	潍柴雷沃智慧农业科技股份有限公司
5	崔强	男		身份证		中级	导航应用子模块主管工程师	硕士	测绘工程	2	课题骨干	①负责显控终端与平台协议制定 ②负责显控	是	潍柴雷沃智慧农业科技股份有限公司

课题预算表

表B1　　课题编号：2025YFD2300404　　课题名称：面向东北水田（水稻）的边缘智能技术开发及精准作业装备创制　　金额单位：万元

序号	预算科目名称	金额
	（1）	（2）
1	一、中央财政专项资金	205.00
2	（一）直接费用	172.85
3	1.设备费	
4	其中：购置设备费	
5	2.业务费	135.33
6	3.劳务费	37.52
7	（二）间接费用	32.15
8	二、其他来源资金	200.00
9	三、合计	405.00

注：1.间接费用无需编制预算说明；2.绩效支出在间接费用中无比例限制。承担单位在统筹安排间接费用时，要处理好合理分摊间接成本和对科研人员激励的关系，绩效支出安排与科研人员在课题工作中的实际贡献挂钩。

课题单位经费预算明细表

表B3 课题编号： 2025YFD2300404 课题名称： 面向东北水田（水稻）的边缘智能技术开发及精准作业装备创制 金额单位：万元

填表说明： 1.单位类型分课题承担单位、课题参与单位；
2.组织机构代码指企事业单位国家标准代码，单位若已三证合一请填写单位统一社会信用代码，无组织机构代码的单位填写“000000000”。

序号	单位名称	组织机构代码-统一社会信用代码		单位类型	任务分工	研究任务负责人	合计	中央财政专项资金		其他来源资金
								小计	其中：间接费用	
	（1）	（2）	（3）	（4）	（5）	（6）	（7）	（8）	（9）	（10）
1	华南农业大学	统一社会信用代码	124400004554165634	课题承担单位	标准一致耕深自保持技术开发及水田旋耕起浆装备创制	汪沛	70.00	70.00	15.40	
2	潍柴雷沃智慧农业科技股份有限公司	统一社会信用代码	91370000766689139Q	课题参与单位	路径协同的秧爪独立驱控与漏插监测技术开发及高速移栽装备创制、长势状态自适应与实时测产技术开发及大喂入量收获装备创制	王朔	300.00	100.00	15.00	200.00
3	东北农业大学	统一社会信用代码	122300004140017248	课题参与单位	多模态感知驱动的精准对靶与动态抑飘技术开发及植保无人机创制	王立军	35.00	35.00	1.75	
累计							405.00	205.00	32.15	200.00

项目牵头承担单位（甲方）：

法定代表人签字（签章）：

（公章）

2025年12月12日

项目负责人签字（签章）：

2025年12月10日

课题承担单位（乙方）：

法定代表人签字（签章）：

（公章）

2025年12月10日

课题负责人签字（签章）：

2025年12月10日

密　级：内部

子课题任务合同书

子课题编号：	NK202315010301
子课题名称：	收获环境感知与自主协同作业技术系统研发
子课题承担单位：	华南农业大学
课题负责人：	汪沛
所属课题编号：	NK2023150103
课题牵头单位：	潍柴雷沃智慧农业科技股份有限公司
执行期限：	2023 年 10 月 至 2026 年 12 月

2023 年 10 月

子课题基本信息表

<table>
<tr><td colspan="2">所属课题</td><td colspan="5">大田谷物收获作业机器人研发</td></tr>
<tr><td colspan="2">所属课题编号</td><td colspan="5">NK2023150103</td></tr>
<tr><td colspan="2">子课题名称</td><td colspan="5">收获环境感知与自主协同作业技术系统研发</td></tr>
<tr><td colspan="2">子课题编号</td><td colspan="5">NK202315010301</td></tr>
<tr><td rowspan="9">子课题承担单位</td><td>单位名称</td><td colspan="5">华南农业大学</td></tr>
<tr><td>法定代表人</td><td colspan="2">薛红卫</td><td>单位性质</td><td colspan="2">大专院校</td></tr>
<tr><td>业务主管部门</td><td colspan="2">广东省教育厅</td><td>纳税人识别号（统一社会信用代码）</td><td colspan="2">12440000455416563 4</td></tr>
<tr><td>通信地址</td><td colspan="2">广东省广州市天河区五山路 483 号</td><td>邮政编码</td><td colspan="2">510642</td></tr>
<tr><td>单位开户名称</td><td colspan="5">华南农业大学</td></tr>
<tr><td>银行账号</td><td colspan="2">3602002609000310520</td><td>开户地点</td><td colspan="2">广东省广州市</td></tr>
<tr><td>开户银行（全称）</td><td colspan="2">中国工商银行广州五山支行</td><td>银行机构代码</td><td colspan="2">102581000546</td></tr>
<tr><td>科研管理部门负责人</td><td colspan="2">倪慧群</td><td>联系方式</td><td colspan="2"></td></tr>
<tr><td>财务管理部门负责人</td><td colspan="2">肖斐</td><td>联系方式</td><td colspan="2"></td></tr>
<tr><td rowspan="6">子课题负责人</td><td>姓 名</td><td>汪沛</td><td>性 别</td><td>女</td><td>出生日期</td><td></td></tr>
<tr><td>国 籍</td><td>中国</td><td>身份证号码</td><td colspan="3"></td></tr>
<tr><td>工作单位</td><td colspan="2">华南农业大学</td><td>职 务</td><td colspan="2">无</td></tr>
<tr><td>最高学位</td><td colspan="5">■博士 □硕士□学士 □其他</td></tr>
<tr><td>职 称</td><td colspan="5">□正高级 ■副高级 □中级 □其他</td></tr>
<tr><td>电子邮箱</td><td colspan="2">wangpei@scau.edu.cn</td><td>联系方式</td><td colspan="2"></td></tr>
<tr><td colspan="2">经费安排</td><td colspan="5">子课题经费按照《课题年度经费预算书（2023—2024 年度）》约定下达。</td></tr>
</table>

子课题任务合同书签署

课题牵头单位（甲方）：

法定代表人签字：

课题负责人签字：

（公章）

年　　月　　日

子课题牵头单位（乙方）：

法定代表人签字：

子课题负责人签字：

（公章）

年　　月　　日

密　级：内部

子课题年度经费预算书

（2023 年度）

子课题编号：	NK202315010301
子课题名称：	收获环境感知与自主协同作业技术系统研发
子课题承担单位：	华南农业大学
子课题负责人：	汪　沛
所属课题编号：	NK2023150103
年度时间：	2023 年 10 月 至 2024 年 06 月

2023 年 10 月

表 1　子课题预算支出科目表

金额单位：万元

序号	预算科目名称	金额
	（1）	（2）
1	一、中央财政资金	36.00
2	（一）直接费用	28.00
3	1.设备费	/
4	其中：购置设备费	/
5	2.业务费	17.75
6	3.劳务费	10.25
7	（二）间接费用	8.00
8	二、其他来源资金	/
9	三、合计	36.00

注：1.间接费用参照《国务院办公厅关于改革完善中央财政科研经费管理的若干意见》（国办发〔2021〕32 号）的有关要求计算，无需编制预算说明，课题的间接费用应为所有课题间接费用的总和；2.绩效支出在间接费用中无比例限制。承担单位在统筹安排间接费用时，要处理好合理分摊间接成本和对科研人员激励的关系，绩效支出安排与科研人员在 GG 工作中的实际贡献挂钩。

子课题年度经费预算签章页

子课题承担单位：

法定代表人签章：

子课题承担单位财务负责人签字（财务专用章）：

子课题负责人签字：

（公章）

年　　月　　日

课题牵头单位：

课题负责人签字：

（公章）

年　　月　　日

密　级：内部

子课题年度经费预算书

（2024 年度）

子课题编号：	NK202315010301
子课题名称：	收获环境感知与自主协同作业技术系统研发
子课题承担单位：	华南农业大学
子课题负责人：	汪　沛
所属课题编号：	NK2023150103
年度时间：	2024 年 7 月 至 2024 年 12 月

2023 年 10 月

表 1　子课题预算支出科目表

金额单位：万元

序号	预算科目名称	金额
	（1）	（2）
1	一、中央财政资金	64.00
2	（一）直接费用	50.00
3	1.设备费	/
4	其中：购置设备费	/
5	2.业务费	32.00
6	3.劳务费	18.00
7	（二）间接费用	14.00
8	二、其他来源资金	/
9	三、合计	64.00

注：1.间接费用参照《国务院办公厅关于改革完善中央财政科研经费管理的若干意见》（国办发〔2021〕32 号）的有关要求计算，无需编制预算说明，课题的间接费用应为所有课题间接费用的总和；2.绩效支出在间接费用中无比例限制。承担单位在统筹安排间接费用时，要处理好合理分摊间接成本和对科研人员激励的关系，绩效支出安排与科研人员在 GG 工作中的实际贡献挂钩。

子课题年度经费预算签章页

子课题承担单位：

法定代表人签章：

子课题承担单位财务负责人签字（财务专用章）：

子课题负责人签字：

（公章）

年　　月　　日

课题牵头单位：

课题负责人签字：

（公章）

年　　月　　日

密　级：内部

子课题年度经费预算书

（2025 年度）

子课题编号：	NK202315010301
子课题名称：	收获环境感知与自主协同作业技术系统研发
子课题承担单位：	华南农业大学
子课题负责人：	汪　沛
所属课题编号：	NK2023150103
年度时间：	2025 年 01 月 至 2025 年 12 月

2023 年 10 月

表 1　子课题预算支出科目表

金额单位：万元

序号	预算科目名称	金额
	（1）	（2）
1	一、中央财政资金	145.00
2	（一）直接费用	121.00
3	1.设备费	15.00
4	其中：购置设备费	/
5	2.业务费	61.00
6	3.劳务费	45.00
7	（二）间接费用	24.00
8	二、其他来源资金	/
9	三、合计	145.00

注：1.间接费用参照《国务院办公厅关于改革完善中央财政科研经费管理的若干意见》（国办发〔2021〕32 号）的有关要求计算，无需编制预算说明，课题的间接费用应为所有课题间接费用的总和；2.绩效支出在间接费用中无比例限制。承担单位在统筹安排间接费用时，要处理好合理分摊间接成本和对科研人员激励的关系，绩效支出安排与科研人员在 GG 工作中的实际贡献挂钩。

子课题年度经费预算签章页

子课题承担单位：

法定代表人签章：

子课题承担单位财务负责人签字（财务专用章）：

子课题负责人签字：

（公章）

年　　月　　日

课题牵头单位：

课题负责人签字：

（公章）

年　　月　　日

部门	项目	凭证日期	凭证编号	摘要	科目编号	科目名称	项目收入	项目支出
				年初余额			0.00	0.00
				期初余额			0.00	0.00
4500/工程学院	A240107/收获环境感知与自主协同作业技术系统研发	2024-06-18	(Z)07128	潍柴雷沃智慧农业科技股份有限公司来款入账A240107	610102010102	自然科学类	360,000.00	0.00
4500/工程学院	A240107/收获环境感知与自主协同作业技术系统研发	2024-06-18	(Z)07128	潍柴雷沃智慧农业科技股份有限公司来款入账A240107扣学校管理费	820103	项目间接费用或管理费	0.00	14,400.00
4500/工程学院	A240107/收获环境感知与自主协同作业技术系统研发	2024-06-18	(Z)07128	潍柴雷沃智慧农业科技股份有限公司来款入账A240107扣学院管理费	820103	项目间接费用或管理费	0.00	7,200.00
4500/工程学院	A240107/收获环境感知与自主协同作业技术系统研发	2024-06-18	(Z)07128	潍柴雷沃智慧农业科技股份有限公司来款入账A240107扣课题组	820103	项目间接费用或管理费	0.00	58,400.00
4500/工程学院	A240107/收获环境感知与自主协同作业技术系统研发	2024-07-11	(Z)06381	汪沛发放等5人研究生科研劳务	7201020202-3022601	科研非财政拨款项目支出-科研劳务费	0.00	7,800.00
4500/工程学院	A240107/收获环境感知与自主协同作业技术系统研发	2024-09-13	(Z)07398	汪沛发放研究生科研劳务	7201020202-3022601	科研非财政拨款项目支出-科研劳务费	0.00	7,000.00
4500/工程学院	A240107/收获环境感知与自主协同作业技术系统研发	2024-09-13	(Z)07454	成月明报梁楚奇、杨禹锟、黄俊成[illegible]	7201020202-3021102	科研非财政拨款项目支出-科研差旅费	0.00	4,025.90
4500/工程学院	A240107/收获环境感知与自主协同作业技术系统研发	2024-10-29	(Z)11800	汪沛发放等7人研究生科研劳务	7201020202-3022601	科研非财政拨款项目支出-科研劳务费	0.00	10,400.00
总计							360,000.00	220,269.03

检索结果

部门	项目	凭证日期	凭证编号	摘要	科目编号	科目名称	项目收入	项目支出
				年初余额			0.00	0.00
				期初余额			0.00	0.00
4500/工程学院	C240233/收获环境感知与自主协同作业技术系统研发	2024-12-25	(Z)18128	潍柴雷沃智慧农业科技股份有限公司来款入账C240233	610102010102	自然科学类	640,000.00	0.00
4500/工程学院	C240233/收获环境感知与自主协同作业技术系统研发	2024-12-25	(Z)18128	潍柴雷沃智慧农业科技股份有限公司来款入账C240233扣学校管理费	820103	项目间接费用或管理费	0.00	25,600.00
4500/工程学院	C240233/收获环境感知与自主协同作业技术系统研发	2024-12-25	(Z)18128	潍柴雷沃智慧农业科技股份有限公司来款入账C240233扣学院管理费	820103	项目间接费用或管理费	0.00	12,800.00
4500/工程学院	C240233/收获环境感知与自主协同作业技术系统研发	2024-12-25	(Z)18128	潍柴雷沃智慧农业科技股份有限公司来款入账C240233扣课题组	820103	项目间接费用或管理费	0.00	101,600.00
4500/工程学院	C240233/收获环境感知与自主协同作业技术系统研发	2025-02-19	(Z)03528	工程学院唐江涛转2月合同工工资	7201020202-3022601	科研非财政拨款项目支出-科研劳务费	0.00	4,000.00
4500/工程学院	C240233/收获环境感知与自主协同作业技术系统研发	2025-03-04	(Z)00844	成月明报满忠贤等6人研究生科研劳务	7201020202-3022601	科研非财政拨款项目支出-科研劳务费	0.00	8,300.00
4500/工程学院	C240233/收获环境感知与自主协同作业技术系统研发	2025-03-11	(Z)03349	成月明报科研实验材料-绝对值编码器等	7201020202-3021802	科研非财政拨款项目支出-科研实验材料	0.00	4,996.00
4500/工程学院	C240233/收获环境感知与自主协同作业技术系统研发	2025-04-29	(Z)11649	成月明报满忠贤等人研究生科研劳务	7201020202-3022601	科研非财政拨款项目支出-科研劳务费	0.00	8,250.00
总计							640,000.00	455,580.16

检索结果

部门	项目	凭证日期	凭证编号	摘要	科目编号	科目名称	项目收入	项目支出
				年初余额			0.00	0.00
				期初余额			0.00	0.00
4500/工程学院	C25039/收获环境感知与自助协同作业技术系统研发	2025-12-20	(Z)16803	潍柴雷沃智慧农业科技股份有限公司来款入账C25039	610102010102	自然科学类	1,450,000.00	0.00
4500/工程学院	C25039/收获环境感知与自助协同作业技术系统研发	2025-12-20	(Z)16803	潍柴雷沃智慧农业科技有限公司来款入账C25039扣学校管理费	820103	项目间接费用或管理费	0.00	58,000.00
4500/工程学院	C25039/收获环境感知与自助协同作业技术系统研发	2025-12-20	(Z)16803	潍柴雷沃智慧农业科技有限公司来款入账C25039扣学院管理费	820103	项目间接费用或管理费	0.00	29,000.00
4500/工程学院	C25039/收获环境感知与自助协同作业技术系统研发	2025-12-20	(Z)16803	潍柴雷沃智慧农业科技有限公司来款入账C25039扣课题组	820103	项目间接费用或管理费	0.00	153,000.00
4500/工程学院	C25039/收获环境感知与自助协同作业技术系统研发	2025-12-24	(Z)19600	成月明报销连接板机架等加工费	7201020202-3029915	科研非财政拨款项目支出-加工试制费	0.00	7,160.00
4500/工程学院	C25039/收获环境感知与自助协同作业技术系统研发	2025-12-24	(Z)19602	成月明报科研实验材料	7201020202-3021802	科研非财政拨款项目支出-科研实验材料	0.00	9,130.40
4500/工程学院	C25039/收获环境感知与自助协同作业技术系统研发	2025-12-24	(Z)19606	成月明报交通费-黄锦成等报销田间试验交通费	7201020202-30239	科研非财政拨款项目支出-其他交通费用	0.00	124.52
4500/工程学院	C25039/收获环境感知与自助协同作业技术系统研发	2025-12-24	(Z)19608	成月明报交通费-报销伍泽轩等机器作业试验交通费	7201020202-30239	科研非财政拨款项目支出-其他交通费用	0.00	434.00
总计							1,450,000.00	308,890.51

子课题编号：JXNK2023080502　　密　级：秘密

江西省农业关键核心技术攻关
子课题任务书

（2023-2025 年）

项目名称：南方红黄壤丘陵山区农业生产适宜农机装备创制及应用

课题名称：丘陵山区农机装备自动导航控制系统研制及应用

子课题名称：缓坡旱地履带底盘农机装备自动导航作业系统的研制

子课题承担单位：华南农业大学（盖章）

子课题负责人：汪　沛　联系电话：

子课题执行期：2023 年 6 月 1 日-2025 年 12 月 31 日

填报日期：2023 年 7 月 3 日

江西省农业农村厅

二0二三年制

七、子课题经费预算（2023 年）

科目名称	预算经费（万元）	经费用途、测算理由
一、直接经费：37.60		
1.设备费	0.00	无
2.材料费	8.00	用于购买传感器、电气元件、机械零部件、空间定位器件、伺服电机组件等，共计 8.00 万元。
3.测试化验加工费	6.00	用于加工测试农机导航系统、空间定位系统、设备联调测试等费用，共计 6.00 万元。
4.燃料动力费	1.00	用于农机导航系统田间测试所用柴油费用，预计 1.00 万元。
5.差旅费/会议费	8.00	项目研发期，于江西、广州等项目相关地方协调项目推进差旅，预计 8.00 万元。
6.出版/文献/信息传播/知识产权事务费	3.00	①用于文献传递、打印费用，约 0.15 万元； ②用于知识产权和论文发表 2.85 万元； 共 3.00 万。
7.劳务费	8.00	①用于支付研究生和其他研究人员的科研劳务费用，计 6.00 万元；②用于支付临时工劳务费，计 2.00 万元；共 8.00 万元。
8.专家咨询费	1.00	用于项目执行过程中聘请专家开展技术研讨、性能测试和田间测产，预计 1.00 万元。
9.其他	2.60	用于试验田租赁、机器运输费用等。
二、间接经费：2.40		
10.管理费	2.40	按单位华南农业大学预拨付 40 万的 6%计算，计 2.40 万元。

九、签约各方

子课题承担单位意见	子课题承担单位（公章）： 负责人（签章）： 年　月　日
子课题负责人意见	子课题负责人（签章）： 年　月　日
课题承担单位意见	课题承担单位（公章）： 负责人（签章）： 年　月　日
课题负责人意见	课题负责人（签章）： 年　月　日
项目牵头单位意见	项目牵头单位（公章）： 负责人（签章）： 年　月　日
项目牵头人意见	项目牵头人（签字）： 年　月　日

缓坡旱地履带底盘农机装备自动导航作业系统的研制（JXNK2023080502）

经费预算（2024 年）

科目名称	预算经费（万元）	经费用途、测算理由
一、直接经费：37.60		
1. 设备费	10.00	购买旋耕机等设备用于开展农机装备自动导航系统研发，预计 10.00 万元。
2. 材料费	6.50	用于购买传感器、电气元件、机械零部件、空间定位器件、伺服电机组件等，共计 6.50 万元。
3. 测试化验加工费	2.00	用于加工农机导航系统关键部件、设备联调测试等费用，共计 2.00 万元。
4. 燃料动力费	0.50	用于农机导航系统田间测试所用柴油费用，预计 0.50 万元。
5. 差旅费/会议费	7.00	项目研发期，于江西、广州等项目相关地方协调项目推进差旅，预计 7.00 万元。
6. 出版/文献/信息传播/知识产权事务费	1.60	①用于文献传递、打印费用，约 0.10 万元； ②用于知识产权和论文发表 1.00 万元； ③购买账号用于机器作业通讯，约 0.50 万元； 共 1.60 万元。
7. 劳务费	7.50	①用于支付研究生和其他研究人员的科研劳务费用，计 5.50 万元；②用于支付临时工劳务费，计 2.00 万元；共 7.50 万元。
8. 专家咨询费	0.50	用于项目执行过程中聘请专家开展技术研讨、性能测试和田间测产，预计 0.50 万元。
9. 其他	2.00	用于试验田租赁、机器运输费用等约 2.00 万元。
二、间接经费：2.40		
10. 管理费	2.40	按单位华南农业大学预拨付 40 万元的 6%计算，计 2.40 万元。

缓坡旱地履带底盘农机装备自动导航作业系统的研制（JXNK2023080502）

经费预算（2025 年）

科目名称	预算经费（万元）	经费用途、测算理由
一、直接经费：37.60		
1. 设备费	8.00	购买旋耕机等设备用于开展农机装备自动导航系统研发，预计 8.00 万元。
2. 材料费	8.50	用于购买传感器、电气元件、机械零部件、空间定位器件、伺服电机组件等，共计 8.50 万元。
3. 测试化验加工费	2.50	用于加工农机导航系统关键部件、设备联调测试等费用，共计 2.50 万元。
4. 燃料动力费	0.50	用于农机导航系统田间测试所用柴油费用，预计 0.50 万元。
5. 差旅费/会议费	7.00	项目研发期，赴江西、广东等项目相关基地开展调研示范、田间试验差旅费，参加相关学术会议、项目年度总结、中期检查以及项目结题会等所需差旅费，共计约 7.00 万元。
6. 出版/文献/信息传播/知识产权事务费	0.60	①用于文献传递、材料打印装订费，图书购买等费用约 0.10 万元； ②买账号用于机器作业通讯，约 0.50 万元； 共 0.60 万元。
7. 劳务费	6.50	①用于支付研究生和其他研究人员的科研劳务费用，计 4.50 万元；②用于支付临时工劳务费，计 2.00 万元；共 6.50 万元。
8. 专家咨询费	1.00	用于邀请专家对技术方案进行论证指导支付的专家咨询费。
9. 其他	3.00	用于试验田租赁、机器运输费用等约 3.00 万元。
二、间接经费：2.40		
10. 管理费	2.40	按单位华南农业大学预拨付 40 万元的 6%计算，计 2.40 万元。

检索结果

部门	项目	凭证日期	凭证编号	摘要	科目编号	科目名称	项目收入	项目支出	项目
				年初余额			0.00	0.00	
				期初余额			0.00	0.00	
4500/工程学院	C230091/缓坡旱地履带底盘农机装备自动导航作业系统的研制	2023-10-11	(Z)02887	江西农业大学来款入账C230091	610102010102	自然科学类	400,000.00	0.00	
4500/工程学院	C230091/缓坡旱地履带底盘农机装备自动导航作业系统的研制	2023-10-11	(Z)02887	江西农业大学来款入账C230091扣学校管理费	820103	项目间接费用或管理费	0.00	16,000.00	
4500/工程学院	C230091/缓坡旱地履带底盘农机装备自动导航作业系统的研制	2023-10-11	(Z)02887	江西农业大学来款入账C230091扣学院管理费	820103	项目间接费用或管理费	0.00	8,000.00	
4500/工程学院	C230091/缓坡旱地履带底盘农机装备自动导航作业系统的研制	2023-10-25	(Z)09299	刘于轩报涂团鹏、岳孟东江西南昌差旅费用	7201020202-3021103	科研非财政拨款项目支出-科研差旅费	0.00	3,212.00	
4500/工程学院	C230091/缓坡旱地履带底盘农机装备自动导航作业系统的研制	2023-11-06	(Z)02233	刘于轩报科研实验材料	7201020202-3021802	科研非财政拨款项目支出-科研实验材料	0.00	7,500.00	
4500/工程学院	C230091/缓坡旱地履带底盘农机装备自动导航作业系统的研制	2023-11-09	(Z)03743	秦浪报刘凯、蒋雄标、傅升湖北省武汉市差旅费用	7201020202-3021103	科研非财政拨款项目支出-科研差旅费	0.00	5,114.00	
4500/工程学院	C230091/缓坡旱地履带底盘农机装备自动导航作业系统的研制	2023-11-09	(Z)03749	刘于轩报徐梓涵、谢佳生湖北省武汉市差旅费用	7201020202-3021103	科研非财政拨款项目支出-科研差旅费	0.00	3,534.00	
4500/工程学院	C230091/缓坡旱地履带底盘农机装备自动导航作业系统的研制	2023-11-10	(Z)04563	秦浪报交通费	7201020202-30239	科研非财政拨款项目支出-其他交通费用	0.00	600.00	
总计							800,000.00	778,871.99	

检索结果

部门	项目	凭证日期	凭证编号	摘要	科目编号	科目名称	项目收入	项目支出
				年初余额			0.00	0.00
				期初余额			0.00	0.00
4500/工程学院	F25029/缓坡旱地履带底盘农机装备自动导航作业系统的研制	2025-06-13	(Z)05821	江西农业大学来款入账F25029-直接经费	610102010202	自然科学类	285,804.15	0.00
4500/工程学院	F25029/缓坡旱地履带底盘农机装备自动导航作业系统的研制	2025-06-13	(Z)05821	江西农业大学来款入账F25029-间接经费	610102010202	自然科学类	114,195.85	0.00
4500/工程学院	F25029/缓坡旱地履带底盘农机装备自动导航作业系统的研制	2025-06-13	(Z)05821	江西农业大学来款入账F25029扣学校管理费	820103	项目间接费用或管理费	0.00	16,000.00
4500/工程学院	F25029/缓坡旱地履带底盘农机装备自动导航作业系统的研制	2025-06-13	(Z)05821	江西农业大学来款入账F25029扣学院管理费	820103	项目间接费用或管理费	0.00	8,000.00
4500/工程学院	F25029/缓坡旱地履带底盘农机装备自动导航作业系统的研制	2025-07-07	(Z)03771	成月明报科研实验材料-接线端子材料费	7201020202-3021802	科研非财政拨款项目支出-科研实验材料	0.00	205.14
4500/工程学院	F25029/缓坡旱地履带底盘农机装备自动导航作业系统的研制	2025-07-10	(Z)06022	成月明报交通费-田间试验交通费	7201020202-30239	科研非财政拨款项目支出-其他交通费用	0.00	439.03
4500/工程学院	F25029/缓坡旱地履带底盘农机装备自动导航作业系统的研制	2025-07-10	(Z)06317	工程学院唐江涛转7月合同工工资	7201020202-3022601	科研非财政拨款项目支出-科研劳务费	0.00	4,000.00
4500/工程学院	F25029/缓坡旱地履带底盘农机装备自动导航作业系统的研制	2025-07-11	(Z)07406	成月明专用燃料费-报销燃油费	7201020202-3022501	科研非财政拨款项目支出-专用燃料费（燃油动力费）	0.00	209.40
总计							400,000.00	320,780.12

技术服务合同

项目名称：2025 年水稻智慧化生产技术指导及试验示范项目

委 托 方：广西壮族自治区农业机械化服务中心

（甲方）

受 托 方：华南农业大学

（乙方）

甲方委托乙方就 2025 年水稻智慧化生产技术指导及试验示范进行专项技术服务，并支付相应技术服务报酬。双方经过平等协商，在真实、充分表达各自意愿的基础上，根据《中华人民共和国民法典》的规定，达成如下协议，并由双方共同恪守。

第一条：甲方委托乙方进行技术服务的标的（成果）及内容如下：

1. 技术服务标的（成果）：制定形成广西水稻智慧化生产技术规范 1 套。

2. 技术服务的内容：（1）在贵港市港北区指导开展广西首个水稻智慧农场及示范基地建设，开展水稻生产各环节：无人驾驶水田旋耕机、无人驾驶水直播机、无人驾驶水稻插秧机、植保无人机和无人驾驶收获机技术及装备试验示范；（2）制定形成广西水稻智慧化生产技术规范 1 套。

3. 技术服务方式：中国工程院罗锡文院士及其团队入桂指导，提供粮食增产智慧农场机械化、智慧化相关技术服务并进行技术规范总结制定工作。

第二条：乙方应按下列要求完成技术服务工作：

乙方由中国工程院罗锡文院士牵头，何杰副教授、汪沛副教授、胡炼研究员、曾山研究员、高巧明、黄培奎高级工程师、赵润茂副教授组成专家组，承接本项目技术指导、服务、咨询及总结等任务。

1. 技术服务地点：广西壮族自治区行政区域范围内。

2. 服务期限：2025 年 1 月 1 日至 2025 年 12 月 31 日。

乙方应在合同期限届满前20个工作日（即12月4日前）出具技术服务成果，并提交甲方评估验收。

3.技术服务次数：乙方提供的技术服务次数根据甲方需求而定，但每年现场服务次数不少于3次。

4.技术服务质量要求：应甲方需求及时解决水稻智慧化生产技术过程中出现的农业智能装备相关技术难题，并总结出一套切实可行的可复制、可推广的广西水稻智慧化生产技术规范。

5.技术服务期限要求：在约定技术服务进度期限内完成约定的技术服务内容。

第三条：为保证技术服务工作顺利进行，甲乙双方应提供下列工作条件和协作事项：

1.甲方提供技术资料及工作条件：

（1）制定水稻智慧农场项目建设实施方案；

（2）配合乙方在港北区水稻智慧农场开展相关技术试验示范的落实、检查和指导等工作。

2.乙方提供技术资料及工作条件：

广西水稻智慧化生产技术总结、技术规范等相应支撑材料。

3.双方确定，服务过程中产生的技术服务成果，其知识产权归甲方所有。

第四条：甲方向乙方支付技术服务工作经费、支付方式为：

1.服务费总额为：壹拾伍万元整(¥150，000 元)。该费

用包括乙方为履行本合同应支出的所有费用（包括但不限于差旅费、资料查询、技术咨询、税金等费用）。

2. 技术服务费由甲方支付给乙方。

具体支付方式和时间如下：甲乙双方签订合同后，乙方开具相应发票提供甲方，经甲方审核无误后在合同签订后一个月内支付给乙方，税费由乙方承担。

乙方开户银行名称、地址和账号为：

名　　称：华南农业大学

开户银行：中国工商银行广东省分行广州市五山支行

地　　址：广州市天河区五山路 483 号

账　　号：3602002609000310520

第五条：本合同的变更必须经双方协商一致，并以书面形式确定。

第六条：双方确定 2025 年底按本合同第一条约定的第 1 点“技术服务标的（成果）”进行验收，并按下列标准和方式对乙方的技术服务工作成果进行验收：

1. 技术服务成果的验收：对技术总结、技术规范的验收，由甲方组织人员进行评估。

2. 验收工作由甲方组织人员对上述验收事项进行验收。

第七条：双方确定，在本合同有效期内，甲方指定黄严为甲方项目联系人，乙方指定　汪沛　为乙方项目联系人。

第八条：双方确定，出现下列情形，致使本合同的履行成为不必要或不可能的，可以解除本合同：

1. 发生不可抗力；

2. 自然灾害、政策调整变化等因素。

第九条：违约责任：

1. 若乙方未按合同约定提供现场指导、技术资料信息提供及咨询服务的，甲方有权按照未完成工作比例追回相应资金；

2. 若乙方出具的技术服务成果经评估为不合格的，乙方应重新作出新的技术服务成果，直至合格，其间产生的费用由乙方自行承担；

3. 若乙方逾期出具合格的技术服务成果，每逾期一日按合同总金额的万分之五承担违约责任；若逾期超过三个月的，则甲方有权解除本合同，乙方应赔偿因此给甲方造成的损失；

4. 因乙方原因造成项目无法继续推进超过三个月的，甲方有权解除本合同，乙方应赔偿因此给甲方造成的损失；

5. 甲方逾期支付服务费的，每逾期一日按逾期金额的万分之五向乙方支付违约金，因不可抗力或政府财政审批原因造成逾期的除外。

第十条：双方因履行本合同而发生的争议，应协商、调解解决。协商、调解不成的，确定按以下第 1 种方式处理：

1. 提交南宁仲裁委员会仲裁；

2. 依法向甲方所在地人民法院起诉。

第十一条：本合同一式肆份，具有同等法律效力。

第十二条：本合同经双方签字盖章后生效。

以下无正文，仅签字盖章页。

甲方：广西壮族自治区农业机械化服务中心　　（盖章）

法定代表人/委托代理人：　　（签名）

2025年 9月8日

乙方：　　（盖章）

法定代表人/委托代理人：　　（签名）

2025年 9月8日

合同编号：

服务合同

项目名称：建设会昌县小密乡水稻智慧农场

委 托 方：会昌县小密硒谷农业发展有限公司
（甲 方）

受 托 方：华南农业大学
（乙 方）

委托方（甲方）：会昌县小密硒谷农业发展有限公司

住　所　地：　会昌县小密乡杉背美食城

法定代表人：　王冬华

项目联系人：刘荣生

联系方式　：

通讯地址：会昌县小密乡富密街 70 号

电

受托方（乙方）：华南农业大学

住　所　地：广州市天河区五山路 483 号

法定代表人：　薛红卫

项目联系人：　汪沛

联系方式　：广州市天河区五山路 483 号华南农业大学

通讯地址：广州市天河区五山路 483 号

电　　传真：020－38676975

电子信箱：hooget@scau.edu.cn

甲方委托乙方就“建设会昌县小密乡水稻智慧农场项目”进行专项服务，并支付相应的服务报酬。双方经过平等协商，在真实、充分地表达各自意愿的基础上，根据《中华人民共和国民法典》的规定，达成如下协议，并由双方共同恪守。

第一条：甲方委托乙方进行服务的内容如下：

1. 服务团队：指定华南农业大学罗锡文院士团队负责实施。

2. 服务目标：建立水稻智慧农业试验区 1 个，推广水稻智慧农场关键技术，应用数字化农业装备，包括高精度农田地图构建、作业路径规划、无人农场生产管控平台等，提高水稻生产智能化水平。

3. 具体内容：（1）指导甲方制定水稻智能农机和智慧农业生产基础设施规划、农田改造建设规划和智能农机配置方案，建立 1 个水稻智慧农业试验区；（2）完成无人化数字农机装备调试工作；（3）制定农场各农田高精度地图构建，规划无人驾驶农机作业路径；（4）建设无人农场生产管控平台，完成农场云管控平台搭建，实现对无人农机的管控；（5）完成智慧物联网设备接入到无人农场现有的管控平台上进行试验示范和技术推广。（6）整理项目的相关资料并交付给甲方。

第二条：乙方应按下列要求完成服务工作：

1. 服务地点：会昌县小密乡小密村水稻种植基地

2. 服务期限：2024 年 06 月 01 日至 2025 年 12 月 31 日

3. 服务进度：2024 年 07 月-12 月，无人化示范方案和智慧农机配置，建立 1 个水稻智慧农业试验区，无人化农机现场作业和田间示范；2024 年 12 月-2025 年 3 月，建设无人农场生产管控平台，制定农场各农田高精度地图构建，规划无人驾驶农机作业路径等，开展推广水稻智慧农场关键技术；2025 年 12 月底前，培训用户无人化农机使用，指导无人农场作业。

第三条：为保证乙方有效进行服务工作，甲方应当向乙方提供相关工作条件和协作事项，甲方提供上述工作条件和协作事项的时间及方式，由双方在合同期共同协商。

第四条：甲方向乙方支付服务费用及支付方式为：

1.服务费总额为：￥200.000（人民币贰拾万元整）。

2.服务费由甲方分期支付乙方。

具体支付方式和时间如下：

（1）签订合同后，乙方开具合同款70%的增值税专用发票提供甲方，经甲方审核无误后七个工作日内支付给乙方，即140.000元（人民币壹拾肆万元整）；

（2）项目完成全部服务内容，并通过验收后，乙方开具合同款30%的增值税专用发票提供甲方，经甲方审核无误后七个工作日内支付给乙方，即60.000元（人民币陆万元整）。

（3）经费支出和使用按照《华南农业大学横向科技项目及经费管理办法》执行。

乙方开户银行名称、地址和账号为：

开户银行：中国工商银行广东省分行广州市五山支行

地　　址：广州市天河区五山路483号

帐　　号：3602002609000310520

第五条：本合同的变更必须由双方协商一致，并以书面形式确定。

第六条：双方确定以下列标准和方式对乙方的服务工作成果进行验收：

1.乙方完成服务工作的形式：　按甲方要求提供。

2.服务工作成果的验收标准：方案合理可靠，完成全部服务内容。

3.服务工作成果的验收方法：完成服务内容后，由甲方按照按项目合同第一条约定服务内容进行验收。

4.验收的时间和地点：2025年12月30日之前，由双方协商确定。

第七条：双方确定

1. 在本合同有效期内，甲方利用乙方提交的服务工作成果所完成的新的技术成果，归甲方所有。

2. 在本合同有效期内，乙方利用甲方提供的技术资料和工作条件所完成的新的技术成果，归双方所有。在甲方书面同意的情况下，乙方可以就有关研究成果发表论文、文章以及各项科技成果奖项等，但乙方应保证该等行为不会披露未经甲方同意披露的技术秘密。

3. 出现下列情形，致使本合同的履行成为不必要或不可能的，可以解除本合同：

（1）发生不可抗力；

（2）自然灾害。

第八条：本合同一式四份，经双方签字盖章后生效，具有同等法律效力。

以下无正文。

甲方：　　（盖章）

法定代表人／委托代理人：　刘荣生　　（签名）

2024 年 3 月 16 日

乙方：　　（盖章）

法定代表人／委托代理人：　　（签名）

年　　月　　日

受理编号：c22JAJH-22-0500000004

项目编号：20222-051252

文件编号：吉市科计字[2022]18号

20222-051252

科技计划项目

合同书

项目名称：南方红壤丘陵区水稻智慧生产关键技术与装备研发及示范应用

业务类型：井冈山农高区省级科技专项“揭榜挂帅”项目

项目起止时间：2022-10-01 至 2025-09-30

管理单位(甲方)：吉安市科学技术局

承担单位(乙方)：华南农业大学

乙方主管部门(丙方)：

通讯地址：广东省-广州市-天河区

邮政编码：510642 单位电话：020-85280011

项目负责人：胡炼 手机：

项目联系人：周志艳 联系电话：020-38676975

二零一七年一月制

一、项目摘要

针对南方红壤丘陵区水稻田块面积较小、形状复杂、农机作业全覆盖难和水田硬底层不平影响无人农机行驶与作业的精度和效率的问题，开展南方红壤丘陵区水稻智慧生产无人化关键技术、适应南方地块的水稻种植装备、水稻生产智能排灌技术与系统开发研究，研究水稻无人化农机农艺融合生产模式和规范以及水稻无人化智慧生产集成技术，创制无人农场高精度地图构建平台，开发适应南方红壤丘陵区的农机自动驾驶系统，创制小型智能化水稻精量穴直播机和无人机载彩绘水稻种植作业装备，开发适宜于南方红壤丘陵区水稻生产的排灌智能管控系统，通过技术集成在井冈山农高区建立水稻无人化智慧农场开展应用示范，示范面积500亩并制定技术规范，在全市选择3-5基地进行全程或至少2个及以上关键环节示范应用推广，且示范基地和推广应用基地作业数据上传至井冈山农高区智慧农业综合服务平台。

四、经费分配情况

承担/参与单位名称（盖章）	经费分摊（万元）	工作分工
华南农业大学	280.00	研究农机自动驾驶技术、障碍物识别技术，开发自主驾驶系统；研究无人化彩绘水稻种植技术，研制水稻种植装备；研究水田水层-水分传感技术，研制水层-水分传感器、排灌水闸门，开发水稻生产排灌智能管控系统。
吉安市农作物良种场	100.00	开展应用场景示范，进行水稻无人化智慧生产集成应用示范和推广应用。
井冈山大学	50.00	研究南方红壤丘陵区水稻智慧技术需求，参与水稻智慧生产集成应用示范，编制示范技术规范。
江西农业大学	70.00	研究基于人工智能的南方水稻农场田埂边界、作物和障碍物等对象目标的分类识别和相对定位，开发无人农场高精度地图构建平台，研制地面小型水稻种植装备。
合计	500.00	

五、项目组人员情况

项目负责人

序号	姓名	职称	E-mail	所在单位	证件号码	工作分工	签名
1	胡炼	副高级-副研究员	lianhu@scau.edu.cn	华南农业大学		负责项目的技术方案的制定与实施	

主要参与人员

序号	姓名	职称	E-mail	所在单位	证件号码	工作分工	签名
1	罗锡文	教授	xwluo@scau.edu.cn	华南农业大学		项目策划与技术指导	
2	何杰	实验师	hooget@scau.edu.cn	华南农业大学		农机自动驾驶技术及系统开发	
3	周志艳	教授	zyzhou@scau.edu.cn	华南农业大学		无人化彩绘水稻种植技术	
4	王国庆	高级农艺师	1243@163.com	吉安市农作物良种场		水稻智慧生产集成应用示范	
5	刘兆朋	讲师	314134582@qq.com	江西农业大学		无人农场高精度地图平台构建	
6	肖根福	副教授	xiaogenfu@163.com	井冈山大学		示范技术规范编制	
7	黄培奎	高级工程师	huangpeiku@scau.edu.cn	华南农业大学		层-水分传感器研制	
8	汪沛	讲师	wangpei@scau.edu.cn	华南农业大学		障碍物识别技术	
9	姜锐	讲师	ruiojiang@scau.edu.cn	华南农业大学		载水稻点射播种装置	
10	刘文安	未取得	123456@163.com	吉安市农作物良种场		水稻智慧生产集成应用示范	
11	刘新生	技术员	13546@163.com	吉安市农作物良种场		水稻智慧生产集成应用示范	
12	杨光华	高级农艺师	13466@163.com	吉安市农作物良种场		水稻智慧生产集成应用示范	
13	郑大腾	教授	yizh9026@163.com	井冈山大学		协助示范基地建设	
14	肖忠跃	副教授	306490389@qq.com	井冈山大学		示范应用推广及技术培训	
15	刘俊安	讲师	806189827@qq.com	江西农业大学		轻小型水稻直播机装备创制	
16	方鹏	讲师	1244860715@qq.com	江西农业大学		无人农场多地物目标识别与边界提取技术规划	
17	陈雄飞	副教授	121686212@qq.com	江西农业大学		直播机技术集成与试验示范	
18	刘木华	教授	714874481@qq.com	江西农业大学		项目组织与示范建设推进	
			403614537@			直播机排种器结构	

八、本合同签约各方

管理单位（甲方）：（盖章）

单位地址：

法定代表人（或授权代表）：_____（签章）

联系人（经办人）姓名：_____（签章）

Email：

电话：

2022年12月20日

承担单位（乙方）：（盖章）

单位地址：

法定代表人（或法人代理）：_____（签章）

联系人（项目主管）姓名：_____（签章）

Email：

电话：

开户单位名称：

开户银行及帐号：

2022年12月20日

乙方主管部门（丙方）：（盖章）

单位地址：

法定代表人（或法人代理）：_____（签章）

联系人（项目主管）姓名：_____（签章）

Email：

电话：

开户单位名称：

开户银行及帐号：

年　月　日

合同编号：

技术开发（委托）合同

项　目　名　称：辅助驾驶导航产品竞争力提升项目

委托方（甲方）：潍柴雷沃智慧农业科技股份有限公司

受托方（乙方）：华南农业大学

签　订　时　间：2023 年 6 月 30 日

签　订　地　点：山东潍坊坊子区

有　效　期　限：2023 年 6 月 30 日-2025 年 6 月 30 日

中华人民共和国科学技术部印制

技术开发（委托）合同

委托方（甲方）：潍柴雷沃智慧农业科技股份有限公司

受托方（乙方）：华南农业大学

本合同甲方委托乙方研究开发【辅助驾驶导航产品竞争力提升】项目，并支付研究开发经费，乙方接受委托并进行研究开发工作。双方经过平等协商，在真实、充分地表达各自意愿的基础上，根据《中华人民共和国民法典》规定，达成如下协议，由双方共同恪守。

第一条　本合同研究开发项目的要求如下：

1. 技术目标：提升自研辅助驾驶导航产品竞争力，达到行业第一梯队水平。

2. 技术内容：

2.1 系统评估当前国内外辅助导航产品的水平，对标联适、华测、天宝、迪尔等国内外一流厂家的辅助导航产品，从功能、性能上评估当前国内外辅助导航产品水平，出具结论报告。

2.2 开发水田、旱地卫星平地系统，包括系统开发、界面设计和控制算法，平地精度2.5cm。

2.3 优化导航控制算法，提高辅助导航控制性能。拖拉机作业时，在10-15km/h速度范围内导航控制精度2.5cm，在15-20km/h范围内导航控制精度3cm，且控制稳定，偶然干扰大误差情况下也可快速稳定入线；插秧机水田作业时，在3km/h速度范围内精度不低于2.5cm，在6km/h速度范围内精度不低于5cm。

2.4 优化曲线导航控制算法，在0.05m^{-1}曲率范围和12km/h速度范围内导航控制精度5cm。

2.5 优化陀螺仪测轮角和无角度传感测轮角算法，在1.2-15km/h范围内角度估算精度0.2°。

2.6 优化单天线组合导航算法，在1.2-10km/h速度范围内定位精度2 cm、姿态精度0.3°。在10-15km/h速度范围内定位精度2cm、姿态精度0.5°。

第二条　乙方应按下列进度完成研究开发工作：

序号	工作内容	交付物	完成时间
1	系统评估当前辅助驾驶导航产品水平	评估报告	2023.08.31
2	开发水田、旱地卫星平地系统	软件、报告	2023.12.30
3	优化导航控制算法	算法、报告	2024.06.30
4	优化曲线导航控制算法	算法、报告	2023.12.30
5	优化陀螺仪测轮角和无角度传感测轮角算法	算法、报告	2024.06.30
6	优化单天线组合导航算法	算法、报告	2024.09.30
7	项目总结与验收	总结报告	2025.06.30

甲方应提供资源配合乙方进行上述各项试验、测试和市场化验证确认工作。

第三条　甲方应向乙方提供的技术资料及协作事项如下：

1. 技术需求规格书；

2. 本合同履行完毕后，上述技术资料交还甲方处置 。

第四条　甲方应按以下方式支付研究开发经费：

1．研究开发经费总额为 200 万元（人民币贰佰万元整，含 3%税），不含税金额 194.174757 万元。

2．研究开发经费由甲方 分期 （一次、分期或提成）支付乙方，其中

合同签订之日后一个月内支付 60 万元（人民币陆拾万元整，含 3%税）；

2024 年 10 月 30 日前支付 100 万元（人民币壹佰万元整，含 3%税）；

2025 年 6 月 30 日前支付 40 万元（人民币肆拾万元整，含 3%税）。

每次付款前，乙方均需提前 10 个工作日向甲方开具符合甲方财务要求的增值税专用发票，若乙方未及时开具相关发票，甲方有权后延付款时间。

甲方财务开票信息为：

名　　称：潍柴雷沃智慧农业科技股份有限公司

纳税人识别号：91370000766689139Q

地 址、电 话：山东省潍坊市坊子区北海南路 192 号 0536-7606223

开户行及账号：中国农业银行股份有限公司潍坊坊子支行 15429001040010937

乙方开户银行名称、地址和账号为：

名　　称：华南农业大学

开户银行：中国工商银行广东省分行广州市五山支行

帐　　号：3602002609000310520

第五条　本合同研究开发经费由乙方按照《华南农业大学横向科技项目及经费管理办法》执行，甲方不得妨碍乙方正常工作。

第六条　本合同的变更必须由双方协商一致，并以书面形式确定。但有下列情形之一的，一方可以向另一方提出变更合同权利与义务的请求，另一方应当在 30 日内予以答复；逾期未予答复的，视为同意：

1．甲方要求乙方提前完成技术服务项目 ；

2．乙方因甲方未按照合同约定提供技术资料或者工作条件、协作事项而推迟服务日期 ；

3．一方向对方提出书面索赔请求 。

第七条　未经甲方同意，乙方不得将本合同项目部分或全部研究开发工作转让第三人承担。但有下列情况之一的，乙方可以不经甲方同意，将本合同项目部分或全部研究开发工作转让第三人承担：

1．通用组件、模块的开发和测试 ；

2．系统的测试 。

第八条　在本合同履行中，因出现在现有技术水平和条件下难以克服的技术困难，导致研究开发失败或部分失败，并造成一方或双方损失的，双方按如下约定承担风险损失：

由甲方自行承担 。

双方确定，本合同项目的技术风险按 专家咨询 的方式认定。认定技术风险的基本内容应当包括技术风险的存在、范围、程度及损失大小等。认定技术风险的基本条件是：

1. 本合同项目在现有技术水平条件下具有足够的难度；

2. 乙方在主观上无过错且经认定研究开发失败为合理的失败。

一方发现技术风险存在并有可能致使研究开发失败或部分失败的情形时，应当在30 日内通知另一方并采取适当措施减少损失。逾期未通知并未采取适当措施而致使损失扩大的，应当就扩大的损失承担赔偿责任。

第九条 双方确定因履行本合同应遵守的保密义务如下：对履行本合同过程中取得的所有非向公众公开的信息承担保密义务，未经双方同意，不得向社会公开合同内容。如因泄密方原因造成信息泄漏，泄密方应当承担赔偿责任。

第十条 乙方应当按以下方式向甲方交付研究开发成果：

1. 研究开发成果交付的形式及数量：当前辅助驾驶导航产品水平评估报告 1 份；旱田、水田平地系统软件 1 份，报告 1 份；导航控制优化算法 1 份，报告 1 份；曲线导航控制算法 1 份，报告 1 份；陀螺仪测轮角与无轮角角度测量优化算法 1 份，报告 1 份；单天线组合导航优化算法 1 份，报告 1 份。项目总结报告 1 份。算法各项指标以华测导航产品为参照进行验收测试。

2. 研究开发成果交付的时间及地点： 第二条各任务完成时间前，山东潍坊 。

第十一条 双方确定，按以下标准及方法对乙方完成的研究开发成果进行验收：针对第一条第 2 款的需求内容逐条核对 。

第十二条 乙方应保证其交付给甲方的研究开发成果不侵犯任何第三方的合法权益，否则由乙方自行承担责任。

第十三条 双方确定，因履行本合同所产生的研究开发成果及其相关知识产权权利归属，按下列方式处理：

1. 双方共同申请专利或发表论文时署名先后由双方协商确定；

2. 甲乙各方单独申请专利或发表论文时需征求对方同意；

3. 专利和论文不能透露合同项目涉及的核心技术机密；

4. 任何一方未经对方书面同意不得向本合同以外的第三方提供本项目研究开发成果，国家法规另有规定的除外。

第十四条 乙方利用研究开发经费所购置与研究开发工作有关的设备、器材、资料等财产，归 乙 方所有。

第十五条 双方确定，乙方应在向甲方交付研究开发成果后，根据甲方的请求，为甲方指定的人员提供技术指导和培训，或提供与使用该研究开发成果相关的技术服务，由此产生的相关差旅费用由甲方承担。

第十六条 甲方有权利用乙方按照本合同约定提供的研究开发成果，进行后续改进。由此产生的具有实质性或创造性技术进步特征的新的技术成果及其权属，由 甲 方享有。

第十七条 双方确定，在本合同有效期内，甲方指定 王辉 为甲方项目联系人，乙

方指定 胡炼 为乙方项目联系人。项目联系人承担以下责任：

1. 负责双方意见的交流和资料传递；
2. 通报工作进展；
3. 协调甲方配合项目研发测试验证工作；
4. 协调双方协作事项。

一方变更项目联系人的，应当及时以书面形式通知另一方。未及时通知并影响本合同履行或造成损失的，应承担相应的责任。

第十八条 双方确定，出现下列情形，致使本合同的履行成为不必要或不可能的，一方可以通知另一方解除本合同：

1. 因发生不可抗力或技术风险；
2. 甲方向乙方提供的基础资料有重大变化；
3. 国家相关法律法规、政策发生重大变化。

第十九条 双方因履行本合同而发生的争议，应协商、调解解决。协商、调解不成的，确定按以下第 2 种方式处理：

1. 提交仲裁委员会仲裁；
2. 依法向合同签订地人民法院起诉。

第二十条 双方约定本合同其他相关事项为：无。

第二十一条 本合同一式 肆 份，具有同等法律效力。

第二十二条 本合同经双方签字盖章后生效。

甲方：潍柴雷沃智慧农业科技股份有限公司 （盖章）

法定代表人/委托代理人： （签名）

年 月 日

乙方：华南农业大学 （盖章）

法定代表人/委托代理人： （签名）

年 月 日

项目编号：

华南农业大学黄埔创新研究院科研项目

任　务　书

项目名称	无人驾驶水田农机抗侧滑突变干扰导航控制方法		
项目类别	科研攻关		
项目起止时间	2023 年 6 月 1 日 至 2024 年 5 月 31 日		
管理单位（甲方）	华南农业大学黄埔创新研究院		
牵头承担单位（乙方）	华南农业大学		
通讯地址	广东省广州市天河区五山路 483 号农业工程楼 307		
邮政编码	510642	单位电话	020-38676975
项目负责人	何杰	联系电话	
项目联系人	汪沛	联系电话	

华南农业大学黄埔创新研究院

二〇二二年制

项目基本信息表

<table>
<tr><td colspan="2">项目名称</td><td colspan="6">无人驾驶水田农机抗侧滑突变干扰导航控制方法</td></tr>
<tr><td colspan="2">项目类别</td><td colspan="6">科研攻关</td></tr>
<tr><td colspan="2">研究方向</td><td colspan="2">水田农机抗侧滑干扰导航控制方法研究</td><td>单位总数</td><td colspan="3">1 个</td></tr>
<tr><td colspan="2">经费预算</td><td colspan="6">总投入 50 万元，其中研究院专项资助经费投入 50.00 万元</td></tr>
<tr><td colspan="2" rowspan="2">项目周期节点</td><td>起始时间</td><td colspan="2">2023 年 6 月 1 日</td><td>结束时间</td><td colspan="2">2024 年 5 月 31 日</td></tr>
<tr><td>实施周期</td><td colspan="2">共 12 个月</td><td>预计中期时间点</td><td colspan="2">2023 年 12 月</td></tr>
<tr><td rowspan="6">项目牵头承担单位</td><td>单位名称</td><td colspan="3">华南农业大学</td><td>单位性质</td><td colspan="2">事业单位</td></tr>
<tr><td>单位所在地</td><td colspan="3">广州</td><td>统一社会信用代码</td><td colspan="2">12440000455416 5634</td></tr>
<tr><td>通信地址</td><td colspan="3">广州市天河区五山路 483 号</td><td>邮政编码</td><td colspan="2">510642</td></tr>
<tr><td>银行账号</td><td colspan="3">3602002609000310520</td><td>法定代表人姓名</td><td colspan="2">刘雅红</td></tr>
<tr><td>单位开户名称</td><td colspan="6">华南农业大学</td></tr>
<tr><td>开户银行（全称）</td><td colspan="6">中国工商银行广东省分行广州市五山支行</td></tr>
<tr><td rowspan="6">项目负责人</td><td>姓 名</td><td>何杰</td><td>性 别</td><td>☑男☐女</td><td>出生日期</td><td colspan="2">1985.8.28</td></tr>
<tr><td>证件类型</td><td>身份证</td><td>证件号码</td><td colspan="4">[redacted]</td></tr>
<tr><td>所在单位</td><td colspan="6">华南农业大学工程学院</td></tr>
<tr><td>最高学位</td><td colspan="6">☑博士 ☐硕士 ☐学士 ☐其他</td></tr>
<tr><td>职 称</td><td colspan="4">☐正高级 ☑副高级 ☐中级 ☐初级 ☐其他</td><td>职务</td><td>无</td></tr>
<tr><td>电子邮箱</td><td colspan="2">hooget@scau.edu.cn</td><td colspan="2">移动电话</td><td colspan="2">[redacted]</td></tr>
</table>

项目联系人	姓 名	汪沛	电子邮箱	wangpei@scau.edu.cn
	固定电话	020-38676975	移动电话	
	证件类型	身份证	证件号码	
项目财务联系人	姓 名	汪沛	电子邮箱	wangpei@scau.edu.cn
	固定电话	020-38676975	移动电话	
	证件类型	身份证	证件号码	

参与单位	序号	单位名称	单位性质	统一社会信用代码
	1			
	2			
	3			
	4			
	…			

项目参加人数	共 12 人。其中：	高级职称 5 人，中级职称 1 人，初级职称 0 人，其他 6 人；
		博士学位 6 人，硕士学位 1 人，学士学位 5 人，其他 0 人。

六、参与人员信息（含项目负责人）

主要研究开发人员：

序号	姓名	性别	年龄	职务	职称	学位	在项目中承担的任务	所在单位	签名
1	何杰	男	38	无	高级实验师	博士	项目总体规划和抗侧滑技术研究	华南农业大学工程学院	
2	汪沛	女	40	无	讲师	博士	数据处理与分析	华南农业大学工程学院	
3	王在满	男	44	无	研究员	博士	样机研制技术	华南农业大学工程学院	
4	臧英	女	50	无	教授	博士	数据分析	华南农业大学工程学院	
5	胡炼	男	39	无	研究员	博士	导航控制系统	华南农业大学工程学院	
6	黄培奎	男	32	无	高级工程师	博士	导航控制设计与试验	华南农业大学工程学院	
7	满忠贤	男	25	无	无	硕士	人工驾驶数据采集与试验	华南农业大学工程学院	
8	李明锦	男	24	无	无	学士	样机研制	华南农业大学工程学院	
9	黄钰峰	男	24	无	无	学士	经验知识分析	华南农业大学工程学院	
10	刘善琪	男	23	无	无	学士	导航算法设计	华南农业大学工程学院	
11	丁帅奇	男	22	无	无	学士	数据驱动	华南农业大学工程学院	
12	黄志钺	男	22	无	无	学士	样机机构设计	华南农业大学工程学院	
13	陈军	男	27	无	无	学士	样机机构设计	华南农业大学工程学院	
14	陈超文	男	24	无	无	学士	数据分析	华南农业大学工程学院	
15	黄大明	男	24	无	无	学士	数据驱动	华南农业大学工程学院	
16	崔子健	男	23	无	无	学士	样机研制	华南农业大学工程学院	
17	樊焯荣	男	23	无	无	学士	样机研制	华南农业大学工程学院	

七、承担、参与单位工作分工及经费分配情况		
承担/参与单位名称（盖章）	工作分工	专项资助经费分配(万元)
华南农业大学	项目方案实施及结题	50
...		
合计		50

八、项目总经费及研究院资助经费预算

（一）研究院专项资助资金拟投入总额：（大写） 伍拾万元 ；（小写）： 50 万元

（二）研究院专项资金分期资助计划（此为正常情况下预计资助计划，中期评估或验收结题不通过的，实验室有权停止或核减资助后续资金）：

经费（万元）	总额	第 1 期	第 2 期
	50	50	0

（三）总经费及研究院专项资助资金投入情况（单位：万元）

	研究院资助专项资金	自筹经费		合计
		自有经费	地方政府投入及其它	
总经费	50	0	0	50

自筹资金投入情况说明：

项目经费预算： (单位：万元)

	项目总经费		实验室专项资助资金	
支出经费	经费额	用途说明	经费额	用途说明
（一）直接费用	39			
1.设备费	2			
其中：购置设备费	2	购买服务器、激光雷达等设备费		
2.业务费	23	用于购买电子材料、关键部件加工、机器作业燃油、发表论文、申请专利、资料打印装订、图书购买、信号传输账号、机器装卸运输等费用		
3.劳务费	14	研究生劳务费、临工工资、科研助理工资等		
（二）间接费用	11	用于学校管理费和科研人员绩效费		
合 计	50			

九、签约页

管理单位（甲方）：华南农业大学黄埔创新研究院　　（盖章）

法定代表人（签章）：

年　　月　　日

项目牵头承担单位（乙方）：　　（盖章）

法定代表人（签章）：

项目负责人（签字）：

年　　月　　日

合同编号：ISTIXS2023070701

技术开发（委托）合同

项目名称：安徽亳州无人农场建设技术服务

委托方（甲方）：安徽中科智能感知股份有限公司

受托方（乙方）：广东工贸职业技术学院

受托方（丙方）：华南农业大学

中华人民共和国科学技术部印制

技术开发（委托）合同书

甲方：安徽中科智能感知科技股份有限公司

住　所　地：芜湖市三山经济开发区龙湖路 8 号创业大街 3 号

法定代表人：张炜

项目联系人：李蜀林

联系方式：安徽中科智能感知科技股份有限公司

通讯地址：芜湖市三山经济开发区龙湖路 8 号创业大街 3 号

电　　话：　　传　　真：

电子信箱：lishulin1909@dingtalk.com

乙方：广东工贸职业技术学院

住　所　地：广州市天河区广州大道北 963 号

法定代表人：何汉武

项目负责人：贺静

项目团队人员：刘益标 、徐勇军、孙涛

项目联系人：贺静

联系方式：　广东工贸职业技术学院机电学院

通讯地址：广州市天河区广州大道北 963 号

电　　话：　　传　　真：020-87647600

电子信箱：hejing_1127@163.com

丙方：华南农业大学

住　所　地：广州市天河区五山路 483 号

法定代表人：刘雅红

项目负责人：何杰

项目团队人员：汪沛、岳孟东、李明锦

项目联系人：何杰

联系方式：　华南农业大学农业工程楼 307

通讯地址：广州市天河区五山路 483 号

电　　话：[redacted]　　传　　真：020-38676975

电子信箱：hooget@scau.edu.cn

甲方委托乙方和丙方就 安徽亳州无人农场 项目进行专项技术服务，并支付相应的技术服务报酬。各方经过平等协商，在真实、充分地表达各自意愿的基础上，根据《中华人民共和国民法典》的规定，达成如下协议，并由各方共同恪守。

第一条：甲方委托乙方和丙方进行技术服务的内容如下：

1. 技术服务的目标：乙方和丙方共同协助甲方建设安徽亳州无人农场，实现耕种管收环节的无人化作业。

2. 乙方技术服务的内容：（1）协助无人驾驶农机调试工作；（2）规划农场各田块作业路径规划；（3）协助指导无人农场作业；（4）培训甲方至少 2 名无人农场技术骨干。

3. 丙方技术服务的内容：（1）协助制定无人农场建设规划和无人农机配置方案；（2）制定无人驾驶农机与云管控平台通讯协议。

第二条：乙方和丙方应按下列要求完成技术服务工作：

1. 技术服务地点：安徽省亳州市谯城区无人农场基地

2. 技术服务期限：2021 年 6 月—2023 年 12 月

3. 技术服务进度：2021 年 6 月制定实施方案与无人驾驶农机配置方案；2021 年 12 月完成无人驾驶农机现场调试；2022 年 12 月完成第一轮无人化作业田间示范；2023 年 12 月完成第二轮无人化作业田间示范。

第三条：为保证乙方和丙方有效进行技术服务工作，甲方应向乙方

和丙方提供下列工作条件和协作事项：

1．提供技术资料：

（1）亳州无人农场基地农田水利建设等相关资料；

（2）建设依托单位（合作社）相关资料；

2．提供工作条件：

（1）为乙方和丙方到基地开展工作提供人员支持；

（2）配合乙方和丙方在基地开展相关技术试验示范的落实、检查和指导等工作。

3．其他：无。

4．甲方提供上述工作条件和协作事项的时间及方式根据项目进度要求，通过技术交流会和电子邮件等方式提供相关技术资料，并配合乙方和丙方在基地现场开展技术调试工作。

第四条：甲方向乙方和丙方支付技术服务费用及支付方式为：

1．技术服务费总额为：30万元（含税）（大写：人民币叁拾万元整），其中乙方技术服务费为20万元（含税）（大写：人民币贰拾万元整）、丙方技术服务费为10万元（含税）（大写：人民币壹拾万元整）。

2．技术服务费由甲方一次（一次或分期）支付乙方和丙方。乙方和丙方分别按照甲方支付金额，提供6%增值税专用发票。

具体支付方式和时间如下：

（1）项目完成第一轮无人化作业田间示范。

（2）甲方付款前，乙方和丙方均应提供合法有效的等额发票，否则甲方有权拒付。

（3）经费的支出和使用乙方和丙方分别按照《广东工贸职业技术

学院横向科技项目及经费管理办法》和《华南农业大学横向科技项目及经费管理办法》执行。

乙方开户银行名称、地址和账号为：

名　　称：广东工贸职业技术学院

开户银行：广东省广州市农业银行五仙桥支行

账　　号：44059801040000144

丙方开户银行名称、地址和账号为：

开户银行：中国工商银行广东省分行广州市五山支行

地　　址：广州市天河区五山路483号

帐　　号：3602002609000310520

第五条：各方确定因履行本合同应遵守的保密义务如下：

甲方：

1.保密内容（包括技术信息和经营信息）:乙方和丙方提供的注明要求保密的技术资料和培训资料。

2．涉密人员范围：参加项目及培训的人员；

3．保密期限：项目合同签订之日起五年内；

4．泄密责任：承担因泄密造成的损失。

乙方：

1.保密内容（包括技术信息和经营信息）：甲方提供的技术资料以及在实施项目的过程中接触到的所有甲方未公开的信息；

2.涉密人员范围：参加项目开发的人员以及与前述人员有密切接触有可能接触到保密信息的人员；

3．保密期限：项目合同签订之日起五年内；

4．泄密责任：承担因泄密造成的损失。

第六条：本合同的变更必须由各方协商一致，并以书面形式确定。但有下列情形之一的，任一方提出变更合同权利与义务的请求，指定被请求方应当在15日内予以答复；逾期未予答复的，视为同意：

1．未能履行合同约定的。

第七条：各方确定以下列标准与方式对乙方和丙方的技术服务工作成果进行验收：

1．乙方和丙方完成技术服务工作的形式：技术培训或现场指导，技术资料和信息提供；

2．技术服务工作成果的验收标准：按项目合同第一条约定的第一点“技术服务的目标”以及技术标准和规范（如有）进行验收；

3．技术服务工作成果的验收方法：现场检查、总结汇报或以及项目示范基地经专家组验收等方式。

4．验收的时间和地点：甲方指定时间和地点。

第八条：各方确定：

在本合同有效期内，各方利用本项目技术服务工作成果所完成的新的技术成果归属由三方协商所有权。

第九条：各方确定，在本合同有效期内，甲方指定李蜀林为甲方项目联系人，乙方指定贺静为乙方项目联系人，丙方指定何杰为丙方项目联系人。

各方变更项目联系人，应当及时以书面形式通知另两方，未及时通知并影响本合同履行或造成损失的，应承担相应的责任。

第十条：各方确定，出现下列情形，致使本合同的履行成为不必要或不可能的，可以解除本合同：

1．发生不可抗力；

2．自然灾害。

第十一条：违约责任

乙方或丙方迟延履行本合同第二条第 3 款的“技术服务进度”中确定的各个阶段的工作的，每个阶段每延误一天，按照技术服务费用总额的千分之五向甲方支付违约金，各个阶段均有迟延的，前述违约金累计计算。

第十二条：各方因履行本合同而发生的争议，应协商、调解解决。协商、调解不成的，确定按以下第 1 种方式处理：

1．提交 芜湖 仲裁委员会仲裁；

2．依法向人民法院起诉。

第十三条：各方确定：本合同及相关附件中所涉及的有关名词和技术术语，其定义和解释如下：

1．无

第十四条：本合同一式 六 份，具有同等法律效力。

第十五条：本合同经各方签字盖章后生效。

（以下无正文）

甲方：安徽中科智能感知科技股份有限公司　（盖章）

法定代表人／委托代理人：李留林　（签名）

2022年7月11日

乙方：广东工贸职业技术学院　（盖章）

法定代表人／委托代理人：　（签名）

年　月　日

丙方：华南农业大学　（盖章）

法定代表人／委托代理人：　（签名）

年　月　日

暨南大学
文献收录证明

检索课题：华南农业大学汪沛发表的文献在 EI 数据库中的收录情况。

检索工具及年限：

EI (Engineering Village2)　　1969-2026 年

检索结果：根据委托方提供的文献目录，经上述数据库及年限范围内检索，共计 3 篇论文被 EI 收录，结果如下：

序号	文献信息	作者顺序	文献类型
1.	Full-coverage Path Planning Algorithm for Dual-helix Driven Robot in Convex Polygonal Farmlands Wang, Pei (College of Engineering, South China Agricultural University, Guangzhou; 510642, China); Luo, Jialong; Xie, Jiasheng; Wang, Jiatao; Luo, Hao; Ning, Jintai; Hu, Lian; He, Jie Source: Nongye Jixie Xuebao/Transactions of the Chinese Society for Agricultural Machinery, v 56, n 12, p 645-656, December 2025 Language: Chinese Database: Compendex Accession number:20255119732556 Document type:Journal article (JA)	第一作者	Journal article (JA)
2.	Real-time 3D Terrain Measurement Method and Experiment in Farmland Leveling Wang, Pei (Key Laboratory of Key Technology on Agricultural Machine and Equipment, Ministry of Education, South China Agricultural University, Guangzhou; 510642, China); Feng, Dawen; Chen, Gaolong;	第一作者	Journal article (JA)

	He, Jie; Hu, Lian; Peng, Jingyi Source: Nongye Jixie Xuebao/Transactions of the Chinese Society for Agricultural Machinery, v 54, n 3, p 41-48, 2023 Language: Chinese Database: Compendex Accession number:20232114129684 Document type:Journal article (JA)		
3.	Agricultural robot positioning system based on laser sensing Hu, Lian (Key Laboratory of Key Technology on Agricultural Machine and Equipment, Ministry of Education, South China Agricultural University, Guangzhou; 510642, China); Wang, Zhimin; Wang, Pei; He, Jie; Jiao, Jinkang; Wang, Chenyang; Li, Mingjin Source: Nongye Gongcheng Xuebao/Transactions of the Chinese Society of Agricultural Engineering, v 39, n 5, p 1-7, March 2023 Language: Chinese Database: Compendex Accession number:20232614311214 Document type:Journal article (JA)	通讯作者	Journal article (JA)

声明：本证明的文献信息由委托人提供，检索结果已由委托人核实确认无误。如果由于委托人提供信息不实而造成任何后果，本查新站概不负责。

检索员：

教育部科技查新工作站(Z15)

暨南大学图书馆学科服务与咨询部

2026 年 3 月 13 日

SCAULIB202626201

检索证明

根据委托人提供的论文材料，委托人华南农业大学工程学院 汪沛(学科类型:自然科学) 8 篇论文收录情况如下表。

序号	论文名称	发表刊物及发表的年月卷期/页码等	作者排名	论文等级	作者文中单位	收录情况	影响因子	中科院大类分区
1	基于激光感知的农业机器人定位系统	农业工程学报 出版年：2023 卷期： 页码：- 文献号： 文献类型：	通讯作者	A 类	华南农业大学	北大核心	无	无
2	农田精准平整过程中三维地形实时测量方法研究	农业机械学报 出版年：2023 卷期： 页码：- 文献号： 文献类型：	第一作者	C 类	华南农业大学	北大核心	无	无
3	Design and Test of Intelligent Farm Machinery Operation Control Platform for Unmanned Farms	AGRONOMY-BASEL 出版年：2024 出版日期：APR 卷期：14 4 页码：- 文献号：804 文献类型：Article	第一作者	A 类	华南农业大学	SCI	IF2-year=3.4 IF5-year=3.8 （2024）	农林科学 2 区 Top 期刊：否 OA 期刊：是 标注：Mega-Journal （2025）

4	无人驾驶农机避障路径跟踪仿真与验证	华南农业大学学报 出版年：2024 卷期： 页码：- 文献号： 文献类型：	第一作者	B 类	华南农业大学	北大核心	无	无
5	Integrated measurement method for field surface topography and tillage depth in rotary tillage operations	COMPUTERS AND ELECTRONICS IN AGRICULTURE 出版年：2025 出版日期：DEC 卷期：239 页码：- 文献号：111000 文献类型：Article	通讯作者	T2 类	华南农业大学	SCI	IF2-year=8.9 IF5-year=9.3 （2024）	农林科学 1 区 Top 期刊：是 OA 期刊：否 （2025）
6	Neural Network-Based SLAM/GNSS Fusion Localization Algorithm for Agricultural Robots in Orchard GNSS-Degraded or Denied Environments	AGRICULTURE-BASEL 出版年：2025 出版日期：JUL 25 卷期：15 15 页码：- 文献号：1612 文献类型：Article	共同通讯作者（倒数第一）	A 类	华南农业大学	SCI	IF2-year=3.6 IF5-year=3.8 （2024）	农林科学 2 区 Top 期刊：否 OA 期刊：是 （2025）
7	疏松土层厚度及其压实量对灌水沉降的影响	农业工程学报 出版年：2025 卷期： 页码：- 文献号：	通讯作者	T2 类	华南农业大学	北大核心	无	无

		文献类型：						
8	双螺旋驱动式机器人全覆盖作业路径规划算法研究	农业机械学报 出版年：2025 卷期：　页码：- 文献号： 文献类型：	第一作者	A 类	华南农业大学	北大核心	无	无

说明：论文等级和中科院大类分区按《华南农业大学学术论文评价方案（试行）》划分。

报告免责声明:如未盖章,报告无效

检索员：张进

华南农业大学图书馆

2026-03-13

美国《工程索引》（Ei）收录期刊
美国《化学文摘》（CA）收录期刊
Scopus数据库收录期刊
中文核心期刊　中国科技核心期刊
中国科学引文数据库来源期刊
RCCSE中国权威学术期刊

ISSN 1000-1298
CODEN NUYCA3

农业机械学报

NONGYE JIXIE XUEBAO

Transactions of the Chinese Society for Agricultural Machinery

第 54 卷

特约专稿

反刍家畜典型行为监测与生理状况识别方法研究综述

张宏鸣　孙　扬　赵春平　王博文　李　斌　王炳科

2023 3

ISSN 1000-1298

中国农业机械学会主办

农业机械学报
NONGYE JIXIE XUEBAO

2023 年　第 3 期（第 54 卷）

目　次

农业信息化工程

农业水土工程

doi:10.6041/j.issn.1000-1298.2023.03.004

农田精准平整过程中三维地形实时测量方法研究

汪　沛[1,2]　冯达文[1]　陈高隆[1]　何　杰[1,2]　胡　炼[1,2]　彭靖怡[1]

(1.华南农业大学南方农业机械与装备关键技术教育部重点实验室,广州 510642;
2.岭南现代农业科学与技术广东省实验室茂名分中心,茂名 525000)

摘要:为提高农田平整作业过程中平后区域田面地形实时测量精度,本文提出一种农田精准平整过程中三维地形实时测量方法(Real-time 3D terrain measurement, Rt3DTM)。以安装有 GNSS 双天线和姿态传感器的支撑轮式旱地平地机为地形测量平台,利用卡尔曼滤波器融合 GNSS 与加速度提高定位精度,通过建立平地铲运动学模型获得支撑轮底点的车体坐标,结合平地铲位姿信息对支撑轮底点进行世界坐标解算,并利用最邻近插值法生成地形图。静态试验表明,Rt3DTM 方法能准确解算支撑轮底点坐标,平面测量均方根误差小于 10 mm,高程测量均方根误差不大于 20 mm。水泥路面试验结果表明,在 3 组不同车速下测量同一段水泥路面三维地形,与真值的高差均方根误差均小于 30 mm。田间试验结果表明,Rt3DTM 测量的高程均方根误差为 16.5 mm,平整度为 16 mm,小于 30 mm 的高差分布列为 95.8%,相比机载 GNSS 测量方法的均方根误差准确性提高 29.5%,平整度准确性提高 11.1%,高差分布列准确性提高 9.5%。提出的 Rt3DTM 方法能实时准确地获取平整作业过程中平后区域的地形信息,为无人化农田平整实时路径规划研究提供基础。

关键词:三维地形;实时测量;农田平整;GNSS;卡尔曼滤波

中图分类号:S281;S29　　**文献标识码**:A　　**文章编号**:1000-1298(2023)03-0041-08　　**OSID**:

Real-time 3D Terrain Measurement Method and Experiment in Farmland Leveling

WANG Pei[1,2]　FENG Dawen[1]　CHEN Gaolong[1]　HE Jie[1,2]　HU Lian[1,2]　PENG Jingyi[1]

(1. *Key Laboratory of Key Technology on Agricultural Machine and Equipment, Ministry of Education, South China Agricultural University, Guangzhou* 510642, *China*
2. *Maoming Branch Center, Lingnan Modern Agricultural Science and Technology Guangdong Laboratory, Maoming* 525000, *China*)

Abstract: In order to improve the real-time measurement accuracy of field surface topography in the area behind the leveling in the process of farmland leveling operation, a real-time measurement method of 3D topography in the process of farmland precision leveling was proposed. Using a supported-wheel dryland grader installed with GNSS dual antennas and attitude sensors as a terrain measurement platform, the Kalman filter was firstly used to fuse GNSS and acceleration to improve the positioning accuracy and frequency, and then the vehicle coordinates of the bottom point of the supported wheel were obtained by establishing the kinematic model of the grader, and finally the geodetic coordinates of the bottom point of the supported wheel were solved by combining the information of the position of grader and the topographic map was generated by using the nearest neighbor interpolation method. The test verification showed that this method can accurately solve the coordinates of the bottom point of the support wheel, and the root mean square error of the plane measurement was less than 10 mm, and the root mean square error of the elevation deviation was not more than 20 mm. The test results of cement pavement showed that the root mean square error of the elevation difference between the measured value and the true value was less than 30 mm when the three-dimensional terrain of the same section of cement pavement was measured at

收稿日期:2022-11-28　修回日期:2023-01-06

基金项目:国家自然科学基金项目(32101623、32071913)、广东省科技计划项目(2021B1212040009)和国家现代农业产业技术体系项目(CARS-13)

作者简介:汪沛(1983—),女,讲师,博士,主要从事无人农场和精准作业研究,E-mail:wangpei@scau.edu.cn

通信作者:胡炼(1984—),男,研究员,博士生导师,主要从事智能农机装备和无人农场研究,E-mail:lianhu@scau.edu.cn

three different speeds. The field test results showed that the root mean square error of the measured terrain was 16.5 mm, flatness was 16 mm, and the elevation difference distribution less than 30 mm was 95.8%. Compared with the airborne GNSS measurement method, the root mean square error accuracy was improved by 29.5%, flatness accuracy was improved by 11.1%, and height difference distribution column accuracy was improved by 9.5%. The method proposed can obtain the topographic information of the area behind the leveling in real time and accurately during the leveling operation, and provide a basis for the research of real-time path planning of unmanned farmland leveling.

Key words: 3D terrain; real-time measurement; farmland leveling; GNSS; Kalman filter

0 引言

农田精准平整可提高农田灌溉效率,增加灌水均匀度和肥料均匀性,并且能抑制杂草生长,起到保水保肥抑草作用[1-3]。因此,农田精准平整技术是农业规模化和精细化生产的有力保障[4-6]。在农田精准平整技术中,全球导航卫星系统(Global navigation satellite system,GNSS)因其使用便捷,无距离限制,能快速获取位置信息等优点得到广泛应用[7-8],但目前在农田平整作业中仍靠操作人员观察未平整农田的地势,再凭经验决定平整基准高度和平整作业路线,导致平整作业效率低,同时平整质量无法保障[9-11],因此亟需研究农田地形信息测量技术,获取农田三维地形[12-13]。

近年来,无人机、摄影和激光雷达等相互结合的遥感技术快速发展,具有覆盖面积大、作业效率高等优点,已被应用于农田测量领域[13-14]。POLAT 等[15]对基于机载激光雷达和无人机的数字高程模型在垂直精度等方面进行了比较,发现基于无人机的模型和基于激光雷达的模型精度相同,且其优点多于激光雷达模型。杜蒙蒙等[16]提出了一种基于多旋翼无人机与激光测距技术的农田地形测绘方法,该方法获取的海拔与手持 PPK-GPS 设备采集海拔的均方根误差为 5.2 cm。GNSS 在农田地形测量方面也得到了应用,张漫等[17]设计了一种 RTD-DGPS 与激光测量相结合的三维地形信息测量系统,测量误差不超过 4 cm。李宏鹏等[18]集成了 RTK-GPS 定位技术和农田地形测量方法,开发了基于 GNSS 的农田快速地形测量系统,在静态试验下高程测量精度小于 1 cm。ZHAO 等[19]采用 GNSS 和姿态航向参考系统(Attitude and heading reference system, AHRS)获取了水田硬底层的高低不平信息,不平等级介于 C 级和 E 级之间。景云鹏等[9]提出了一种基于 GNSS 双天线和姿态航向参考系统组合的地形测量方法,试验结果表明与单天线地形测量方式相比,双天线测量得到的农田平整度的准确性提高约 10%,有效降低了测量误差。

综上,目前农田三维地形测量技术主要分为机载 GNSS 和无人机搭载的传感器两种方式。机载 GNSS 地形测量方法是通过采集 GNSS 天线的坐标,依据天线与铲刀间的固定高差计算铲刀的位置信息,进而测量农田地形,但液压油缸的运动导致平地铲无法准确反映地形变化,使得 GNSS 定位不能准确表达农田地形。无人机搭载传感器的方式受电池续航等因素影响[20],不能持续在空中进行农田地形实时测量,且需在平整前、平整后分别测量才能获得农田地形,后台软件处理无人机获取的数据也需要一定时间[21]。因此,以上农田表面三维地形测量方法主要应用于平整前计算平整基准和平整后评估平整效果,而平整过程中实时获得平整后区域的地形信息是根据平整质量动态规划平整路径的基础。为此,本文针对在农田平整过程中无法实时测量平后地形问题,以支撑轮式旱地平地机为平台,构建平地铲运动学模型,结合平地铲位姿信息解算出支撑轮底的三维坐标信息表征农田地形,最后进行田间平整作业试验验证。

1 农田平整过程中三维地形实时测量方法

1.1 平整过程中三维地形实时测量原理

农田平整过程中三维地形实时测量方法(Real-time 3D terrain measurement, Rt3DTM)通过测量旱地平地机支撑轮底点坐标实现平整过程中平后区域三维地形实时测量,如图 1 所示。以安装有 GNSS 双天线和姿态传感器的支撑轮式旱地平地机为地形实时测量研究平台[22],建立以定位天线相位中心为原点的车体坐标系。采用卡尔曼滤波器[23]融合 GNSS 与三轴加速度信息以获取最优估计 GNSS 定位信息,利用平地机支撑轮始终由平整后农田地表支撑的特性,通过平地铲机械结构与位移传感器实时测量液压油缸长度建立平地铲运动学模型,获取支撑轮底点在车体坐标系下的坐标信息,并结合 GNSS 双天线航向信息与平地铲姿态信息解算各支撑轮底点在世界坐标系下的位置信息,进而实时得到平整后农田三维地形。

1.2 GNSS 和加速度卡尔曼融合测量算法

GNSS 测量平地铲的精度直接影响地形测量精

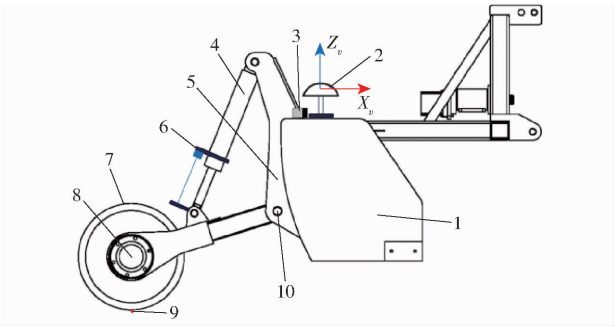

图 1　平整过程中三维地形实时测量示意图

Fig. 1　Schematic of 3D terrain measurement in real time during grading process

1. 平地铲　2. GNSS 天线　3. 姿态传感器　4. 液压油缸　5. 高程调节架　6. 位移传感器　7. 支撑轮　8. 支撑轮中心　9. 支撑轮底点　10. 支撑轮架转动点

度，在复杂田间作业时平地铲位姿频繁变化会导致 GNSS 输出数据精度降低[24]。因此，采用卡尔曼滤波器融合 GNSS 定位与姿态传感器输出的加速度以获取更高精度的定位信息。

加速度输出误差处理。机具频繁振动会引起姿态传感器输出的数据中含异常值，采用 3σ 准则剔除异常加速度[25]，计算式为

$$|a_i - L| > 3\sigma \tag{1}$$

式中　a_i——采样时刻 i 加速度，m/s^2

L——加速度算术平均值，m/s^2

σ——采样时刻 i 加速度标准差，m/s^2

误差若大于这个区间，则认为该加速度为异常值进行剔除。

卡尔曼滤波器融合 GNSS 定位天线三轴位移与三轴加速度。调整平地铲至合适的高度，获取一个世界基准坐标点。平地铲作业时，依据定位天线实时定位与基准坐标得到的三轴位移与加速度融合获取精准位移，定位天线的三轴位移和速度计算式为

$$S_k = S_{k-1} + \dot{S}_{k-1}T_0 + 0.5a_{k-1}T_0^2 \tag{2}$$

$$\dot{S}_k = \dot{S}_{k-1} + a_{k-1}T_0 \tag{3}$$

式中　S_{k-1}——定位天线第 $k-1$ 个采样时刻位移，mm

$\dot{S}_{k-1}$——定位天线第 $k-1$ 个采样时刻速度，mm/s

a_{k-1}——定位天线第 $k-1$ 个采样时刻加速度，mm/s^2

T_0——采样时间，s

将 S_{k-1} 和 $\dot{S}_{k-1}$ 作为运动空间的二维状态向量 $\boldsymbol{x}_k = (S_{k-1}, \dot{S}_{k-1})$。建立运动递推方程与观测方程

$$\boldsymbol{x}_k = \boldsymbol{A}\boldsymbol{x}_{k-1} + \boldsymbol{B}\boldsymbol{u}_{k-1} + \boldsymbol{w}_{k-1} \tag{4}$$

$$\boldsymbol{z}_k = \boldsymbol{H}\boldsymbol{x}_k + \boldsymbol{v}_k \tag{5}$$

其中　$\boldsymbol{A} = \begin{bmatrix} 1 & T_0 \\ 0 & 1 \end{bmatrix}$　$\boldsymbol{B} = \begin{bmatrix} 0.5T_0^2 \\ T_0 \end{bmatrix}$　$\boldsymbol{H} = \begin{bmatrix} 1 \\ 0 \end{bmatrix}$

式中　$\boldsymbol{A}$——状态转移矩阵　　$\boldsymbol{B}$——输入矩阵

$\boldsymbol{H}$——观测矩阵　　$\boldsymbol{u}_{k-1}$——输入向量

$\boldsymbol{w}_{k-1}$——过程噪声　　$\boldsymbol{v}_k$——观测噪声

融合流程如图 2 所示，通过卡尔曼滤波器融合得到 GNSS 定位天线三轴最优位移 $\boldsymbol{x}_{d,k}^{kf}$ 与世界基准坐标点 $\boldsymbol{P}_{b\_w}$ 计算得到最优世界坐标矩阵为

$$\boldsymbol{P}_k^{kf} = \boldsymbol{x}_{d,k}^{kf} + \boldsymbol{P}_{b\_w} \tag{6}$$

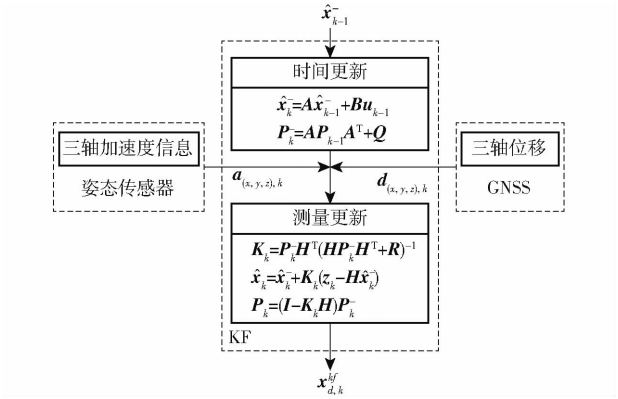

图 2　定位融合算法流程图

Fig. 2　Principle diagram of localization estimation algorithm

1.3　平地铲运动学模型

如图 3 所示，模型涉及车体坐标系（$O_vX_vY_vZ_v$）与世界坐标系（$O_wX_wY_wZ_w$）。设平地铲为刚体，建立车体坐标系以 GNSS 定位天线的定位点为原点 O_v，X_v 轴垂直双天线连线指向前方，Y_v 轴与双天线连接线重合指向定向天线，Z_v 轴垂直于 $X_vO_vY_v$ 指向上方；姿态传感器的 XYZ 三轴分别与 $X_vY_vZ_v$ 保持同一方向。模型中，油缸长度由位移传感器测量获取，位移传感器的输出值与油缸长度拟合得到关系式

$$\begin{cases} c_1 = -0.024\,34p_1 + 2\,953 \\ c_2 = -0.023\,19p_2 + 2\,629 \end{cases} \tag{7}$$

式中　c_1、c_2——右侧与左侧油缸实时测量长度，mm

p_1、p_2——位移传感器输出

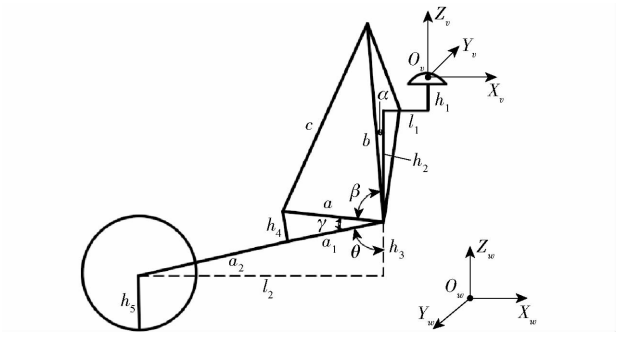

图 3　平地铲运动模型示意图

Fig. 3　Schematic of grading shovel movement model

在车体坐标系中,首先计算相对平地铲前进方向最右侧一个支撑轮底点的车体坐标,原点减去天线安装处至支撑轮中心在 $X_vO_vY_v$ 的投影距离可得到该支撑轮底点在 X_v 轴上的距离;因在 Y_v 轴方向上,平地铲与支撑轮表现为刚体,所以该支撑轮底点存在固定距离 d_y;Z_v 轴方向上,原点与田面的距离即为定位原点与田面的高差,其中包括天线与平地铲垂直固定距离和由液压油缸伸缩引起的垂直变化高度。综上可得到最右侧支撑轮底点车体坐标的解算方程组为

$$\begin{cases}\alpha=\arccos\dfrac{h_2^2+b^2-26.5^2}{2h_2b}\\ \beta=\arccos\dfrac{a^2+b^2-c^2}{2ab}\\ \gamma=\arccos\dfrac{a^2+a_1^2-h_4^2}{2aa_1}\\ \theta=180-\alpha-\beta-\gamma\\ l_2=(a_1+a_2)\sin\theta\\ h_3=(a_1+a_2)\cos\theta\end{cases}\tag{8}$$

式中 a、a_1、a_2、b、l_1、h_1、h_2、h_4、h_5、α——平地铲结构性常量

θ——支撑轮架与与垂直线间的夹角,(°)

β——支撑轮架与高程调节架间的夹角,(°)

c——油缸长度,mm

l_2——支撑轮底点与支撑轮架转动点在 X_v 轴上的距离,mm

h_3——支撑轮架转动点与支撑轮中心在 Z_v 轴上的距离,mm

在平整过程中,依据实时测量的右侧油缸长度 c_1 代入式(8)可得到最右侧支撑轮底点在车体坐标矩阵为

$$\boldsymbol{P}_{v1}=\begin{bmatrix}X_{v1}\\Y_{v1}\\Z_{v1}\end{bmatrix}=\begin{bmatrix}-l_1-l_2\\d_y\\-h_1-h_2-h_3-h_5\end{bmatrix}\tag{9}$$

在模型中,可依据支撑轮的间距由最右侧支撑轮坐标平移得到任意一个支撑轮底点的车体坐标,如已知最左侧与最右侧支撑轮的间距为 d_b,坐标平移得到最左侧支撑轮中心与 Y_v 轴垂直交点的坐标 $\boldsymbol{P}'_v=[0\quad d_y+d_b\quad 0]^{\mathrm{T}}$,结合左侧油缸长度 c_2 与式(8)可求取最左侧支撑轮底点在车体坐标矩阵为

$$\boldsymbol{P}_{v2}=[X_{v2}\quad Y_{v2}\quad Z_{v2}]^{\mathrm{T}}=\boldsymbol{P}'_v+\boldsymbol{P}_{v1}\tag{10}$$

根据姿态传感器输出的横滚角、俯仰角和 GNSS 双天线获取的航向角信息,建立姿态传感器绕 XYZ 三轴旋转的矩阵 $\boldsymbol{R}_x$、$\boldsymbol{R}_y$、$\boldsymbol{R}_z$,得到综合旋转矩阵为

$$\boldsymbol{R}_v^w=\boldsymbol{R}_z^{\mathrm{T}}\boldsymbol{R}_y^{\mathrm{T}}\boldsymbol{R}_x^{\mathrm{T}}=\begin{bmatrix}\cos\varphi_y&-\sin\varphi_y&0\\\sin\varphi_y&\cos\varphi_y&0\\0&0&1\end{bmatrix}\begin{bmatrix}\cos\varphi_p&0&\sin\varphi_p\\0&1&0\\-\sin\varphi_p&0&\cos\varphi_p\end{bmatrix}\cdot\begin{bmatrix}1&0&0\\0&\cos\varphi_r&-\sin\varphi_r\\0&\sin\varphi_r&\cos\varphi_r\end{bmatrix}\tag{11}$$

式中 φ_y——航向角,(°)

φ_p——俯仰角,(°)

φ_r——横滚角,(°)

基于式(6)得到的定位天线最优世界坐标矩阵 $\boldsymbol{P}_k^{kf}$,结合式(8)~(11)可得两侧支撑轮底点在世界坐标系下的坐标为

$$\begin{cases}\boldsymbol{P}_{w1}=\boldsymbol{R}_v^w\boldsymbol{P}_{v1}+\boldsymbol{P}_k^{kf}\\\boldsymbol{P}_{w2}=\boldsymbol{R}_v^w\boldsymbol{P}_{v2}+\boldsymbol{P}_k^{kf}\end{cases}\tag{12}$$

式中 $\boldsymbol{P}_{w1}$、$\boldsymbol{P}_{w2}$——最右与最左侧支撑轮底点的世界坐标矩阵

平地铲支撑轮底点为支撑轮与田面的切点,平地铲运动学模型输出点信息即为支撑轮与田面切点的坐标信息,对所有输出的支撑轮底点集合可获取农田地形点云,并采用最邻近插值法生成地形图。

2 地形测量试验

2.1 试验材料与评价方法

2.1.1 试验材料

如图 4 所示,采用久保田 704 型拖拉机和悬挂多轮式旱地平地机(铲宽为 2.2 m)为试验平台,试验选择最左与最右侧支撑轮进行地形测量验证。农田三维地形实时测量方法集成到团队前期研发的基于 Android 的 GNSS 农田平整系统中。采用布瑞特科技公司生产的 BRT38 型位移传感器测量液压油缸长度,其拉绳长为 1 000 mm,分辨率为 4 096 bits,

图 4 地形实时测量平台与测试现场

Fig. 4 Topographic real-time measurement platform and test site

1. 定位天线 2. 定向天线 3. 姿态传感器 4. 最左侧支撑轮 5. 平整控制系统 6. 位移传感器 7. 平地铲 8. 最右侧支撑轮

线性精度达到 ±0.1%，最大工作速度为 1 m/s。采用维特智能公司制造的 HWT－6052 型姿态传感器，其横滚角和俯仰角精度在无磁场干扰且校准下均小于 0.01°，加速度静态测量误差为 0.02 m/s^2。定位系统采用北京和芯星通科技有限公司生产的 UB482 型全系统双天线卫星定位板卡，其 RTK 精度在平面测量时为 10 mm ± 1 mm，高程测量为 15 mm ± 1 mm，双天线航向精度为 0.2(°)/R，其中，R 为基线距离，单位 m。试验使用 Leica Ms60 型全站仪（50 m 范围内，扫描精度为 0.6 mm，扫描点间隔为 100 mm）采集农田表面数据作为三维地形参照标准。

2.1.2　测量精度评价方法

为评价地形测量方法的精度，采用均方根误差和高差分布列进行分析评价。均方根误差用于衡量测量值与真实值之间的误差，本文所提方法测量的高程与对应的路面真实高程差值均方根误差越小，说明该方法测量地形与真实地形越接近[26]。高差分布列用于评价测量的地形与真实地形的差异与分布特征，即通过计算统计所有测量点与其对应真实点的高差小于某一距离的百分比[3]。

2.2　静态试验

为验证 Rt3DTM 的可行性，设计了静态试验分析测量精度，试验现场如图 5 所示，采用全站仪测量放置在最左侧与最右侧支撑轮顶端的棱镜三维坐标信息，依据支撑轮轮径计算支撑轮底点的三维坐标信息，并以此底点三维坐标信息作为真值与 Rt3DTM 的测量数据对比得到 X、Y、Z 方向的偏差，试验设置液压油缸长度分别为 735、704、671、650、630 mm，其结果如表 1 所示。对表 1 进行统计分析，结果如表 2 所示。

图 5　静态试验现场

Fig. 5　Static test site

1. 全站仪　2. 棱镜

由表 2 可知，在静态下，使用 Rt3DTM 测量的支撑轮底点坐标在平面方向的均方根误差均不大于 9 mm。高程方向的均方根误差不大于 20 mm。显然，平面测量精度明显优于高程测量精度，主要是由于 GNSS 的高程测量精度低于平面测量精度。同时，

表 1　静态试验测量结果

Tab. 1　Static test measurement results　mm

位置	油缸长度	X 方向偏差	Y 方向偏差	Z 方向偏差
最右侧支撑轮底点	735	1	9	17
	704	5	9	21
	671	9	10	14
	650	7	6	7
	630	5	3	20
最左侧支撑轮底点	735	7	1	4
	704	3	9	18
	671	2	12	25
	650	1	9	26
	630	0	9	19

表 2　静态试验结果偏差统计

Tab. 2　Deviation statistics of static test results　mm

位置	方向	最小偏差	最大偏差	均方根误差
最右侧支撑轮底点	X	1	9	6
	Y	3	10	8
	Z	7	21	17
最左侧支撑轮底点	X	0	7	4
	Y	1	12	9
	Z	4	26	20

各支撑轮底端与农田接触部分为小平面，此区域下农田高程基本保持一致，则平面精度存在毫米级损失并不影响高程精度。因此，在高精度平面信息与区域高程一致的原则下，动态试验中将高程测量作为研究对象。

2.3　水泥路面试验

为了验证 Rt3DTM 在动态环境下的性能，在华南农业大学增城教学科研基地选用一条长约 80 m 的水泥地进行试验。卡尔曼滤波器参数 $\boldsymbol{Q}$ 与 R 比例决定滤波效果[27]，基于试验数据的试错搜索处理，得到 $\boldsymbol{Q}=\begin{bmatrix}5 & 0\\ 0 & 5\end{bmatrix}$；在 XY 方向融合时 $R=10$，在 Z 方向 $R=15$。使用平地机控制系统调整平地铲刀距地一定高度，将此高度作为基准高程并打开自动平整模式，平地机分别以行驶速度 0.75、1.2、1.6 m/s 模拟平整作业并同时进行地形测量，完成后利用全站仪扫描水泥路面的三维信息作为路面的真实三维信息。以测量点的平面坐标在路面真实三维点云信息遍历出最近的真实点，通过比较测量点与真实点的高程，得到 3 个速度下测量点的高差如图 6 所示。

由图 6 可知，经过卡尔曼滤波器融合后的定位数据波动明显减小，3 组速度试验下基于滤波后定位数据获取的支撑轮底点测量值与真实值高差的均方根误差分别为 11.8、19.6、27.4 mm；小于 30 mm

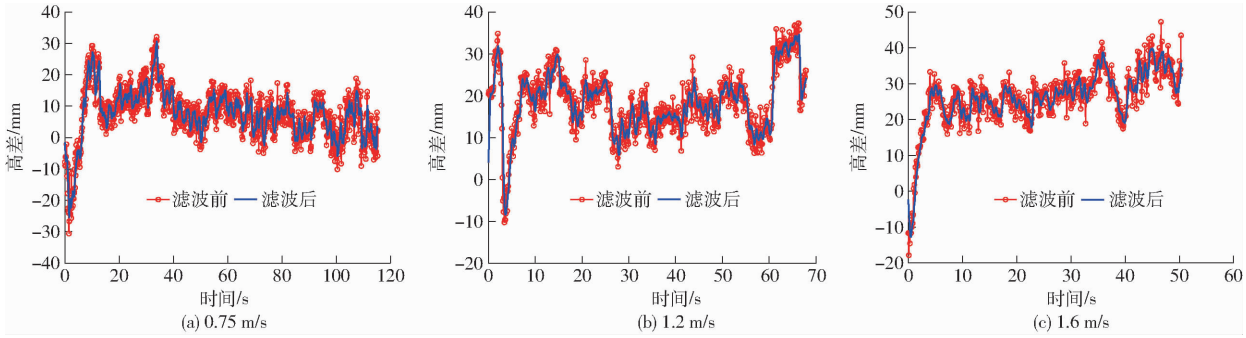

图 6 不同车速下测量值与真实值的高差

Fig. 6 Elevation difference between measured and true values at different vehicle speeds

的高差分布列分别为 99.83%、92.35% 和 72.42%。试验结果表明,设计的卡尔曼滤波器能有效提高定位精度,以及 Rt3DTM 能够在模拟平地作业过程中准确地测量路面高程,绘制的路面地形与路面真实地形高度重合。

2.4 田间试验

为验证 Rt3DTM 在实际作业中的测量性能,分别使用 Rt3DTM 与机载 GNSS 农田地形测量方法进行地形采集。在华南农业大学增城教学科研基地选用一块农田(面积为 80 m×30 m)进行平整作业,并实时测量平整后区域的农田地形,平整作业以连环式路径进行,平均作业速度为 1.24 m/s。全站仪架设在作业农田的中间位置进行扫描,以保证全站仪测量精度,如图 7 所示。

图 7 全田地形测量

Fig. 7 Whole field topographic survey

将 3 种方法采集的地形点云信息通过 Matlab 插值后得到地形图如图 8 所示。由图 8 可知,Rt3DTM 明显优于机载 GNSS 测量方法,地形相似度更高。由图 8b 可知,多处地形略高于真实地形,原因是在平整过程中平地铲空载且铲刀与真实田面有一定高差,而 Rt3DTM 中的支撑轮始终紧贴地面行驶,因此解决了机载 GNSS 测量方法由于平地铲空载时造成的测量误差,提高了地形测量精度。

采用均方根误差、平整度[18]和高差分布列对两种方法的测量结果进行评价,结果如表 3 所示。相比于机载 GNSS 测量方法,Rt3DTM 测量结果的均方根误差由 23.4 mm 下降到 16.5 mm,准确性提高 29.5%;平整度由 22 mm 下降到 16 mm,准确性提高 11.1%;小于 30 mm 的高差分布列由 87.5% 提高到 95.8%,准确性提高 9.5%。试验结果表明,Rt3DTM 测量得到的农田地形与真实地形重合度更高,其性能更优于机载 GNSS 测量方法。

3 结论

(1)提出了平整作业过程中农田三维地形实时测量方法,构建了平地铲运动学模型,结合平地铲位姿信息准确地解算到了支撑轮底点位置坐标。

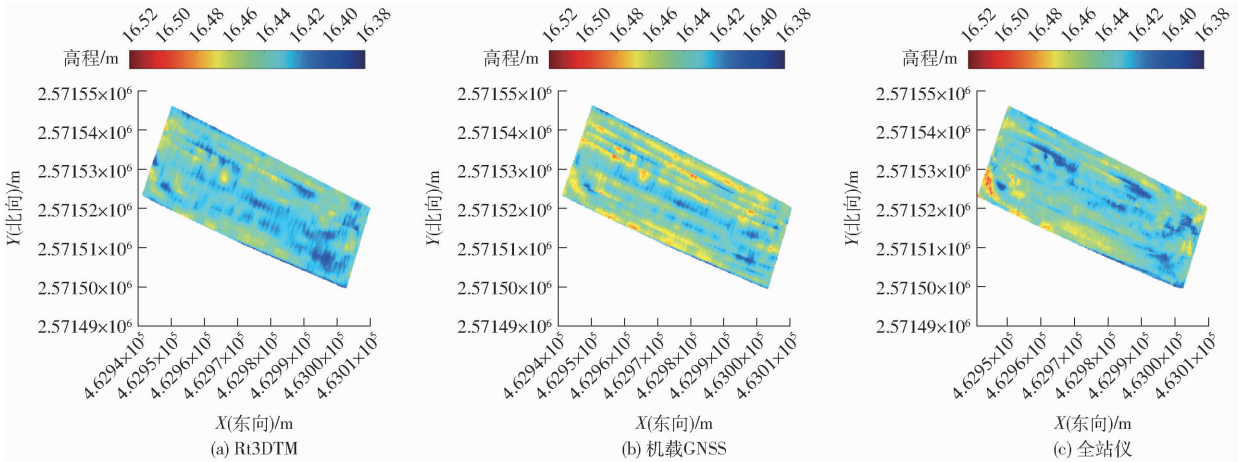

图 8 不同测量方式地形测量结果

Fig. 8 Topographic measurement results of different measurement methods

表 3　Rt3DTM 与机载 GNSS 测量方法地形测量结果统计

Tab. 3　Statistics of topographic measurements by Rt3DTM and airborne GNSS measurement methods

方法	均方根误差/mm	平整度/mm	高差分布列（<30 mm）/%
全站仪		18	
Rt3DTM	16.5	16	95.8
机载 GNSS	23.4	22	87.5

注：全站仪测量地形为真实地形，其不存在均方根误差和高差分布列。

（2）设计了融合 GNSS 定位与三轴加速度的卡尔曼滤波器，提高了平地铲田间作业时位姿频繁变化时的定位精度。

（3）静态、水泥路面动态和田间作业 3 组试验结果表明：静态平面测量均方根误差小于 10 mm，高程测量均方根误差不大于 20 mm；实时测量方法在动态下可准确获取水泥路面地形信息，平地机在速度 0.75、1.2、1.6 m/s 行驶下测量结果的均方根误差分别为 11.8、19.6、27.4 mm；田间作业中测量的均方根误差为 16.5 mm，平整度为 16 mm，小于 30 mm 的高差分布列为 95.8%，相比传统测量方法的均方根误差准确性提高 29.5%，平整度准确性提高 11.1%，高差分布列准确性提高 9.5%，结果表明实时测量方法测量的地形与真实地形重合度更高，可为平整作业实时路径规划研究提供准确的实时三维地形。

参　考　文　献

[1] 胡炼，罗锡文，林潮兴，等. 1PJ－4.0 型水田激光平地机设计与试验[J]. 农业机械学报，2014，45(4)：146－151.
HU Lian，LUO Xiwen，LIN Chaoxing，et al. Development of 1PJ－4.0 laser leveler installed on a wheeled tractor for paddy field[J]. Transactions of the Chinese Society for Agricultural Machinery，2014，45(4)：146－151.（in Chinese）

[2] TANG L，HU L，ZANG Y，et al. Method and experiment for height measurement of scraper with water surface as benchmark in paddy field[J]. Computers and Electronics in Agriculture，2018，152：198－205.

[3] 李笑，李宏鹏，牛东岭，等. 基于全球导航卫星系统的智能化精细平地系统优化与试验[J]. 农业工程学报，2015，31(3)：48－55.
LI Xiao，LI Hongpeng，NIU Dongling，et al. Optimization of GNSS-controlled land leveling system and related experiments[J]. Transactions of the CSAE，2015，31(3)：48－55.（in Chinese）

[4] 董玉娟，石奉华. GPS－RTK 结合手机奥维互动地图在农田土地平整测量中的应用[J]. 安徽农业科学，2016，44(31)：238－241.
DONG Yujuan，SHI Fenghua. Application of GPS－RTK and mobile phone orville interactive map in the agricultural land leveling survey[J]. Journal of Anhui Agriculture Science，2016，44(31)：238－241.（in Chinese）

[5] ZHAO R，HU L，LUO X，et al. Method for estimating vertical kinematic states of working implements based on laser receivers and accelerometers[J]. Biosystems Engineering，2021，203：9－21.

[6] 翟长远，杨硕，王秀，等. 农机装备智能测控技术研究现状与展望[J]. 农业机械学报，2022，53(4)：1－20.
ZHAI Changyuan，YANG Shuo，WANG Xiu，et al. Status and prospect of intelligent measurement and control technology for agricultural equipment[J]. Transactions of the Chinese Society for Agricultural Machinery，2022，53(4)：1－20.（in Chinese）

[7] 夏友祥，刘刚，康熙，等. 基于 GNSS 的农田平整定位精度优化与试验[J]. 农业机械学报，2017，48(增刊)：40－44.
XIA Youxiang，LIU Gang，KANG Xi，et al. Optimization and analysis of location accuracy based on GNSS-controlled precise land leveling system[J]. Transactions of the Chinese Society for Agricultural Machinery，2017，48(Supp.)：40－44.（in Chinese）

[8] 胡炼，杨伟伟，许奕，等. 基于 GPS 技术的水田平地机的设计与试验[J]. 华南农业大学学报，2015，36(5)：130－134.
HU Lian，YANG Weiwei，XU Yi，et al. Design and experiment of paddy field leveler based on GPS[J]. Journal of South China Agricultural University，2015，36(5)：130－134.（in Chinese）

[9] 景云鹏，金志坤，刘刚. GNSS 双天线结合 AHRS 测量农田地形[J]. 农业工程学报，2019，35(21)：166－174.
JING Yunpeng，JIN Zhikun，LIU Gang. Topographic survey of farmland based on GNSS dual antenna combined with AHRS[J]. Transactions of the CSAE，2019，35(21)：166－174.（in Chinese）

[10] 王岩，李宏鹏，牛东岭，等. GNSS 平地作业路径实时规划与导航方法研究[J]. 农业机械学报，2014，45(增刊)：271－275.
WANG Yan，LI Hongpeng，NIU Dongling，et al. Real-time path planning and navigation in GNSS-controlled land leveling[J]. Transactions of the Chinese Society for Agricultural Machinery，2014，45(Supp.)：271－275.（in Chinese）

[11] 刘刚，康熙，夏友祥，等. 基于 GNSS 农田平整全局路径规划方法与试验[J]. 农业机械学报，2018，49(5)：27－33.
LIU Gang，KANG Xi，XIA Youxiang，et al. Global path planning algorithm and experiment based on GNSS-controlled precise land leveling system[J]. Transactions of the Chinese Society for Agricultural Machinery，2018，49(5)：27－33.（in Chinese）

[12] 郎晓哲，刘刚，谢幸福，等. 机载式农田三维地形测量系统设计与试验[J]. 农业机械学报，2009，40(增刊)：69－72.
LANG Xiaozhe，LIU Gang，XIE Xingfu，et al. Tractor-mounted field 3-D topography surveying system[J]. Transactions of the Chinese Society for Agricultural Machinery，2009，40(Supp.)：69－72.（in Chinese）

[13] 金志坤，景云鹏，刘刚. 基于无人机 LiDAR 的农田平整地势测量方法[J]. 农业机械学报，2021，52(增刊)：51－57.
JIN Zhikun，JING Yunpeng，LIU Gang. Farmland leveling topography measurement method based on UAV LiDAR[J]. Transactions of the Chinese Society for Agricultural Machinery，2021，52(Supp.)：51－57.(in Chinese)

[14] 杨普，赵远洋，李一鸣，等. 基于多源信息融合的农业空地一体化研究综述[J]. 农业机械学报，2021，52(增刊)：185－196.
YANG Pu，ZHAO Yuanyang，LI Yiming，et al. Review of research on integration of agricultural air-ground integration based on multi-source information fusion[J]. Transactions of the Chinese Society for Agricultural Machinery，2021，52(Supp.)：185－196.(in Chinese)

[15] POLAT N，UYSAL M. An experimental analysis of digital elevation models generated with LiDAR data and UAV photogrammetry[J]. Journal of the Indian Society of Remote Sensing，2018，46(7)：1135－1142.

[16] 杜蒙蒙，刘颖超，姬江涛，等. 基于无人机与激光测距技术的农田地形测绘[J]. 农业工程学报，2020，36(22)：60－67.
DU Mengmeng，LIU Yingchao，JI Jiangtao，et al. Farmland topographic mapping based on UAV and LiDAR technology[J]. Transactions of the CSAE，2020，36(22)：60－67.(in Chinese)

[17] 张漫，陈雨，贾文涛，等. 三维地形信息测量系统的设计[J]. 吉林大学学报(工学版)，2007，37(6)：1451－1454.
ZHANG Man，CHEN Yu，JIA Wentao，et al. Design of three dimensional topographic information measuring system[J]. Journal of Jilin University (Engineering and Technology Edition)，2007，37(6)：1451－1454.(in Chinese)

[18] 李宏鹏，牛东岭，王岩，等. 基于 RTK－GNSS 定位的农田地形快速测量技术[J]. 中国农业大学学报，2014，19(6)：188－194.
LI Hongpeng，NIU Dongling，WANG Yan，et al. Rapid survey technology of farmland terrain based on RTK－GNSS[J]. Journal of China Agricultural University，2014，19(6)：188－194.(in Chinese)

[19] ZHAO R，HU L，LUO X，et al. A novel approach for describing and classifying the unevenness of the bottom layer of paddy fields[J]. Computers and Electronics in Agriculture，2019，162：552－560.

[20] KUMAR A，YOON S，KUMAR V R S. Mixed reality simulation of high-endurance unmanned aerial vehicle with dual-head electromagnetic propulsion devices for earth and other planetary explorations[J]. Applied Sciences，2020，10(11)：3736.

[21] 周方圆，杨鹏举. 无人机航拍图像拼接技术研究与实现[J]. 电子测试，2022，36(11)：50－52.
ZHOU Fangyuan，YANG Pengju. Research and implementation of UAV aerial image mosaic technology[J]. Electronic Test，2022，36(11)：50－52.(in Chinese)

[22] 胡炼，杜攀，罗锡文，等. 悬挂式多轮支撑旱地激光平地机设计与试验[J]. 农业机械学报，2019，50(8)：15－21.
HU Lian，DU Pan，LUO Xiwen，et al. Design and experiment on multi-wheel support laser land leveler hanging on tractor[J]. Transactions of the Chinese Society for Agricultural Machinery，2019，50(8)：15－21.(in Chinese)

[23] 赖韬，伊廷华，王健宇，等. 基于多速率卡尔曼滤波方法的位移和加速度数据融合[J]. 防灾减灾工程学报，2012，32(6)：707－713.
LAI Tao，YI Yanhua，WANG Jianyu，et al. Data fusion of displacement and acceleration measurements based on multi-rate Kalman filtering technique[J]. Journal of Disaster Prevention and Mitigation Engineering，2012，32(6)：707－713.(in Chinese)

[24] 任钊，戴吾蛟，余文坤，等. 复杂环境下 GNSS/INS 紧组合垂直振动监测精度评估[J]. 导航定位学报，2022，10(4)：81－88.
REN Zhao，DAI Wujiao，YU Wenkun，et al. Accuracy evaluation of GNSS/INS tight combination vertical vibration monitoring in complex environment[J]. Journal of Navigation and Positioning，2022，10(4)：81－88.(in Chinese)

[25] 贺静，何杰，罗锡文，等. 基于多传感器融合的水稻行识别与跟踪导航研究[J]. 农业机械学报，2022，53(3)：18－26.
HE Jing，HE Jie，LUO Xiwen，et al. Rice row recognition and navigation control based on multi-sensor fusion[J]. Transactions of the Chinese Society for Agricultural Machinery，2022，53(3)：18－26.(in Chinese)

[26] 于子钧，刘斌，姜琦刚，等. 基于 RTK 的高程数据对比分析[J]. 世界地质，2019，38(2)：549－555.
YU Zijun，LIU Bin，JIANG Qigang，et al. Comparison and analysis of elevation data based on RTK[J]. World Geology，2019，38(2)：549－555.(in Chinese)

[27] AKHLAGHI S，ZHOU N，HUANG Z. Adaptive adjustment of noise covariance in Kalman filter for dynamic state estimation[C]//2017 IEEE Power & Energy Society General Meeting，2017.

agronomy

Saved Queries

Sign In to use this feature.

Search Filter

Reset All

Years

Between: 1996 - 2026

Article Types

Select Article Types

Countries / Regions

Select Countries / Regions

Update Search

Search Results (1)

Search Parameters:
Keywords = Design and Test of Intelligent Farm Machinery Operation Control Platform for Unmanned Farms
Journal = Agronomy

Order results: Publication Date | Result details: Normal | Results per page: 50

Show export options

Open Access Article — 25 pages, 13019 KB

Design and Test of Intelligent Farm Machinery Operation Control Platform for Unmanned Farms

by **Pei Wang, Mengdong Yue, Luning Yang, Xiwen Luo, Jie He, Zhongxian Man, Dawen Feng, Shanqi Liu, Chuqi Liang, Yufei Deng, He Huang** and **Lian Hu**

Agronomy 2024, *14*(4), 804; https://doi.org/10.3390/agronomy14040804 - 12 Apr 2024

Cited by 6 | Viewed by 3290

Abstract The unmanned farm control platform is of great significance in promoting the supervision of farm production with less manpower or autonomous operation of farm machinery and the construction of farm informatization. Addressing the existing control platform for farm location information acquisition is time-consuming, [...] Read more.

(This article belongs to the Section Precision and Digital Agriculture)

► Show Figures

Show export options

Displaying article 1-50 on page 1 of 1.

agronomy

MDPI

Article

Design and Test of Intelligent Farm Machinery Operation Control Platform for Unmanned Farms

Pei Wang [1], Mengdong Yue [1], Luning Yang [1], Xiwen Luo [1], Jie He [1], Zhongxian Man [1], Dawen Feng [1], Shanqi Liu [1], Chuqi Liang [1], Yufei Deng [1], He Huang [2] and Lian Hu [1,*]

[1] College of Engineering/Guangdong Laboratory for Lingnan Modern Agriculture, South China Agricultural University, Guangzhou 510642, China; wangpei@scau.edu.cn (P.W.); yuemengdong@stu.scau.edu.cn (M.Y.); 18805486187@163.com (L.Y.); xwluo@scau.edu.cn (X.L.); hooget@scau.edu.cn (J.H.); manzhx@scau.edu.cn (Z.M.); 381383864@scau.edu.cn (D.F.); liushanqi7@163.com (S.L.); liangchuqi@stu.scau.edu.cn (C.L.); dengyufei@stu.scau.edu.cn (Y.D.)

[2] Anhui Zhongke Intelligent Sense Industrial Technology Research Institute, Anhui 241002, China; hhuang@iim.ac.cn

* Correspondence: lianhu@scau.edu.cn; Tel.: +86-15915767370

Abstract: The unmanned farm control platform is of great significance in promoting the supervision of farm production with less manpower or autonomous operation of farm machinery and the construction of farm informatization. Addressing the existing control platform for farm location information acquisition is time-consuming, labor-intensive, and lacks the whole process control of multiple types of farm machinery. In this paper, we propose an Internet of Things (IoT) control scheme for intelligent farm machinery operation of unmanned farms and design the access standards for multiple types of farm machinery, as well as realize the remote control of intelligent farm machinery operation by constructing a remote control model. A high-precision map construction method is designed to improve the DeepLabV3+ algorithm to identify fields and roads. The control models of path planning, remote task, remote control, and safety system are built to achieve the remote control of intelligent agricultural machinery operation. The proposed technology is implemented in the platform integration and application tests are carried out. The error of the constructed high-precision map is less than 3 cm, the completeness rate of the automatic boundary extraction rate is 96.71%, and the correctness rate is 95.63%, which can be used to obtain the boundary instead of manual labeling or on-site point picking. The use of the platform for the simultaneous control of three farm machinery operations reduces the number of people in operation and production and reduces the professional requirements of the personnel, which will promote the management of the entire farm by one person or even by no one in the future.

Keywords: high-precision maps; remote management and control; IoT platform

Citation: Wang, P.; Yue, M.; Yang, L.; Luo, X.; He, J.; Man, Z.; Feng, D.; Liu, S.; Liang, C.; Deng, Y.; et al. Design and Test of Intelligent Farm Machinery Operation Control Platform for Unmanned Farms. *Agronomy* **2024**, *14*, 804. https://doi.org/10.3390/agronomy14040804

Academic Editors: Baohua Zhang and Yanbo Huang

Received: 24 February 2024
Revised: 28 March 2024
Accepted: 9 April 2024
Published: 12 April 2024

1. Introduction

Industrialization and urbanization continue to accelerate. According to data from the Seventh National Population Census, in 2020, the proportion of the elderly population aged 60 and over, as well as 65 and over, in China's rural areas relative to the total rural population was 23.81% and 17.72%, respectively. China's urbanization rate of the resident population has risen from 17.92% in 1978 to 64.72% in 2021. Consequently, the proportion of individuals employed in primary industries has declined from 70.53% to 22.87%. The decline in the rural labor force and the aging of the workforce have raised concerns regarding "who will farm and how to farm" [1]. The development of smart agriculture provides technical support to alleviate labor shortages [2–7]. As a significant facet of smart agriculture, unmanned farms achieve the integration of information perception, quantitative decision-making, intelligent control, precise inputs, and personalized services throughout the agricultural production process [8–15]. The remote control platform of

unmanned farms realizes remote transmission, with cloud management and intelligent analysis of online monitoring data, providing crucial data support for fault diagnosis and real-time early warning, significantly improving the management efficiency of agricultural machinery while reducing production costs [16].

Presently, several research efforts and practical applications are dedicated to developing an unmanned farm control platform for comprehensive monitoring and intelligent scheduling of farm production activities. Kaloxylos et al. [17] proposed an architecture comprising a cloud management system and a local management system. They found that 88% of respondents believed such a system could reduce their operational costs, and 90% found it easy to use. Fountas et al. [18] examined farm management information systems (FMIS) from academic and business perspectives, identifying common issues and solutions. Feng Minkang et al. [19] established an unmanned farm control platform to facilitate task allocation and remote supervision of farm machinery operations. Lu Bang et al. [20] designed a platform for online path planning of high-precision maps, remote control of farm machinery, and operation monitoring for tractor rapeseed sowing, achieving a maximum map plane accuracy error of 3.23 cm. Chen Huailin et al. [21] developed an FMIS interaction strategy by considering user, operational, environmental, and equipment contexts, and aligning them with FMIS tasks. Li Han et al. [22] created a multi-machine navigation service platform through WEBGIS, offering an efficient solution for multi-machine operation path planning and task allocation. Liu Zhenyu et al. [23] devised a platform for scheduling and operating agricultural machines, enabling intelligent scheduling according to supply and demand, as well as monitoring the entire process. Wang Chunshan et al. [24] proposed a layered management platform architecture to enhance system scalability. Lv Yacong [25] crafted a highly cohesive and low-coupling intelligent agricultural vehicle monitoring system using microservices architecture to improve scalability and responsiveness.

The aforementioned technology research primarily focuses on field data collection and collation, as well as agricultural machinery geographic location and operation data collection and collation, and furthermore agricultural machinery scheduling and information sharing. However, manual collection of field and road boundary information is both time-consuming and costly. Moreover, while certain aspects of operations such as ploughing, planting, management, and harvesting are often controlled, there is limited research on unmanned farm control platforms encompassing the entire process of intelligent farm machinery operation. Given the aforementioned status quo, the objectives of this study are as follows: (1) To establish an Internet of Things (IoT) platform for the operation and control of various types of intelligent farm machinery; (2) to employ machine learning algorithms for comprehensive identification of farm roads and fields and to construct high-precision maps; and (3) to facilitate real-time data interactions with farm machinery to achieve remote supervision of the operational processes. The research contents and innovations of this paper encompass the following: (1) Design of the control platform architecture for intelligent farm machinery operation; (2) establishment of an efficient, high-precision, and diversified information fusion digital map of the farm; and (3) development of a remote control methodology for intelligent farm machinery throughout the entire process of ploughing, planting, management, and harvesting.

2. Materials and Methods

2.1. Technical Routes

The research technology pathway outlined in Figure 1 encompasses platform design, high-precision map construction, and remote control of intelligent farm machinery operations. By acquiring farm images, the construction of a high-precision map for the farm entails identifying farmland and roads to derive layers and integrate diverse information into the map. This completed high-precision farm map serves the purpose of information collection and visualization concerning farm machinery operations. Moreover, access standards for various types of farm machinery are established to enable remote control of intelligent farm machinery operations through the development of a remote control model.

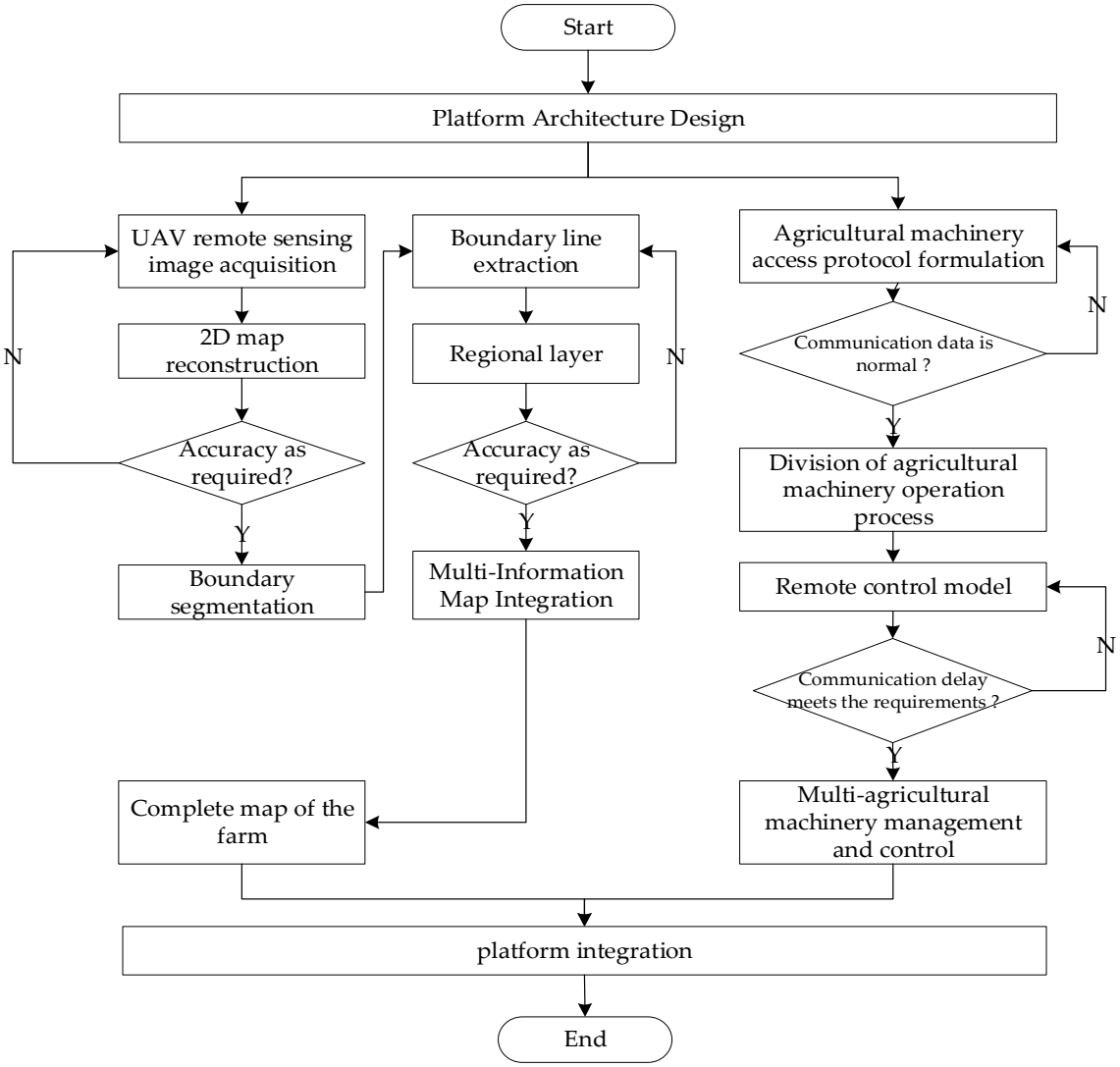

Figure 1. Technical route.

2.2. Platform Infrastructure

In this paper, the design of the platform architecture begins with a focus on farm machinery operation services. Based on the specific requirements of farm operations and the intelligent control processes involved, the overall architecture of the platform is delineated, as depicted in Figure 2. This architecture comprises the device layer, the network layer, the interface protocol layer, the basic platform layer, and the business application layer.

The equipment layer comprises intelligent farm machinery or equipment, serving as the primary component throughout the entire agricultural production process in unmanned farms. It constitutes the central element in production operations within unmanned farms, encompassing monitoring and sensors as key components.

The network layer serves as the conduit for data transmission between intelligent farm machinery, devices, and platforms, facilitating communication of data between the equipment layer and higher-level data.

The interface protocol layer facilitates the structured storage of various types of intelligent farm machinery and orchestrates the collection, control, and attribute binding of data through the specification of integration protocols for intelligent farm machinery, devices, and communication data. The use of the MQTT (Message Queuing Telemetry Transport) protocol enables communication between integrated display and control terminals and

the platform. This protocol is particularly suited for scenarios with constrained hardware storage or limited network bandwidth, offering features such as long connections and real-time capabilities, making it highly suitable for real-time control environments and actuators [26,27].

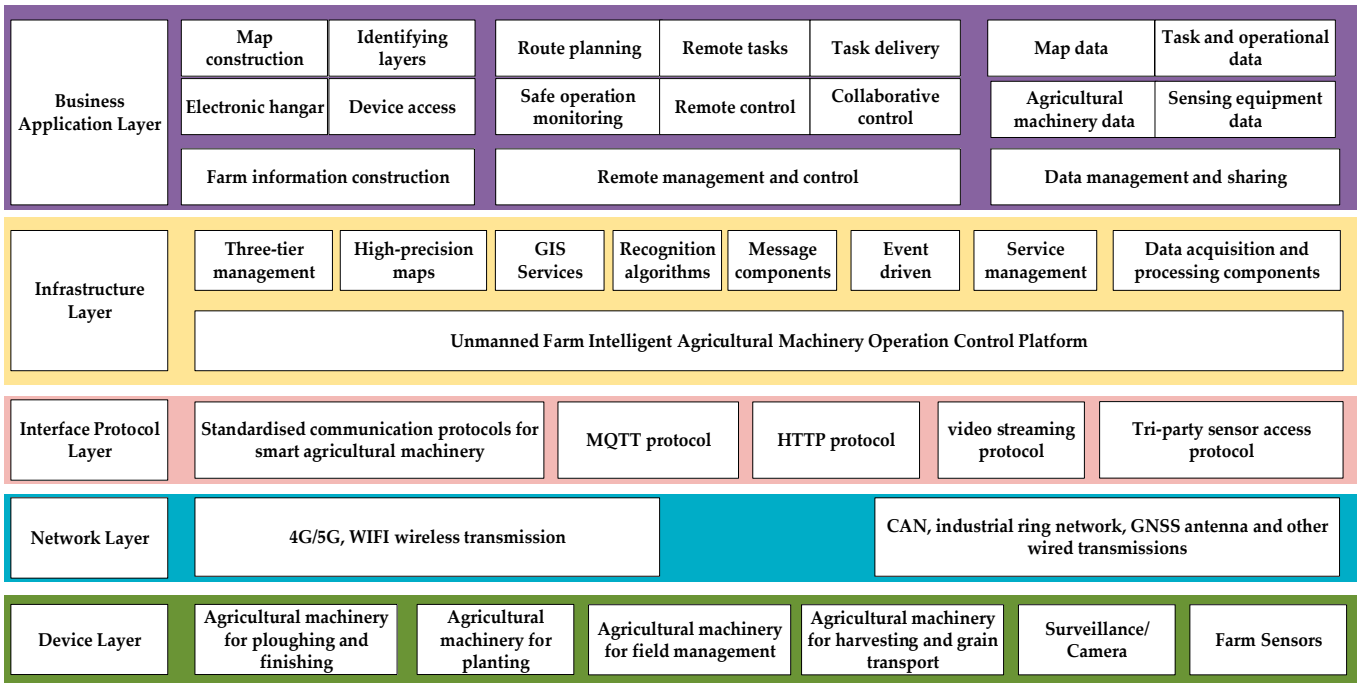

Figure 2. Overall platform architecture.

The basic platform layer constitutes an unmanned farm intelligent agricultural machinery operation control platform, which is structurally designed with considerations for both management and technology aspects. The management aspect involves the design of a "three-level" management mode for hierarchically overseeing multiple farms. On the other hand, the technical design encompasses network architecture, map construction, remote control, data collection and processing, and service management. The platform adopts the B/S network architecture (Browser/Server) to integrate high-precision maps, GIS (Geographic Information System) services, and recognition algorithms for farm map construction. Remote control functionality is achieved through the implementation of message components and event drivers for diverse command control and module processing. Furthermore, the platform is configured with multiple services and facilitates their discovery.

The business application layer involves the realization of business processes and core functions as per practical requirements. These functions encompass farm information construction, remote control, data management, and sharing. The focal point of the unmanned farm intelligent machinery operation control platform is the intelligent farm machinery. Map construction facilitates accurate visualization of areas and aids in location determination for the transfer and operation of farm machinery in the field. The electronic hangar serves as a digital repository for intelligent farm machinery. Equipment management provides requisite data support to ascertain the operational readiness of farm machinery and the suitability of prevailing conditions. Remote control functionality enables the remote execution of tasks, task assignment, safety, and operational monitoring, as well as collaborative management and control. Data management and sharing entail the classification and management of various farm data segments and their sharing over the Internet.

2.3. High-Precision Map Construction

Farmland maps utilized by drones require enhanced positioning accuracy and reliability [28–30]. By employing high-precision maps, key farm information can be identified or annotated, thereby facilitating efficient and precise marking and data collection for various elements such as farm fields, roads, equipment positioning, obstacles, hangar areas, and waypoints for intelligent farm machinery path planning.

2.3.1. Farm Image Acquisition and Original Map Construction

A small multi-rotor high-precision aerial survey UAV is employed for farm image collection, involving the following steps: (1) Selection of the farm area and formulation of the flight route; (2) configuration of flight parameters, including flight altitude, sampling distance, flight speed, heading overlap rate, bypass overlap rate, and the time interval for capturing images, aimed at enhancing image quality and model training efficacy; (3) utilization of collected image data for 2D reconstruction; (4) verification of reconstruction results and rectification of any anomalous outcomes or artifacts; and (5) acquisition of reconstructed RGB and TIF map images.

Given the typically large size of the output map image files, which can lead to slow upload speeds and laggy zoom-in and zoom-out displays, a map image raster pyramid is constructed to enhance user experience. This construction involves loading lower-resolution layer data from the pyramid when zooming out and higher-resolution layer data when zooming in, ensuring uninterrupted performance regardless of the displayed area size and thereby accelerating map display speed. ArcGIS Server is utilized to deploy online map service technology, generating image link addresses for cloud-based retrieval, eliminating the need for direct image file uploads, and further enhancing upload speeds. The process of map construction and publication entails: (1) Adding map image files to ArcMap software, selecting the nearest pixel method as the resampling technique, and constructing the raster pyramid; (2) sharing the completed map image files as an online service, specifying the server address folder and assigning names to image files; (3) selecting the WMS (Web Map Service) service and uploading image files to generate map image link addresses for the WMS service; and (4) employing WEBAPI to call the map image links for layer fitting and display with aerial imagery, thereby generating farm maps and enabling online zoom-in operations to extract farm positioning, distance, and area information.

2.3.2. Identification of Field and Road Boundaries

In the process of unmanned farm development, the accurate and rapid acquisition of farmland boundary information and machine-tillage road locations is crucial for realizing the unmanned and precise operation of intelligent farm machinery, as well as for accurate farmland management. Presently, handheld RTK (real-time kinematic) methods are commonly employed to acquire farmland boundary and machine-tillage road information. However, with the increase in the number of farm plots, the manual workload has significantly escalated.

To address the need for accurate and swift acquisition of farm field and machine track boundary information, this paper proposes an enhanced UAV remote sensing image segmentation algorithm for field and machine track boundary segmentation utilizing DeepLabV3+. DeepLabV3+ is a semantic segmentation model that combines Encoder and Decoder components [31]. The Encoder utilizes the Xception backbone network and deep features extracted by Atrous Spatial Pyramid Pooling (ASPP) [32]. These features are then fed into the Decoder through upsampling, where they are fused with the original shallow feature map. Subsequently, upsampling is employed to restore the fused feature map to its original size [33]. The original structure of the DeepLabV3+ network is illustrated in Figure 3.

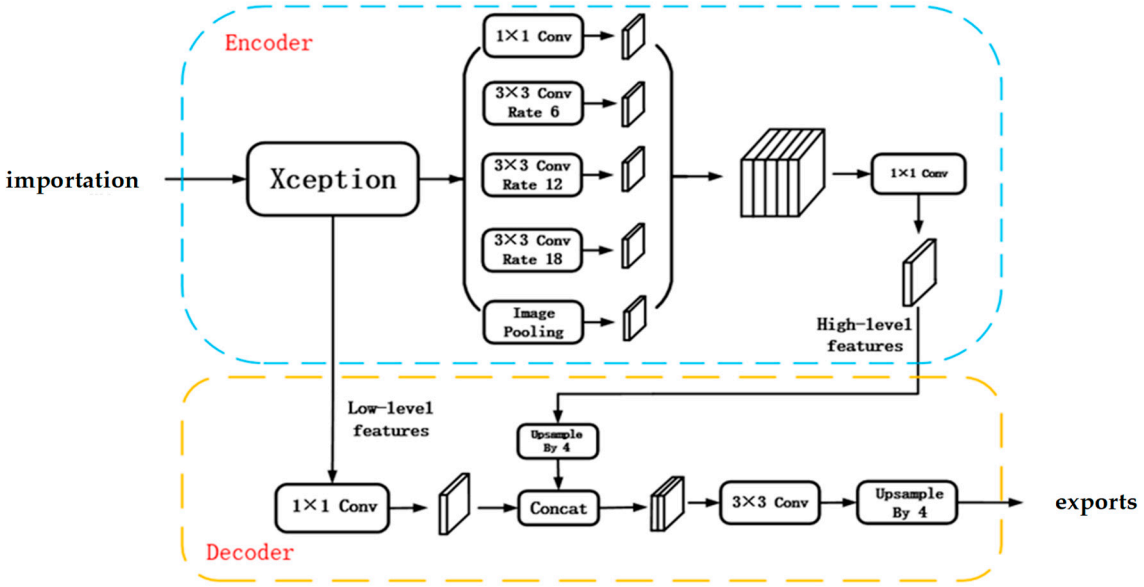

Figure 3. DeepLabV3 + network structure.

By enhancing the DeepLabV3+ algorithm, this study aims to mitigate the issues of incomplete boundary segmentation, adhesion, and breakage commonly observed in the traditional DeepLabV3+. The improvement of the DeepLabV3+ algorithm involves four key aspects:

(1) Replacement of the backbone network

The ConvNeXt network is utilized in place of the conventional Res-Net (Residual Network) backbone network. In the ConvNeXt network, the convolution kernel size is increased from 3 × 3 to 7 × 7. It is observed that the learning capability of the network is positively correlated with the size of the convolution kernel, with the 7 × 7 kernel exhibiting the strongest learning ability. Additionally, the ReLU (Rectified Linear Unit) activation function in the ConvNeXt network is replaced by the GELU (Gaussian Error Linear Unit) activation function. This substitution leads to smoother gradients at 0, while also introducing negative values to the value domain range, thereby accelerating the convergence speed of the network.

(2) Introduction of the CBAM attention mechanism

The CBAM mechanism is incorporated to mitigate feature loss. This mechanism involves spatial pooling and maximum pooling of the feature map to obtain two sets of 1 × 1 × C channels. Subsequently, these channels undergo processing by an MLP (Multilayer Perceptron) neural network. The results of this processing are then subjected to element-wise addition operation and activation by the sigmoid function to obtain the output results. The expression for channel attention processing is as follows:

$$M_c(F) = \sigma(MLP(AvgPool(F)) + MLP(MaxPool(F))) = \sigma(W_1\left(W_0\left(F^c_{avg}\right)\right) + W_1(W_0(F^c_{max}))). \quad (1)$$

Following the channel attention processing of the feature maps, the results undergo pooling once for maximum pooling and once for average pooling. Subsequently, these results are concatenated by channel. The final weight coefficients are obtained after passing through a 7 × 7 convolutional layer and activation using a sigmoid function. This process can be expressed as follows:

$$M_s(F) = \sigma\left(f^{7\times7}([AvgPool(F);\ MaxPool(F)])\right) = \sigma\left(f^{7\times7}\left(\left[F^s_{avg}; F^s_{max}\right]\right)\right) \quad (2)$$

where σ represents the sigmoid operation, and 7×7 denotes the size of the convolution kernel.

(3) Improvement of ASPP

The primary aim of this study is to enhance model performance by modifying the parallel branch within the ASPP module. An additional branch with an expansion rate of 8 is introduced alongside the original ASPP module. Features extracted from each channel are fused using cascade operations, allowing for better consideration of subtle small-scale features and overall features through convolutions with varying expansion rates.

(4) Hybrid Loss Function

The loss function characterizes the degree of disparity between the network's predicted values and the actual values. In this paper, a hybrid loss function is proposed, which combines the Dice Loss and cross-entropy loss functions. This approach aims to address issues such as positive and negative category imbalance and gradient descent saturation during training. The expression for the hybrid loss function is as follows:

$$Loss = Loss_{dice} + \lambda Loss_{focal} = C - \sum_{C=0}^{C-1} \frac{TP(c)}{TP(c) + \alpha FN(c) + \beta FP(c)} - \lambda \frac{1}{N} \sum_{C=0}^{C-1} \sum_{n=1}^{N} g_n(c)(1 - P_n(c))^2 ln P_n(c) \quad (3)$$

where N is the total number of samples and C is the total number of labeling categories. $\mathrm{TP}(c) = \sum_{n=1}^{N} g_n(c) P_n(c)$, $\mathrm{FN(c)} = \sum_{n=1}^{N} (1 - P_n(c)) g_n(c)$, $\mathrm{FP}(c) = \sum_{n=1}^{N} P_n(c)(1 - g_n(c))$. $P_n(c)$ denotes whether category c is predicted at pixel location n, and $g_n(c)$ denotes whether the true category at pixel location n is category c. TP(c) represents the true positive rate of category c, FN(c) is the false negative rate of category c, and FP(c) is the false positive rate of category c. Parameters α and β in this model are both set to 1, and λ denotes the weight between $Loss_{focal}$ and $Loss_{dice}$. Different sizes are assigned based on the performance of the validation set; in this paper, we set $\lambda = 1$. The network structure of the improved DeepLabV3+ algorithm is depicted in Figure 4.

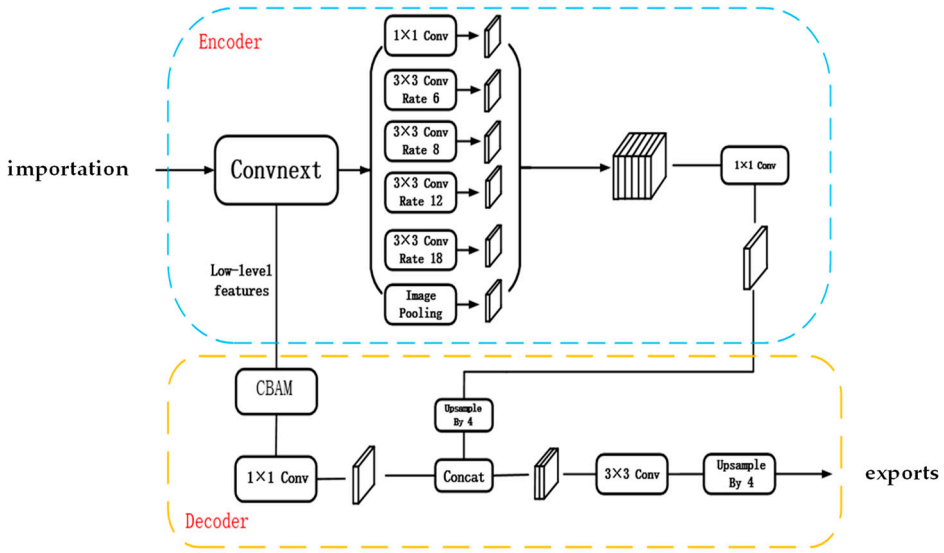

Figure 4. Network architecture diagram of the improved DeepLabV3+.

After performing semantic segmentation using the enhanced DeepLabV3+ segmentation algorithm, the semantic segmentation results undergo optimization through threshold segmentation and morphological processing via blob analysis. Subsequently, the Hough transform is employed to extract the boundary lines of the farmland and the machinery path. The obtained boundary lines are extended to fit any broken segments, and finally, the generated boundary layer information is integrated with the high-precision farm map.

2.3.3. Farm Information Map Integration

To create a clearer and more intuitive representation of farm information, various data about the farm are integrated into a single map. The farm map information is categorized into three basic elements: the farm itself, the equipment, and the farm machinery, as illustrated in Figure 5. The basic element information is integrated with the platform through layers, while equipment points are obtained online via high-precision maps and data retrieval through third-party protocols. For intelligent farm machinery, standardized communication protocols are utilized to access and display information such as machinery location, online status, and operation trajectory on the map.

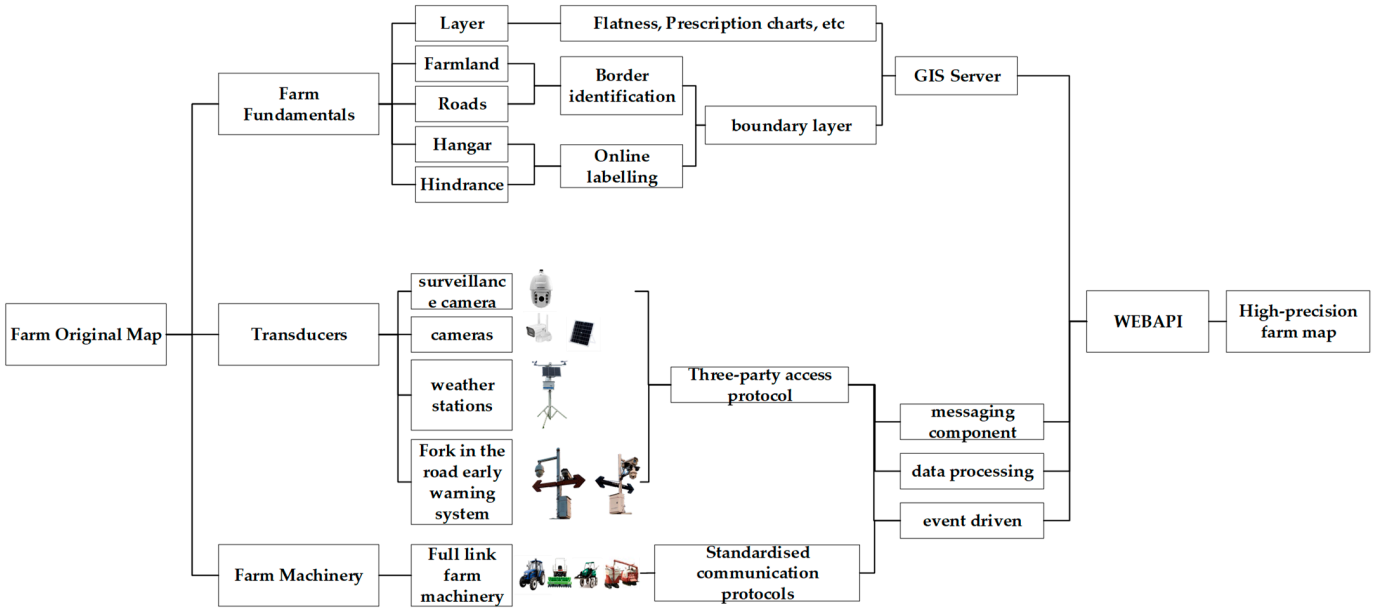

Figure 5. Farm information map integration.

2.4. Remote Management and Control

2.4.1. Standardized Access for Smart Farm Machinery

To enable the expandability, convenience, and practicality of accessing intelligent agricultural machines across different platforms, standardized docking protocols for cultivation, planting, management, and harvesting are formulated. A "three-level" protocol stack is devised for the intelligent farm machine, integrated display and control terminal, and platform, facilitating standardized access to the platform for information data reporting and command control of farm machine components and terminal modules. Based on the structural composition of intelligent agricultural machines and the one-to-one relationship between the integrated display and control terminal and the agricultural machine, the standard access relationship is divided into three categories: agricultural machine end and display/control terminal, agricultural machine end and platform end, and display/control terminal and platform end. The access protocol is further categorized into communication protocol and data protocol. The communication protocol determines the communication mode between different relationships, while the data protocol establishes communication data integration specifications. The standardized access design of intelligent farm machinery is depicted in Figure 6.

In Figure 6, concerning the relationship between the agricultural machine end and the display/control terminal, the NEMA (National Electrical Manufacturers Association) protocol is utilized to parse satellite signals for obtaining location information. The CAN bus is employed to receive information from the underlying modules of the agricultural machine as well as for command and control purposes. Additionally, the UVC (USB Video Class) protocol facilitates access to video and image data from the vehicle-mounted

camera. For the relationship between the agricultural machine terminal and the platform terminal, a standardized integrated camera is directly connected to the platform. Regarding the relationship between the display/control terminal and the platform terminal, the HTTP protocol is utilized for file downloads and interface calls. The MQTT protocol is employed for message subscription and release between the display/control terminal and the platform terminal. Furthermore, the RTMP (Real-Time Messaging Protocol) is utilized for accessing video streams. Among the aforementioned protocols, the CAN bus, HTTP protocol, MQTT protocol, and broadcasting fall under communication protocols, while the NEMA protocol, UVC protocol, entry rules, remote control command protocol, agricultural machine data reporting protocol, and video streaming three-way protocol pertain to data structure protocols.

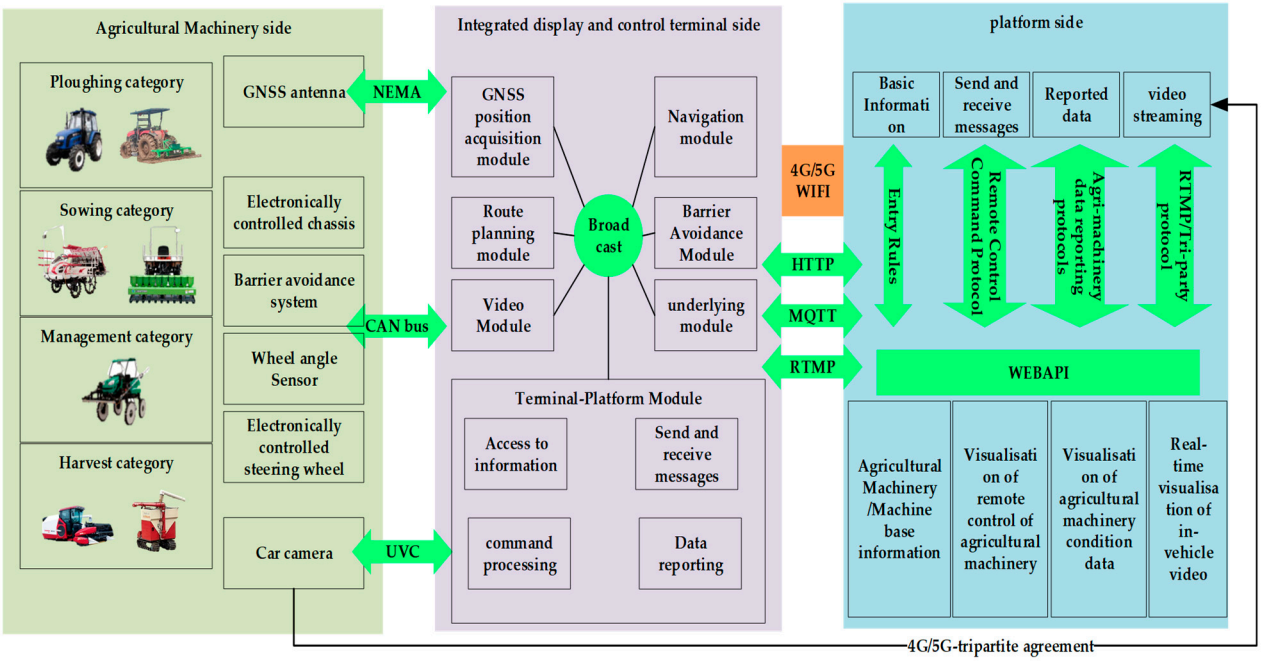

Figure 6. Standardized access to smart farm machinery data.

2.4.2. Remote Management and Control Model

(1) Path Planning

The path planning design encompasses map point collection, inputting agricultural machine information, setting algorithm parameters, calling algorithms, visualizing the correction of erroneous points, and storing path files. Map point collection is accomplished through high-precision maps to gather data and establish data collections of boundary points and transport points:

$$U_P = \{P_{bc}, P_{mt}\}, l_{P_{bc}} > 0, l_{P_{mt}} \geq 0 \tag{4}$$

where P_{bc} represents the collection of field boundary points and P_{mt} represents the collection of transport points; $l_{P_{bc}}$ denotes the length of the collection of field boundary points; and $l_{P_{mt}}$ denotes the length of the collection of transport points. Constructing the input farm object AM,

$$AM = \{SN, typeOP, widOP, capOP, speedR, oilOP, oilUOP, turnT, OPT, locM, r, l\} \tag{5}$$

where SN denotes the terminal serial number to which the farm machine is bound, $typeOP$ denotes the operation type, $widOP$ denotes the operation width, $capOP$ denotes the operation capability, $speedR$ denotes the road speed, $oilOP$ denotes the fuel consumption during operation, $oilUOP$ denotes the non-operation fuel consumption, $turnT$ denotes the

turnaround time, OPT denotes the day during which the farm machine operates, $locM$ denotes the position of the farm machine, r denotes the turnaround radius, and l denotes the distance from the control point of the farm machine to the end of the machine $widOP$, r, l, which is utilized solely for path planning. The path planning algorithm parameter settings include path type, turning mode, whether to close the loop, and whether to group.

(2) Remote Task

The remote task is devised to transmit the path file to the designated intelligent farm machine. To ensure the uniqueness of the intelligent farm machine's ID, the serial number of the integrated display and control terminal is utilized as a variable to generate the message subject. The task-sending process design comprises task creation, security confirmation, path file transmission, downloading and activation of the intelligent farm machine path, and message feedback. The task object is constructed following the requirements of agricultural machine operation:

$$T = \{tkID, far, fld, tkTp, AM, route, ctTime, sta\} \text{ and } far \rightarrow \{fld, AM, route\},\ fld\&tkTp \rightarrow route \quad (6)$$

where $tkID$ denotes the task sequence number, far denotes the farm, field denotes the field, $tkTp$ denotes the task type, AM denotes the farm machine object, route denotes the path file, $ctTime$ denotes the creation time, and sta denotes the task status. Constraints are imposed on the field, farm machine, and path; the farm determines the selection of the field, farm machine, and path; and the field and the type of operation determine the selection of the path. The command message data object Msg and feedback message data object are constructed according to the task object and farm machine object $MsgAck$,

$$Msg = \{msgID, SN, tkID, cmdCd, link, ept\}, SN \in AM, tkID \in T \quad (7)$$

$$MsgAck = \{msgID, resID, SN, tkID, cmdCd, resFlag, ept\}, resID \in Msg, SN \in AM, tkID \in T, resFlag \in \{1, 2\} \quad (8)$$

where $msgID$ denotes a message sequence number, $cmdCd$ denotes an instruction code, link denotes a path link, ept denotes the content of the message description, $resID$ denotes a feedback message sequence number, and resFlag denotes the result of message execution, with 1 indicating success and 2 indicating failure.

(3) Remote Control

Remote control is divided into the control of the intelligent agricultural machinery navigation and the bottom, using the implementation of the control of different modules, taking the value of the definition of the design of Table 1.

Table 1. Command code definition.

The Value of *cmdCd*	Meaning
1	Self-inspection of operations
2	Execution
3	Emergency stop
4	Stopping the job
5	Setting initial master–slave job parameters
6	Job Delivery
7	Stop navigation
8	Start navigation
9	One-touch ignition
10	One-touch ignition off
11	Master notifies slave of arrival at the designated point
12	The slave notifies the master that it has arrived at the designated point
13	Master notifies slave to return
14	Apparatus start
15	Machine stop

Table 1. *Cont.*

The Value of *cmdCd*	Meaning
16	Emergency stop cancellation
17	Machine height adjustment

(4) Safety system

Intelligent farm machinery operation safety and operation quality monitoring is an important part of remote control. The establishment of agricultural machinery reporting data objects to monitor the status of agricultural machinery:

$$Sdata = \{dataID, SN, cltTime, dvcSta, tkID, chs, GNSS, atc\}, SN \in AM, tkID \in T \quad (9)$$

where *dataID* denotes the packet sequence number, *cltTime* denotes the acquisition time, dvcSta denotes the navigation status of farm machinery, chs denotes the underlying data, GNSS denotes the GNSS position data, and atc denotes the navigation data. Integration of farm multi-intelligent devices to monitor the environmental safety and operation quality of smart farm machine operations and construction of environmental data objects *Evt* is

$$Evt = \{mtr, AMMC, rdWn, otcScan\} \quad (10)$$

where *mtr* denotes farm monitoring data; *AMMC* denotes video data from the onboard camera of the farm machine to view the forward direction environment, the cockpit environment, and the effect of the operation of the farm machine; *rdWn* denotes turnoff blind zone warning data, which provides early warning information for the smart farm machine when it shifts on the road; and *otcScan* denotes obstacle scanning data of the smart farm machine, which performs obstacle scanning for the smart farm machine's forward direction, at a distance that can be customized.

Through the data model design results of path planning, remote task, remote control, and safety system, the three-part remote control model comprising the web end, transceiver end, and intelligent farm machinery terminal is constructed, as illustrated in Figure 7.

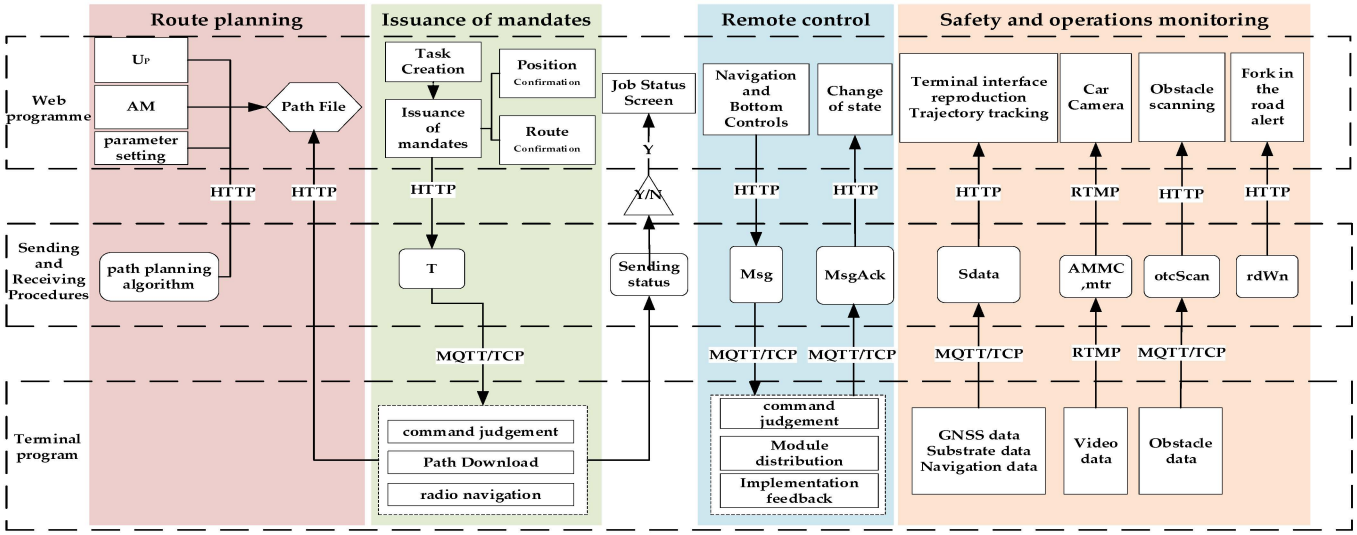

Figure 7. Remote control model.

2.4.3. Multi-Agricultural Machinery Management and Control

There are various types of intelligent farm machines on the farm, and multiple types of operation tasks occur simultaneously. Additionally, there are constraints on the order of agricultural tasks and operational conditions between different operation types. Therefore,

operation types are categorized based on agricultural tasks, and their sequence and interval times are determined. The fulfillment of operation conditions is assessed using data from farm sensing equipment. Online tasks are then established for different types of agricultural tasks, with their starting times set accordingly. Concurrently, the safety and operation processes are controlled by establishing a collaborative network of multiple farm machines based on the logical model of remote control. During operations, to oversee various types or multiple scenarios involving intelligent farm machinery, a multi-agricultural machinery cooperative network is established based on the remote control logical model. This enables simultaneous control of agricultural machinery operation safety and processes. Cooperative control of multiple types of agricultural machines primarily achieves unified control of operating agricultural machines. It also allows for the display of operation statuses and distributions of all agricultural machines through a single interface, facilitating monitoring of safety and operations.

The management and control process is designed as follows: (1) Create a plowing, planting, management, and harvesting type operation task $T_s = \{T_1, T_2, \ldots, T_n\}$. (2) Select multiple tasks $T_k(T_k \epsilon T_s)$ to join the collaborative group network, acquire task data, and issue tasks. (3) According to the acquired task data, display the field area, planned path, and location of farm machinery of all tasks in the high-precision map visualization. (4) Establish unique farm machine message topics and use different values of $cmdCd(cmdCd \in Msg)$ to achieve remote control of farm machines in the network, and monitor safe operations based on *Sdata* and *Evt* object data.

2.5. Experimental Area and Materials

The test site selected was the Zengcheng Teaching and Research Base of South China Agricultural University (SCAU), comprising four high-standard farmlands, concrete mechanized plowing paths, and agricultural machinery storage facilities, covering an area of approximately 80 acres, as depicted in Figure 8.

Figure 8. Test zone. Note: 1–5. Field 1–Field 5. 6. Hanger 7. Roads.

(1) High-precision map construction test materials

The high-precision map construction process includes farm image acquisition and original map construction, boundary recognition of fields and roads, and farm information map integration. In the construction process, the materials used are shown in Table 2.

Table 2. Map building materials.

Procedure	Resource Requirement	Parameters/Versions	Function
Farm Image Acquisition and Original Map Construction	DJI Elf 4-RTK drone with remote control	Camera lens: FOV 84°; 8.8 mm/24 mm image resolution: 4864 × 3648 (4:3) 5472 × 3648 (3:2) Photo format: JPEG Maximum flight speed: 50 km/h (positioning mode) 58 km/h (Attitude Mode) position accuracy: perpendicular1.5 cm + 1 pp (RMS); level 1 cm + 1 pp (RMS)	Acquisition of farm image data
	Mapping software and map servers	DJI Terra (version: 3.6.6) ArcGIS Server (version: 10.2)	Image stitching and map services
Identification of field and road boundaries	Farm Map Image Dataset	Small image blocks of 512 × 512 pixels	Provide samples for model training
	Dirt, concrete, and road boundary data sets	Label map generated with Labelme annotation	Provide boundary datasets for model training
	Model Training Host	CPU: Intel i9-10980XE GPU: NVIDIA RTX3090 AERO RAM: 32 G CUDA: 11.3 operating system: Ubuntu 20.04	Provide a test environment for model training and running
Farm Information Map Integration	WEBGIS Service	OpenLayers (version:7.4.0) Leaflet (version:1.9.4) ArcGIS API for js (version:3.17)	Front-end maps, layers, and function calls
	Farm Elements Layer	Vector layers in tif, shp, and other formats	Providing visual annotation of different types of geographic information on farms

Note: 1 ppm indicates that the measurement error increases by 1 mm for every 1 km increase in distance between the mobile station and the base station.

To verify the accuracy of the map, an accuracy comparison was conducted using RTK field collection and map collection to validate the point information. For field collection, the Huasi i70 intelligent RTK was selected, with its main parameters shown in Table 3.

Table 3. i70 Intelligent RTK Technical Parameter Table.

Designation	Intelligent RTK i70
Data Update Rate	1 Hz, 2 Hz, 5 Hz, 10 Hz
Communication Interface	UHF antenna interface/RS232/USB and other interfaces
Static Accuracy	Horizontal accuracy: 2.5 mm + 1 ppm High-range accuracy: 5.0 mm + 1 ppm
Dynamic Accuracy	Horizontal accuracy: 8 mm + 1 ppm High-range accuracy: 15 mm + 1 ppm

Note: 1 ppm indicates that the measurement error increases by 1 mm for every 1 km increase in distance between the mobile station and the base station.

(2) Remote Control Test Materials

The rice directing machines comprised three sets of Seydal Star2BDXZ-10SCA (20) self-propelled rice hole directing machines equipped with self-developed unmanned systems, as depicted in Figure 9. These agricultural machines are equipped with GNSS (Global Navigation Satellite System) antennas, electronically controlled steering wheels, wheel angle sensors, electronically controlled chassis, obstacle avoidance systems, on-board cameras, and integrated display and control terminals. They feature wire-controlled clutch, implement, throttle, and gear systems, with the steering control equipped with electronically controlled steering wheels and wheel angle sensors. The unmanned system consists of an integrated display control terminal and GNSS antenna. The display and control terminal integrates a high-precision BeiDou positioning module, providing a positioning accuracy of ±1 cm, while the controller's linear navigation control accuracy is ±2.5 cm. Additionally, it integrates a 4G communication module. Each live broadcasting machine is equipped with a millimeter-wave obstacle avoidance radar, with a dynamically adjustable scanning range.

Moreover, it is installed with front and rear onboard cameras, enabling remote monitoring of cockpit status and operational effects through the wireless network.

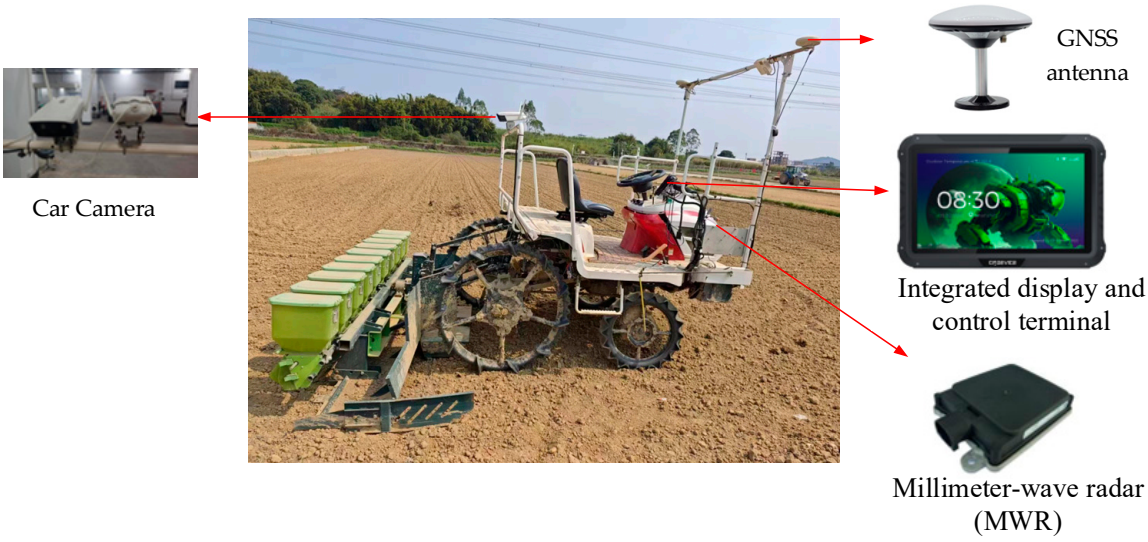

Figure 9. Unmanned driving rice direct seeding machine.

To enable remote control, a computer, tablet, or mobile phone with network communication capability is utilized. The platform's link address is accessed through a web browser, and the unmanned farm in Zengcheng is selected to remotely control the operation of agricultural machinery.

2.6. Experimental Design

2.6.1. High-Precision Map Construction Test

For the improved recognition algorithm, performance verification tests and application tests were designed. The UAV was employed to partition the farm map in clear weather. The flight parameter settings included a flight altitude set to 100 m, with a ground sampling distance (GSD) capable of reaching 2.74 cm. The flight speed was set to 8 km/h, with a heading overlap rate and bypass overlap rate of 70%, and a time interval for taking pictures of 2 s. The images captured during the flight were imported into DJI Zhitu software to establish a two-dimensional creation task. The output coordinate system used was the WGS 84 geodetic coordinate system. The sampled data was spliced to obtain the farm map, and the reconstructed farm map was employed to crop the remote sensing image of the farm using OpenCV. Each small image block was set to a size of 512 × 512 pixels to construct the dataset. The semantic segmentation model was trained with 4000 images under the same parameters, and the model performance was tested with 1000 images. Evaluation metrics such as mean intersection over union ratio (*mIoU*), mean pixel accuracy (*MPA*), and training loss function were selected to assess the performance of the network. *mIoU* represents the ratio of intersection and union of the standard image and the manually annotated image computed by the network prediction. *MPA* denotes the number of pixels correctly discriminated as class I but incorrectly discriminated as class II. The calculation formulas are as follows:

$$mIoU = \frac{1}{k+1}\sum_{n=0}^{k}\frac{P_{nn}}{\sum_{m=0}^{k}P_{mn}+\sum_{m=0}^{k}P_{mn}-P_{mm}} \tag{11}$$

$$MPA = \frac{1}{k+1}\sum_{i=0}^{k}\frac{P_{ii}}{\sum_{j=0}^{k}P_{ij}} \tag{12}$$

where k denotes the number of categories. P_{mn} denotes the number of false-negative examples. $K + 1$ denotes that the number of categories contains a class of background.

P_{nn} denotes the number of pixels of true examples. P_{nm} denotes the number of pixels of false-positive examples. P_{ii} denotes the number of pixels that are accurately discriminated as class i. P_{ij} denotes the amount of pixels that are correctly discriminated as class i, but are incorrectly discriminated as class j. P_{ji} denotes the amount of pixels that are correctly discriminated as class j, but are incorrectly discriminated as class i. In this study, a hybrid loss function combining the cross-entropy loss function and the Dice Loss loss function is chosen.

After verifying the improved recognition algorithm, image data are collected from the test area according to the aforementioned dataset construction method, and the dataset is generated. The improved semantic segmentation model is then applied to predict the small image blocks after cropping. Finally, the small modules are spliced together, and boundary lines are extracted to generate the farm road and field recognition layer. The existing equipment and farm machinery in the farm are accessed and integrated on the map. The accuracy of the completed map is verified by selecting the 5 points shown in Figure 10a. The coordinate system used for GPS positioning in this paper is the WGS-84 geodetic coordinate system, and the planar projection used is the "Gauss-Kruger" projection, which transforms the collected point information into a spatial Cartesian coordinate system for comparison. Fifteen feature points, such as the vertices of parcels 2–4 and the inflection points of the ploughing road, were selected for accuracy verification, as shown in Figure 10b. The manual point information was then compared with the extracted information, and the extraction results of the experimental area were evaluated using the indicators of boundary extraction completeness (*COR*) and accuracy (*COM*). The calculation formulas were as follows:

$$COR = \frac{TP}{TP + FP} \tag{13}$$

$$COM = \frac{TP}{TP + FN} \tag{14}$$

where FP is the length of the correct linear region (number of pixel points) that was extracted, FN is the length of the region that was not extracted, and TP is the length of the correctly extracted road region.

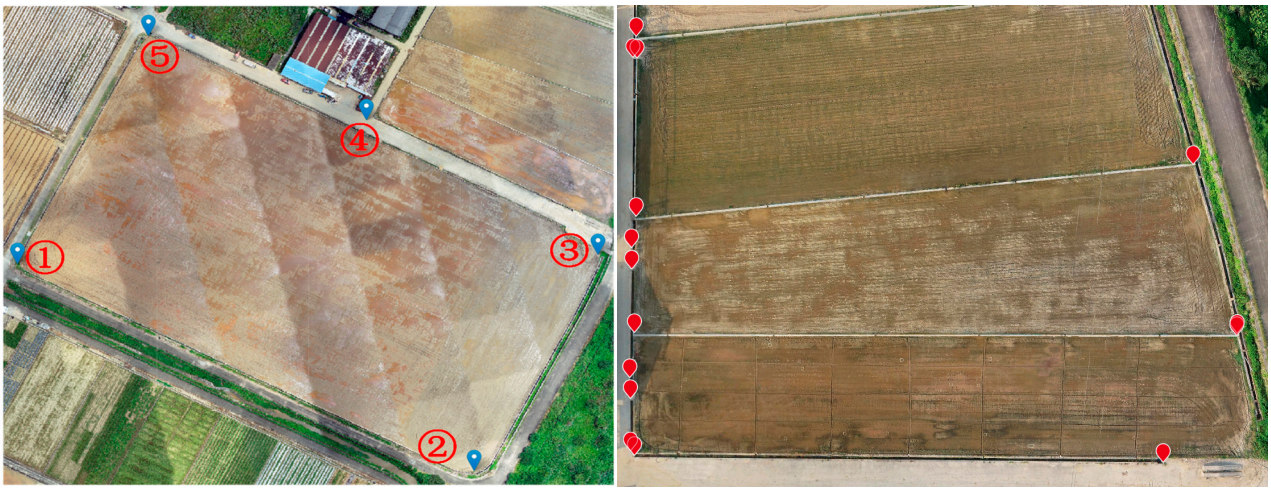

(**a**) (**b**)

Figure 10. Feature point selection. (**a**) Map accuracy verification point. (**b**) Identification accuracy verification point position.

2.6.2. Remote Control Experiment

Verification tests and application tests were designed for the remote control method. Communication tests were conducted using the integrated display and control terminal, and the frequency of data interaction for standardized access to agricultural machinery

information was verified and tested. The path planning accuracy test involved formulating paths using a platform and testing the position display accuracy on the machine plowing path using an unmanned live machine. Additionally, the real-time data interaction of the remote control and safety system during the operation of agricultural machinery was verified.

Upon verifying the feasibility of the remote control method, the platform was designed to control the "3-machine simultaneous operation" application test in the test area. A large field with an area of 50 acres in plot 1 was selected as the operation field, and three unmanned broadcasting machines were used as the control objects. Path planning requirements for three sets of agricultural machinery were established from the hangar to the road transport to plot 1. The field operation was divided into three non-interfering pieces with full-coverage paths. Path planning parameters were designed as outlined in Table 4. Tasks were sent through the platform to achieve the simultaneous operation of the three sets of agricultural machinery in the remote control test.

Table 4. Route planning data entry.

Categories	Data
U_P	Field boundary point $P_{bc} = \{A, B, C, D\}$ Road transport point $l_{P_{mt}} = 6$
AM	Operating width $widOP$ = 2.5 m Turning radius r = 1.4 m Distance from the end of the machine l = 1.32 m
Algorithmic parameter	Path type: Full-coverage proctor work Turning mode: Bulb-shaped Whether to seal the circle: Yes Whether grouping: Yes, 3 groups

3. Results

3.1. High-Precision Map Construction Results

The comparison with other mainstream recognition algorithms is depicted in Figure 11. In Figure 11a, the algorithm proposed in this paper demonstrates a 4.64% higher mIoU value compared to the PSPNet algorithm, a 3.28% higher mIoU value relative to the UNet algorithm, and a 3.15% higher mIoU value compared to the original DeepLabV3+ algorithm. The training loss curves are illustrated in Figure 11b, where the solid line graph represents the training loss curve for the model's training set described in this study, and the dashed line represents the loss curve for the test set. From the loss function curve in Figure 11b, it can be observed that during the pre-training period, the loss rate decreases rapidly and exhibits a continuous oscillation phase. As the number of training iterations increases, the loss rate gradually decreases and approaches convergence, indicating the stabilization of the model.

A comparison of the recognition results with the original DeepLabV3+ algorithm for roads, concrete ridges, and earthen field plowing is shown in Table 5. The MPA is improved by 3.8 percentage points compared to the original DeepLabV3+ model.

Table 5. MPA indices by category.

Algorithmic Model	Roads	Concrete Ridges	Earth Ridges	MPA
DeepLabV3+	96.13	88.62	84.65	91.51
Improvements to DeepLabV3+	98.36	93.71	90.45	95.31

The recognition results of farmland and the mechanic road are depicted in Figure 11, with the splicing results presented in Figure 12b. For the segmentation outcomes, farmland and road boundary line information is extracted using blob analysis and Hough transform. Semantic segmentation results are further optimized through threshold segmentation and morphological processing to eliminate noise patches caused by interfering field information, with the optimization results showcased in Figure 12c.

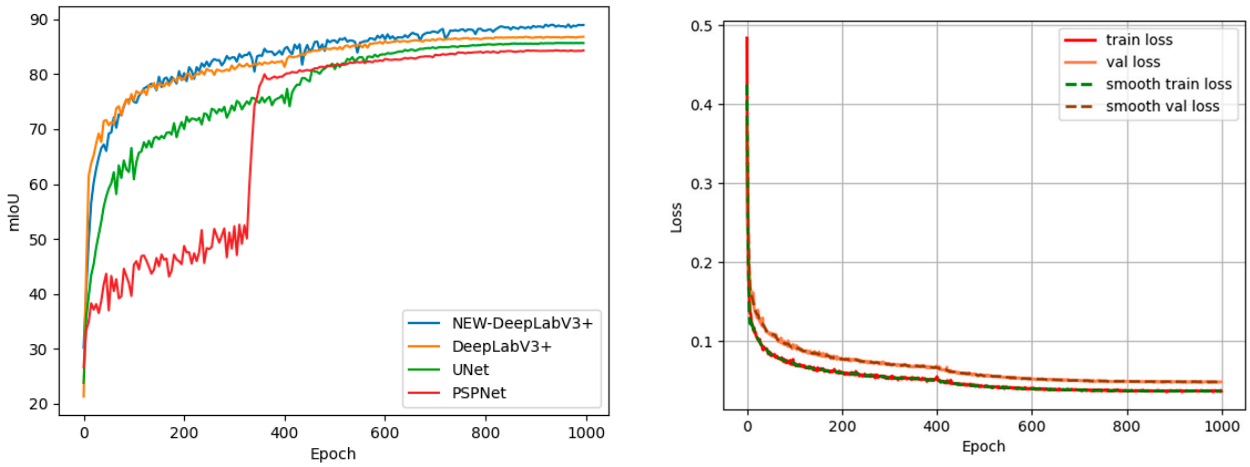

(**a**) (**b**)

Figure 11. Comparative test results. (**a**) mIoU index of different image segmentation algorithms. (**b**) Improved semantic segmentation model training loss curve.

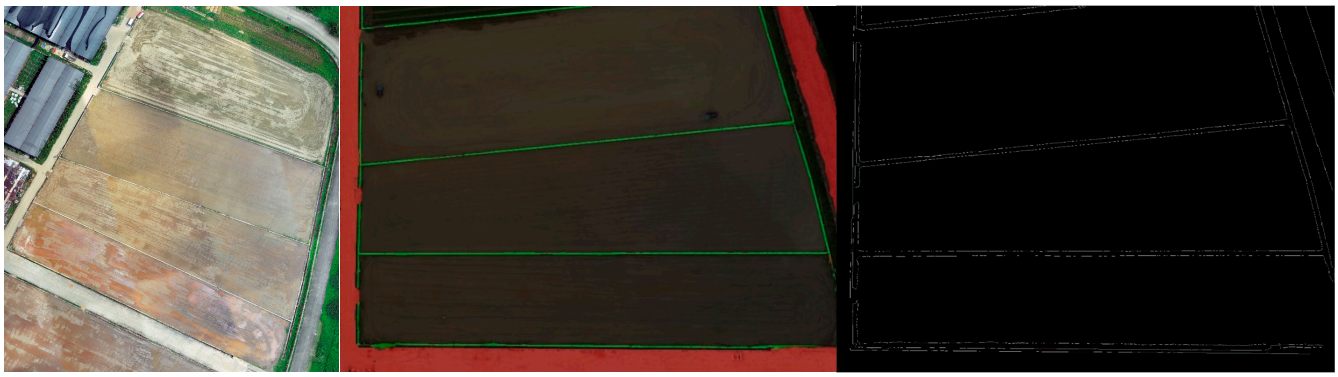

(**a**) (**b**) (**c**)

Figure 12. Results of the identification of the boundaries of agricultural land and mechanized tracks. (**a**) Original image; (**b**) semantic segmentation results; (**c**) boundary line of farmland machine-travelled tracks.

The verification of the accuracy of the acquired raw maps is shown in Table 6. The maximum error of the five points is 3.2 cm, and the average error of the five points is 2.98 cm. The error of the points of the high-precision map constructed by UAV is less than 3 cm.

Table 6. High-precision map accuracy verification.

Point	RTK Coordinates/xy	Title 3 High-Precision Map Coordinates/xy	Tolerance/cm
1	2571374.215, 462724.598	2571374.192, 462724.618	3.05
2	2571269.245, 462938.651	2571269.221, 462938.668	2.94
3	2571381.101, 462990.638	2571381.081, 462990.656	2.69
4	2571489.807, 462785.193	2571489.785, 462785.214	3.04
5	2571450.663, 462886.902	2571450.638, 462886.922	3.20

The result of accuracy verification of the recognition results after recognition using the 15 feature points selected above is shown in Figure 13. The error range of the 15 target points selected for the concrete ridges and roads falls between 4–7 cm, with the maximum deviation being 6.16 cm and the average absolute error being 5.15 cm.

The recognition results were analyzed using completeness and accuracy rates. The completeness rate of the boundary line extraction for the concrete ridge and road is 96.71%,

with a correct extraction rate of 95.63%. These findings indicate that the boundary recognition algorithm can achieve precise and complete extraction of the boundaries of the farm machinist's road and farmland with high accuracy.

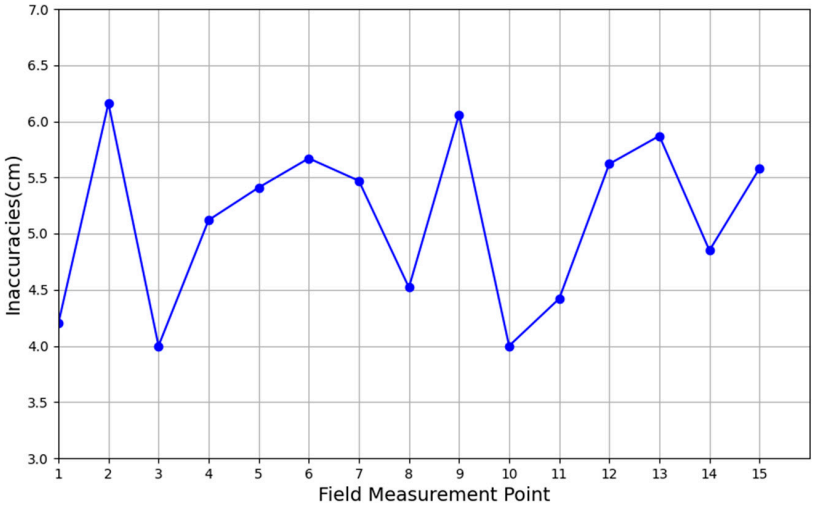

Figure 13. Recognition result accuracy validation.

In conclusion, the accuracy of high-precision maps and the accuracy of recognition meet the needs of unmanned agricultural machine operations. Utilizing the recognition algorithm, the field and road area layers are generated, and obstacles are collected in the high-precision map to generate the area layer for hangar boundary points. These layers are then released as an online service and integrated into the farm map. Completion of access for sensing equipment and intelligent farm machinery results in the generation of the overall farm map. The construction of the platform map is depicted in Figure 14.

Figure 14. Constructed map of unmanned farms. Note: 1. Hangars. 2. Fields. 3. Roads. 4. Obstacles. 5. Farm machinery. 6. Sensors.

3.2. Remote Management Test Results

Using the amount of data received by the platform to test the frequency of reporting data from agricultural machines, the terminal connects to the MQTT server and sets the message publishing level QoS to 0. It then pushes 100 pieces of data to the platform using reporting frequencies of 0.5 Hz, 1 Hz, and 2 Hz, respectively, and evaluates them according to the packet loss rate, data correctness rate, and real-time performance. The results are shown in Table 7.

Table 7. Data reporting frequency test.

Reporting Frequency/Hz	Receive Data Volume/Packet	Packet Loss Rate/%	Data Correctness/%	Real-Time/s
0.5	100	0	100	2
1	100	0	100	1
2	95	5	96	0.5

As shown in Table 7, at reporting frequencies of 0.5 Hz and 1 Hz, the packet loss rate and data correctness are optimal. However, at 1 Hz frequency, real-time performance is higher, indicating more intensive data transmission over time. Conversely, using a 2 Hz reporting frequency resulted in packet loss and data correctness issues. The analysis suggests that packet loss may stem from the QoS level settings. Increasing QoS levels from low to high improves message reliability but also increases transmission complexity, making it less suitable for high-frequency scenarios. Additionally, the decrease in data correctness may be attributed to inconsistencies in terminal information acquisition and data reporting at different frequencies, leading to inaccurate data readings. Based on this analysis, it is concluded that a reporting frequency of 1 Hz for agricultural machinery aligns better with the operational requirements of intelligent agricultural machinery.

The validation of the path planning results is shown in Table 8. The relative error of the trajectory of agricultural machinery operation on the high-precision map is around 2 cm.

Table 8. Route planning validation.

Agricultural Machinery	Navigation Average Tracking Error/cm	Average Trajectory and Path Error/cm	Relative Error/cm
Vehicle 1	3.3	5.5	2.2
Vehicle 2	4.0	6.1	2.1
Vehicle 3	3.1	4.3	2.2

For the update of farm machinery trajectories, control instructions, and real-time video validation, the validation results are presented in Table 9. Trajectory updates occur at a rate of 1 s per point, dependent on the frequency of data reported by the farm machine. Sending control command messages and receiving feedback takes only 0.28 s.

Table 9. Real-time analysis.

Categories	Data Protocols	Communication Protocols	Time/s
trajectory updates	agricultural machine reporting data protocol	MQTT	1
control commands	remote control command protocol	MQTT	0.28
car camera	fluorite EZOPEN protocol	HTTP	1.2

In summary, the communication, path error, and real-time verification of agricultural machines meet the requirements of remote control of agricultural machines. According to the platform architecture design, the platform integrates the corresponding functions. The results of the field operation control test conducted on smart agricultural machines using the platform are depicted in Figure 15. They are integrated into the platform as described in the appeal. Following the remote control process, the steps of farm machine access, path planning, remote task execution, and safety monitoring are carried out sequentially, and records of completed operations are tallied.

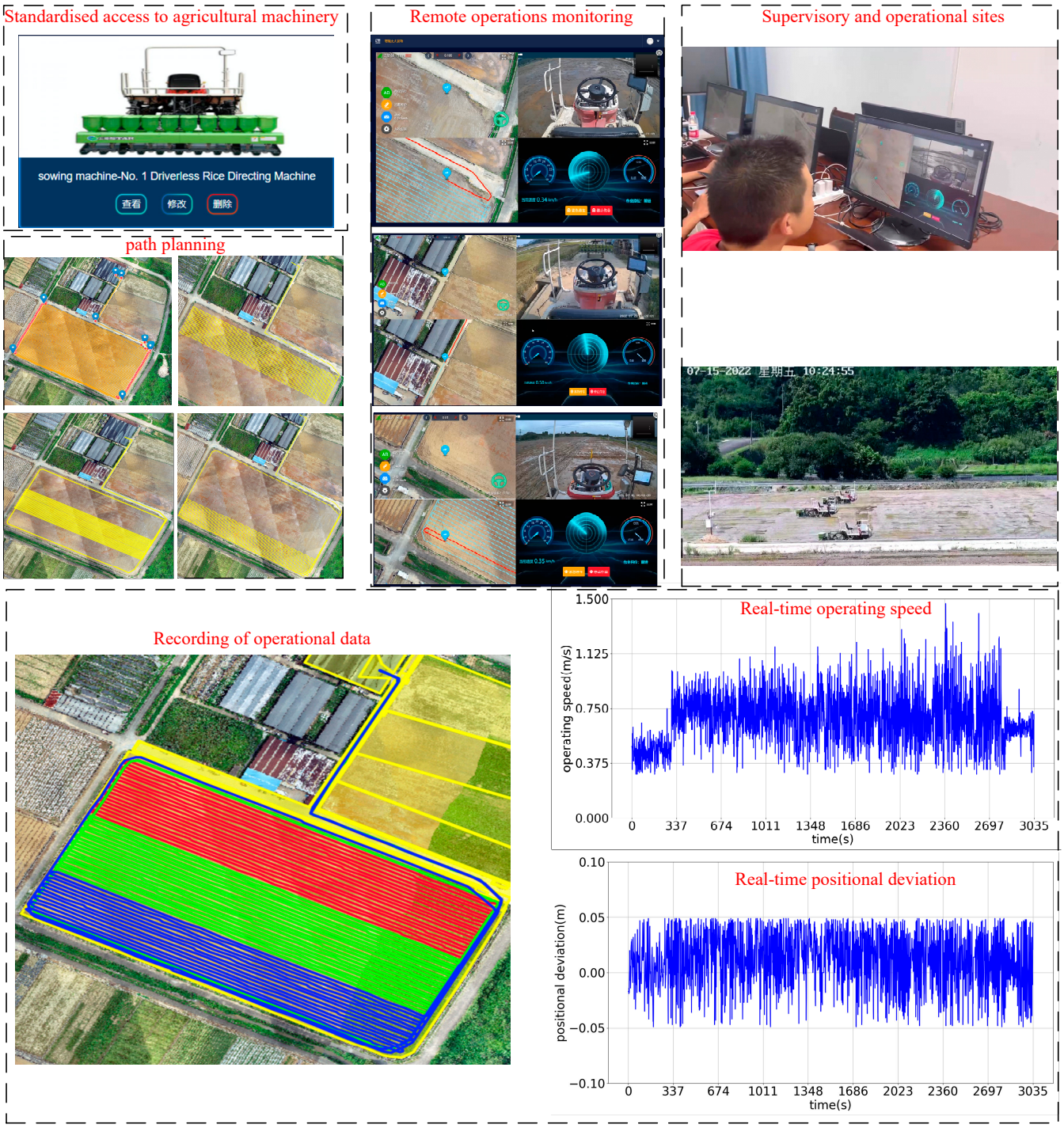

Figure 15. Application test process. Note: In the Remote operations monitoring page, the Chinese on the top left indicates the path information, diagnosis and maintenance, speed and system settings of the navigation interface of the integrated display and control terminal, the Chinese on the top is the received GNSS signal, and the following is the area that has been operated. The Chinese buttons at the bottom right indicate the control of the agricultural machine to start and stop operation.

For the completion of operations, path tracking, error calculation, filtering of traps, and averaging of large data fluctuations, statistical analysis was performed on various parameters, including the average speed of agricultural machinery during operation and completion time. The statistical results are presented in Table 10.

Table 10. Data statistics.

Categories	Vehicle 1	Vehicle 2	Vehicle 3
Degree of completion of operations/%	100%	100%	100%
Average navigation error/cm	3.8	4.6	4.8
Average operation speed/m/s	0.65	0.58	0.63
Completion time/h	2.2 h	2.5 h	2.4 h

During the test, one person successfully conducted the control operation of three farm machinery operations. The entire process, including path planning, remote task assignment, remote control, and safety system monitoring of intelligent farm machinery operations, was achieved with high real-time performance and visual supervision through remote access.

4. Discuss

4.1. Analysis of Results

The results of high-precision map construction are analyzed for comparison based on recognition accuracy and acquisition efficiency. In the performance verification results, the mean pixel accuracy (MPA) is 95.31% and the mean intersection over union (mIoU) is 88.96%. Additionally, the extraction completeness rate is 96.71%, and the extraction correctness rate is 95.63% in the application experiments. Currently, manual labeling methods are primarily used for farmland identification, often relying on agricultural experts' accumulated experience and relevant theoretical knowledge. For instance, Wang Yuli et al. [33] employed software tools like ArcGIS and ENVI to manually decode and analyze multispectral images of cultivated land in the Xinjiang region, generating maps through layer overlay. Although simpler to operate, manual annotation methods for farmland identification suffer from lower accuracy and efficiency. Ming Dongping et al. [34] utilized spatial statistics and threshold segmentation methods to extract farmland from remote sensing images, achieving an overall accuracy of 84.15% and enhancing the efficiency and automation of farmland extraction. However, simple machine vision approaches require high-quality remote sensing images and lack generality and robustness. Ji Xusheng [35] accomplished the rapid and accurate acquisition of small field boundaries through edge detection and morphological processing of farmland, achieving a farmland-matching completion rate of 85%. Meanwhile, Liu Dong et al. [36] proposed a farmland boundary identification method based on the normalized vegetation index, utilizing threshold segmentation and the Canny operator edge detection method to achieve effective segmentation of farmland boundaries. Deng Hong et al. [37] introduced a deep learning-based semantic segmentation algorithm for UAV water field images, enhancing the segmentation accuracy by improving the DeepLabV3+ network. After testing, they obtained a mIoU of up to 85.90%. Compared to existing research results, the method proposed in this paper demonstrates high efficiency and accuracy in farmland and road recognition. It can potentially replace manual parcel and road annotation methods, leading to reduced labor costs and investment.

In the process of conducting remote control application tests, the effectiveness of remote control is analyzed based on labor cost considerations. Presently, traditional operations of intelligent farm machinery entail pre-operation preparations, on-site supervision during operations, and post-operation data analysis. Pre-operation tasks involve collecting point information on the farm for path planning and debugging machinery data. During operations, technicians are required to operate integrated display and control terminals on-site to issue tasks, initiate operations, and monitor machinery status. After completion, data is then copied and analyzed. In the "Three rice seeders simultaneous operation" test scenario, only one person is required to manage machinery operations. In contrast, traditional supervision methods for intelligent machinery operations require three individuals to oversee three machines simultaneously, necessitating more personnel with advanced skills such as field point collection and unmanned system operation. Traditional methods of acquiring agricultural machinery operation information are limited and less comprehensive, while the concentrated visualization of operation information enhances supervision

quality and data acquisition efficiency compared to conventional methods. Consequently, the approach presented in this paper reduces the need for multiple participants, lowers technical skill requirements for controllers, and enhances the quality of control over intelligent agricultural machinery operations.

4.2. Platform Comparison

The unmanned farm intelligent farm machinery operation control platform proposed in this paper aims to provide precise services for intelligent farm machinery operations, offering three distinct advantages over existing control platforms. Firstly, it offers rapidly constructed and highly available high-precision maps that facilitate online point collection and diversified information visualization [19]. Compared to existing high-precision map geographic information annotation methods, which often rely on manual map annotation or on-site point collection, the approach presented in this paper leverages machine learning algorithms to efficiently identify fields and roads utilized in agricultural machinery operations, generating boundary layers to achieve platform integration. The completeness and correctness of the recognition results are verified through experiments, enhancing the efficiency of data collection.

Secondly, it incorporates remote control technology for the entire chain of intelligent agricultural machinery operations [38–40]. While current control platforms primarily focus on specific types of farm machinery or segments of the machinery control process, this paper establishes protocol unification across the entire machinery chain by developing communication protocols for farm machinery, terminals, and platforms. This approach provides users with convenient access to farm machinery and enhances the richness of operation information supervision. Existing platforms typically offer limited services for the entire process of intelligent farm machinery operation and lack comprehensive supervision of operational information. In contrast, this paper comprehensively addresses the operational services of farm machinery before, during, and after operations, not only reducing labor costs but also significantly improving supervision quality.

Finally, the platform architecture proposed in this paper can better serve agricultural machinery operations. From a software perspective, the platform presented herein demonstrates superior performance, addressing the issue of slow uploading and loading of traditional maps through optimized map uploading methods. The remote control validation test illustrates the platform's high real-time communication capability. Moreover, it exhibits robust security features, leveraging GateWay gateway, SpringSecurity, OAuth2, and farm unique ID to generate tokens, ensuring data security. From the user's standpoint, the platform offers high usability. The construction of high-precision farm maps and remote control tests verify the platform's ability to visualize farm information and farm machinery operations effectively. Additionally, it achieves functional division for the process of farm machinery operations, thereby reducing users' technical difficulties in utilization. Regarding application services, the platform has been implemented in 30 unmanned farms since its inception. Users' evaluations of map construction and operation control are positive, with a high level of acceptance for the control functionalities.

5. Conclusions

In this paper, we propose a control platform for intelligent farm machinery operations, focusing on an unmanned farm as an implementation scenario. This platform enables remote control of farm machinery equipped with unmanned systems. To simplify implementation complexity and enhance platform scalability, we adopt a layered platform architecture tailored to the needs and processes of farm machine operations. Our platform utilizes UAV recognition integration to achieve high-precision and efficient construction of farm maps. Field tests confirm map construction errors of less than 3 cm and field/road recognition errors of 5.15 cm, validating the feasibility of the map application. We introduce a remote control method for intelligent farm machinery operation, alongside a "three-level" protocol stack for standardized access to multiple farm machinery types, facilitating remote

control throughout the operational process. Field test results demonstrate that our method reduces the number of personnel involved in production compared to traditional methods, while also lowering technical requirements and simplifying operation procedures, thereby enhancing control quality and positively contributing to unmanned farm realization.

The application of our intelligent farm machinery operation control platform offers two key benefits to unmanned farms. Firstly, the high-precision map serves as the foundation for smooth operation implementation. Users can leverage the platform to construct detailed maps reflecting the farm's actual conditions accurately, including fields, roads, and integrated sensing information, thereby improving information acquisition efficiency. Secondly, our platform considers the entire agricultural machinery operation process and implements functional division, enabling one-button management of farm machinery within the farm, streamlining operation procedures and reducing labor costs.

Our proposed control method, rooted in the study of agricultural machines equipped with unmanned systems, offers modularity for access by intelligent robots and drones in unmanned farms. By analyzing the operation processes of different production equipment, we develop remote control methods and formulate standardized access protocols to control other highly intelligent production equipment on the farm. Looking ahead, we envision the unmanned farm control platform evolving towards smarter functionalities, integrating the latest technology to cater to personalized and refined agricultural production needs, as well as managing complex agricultural machinery operation scenarios. Future work will focus on researching multi-type intelligent equipment control methods and cooperative operation scheduling methods.

Author Contributions: Conceptualization, M.Y., P.W., X.L. and L.Y.; methodology, M.Y., P.W., L.Y. and L.H.; software, M.Y., P.W., L.Y., Z.M., D.F. and Y.D.; validation, M.Y., P.W., L.Y., S.L. and C.L.; formal analysis, M.Y., P.W. and L.Y.; investigation, M.Y., P.W., Z.M. and S.L.; resources, L.H., X.L., J.H. and P.W.; data curation, M.Y., P.W., L.H., J.H. and L.Y.; writing—original draft preparation, M.Y., P.W. and L.Y.; writing—review and editing, M.Y., P.W., L.H., X.L. and J.H.; visualization, M.Y., P.W., H.H., D.F. and Z.M.; supervision, X.L., L.H., J.H. and P.W.; project administration, L.H.; funding acquisition, X.L., L.H. and J.H. All authors have read and agreed to the published version of the manuscript.

Funding: This research was funded by the National Key Research and Development Program of China (Grant No.2022YFD200150502), the Science and Technology Planning Project of Guangdong Province (Grant No.2023B0202010023), and the project of Specialized Discipline of Specific Universities (Grant No.2023B10564002).

Data Availability Statement: The data that support this study will be shared upon reasonable request to the corresponding author.

Acknowledgments: We would like to thank our partners at the Zengcheng Teaching Base of South China Agricultural University and Anhui Zhongke Intelligent Sense Industrial Technology Research Institute.

Conflicts of Interest: The authors declare no conflicts of interest.

References

1. Luo, X.W.; Liao, J.; Zang, Y.; Ou, Y.G.; Wang, P. Developing from Mechanized to Smart Agricultural Production in China. *Strateg. Study CAE* **2022**, *24*, 46–54. [CrossRef]
2. Zhao, C.J.; Fan, B.B.; Li, J.; Feng, Q.C. Agricultural Robots: Technology Progress, Challenges and Trends. *Smart Agric.* **2023**, *5*, 1–15.
3. Zhou, X.S.; Fan, S.G. Solving the Problem of "Who Will Grow Grain": The Foundation and Path of Comprehensively Promoting Agricultural Mechanization. *Acad. J. Zhongzhou* **2023**, *45*, 54–60.
4. Wu, Y.H.; Wang, H.S.; Zhou, R.Z.; Zhu, N.; Zhang, X.W. Regional differences and convergence characteristics of comprehensive development level of agricultural mechanization. *J. Chin. Agric. Mech.* **2024**, *45*, 311–319. [CrossRef]
5. Chu, B.Q.; Li, C.F.; Ding, L.; Guo, Z.Y.; Wang, S.Y.; Sun, W.J.; Jin, W.Y.; He, Y. Nondestructive and Rapid Determination of Carbohydrate and Protein in *T. obliquus* Based on Hyperspectral Imaging Technology. *Spectrosc. Spectr. Anal.* **2023**, *43*, 3732–3741.
6. Sun, J.L.; Li, D.H.; Xu, S.W.; Wu, W.B.; Yang, Y.P. Development Strategy of Agricultural Big Data and Information Infrastructure. *Strateg. Study CAE* **2021**, *23*, 10–18. [CrossRef]
7. Wang, J.F. Research on Development Situation of Big Data Application in the Era of Smart Agriculture. *J. Tech. Econ. Manag.* **2020**, *41*, 124–128.

8. Zhao, B.; Zhang, W.P.; Yuan, Y.W.; Wang, F.Z.; Zhou, L.M.; Niu, K. Research Progress in Information Technology for Agricultural Equipment Maintenance and Operation Service Management. *Trans. Chin. Soc. Agric. Mach.* **2023**, *54*, 1–26.
9. Yin, Y.X.; Meng, Z.J.; Zhao, C.J.; Wang, H.; Wen, C.K.; Chen, J.P.; Li, L.W.; Du, J.W.; Wang, P.; An, X.F.; et al. State-of-the-art and Prospect of Research on Key Technical for Unmanned Farms of Field Corp. *Smart Agric.* **2022**, *4*, 1–25.
10. Luo, X.W.; Hu, L.; He, J.; Zhang, Z.G.; Zhou, Z.Y.; Zhang, W.Y.; Liao, J.; Huang, P.K. Key technologies and practice of unmanned farm in China. *Trans. Chin. Soc. Agric. Eng.* **2024**, *40*, 1–16.
11. Dou, H.J.; Chen, Z.Y.; Zhai, C.Y.; Zou, W.; Song, J.; Feng, F.; Zhang, Y.L.; Wang, X. Research Progress on Autonomous Navigation Technology for Orchard Intelligent Equipment. *Trans. Chin. Soc. Agric. Mach.* **2024**, accepted.
12. Lan, Y.B.; Zhao, D.N.; Zhang, Y.F.; Zhu, J.K. Exploration and development prospect of eco-unmanned farm modes. *Trans. Chin. Soc. Agric. Eng.* **2021**, *37*, 312–327.
13. Qian, Z.J.; Jin, C.Q.; Liu, Z.; Yang, T.X. Development status and trends of intelligent control technology in unmanned farms. *J. Intell. Agric. Mech.* **2023**, *4*, 1–13.
14. Cui, K.; Feng, X. The application logic, practice scenarios, and promotion suggestions of intelligent agricultural machinery equipment towards agriculture 4.0. *Res. Agric. Mod.* **2022**, *43*, 578–586.
15. Li, D.L.; Li, Z. System Analysis and Development Prospect of Unmanned Farming. *Trans. Chin. Soc. Agric. Mach.* **2020**, *51*, 1–12.
16. Luo, X.W.; Liao, J.; Hu, L.; Zhou, Z.Y.; Zhang, Z.G.; Zang, Y.; Wang, P.; He, J. Research progress of intelligent agricultural machinery and practice of unmanned farm in China. *J. South China Agric. Univ.* **2021**, *42*, 8–17+5.
17. Kaloxylos, A.; Groumas, A.; Sarris, V.; Katsikas, L.; Magdalinos, P.; Antoniou, E.; Politopoulou, E.; Wolfert, S.; Brewster, C.; Eigenmann, R.; et al. A cloud-based Farm Management System: Architecture and implementation. *Comput. Electron. Agric.* **2014**, *100*, 168–179. [CrossRef]
18. Fountas, S.; Carli, G.; Sørensen, C.G.; Tsiropoulos, Z.; Cavalaris, C.; Vatsanidou, A.; Liakos, B.; Canavari, M.; Wiebensohen, J.; Tisserye, B. Farm management information systems: Current situation and future perspectives. *Comput. Electron. Agric.* **2015**, *115*, 40–50. [CrossRef]
19. Feng, M.K.; Gong, Z.F.; Xu, J.; Wu, X.J.; Lin, L.J.; Xu, J.Y.; Li, X.Y.; Wang, Z. Design and Implementation of Intelligent Control Platform for Unmanned Farms. *Agric. Technol.* **2022**, *42*, 52–55.
20. Lu, B.; Dong, W.J.; Ding, Y.C.; Sun, Y.; Li, H.P.; Zhang, C.Y. An Rapeseed Unmanned Seeding System Based on Cloud-Terminal High Precision Maps. *Smart Agric.* **2023**, *5*, 33–44.
21. Chen, H.L.; Li, W.X.; Du, X.T.; Zhang, W.L. Interaction Design of Intelligent Agricultural Machinery Management and Control System Based on Context-awareness. *Packag. Eng.* **2023**, *44*, 123–130.
22. Li, H.; Zhong, T.; Zhang, K.Y.; Wang, Y.; Zhang, M. Design of Agricultural Machinery Multi-machine Cooperative Navigation Service Platform Based on WebGIS. *Trans. Chin. Soc. Agric. Mach.* **2022**, *53*, 28–35.
23. Liu, Z.Y.; Liang, J.P. Design and application of precision scheduling and efficient operation platform for agricultural machinery based on BDS. *J. Chin. Agric. Mech.* **2018**, *39*, 97–102. [CrossRef]
24. Wang, C.S.; Zhang, F.; Teng, G.F.; Matthew, E.T.; Wang, K.J.; Wang, B. Design and implementation of smart agricultural machinery management platform. *J. Chin. Agric. Mech.* **2018**, *39*, 61–68. [CrossRef]
25. Lv, Y.C. Design and Implementation of Intelligent Agricultural Machinery Data Management Application System Based on Microservice Architectur. Master's Thesis, Chongqing University of Posts and Telecommunications, Chongqing, China, 2019.
26. Jia, F.; Xiong, G.; Zhu, F.H.; Tian, B.; Han, S.S.; Chen, S.C. Research and implementation of industrial Internet of things communication system based on MQTT. *Chin. J. Intell. Sci. Technol.* **2019**, *1*, 249–259.
27. Chen, W.Y.; Gao, J.; Yang, H. Design and implementation of Internet of Things communication system based on MQTT protocol. *J. Xi'an Univ. Posts Telecommun.* **2020**, *25*, 26–32.
28. Tsolakis, N.; Bechtsis, D.; Bochtis, D. AgROS: A robot operating system based emulation tool for agricultural robotics. *Agronomy* **2019**, *9*, 403. [CrossRef]
29. Jensen, K.; Larsen, M.; Nielsen, H.S.; Larsen, B.L.; Olsen, S.K.; Jørgensen, N.R. Towards an Open Software Platform for Field Robots in Precision Agriculture. *Robotics* **2014**, *3*, 207–234. [CrossRef]
30. Jo, K.; Kim, C.; Sunwoo, M. Simultaneous localization and map change update for the high definition map-based autonomous driving car. *Sensors* **2018**, *18*, 3145. [CrossRef]
31. Chollet, F. Xception: Deep Learning with Depthwise Separable Convolutions. *arXiv* **2016**, arXiv:1610.02357.
32. Li, W.; Liu, K. Confidence-Aware Object Detection Based on MobileNetv2 for Autonomous Driving. *Sensors* **2021**, *21*, 2380. [CrossRef] [PubMed]
33. Wang, B.L.; Ma, Z. Visual Interpretation TM Image Land Use Classification by Applied the Software of ENVI. *Mod. Surv. Mapp.* **2011**, *34*, 11–13.
34. Ming, D.P.; Qiu, Y.F.; Zhou, W. Application of Spatial Statistics in Remote Sensing Pattern Classification—An Example of Object-Oriented Farmland Extraction from Remote Sensing Images. *Acta Geogr. Sin.* **2016**, *45*, 825–833.
35. Ji, X.S. Delineation of Farmland Boundaries and Estimation of Aboveground Biomass in Rice Using High Resolution Satellite Imagery. Master's Thesis, Nanjing Agricultural University, Nanjing, China, 2019.
36. Liu, D.; Ou, Y.A.; Chen, C.; Li, Y.B. Farmland boundary recognition method based on NDVI. *Jiangsu Agric. Sci.* **2022**, *50*, 196–201.
37. Deng, H.; Yang, Y.T.; Liu, Z.P.; Liu, M.H.; Chen, X.F.; Liu, X. Semantic segmentation of paddy image by UAV based on deep learning. *J. Chin. Agric. Mech.* **2021**, *42*, 165–172.

38. Wu, C.; Chen, Y.; Yang, W.Z.; Yang, L.L.; Qiao, P.; Ma, Q.; Zhai, W.X.; Li, D.; Zhang, X.Q.; Wan, C.F.; et al. Construction of big data system of agricultural machinery based on BeiDou. *Trans. Chin. Soc. Agric. Eng.* **2022**, *38*, 1–8.
39. Wu, C.C.; Cai, Y.P.; Luo, M.J.; Su, H.H.; Ding, L.J. Time-windows Based Temporal and Spatial Scheduling Model for Agricultural Machinery Resources. *Trans. Chin. Soc. Agric. Mach.* **2013**, *44*, 237–241+231.
40. Wu, L.C.; Li, Q.L.; Yuan, D.G.; Sun, L.L.; Yang, S.B. Big Data Analysis of Diesel Engine Coolant Temperature Distribution under Actual Operating Conditions of Agricultural Machinery with Internet of Vehicles. *Agric. Eng.* **2023**, *13*, 102–107.

华南农业大学学报

ISSN 1001-411X
CN 44-1110/S
CODEN HNDXBH

華南農業大學学报

JOURNAL OF SOUTH CHINA AGRICULTURAL UNIVERSITY

中国·广州
GUANGZHOU CHINA

《中文核心期刊要目总览》核心期刊
《中国科学引文数据库(CSCD)》来源期刊
RCCSE中国核心学术期刊

封面论文

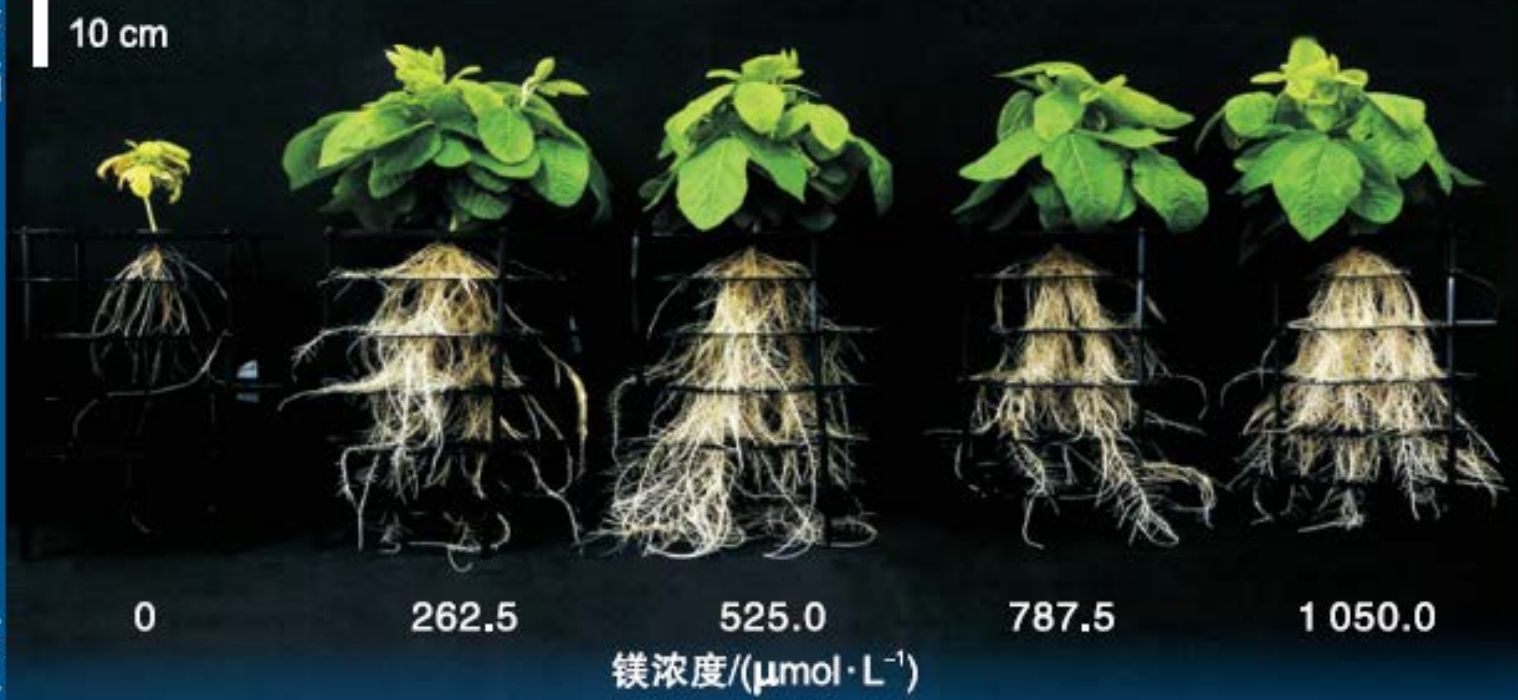

第四十五卷 第三期 二〇二四年五月

2024 5月 May 第45卷 Vol. 45 第3期 No. 3

華南農業大學学报

JOURNAL OF SOUTH CHINA AGRICULTURAL UNIVERSITY

· 双月刊 ·

2024 年第 3 期

（第 45 卷）

華南農業大學学报

JOURNAL OF SOUTH CHINA AGRICULTURAL UNIVERSITY

华南农业大学学报

Huanan Nongye Daxue Xuebao

（双月刊，1959 年创刊，1980 年复刊）

第 45 卷　第 3 期　2024 年 5 月

Journal of South China Agricultural University

(Bimonthly, Started 1959, Resumed 1980)

Vol. 45 No. 3 May 2024

主管单位：华南农业大学

主办单位：华南农业大学

主　　编：薛红卫

编辑出版：《华南农业大学学报》编辑部

地　　址：广州市天河区五山路483号(510642)

网　　址：https://journal.scau.edu.cn/

电子邮箱：journal@scau.edu.cn

电　　话：(020)85280069/38746672

印刷单位：广州一龙印刷有限公司

发行订购：《华南农业大学学报》编辑部

国外发行：中国国际图书贸易总公司（中国国际书店）北京399信箱

Responsible Institution: South China Agricultural University

Sponsor: South China Agricultural University

Chief Editor: XUE Hongwei

Edited and Published by Editorial Department, Journal of South China Agricultural University

Address: Wushan, Guangzhou, 510642, China

Website: https: // journal.scau.edu.cn/

E-mail: journal@scau.edu.cn

Tel: (86-20)85280069/38746672

Distributed by China International Book Trading Corporation(P.O.Box 399 Beijing, China)

ISSN 1001-411X

CN 44-1110/S

国内外公开发行

国内定价：15.00 元/册

ISSN 1001-411X

9 771001 411249 05>

华南农业大学学报

第 45 卷　第 3 期　2024 年 5 月

目　　次

期刊基本参数: CN44 * 1110/S * 1959 * b * A4 * 146 * zh * P * ¥15.00 * 1000 * 16 * 2024-05

JOURNAL OF SOUTH CHINA AGRICULTURAL UNIVERSITY

Vol. 45 No. 3 May 2024

CONTENTS

汪沛, 曾思晓, 何杰. 无人驾驶农机避障路径跟踪仿真与验证 [J]. 华南农业大学学报, 2024, 45(3): 416-426.
WANG Pei, ZENG Sixiao, HE Jie. Simulation and verification for obstacle avoidance path tracking of unmanned agricultural machinery[J]. Journal of South China Agricultural University, 2024, 45(3): 416-426.

无人驾驶农机避障路径跟踪仿真与验证

汪　沛，曾思晓，何　杰
(华南农业大学 工程学院, 广东 广州 510642)

摘要:【目的】为便于验证无人驾驶农机避障路径跟踪的效果，减少实际无人农机试验次数与消耗，设计一种无人驾驶农机避障路径跟踪仿真验证方法，构建一个仿真验证应用系统。【方法】以无人农机为基础，集成真实复杂地形环境仿真、实际作业农机仿真和路径规划算法植入，构建一个一体化仿真验证应用系统。基于三维SLAM技术，采集环境点云数据，实现农田地形环境仿真建模，构建阿克曼转向机械结构的农机仿真建模，提出一种基于农机动力学约束的TEB局部路径规划算法；在仿真验证应用系统中实现路径规划跟踪及避障，并通过多次测试验证该算法的有效性。【结果】避障路径跟踪有效性对比测试和避障路径跟踪平顺性验证测试结果表明，无人农机行驶过程中可有效动态避障，最短有效避障距离为4.1 m。路径跟踪控制效果良好，障碍物距离大于5.0 m时，可控平均误差≤0.430 5 m，均方根误差≤0.315 1 m；障碍物距离在4.5~5.0 m时，可控误差均值≤1.353 8 m，均方根误差≤1.612 6 m。【结论】本文提出的改进TEB算法具有较强的作业能力以及较高的作业精度，满足农业机械导航避障路径跟踪仿真验证的需求，该算法可应用于无人农机在实际农田环境的避障路径跟踪。该应用系统易于扩充，为精准农业中针对各种复杂作业环境的农机运作状态的优化设计研究提供基础。

关键词: 无人驾驶农机；路径跟踪；仿真建模；机器人操作系统；避障；路径规划
中图分类号: S24；S237　　**文献标志码:** A　　**文章编号:** 1001-411X(2024)03-0416-11

Simulation and verification for obstacle avoidance path tracking of unmanned agricultural machinery

WANG Pei, ZENG Sixiao, HE Jie
(College of Engineering, South China Agricultural University, Guangzhou 510642, China)

Abstract:【Objective】In order to facilitate the verification of the effectiveness of obstacle avoidance path tracking for unmanned agricultural machinery, reduce the number of actual unmanned agricultural machine tests and consumables, a simulation verification method for obstacle avoidance path tracking for unmanned agricultural machinery was designed, and a simulation verification application system was constructed.【Method】Based on unmanned agricultural machinery, an integrated simulation and verification application system was constructed by integrating real complex terrain environment simulation, actual operation agricultural machinery simulation, and path planning algorithm implantation. Based on three-dimensional SLAM technology, environmental point cloud data was collected to achieve simulation modeling of farmland terrain

收稿日期:2023–08–02　　**网络首发时间:**2024–04–02 17:33:53
首发网址:https://link.cnki.net/urlid/44.1110.S.20240328.1422.002
作者简介:汪　沛，副教授，博士，主要从事智能农机检测和农情信息采集研究，E-mail: wangpei@scau.edu.cn；通信作者：何　杰，副教授，博士，主要从事智能农机装备和无人农场关键技术研究，E-mail: hooget@scau.edu.cn
基金项目:科技创新2030“新一代人工智能”重大项目(2021ZD0110902，2021ZD0110905)；广东省科技计划(2021B1212040009)

environment. A simulation modeling of agricultural machinery was completed using unmanned agricultural machinery combined with ackermann steering mechanical structure. A TEB local path planning algorithm based on agricultural machinery dynamics constraints was proposed. Path planning tracking and obstacle avoidance were implemented in the simulation verification application system, and the effectiveness of the algorithm was verified through multiple tests. 【Result】The comparison test of obstacle avoidance path tracking effectiveness and the verification test of obstacle avoidance path tracking smoothness showed that the unmanned agricultural machine could effectively avoid obstacles dynamically during driving, with the shortest effective obstacle avoidance distance of 4.1 m. The path tracking control effect was good. When the distance between obstacles was greater than 5.0 m, the controllable average error was within 0.430 5 m, and the root mean square error was within 0.315 1 m. When the distance between obstacles was 4.5−5.0 m, the controllable average error was within 1.353 8 m, and the root mean square error was within 1.612 6 m. 【Conclusion】The improved TEB algorithm proposed in this article has strong operational capability and high operational accuracy, which meets the needs of simulation verification for obstacle avoidance path tracking in agricultural machinery navigation. This algorithm can be applied to obstacle avoidance path tracking of unmanned agricultural machinery in actual farmland environments in the future. This application system is easy to expand and can provide a foundation for the optimization design research of agricultural machinery operation status in precision agriculture for various complex working environments.

Key words: Unmanned agricultural machinery; Path tracking; Simulation modeling; Robot operating system(ROS); Avoiding obstacle; Path planning

中共二十大指出，加快建设农业强国，把握精准农业技术是现代化农业建设中不可或缺的一部分。提高农业机械化和智能化水平可以大幅度提高劳动生产率、资源利用率和土地产出率，无人农机可为此提供装备支撑[1]。然而，无人农机在实际生产中会受到环境等因素影响[2-3]。近年来，传感器技术与定位技术的高速发展使得农机作业的复杂情境可通过仿真建模来实现较高程度的还原[4-7]，在仿真环境中的测试可分析并解决一部分的技术难点；同时，经过多次仿真测试验证后再开展实际试验的工作模式可适当规避复杂自然环境中的偶然影响因素并提高作业效率[8]。因此构建一个一体化应用系统，模拟农机在实际环境中的运作情况是农业自动化作业研究的重要方法。

路径规划是农业机械自动导航的关键技术之一[9]，可分为全局路径和局部路径规划。全局路径规划是在已知环境中进行，更新和修正静态的全局路径[10]，动态调整路径躲避障碍物。局部路径规划算法针对环境完全未知或部分已知，侧重于作业时的局部环境信息，将在实时路况发生变化时直接影响自主导航的避障性能，进而影响对全局路径规划的修正效果。

郑凯林等[11]在 Stage 仿真平台中测试机器人路径规划与导航避障效果，采用直接插入模型的方法，选择了仿真平台列表中的可用模型。王宾[12]通过调用快速扩展随机树算法 (Rapidly-exploring random trees，RRT) 节点实现机器人避障，模型采用 Gazebo 软件列表中可用模型搭建的虚拟机器人模型。郑凯强[13]提出一种软件定义无人车框架设计，对不同导航算法的可行性进行验证，使用 3D Max 软件中配套组件进行环境的三维建模，为无人车试验提供环境模型。李献雯[14]使用单目摄像机采集实际环境路面场景数据，并采用运动恢复结构 (Structure from motion，SFM) 算法逆向生成实际环境三维模型，该方法虽然能根据作业环境的实际特征仿真并复现环境，但摄像机采集图像的处理过程比较复杂，且可获取点云有限，不能很好地描述较为复杂的地形地貌特征。

上述几种模拟仿真系统未能根据实际作业机器人的物理特性与碰撞属性实现模型仿真，忽略了实际作业机器人自身及引起的影响因素；对于实际地形环境的建模未能真实地体现地形地貌特征，欠缺对机器人行驶的平稳性与抗干扰性的考虑。针对上述缺点与农业机械化精准作业的高效性要求，本文设计一种无人驾驶农机避障路径跟踪仿真验证方法，以无人农机为基础，集成真实复

杂地形环境仿真、实际作业农机仿真和路径规划算法植入构建一个一体化仿真验证应用系统。本文基于农机阿克曼结构约束改进了定时弹性带(Time elastic band，TEB) 局部路径规划算法，实现无人农机的避障路径跟踪仿真，并在仿真验证应用系统中测试该算法下的路径规划与自主导航避障效果。

1 材料与方法

1.1 试验材料

农机自主导航系统实现路径跟踪需实际行驶路径与规划路径的横向和航向偏差保持在一定的精度范围之内[15]，以满足农业生产的需要。

机器人操作系统 (Robot operating system，ROS) 为基于 Linux 操作系统的机器人软件框架，是一个开源机器人软件平台，通过整合不同研究成果实现算法的发布与代码的重用，可实现硬件抽象、底层驱动程序管理、进程间消息传递、程序发行包管理等功能。该平台已实现了硬件驱动、模拟仿真、运动规划、运动控制、环境感知等方面的开发。其核心是提供一种点对点的通信机制，进程之间可以直接实现通信并进行数据交换，不需要中转。ROS 是进程的分布式框架，使得异构的运算平台从基站服务器到小型的 ARM 嵌入式系统都可以成为机器人系统的一部分，分散计算压力、降低功能模块间的耦合度。

本试验采用 ROS 中的 Gazebo 仿真软件作为仿真平台，该软件可展示作业机器人的各种物理性能如重力、尺寸、惯性、材料、碰撞等。试验环境为崎岖颠簸的田地，需考虑到农机在行驶时由于车速过快或转弯程度过大而翻车的情况，Gazebo 仿真环境可以充分体现惯性参数以及碰撞参数对农机行驶平稳性能的影响，为后续研究提供参考。此外，Gazebo 还能提供传感器功能，例如，为农机配置的激光雷达模块和惯性测量传感器 (Inertial measurement unit，IMU) 模块等。本试验采用 ROABAG 播放采集的实际农田地形环境三维点云数据包，并采用 EVO 软件进行路径轨迹的误差评估。

无人农机模型为洋马 YR-10D 型直播机，四轮驱动式小农机，可播种 10 行，行距 25 cm，有 11 条排水沟，其中，深排水沟 3 条、浅排水沟 8 条，适用于南方田间作业，可代表典型水田作业时的农机情况。根据该农机及现有的转向控制模型建模，在仿真验证应用系统中多次测试，完成测试算法的有效性验证后，即可运用该算法为洋马 YR-10D 型直播机在实际农田中的作业提供路径规划与自主导航服务。

洋马 YR-10D 型直播机型号为 2BDZ-10D(G4)(YR10D)，长、宽、高分别为 3 430、2 640、2 330 mm，整机质量为 860 kg，发动机型号为 3TNM74F-SC，结构型式为水冷 3 缸 4 冲程柴油发动机，标定功率为 16.0 kW，转速为 3 200 r/min；行走部驱动型式为四轮驱动，采用 HMT 高效液压无极变速方式，变速级数为前进 2(播种 1)、后退 1×HMT 无极变速。播种方式为自然落种，播种深度为表面落种，种子箱容量为 120 L(12 L/个×10 个)，行数为 10 行，行距为 250 mm，每穴播种量为 5~10 粒，有 10 个外槽轮型式的排种器、10 个排种沟开沟器、11 个蓄水沟开沟器，采用机械自动平衡装置。该直播机的作业效率 (理论值) 为 0.703 5 hm^2/h。

采用 Velodyne16 线激光雷达采集地形环境数据，通过返回测量点到雷达信号接收端的距离与角度计算出各采集点在以雷达为原点坐标系的三维坐标。如图 1 所示，激光雷达测量机构绕 2 个互相垂直的轴线旋转 (绕 Z 轴旋转 ± 180°，绕 X 轴旋转 ± 15°)。

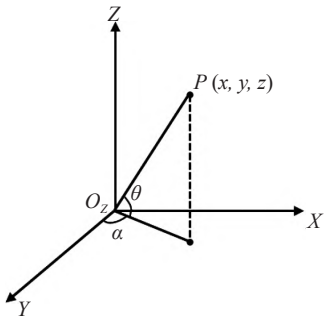

P 为测量点的坐标；O_Z 为雷达信号接收端坐标原点；α为方位角；θ为仰角

P is the coordinate of the measurement point; O_Z is the coordinate origin of the radar signal receiving end; α is the azimuth angle; θ is the elevation angle

图 1 3D 激光雷达测量目标示意图

Fig. 1 Schematic diagram of 3D LiDAR measurement target

测量时系统预先设定范围并扫描，最终得出测量目标的三维坐标 $P(x, y, z)$ 的计算公式：

$$\begin{cases} x = l\cos\theta\sin\alpha \\ y = l\cos\theta\cos\alpha \\ z = l\sin\theta \end{cases}, \tag{1}$$

式中，l 为测量点 P 到雷达信号接收端坐标原点 O_Z 的距离，m；α为方位角，(°)；θ为仰角，(°)。

1.2　试验方法

为验证避障路径跟踪仿真验证方法的有效性，本文提出一种基于阿克曼结构动力学约束的改进 TEB 算法，并测试算法的性能。设计避障路径跟踪有效性对比试验和避障路径跟踪平顺性验证试验 2 组试验进行验证。

在行驶路径上实时添加障碍物，分别采用 DWA 算法、改进 TEB 路径跟踪算法，仿真验证无人驾驶农机实时避障效果，进行避障路径跟踪有效性试验。测试时，在行驶路途中分别在距农机不同位置处放置圆柱体障碍物，观察农机是否能准确规划路径避开障碍物，避免陷入障碍物死区或者由于规划路径紊乱而失控。设定一系列农机与 Gazebo 仿真环境中圆柱障碍物距离，每段距离在仿真环境进行 10 次导航测试，观察其在行进过程中遇到障碍物时是否绕开障碍物并继续往设定目标点前进。

避障路径跟踪平顺性验证试验主要考察无人驾驶农机避障行驶的平顺性和路径跟踪精度。测试时设置相同的起点与终点，在 Gazebo 仿真环境中行驶途中放置障碍物，获取农机导航避障过程中实际行驶路径坐标数据，以及由局部路径规划器根据突然添加的障碍物对全局路径更新修正所得规划路径的坐标数据，分析二者轨迹误差。

2　无人驾驶农机及田间环境建模

2.1　农田环境建模

安装 Velodyne16 线激光雷达的农机巡检作业进行 3D 数据的测量和采集，该雷达是可以同时发射并接收多束激光雷达的机械式旋转测距雷达[16]，每秒可输出高达 30 万个点数据，具备 ± 15°的垂直视场、360°的水平视场，测量距离半径达 100 m 以上。即时定位与地图构建 (Simultaneous localization and mapping，SLAM) 指机器人在试验区域移动的过程中根据位姿估计以及地图进行定位并在此基础上构建增量式地图。基于 Cartographer SLAM 算法[17]，通过在试验区域遍历完成三维环境点云的采集，创建三维点云地图。Cartographer SLAM 算法通过非线性最小二乘法实现，处理闭环检测数据，获取后端优化后的静态全局地图，使用里程计数据结合传感器接收的激光数据、IMU 数据[18] 进行位姿估计，其中 IMU 辅助激光雷达去除运动畸变部分并进行积分，其积分值作为激光点进行迭代最近邻点 (Iterative closest point，ICP) 配准的初值并据此迭代求解得到载体位姿与局部子图位姿，激光帧经叠加后形成子图。局部 SLAM 模块据此进行实时位姿更新与局部子图的建立，全局 SLAM 实现回环检测功能，根据局部子图优化形成全局地图。

试验农田位于广州市增城区，尺寸为 230 m× 123 m。首先在 ROS 系统中搭建 SLAM 工作环境，运行 SLAM 功能包，将激光雷达装于无人农机适当位置后，运行建图程序，随着无人农机在试验区域内行驶，激光雷达采集各处点云数据。运行 ROS BAG 指令开始录制数据，当无人农机在试验区域内遍历完成后，停止录制数据。播放数据包，进行坐标变换的处理，即可得到 PCD 格式的点云地图。

由于农机行驶采集点云数据过程中获取信息非常频繁，导致 2 帧数据有大量的重叠。如图 2 所示，点云信息数据量庞大，计算开销大，因此本文使用 Cloudcompare 软件对三维点云图进行降采样 (Downsample) 处理，实现数据匹配以及点云噪声点的滤除，子样本保持原始点云的其他性质。选择八叉树方式根据不同区域点云密度相应调节削减程度，即密度大的区域的点云数据被削减的程度更大。经处理后，点云数由原来的3 408 484 被削减为13 473。

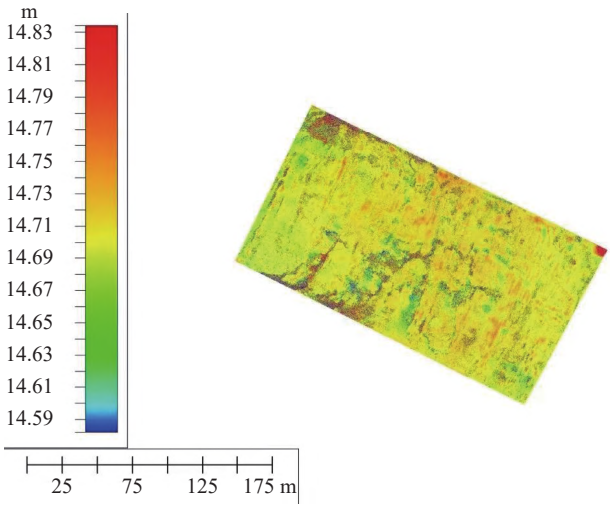

图 2　农田环境点云图

Fig. 2　Point cloud map of farmland environment

在点云图的原始三维坐标的基础上计算并配置法向量，并对方向不一的法向量进行最小生成树二次处理，重新定位点云所有法向量后即可呈现清晰正反亮暗两面效果。通过 Meshlab 软件重建为 3D 地形模型，然后导入 Gazebo 仿真环境中，作为仿真地形环境模型。针对不同的作业情境，使用激光雷达采集三维点云数据，通过上述三维重建方法

生成不同的地形环境仿真模型，即可集成至应用系统进行相应测试，具备一定通用性。

2.2 无人驾驶农机仿真建模

2.2.1 *阿克曼转向模型* 轮式农机多采用阿克曼转向结构，这种结构可以通过构建各轴车轮转向的传动机构约束[19]减小无人农机在行驶过程中的阻力和轮胎的磨损，使各车轮在转向中处于纯滚动无侧滑的状态，有利于提升转向响应速度和农机行驶的平稳性[20]。

当农机转向时，车轮运动如图 3 所示，农机的基坐标旋转中心为后轮转轴中点 O，当转向轮前轮转弯程度到达极限时，由外转向轮中心引出的垂线与后轮旋转轴所在直线的交点，与旋转中心之间的距离，称为最小转弯半径 (R)，可以反映农机通过最小曲率半径弯曲道路和在狭窄路面掉头行驶的能力。为实现纯滚动运动，须使得 2 个前轮运动方向的法线与通过车轮转动实现前后移动的后轮运动方向的法线，即后轮旋转轴的延长线相交于一点。

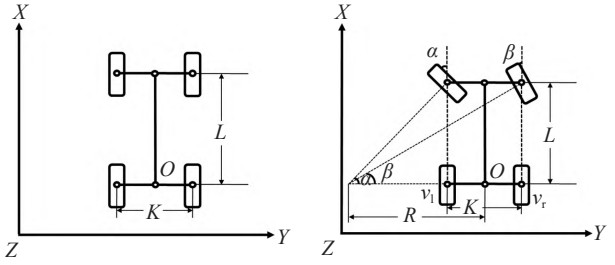

α 为左前轮转向角；β 为右前轮转向角；K 为后轮两轮距；L 为前后轮旋转轴轴距；R 为转弯半径；v_l 为左后轮线速度；v_r 为右后轮线速度

α is the left front wheel steering angle; β is the right front wheel steering angle; K is the wheelbase of the two rear wheels; L is the wheelbase of rotation axis for front and rear wheel; R is the turning radius; v_l is the linear speed of the left rear wheel; v_r is the linear speed of the right rear wheel

图 3 阿克曼结构转向示意图

Fig. 3 Schematic diagram of ackermann structure turning

根据上述模型中几何结构得出以下约束：

$$\tan\alpha = L/(R - K/2), \tag{2}$$

$$\tan\beta = L(R + K/2), \tag{3}$$

式中，L 为前后轮旋转轴轴距，m；R 为转弯半径，m；K 为后轮两轮距，m；α为左前轮转向角，(°)；β为右前轮转向角，(°)。因此转弯半径受前后轮转轴轴距、后轮两轮距、转向角限制，该控制策略限制了转弯半径的最小值即最大转弯程度。根据上述几何关系可以得到农机在进行转弯运动时的线速度和角速度 (以左轮为例，右轮类同)：

$$\dot{x} = v\cos\alpha, \tag{4}$$

$$\dot{y} = v\sin\alpha, \tag{5}$$

$$\dot{\theta} = v\tan\alpha/L, \tag{6}$$

式中，$\dot{x}$为 x 轴方向的线速度，m/s；$\dot{y}$为 y 轴方向的线速度，m/s；$\dot{\theta}$为角速度，(°)/s；v 为农机的总线速度。

阿克曼结构中四连杆是闭环机械结构，无法通过 ROS 系统中机器人建模 URDF 文件描述[21]，因此在实际的导出模型中，通过设置车轮关节替代四连杆的机械结构实现前轮转向控制。

基于无人农机配置阿克曼结构农机 Solidworks 模型，并根据实际运动状态对作用于运动控制的连杆与关节进行配置，包括连杆父子关系、关节运动形式、关节运动中心或旋转轴的配置等，通过插件 Solidworks to URDF Exporter 将 Solidworks 模型导出至 ROS 系统 Gazebo 仿真环境中。

2.2.2 *运动控制* 在 ROS 仿真环境中，实现运动控制包括运动控制器配置和关节控制消息发布。为四轮配置速度控制器，并为前轮配置位置控制器，将四轮转速、前轮转向角消息的指令信号发布到对应的运动关节以驱动关节运动。

农机的运动信息包括坐标、转向角 (ψ)、线速度等，运动学模型如下所示。

农机在 t 时刻状态向量为：

$$\vec{X}_t = (x_t, y_t, \psi_t, \dot{x}_t, \dot{y}_t)^{\mathrm{T}}, \tag{7}$$

式中，(x_t, y_t)为农机在 t 时刻的坐标，ψ_t为农机在 t 时刻的转向角，$\dot{x}_t$、$\dot{y}_t$分别为农机在 t 时刻 X 和 Y 轴方向线速度。

则农机在 t+1 时刻沿全局坐标系的速度为：

$$\dot{x}_{t+1} = \frac{\dot{x}_{\mathrm{r},t} + \dot{x}_{\mathrm{l},t}}{2}\cos\psi + \ddot{x}\Delta t, \tag{8}$$

$$\dot{y}_{t+1} = \frac{\dot{y}_{\mathrm{r},t} + \dot{y}_{\mathrm{l},t}}{2}\sin\psi + \ddot{y}\Delta t, \tag{9}$$

式中，$\ddot{x}$、$\ddot{y}$分别为农机在 t 时刻沿全局坐标系的 X 轴、Y 轴方向的加速度，$\dot{x}_{\mathrm{r},t}$和$\dot{y}_{\mathrm{r},t}$分别表示右轮在 t 时刻 X 轴和 Y 轴方向的线速度，$\dot{x}_{\mathrm{l},t}$和$\dot{y}_{\mathrm{l},t}$分别显示左轮在 t 时刻 X 轴和 Y 轴方向的线速度，Δt为时间增量。

则农机在 t+1 时刻的位移、转向角计算公式为：

$$x_{t+1} = x_t + \dot{x}_t\Delta t + 0.5\ddot{x}\Delta t^2, \tag{10}$$

$$y_{t+1} = y_t + \dot{y}_t\Delta t + 0.5\ddot{y}\Delta t^2, \tag{11}$$

$$\psi_{t+1} = \psi_t + \dot{\theta}\Delta t。 \tag{12}$$

综上所述，农机运动学模型为：

$$\vec{\boldsymbol{X}}_{t+1}=\vec{\boldsymbol{X}}_t+\Delta\vec{\boldsymbol{X}}=$$

$$\begin{bmatrix} x_t+0.5\left(\dot{x}_{\mathrm{r},t}+\dot{x}_{\mathrm{l},t}\right)\Delta t\cos\psi+0.5\ddot{x}\Delta t^2 \\ y_t+0.5\left(y_{\mathrm{r},t}+v_{\mathrm{l},t}\right)\Delta t\sin\psi+0.5\ddot{y}\Delta t^2 \\ \psi_t+1/K\left(v_{\mathrm{r},t}+v_{\mathrm{l},t}\right)\Delta t \\ 0.5\left(v_{\mathrm{r},t}+v_{\mathrm{l},t}\right)\cos\psi 0.5\ddot{x}\Delta t \\ 0.5\left(v_{\mathrm{r},t}+v_{\mathrm{l},t}\right)\sin\psi 0.5\ddot{y}\Delta t \end{bmatrix}。\quad (13)$$

农机模型机械结构如图 4 所示，采用 ros_control 插件处理所接收的转速、转向角信息。速度控制器在接收转速指令信号后将驱动对应车轮关节转动实现前后移动；位置控制器在接收转向角指令信号后作用于转向轮关节驱动连杆摆动带动

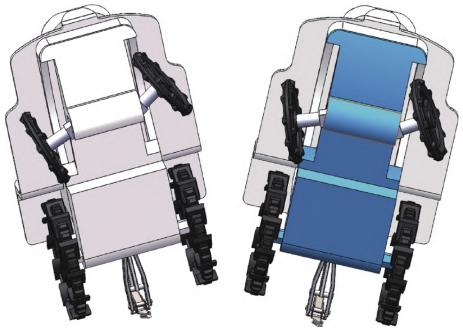

图 4　农机模型机械结构

Fig. 4　Mechanical structure of agricultural machinery models

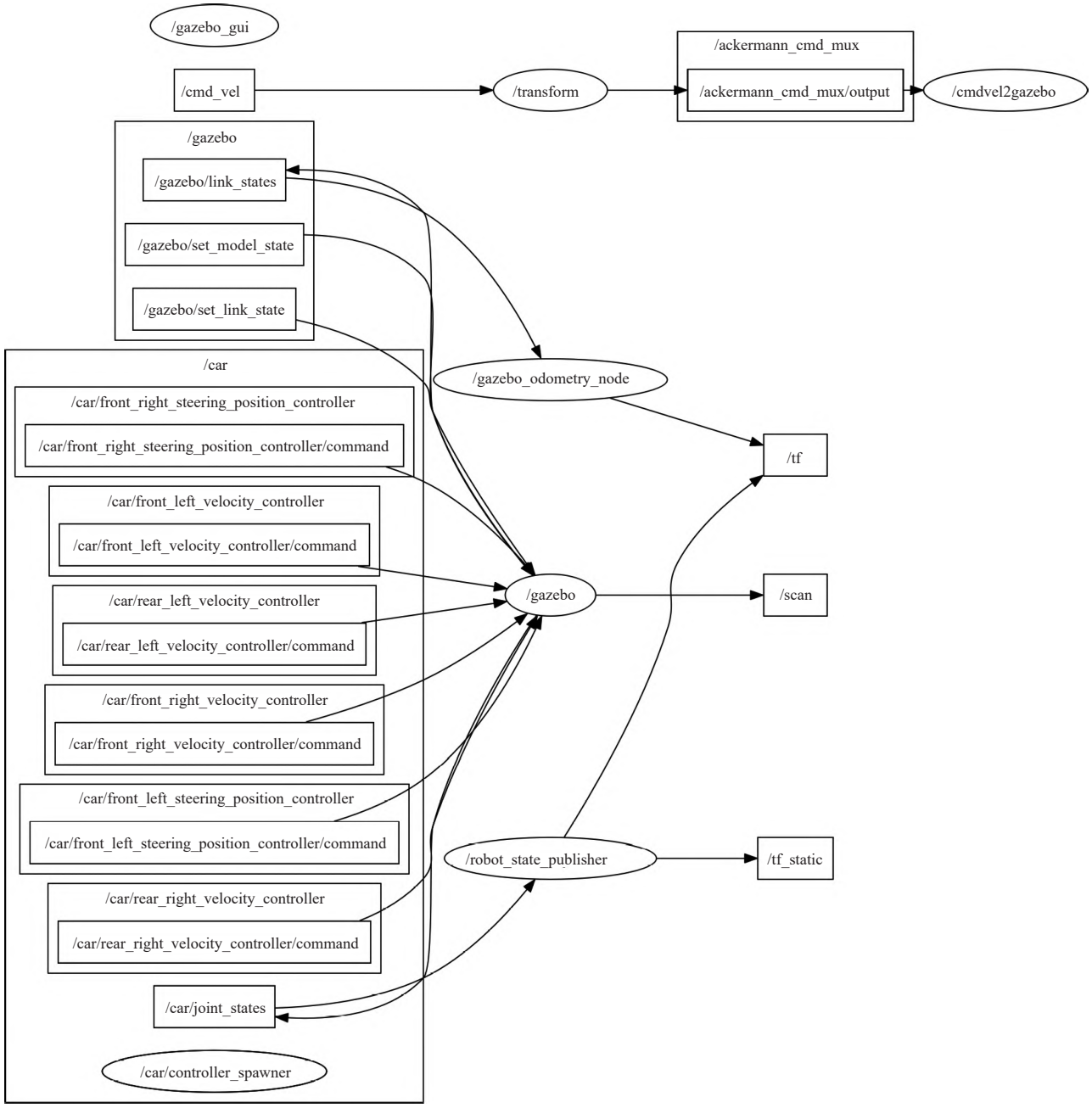

图 5　运动控制系统节点关系

Fig. 5　Node relationships in motion control system

前轮转向实现转向控制。各节点之间关系如图 5 所示。

农机运动控制的核心是对该阿克曼转向结构中各关节的控制，因此在该仿真验证应用系统中的测试结果亦适用于具备相同阿克曼转向结构的农机。由于该应用系统试验平台为 ROS 系统，采用了话题通信机制，当需要对不同农机进行作业效果测试时，可通过话题的转换实现农机模型模块化的移植与集成。

2.2.3 路径跟踪控制 全局路径规划基于全局地图进行。在获取里程计数据、激光雷达数据以及融合 IMU 传感器数据后，对/map 坐标系下的农机进行基于自适应蒙特卡洛定位算法[22](Adaptive monte carlo localization，AMCL) 的位姿估计。

AMCL 算法是一种多传感器融合定位算法，使用贝叶斯概率实现利用栅格、格子等描述移动机器人的状态空间，递归计算出概率分布[23]。将里程计信息作为预测量，并融合 IMU 获取的精确角度信息来弥补里程计中较大的角度累积误差。移动机器人在任意状态下都可推算出自己位姿，AMCL 算法通过概率统计的方法利用粒子滤波在已知地图中估计农机位姿，具体流程如下：

初始化粒子群，定义一个大小为 m 的粒子群，其中每个粒子代表农机在环境中的一个位姿信息，如果初始位姿未知，则每个粒子的位置都是随机的；模拟粒子运动，得出系统初始状态分布 $N(x_0,P_0)$，并在农机状态空间分布中采集 n 个粒子，如式 (14) 所示：

$$\left\{x_0^{[i]}\right\}_{i=1}^{n} \sim N(x_0,P_0), \tag{14}$$

式中，x 为粒子。

计算粒子权重，根据粒子权重长期变化均值 w_{slow} 和短期变化均值 w_{fast}，加入经验测量似然 w_{avg} 并通过设定好的长期变化率 α_{slow} 和短期变化率 α_{fast} 对上述 2 种均值进行修正，根据式 (15) 更新：

$$\begin{cases} w_{\text{slow}} = w_{\text{slow}} + \alpha_{\text{slow}}\left(w_{\text{avg}} - w_{\text{slow}}\right) \\ w_{\text{fast}} = w_{\text{fast}} + \alpha_{\text{fast}}\left(w_{\text{avg}} - w_{\text{fast}}\right) \end{cases}, \tag{15}$$

其中，加入随机粒子、重复性采样的概率由式 (16) 确定：

$$\max\left\{0.0, 1.0, -\frac{w_{\text{fast}}}{w_{\text{slow}}}\right\}。 \tag{16}$$

粒子群重采样时为了减少无效计算量，AMCL 利用库尔贝克−莱布勒散度 (Kullback-leibler divergence，KLD) 采样，计算粒子及对应的数目：

$$n = (k-1)/2\varepsilon\left[1-2/9(k-1)+\sqrt{2/9(k-1)}z_{1-\delta}\right]^3, \tag{17}$$

式中，δ 为标准正态分布下的 α 分位点，即满足条件 $P(x\leqslant\delta)=\alpha$ 的实数；$z_{1-\delta}$ 是上界为 $1-\delta$ 的标准正态分布置信度；ε 表示一个非常小的正数的阈值。

计算机器人在 t 时刻的位姿，即粒子集的数学期望：

$$x_t = E\left[\left\{x_t^{[i]}\right\}_{i=1}^{n}\right]。 \tag{18}$$

在上述位姿估计信息的基础上，即可基于 Gmapping SLAM 算法构建出试验区域的二维全局地图。

将所建全局地图应用于导航中的全局规划，如图 6 所示，农机在导航行驶时要求避免与代价地图接触，系统根据位姿估计实时更新路径规划，对障碍物的检测识别将会减小局部地图局部路径规划器代价地图覆盖范围，进而对全局路径进行修正，实现实时避障。

本文基于 move_base 算法实现导航，默认局部路径规划算法为动态窗口法 (Dynamic windows

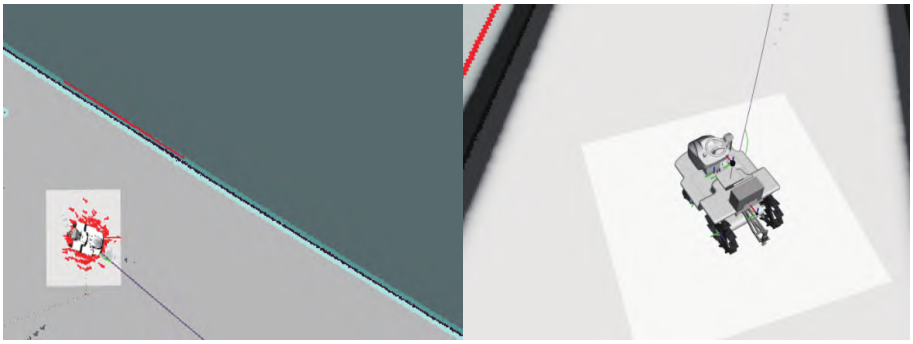

全局路径以紫色曲线表示，局部路径规划以农机行驶时沿实际运动方向的绿色短线表示

The global path is represented by a purple curve, while the local path planning is represented by a green short line along the actual movement direction of the agricultural machinery during operation

图 6 导航过程示意图

Fig. 6 Navigation process diagram

approaches，DWA)，通过V_s、V_d、V_a 3 种约束条件精确化减小速度空间的搜索范围，最终获取该时刻机器人的无碰撞速度，在该速度约束空间内机器人不会发生碰撞。然后通过评价函数评价可选轨迹，选取最优解[24]。但是该算法并未充分考虑针对本文农机阿克曼动力学结构的非完整约束动力学情况，当遇到障碍物时，该算法无法决策出适用于阿克曼转向结构的有效避障路径，完成有效地避障操作。

在局部路径规划中，动力学模型将成为更重要的影响因素，因此，本文提出基于阿克曼机械结构约束的改进 TEB 局部路径规划算法，不断在适量空间中获取实时转向控制信息并将其发送至前轮的位置控制器，完成所设定的各项约束。相比于 move_base 导航算法默认采用的 DWA 局部路径规划算法，该算法实现了对具有非完整约束的阿克曼无人农机动力学的考虑，当遇到障碍物时可实现车轮转向关节、驱动关节准确并快速地响应，决策出有效的避障路径。

TEB 算法通过在全局路径中根据设定约束插入 N 个控制点对全局路径修正，这些控制点是一些规划的各个时刻的离散位姿数据，这些离散位姿用 P 表示，表示为式 (19)。

$$P = \{p_i\}_{i=0,\cdots,n}, nN, \tag{19}$$

式中，每个点的位姿用 $p_i = (x_i, y_i, \psi_i)$ 表示，分别描述所处位置的横坐标、纵坐标和转向角。

在 2 个位姿点之间设置时间间隔 Δt_i。将所有相邻位姿点时间间隔集合用 T 表示：

$$T = \{\Delta t_i\}_{i=0,\cdots,n-1}, n \epsilon N。 \tag{20}$$

因此，TEB 路径定义为 2 个序列的元组 (M)：

$$M = (P, T)。 \tag{21}$$

TEB 路径约束包括机器人动力学约束、最快路径约束、速度约束、路径避障约束等。其中，速度约束 (f_{vel}) 限制机器人的最大线速度与角速度，速度限制以损失的形式实现，线速度 $\dot{x}_i$、$\dot{y}_i$ 以及角速度 $\dot{\theta}_i$ 根据向后差分可得：

$$\dot{x}_i = (x_{i+1} - x_i)/\Delta t_i, \tag{22}$$

$$\dot{y}_i = (y_{i+1} - y_i)/\Delta t_i, \tag{23}$$

$$\dot{\theta}_i = (\theta_{i+1} - \theta_i)/\Delta t_i, \tag{24}$$

$$f_{\text{vel}} = f\left(\dot{x}_i, \dot{y}_i, \dot{\theta}_i\right)。 \tag{25}$$

最快路径约束 (f_{t}) 计算公式为：

$$f_{\text{t}} = \min_M \left(\sum \Delta t_i\right)^2。 \tag{26}$$

路径避障约束 f_{path} 与 f_{obs}，在 TEB 算法规划局部路径时，须以跟踪全局路径为基础，通过 f_{path} 实现；并基于此避开实时障碍物，即全局路径吸引 TEB 路径规划点，通过 f_{obs} 实现。约束以惩罚函数行驶实现如式 (27)、(28) 所示。

$$f_{\text{path}} = f\left(d_{\min}, r_{p\max}, S, n, \varepsilon\right), \tag{27}$$

$$f_{\text{obs}} = f(-d_{\min}, -r_{o\min}, S, n, \varepsilon), \tag{28}$$

式中，$d_{\min}$ 为 TEB 局部路径规划点和障碍物的最小距离，m；$r_{p\max}$ 为 TEB 局部路径规划点与全局路径规划点的最大距离，m；$r_{o\min}$ 为 TEB 局部路径规划点与全局路径规划点的最小距离，m；S 表示缩放系数；n 是多项式阶数；ε 为边界值附近的 1 个小位移，为约束增加裕度。

针对阿克曼机械结构，结合式 (2)、(3)，在局部路径算法中对农机的最小转弯半径等几何参数加以约束，针对实际地势起伏不平的田地环境，有效提高农机行驶过程中对规划路径的跟踪程度以及避障的有效性。

以上 TEB 约束的求解采用图优化方法，将每一个状态和时间间隔作为顶点，各种约束作为建立超图的元素进行多目标优化，并使用 g2o 框架求解。

测试时将农机模型的基坐标模型起点设定为 [−5.5, 0]，终点设为 [5.5, 0]，农机模型的前、后轮距离为 1.10 m，由式 (2)、(3) 可知该农机模型的最小转弯半径应为 2.177 m。多次测试调试后，整定的参数为：改进 TEB 算法中最小期望距离为 2 m，轨迹时间分辨率为 0.1 s，最大线速度为 2 m/s，线加速度为 0.5 m/s^2，倒车最大速度为 0.5 m/s，最大角速度为 286.48 (°)/s，角加速度为 143.24 (°)/s^2，考虑优化全局路径子集最大长度为 1 m，到达目标允许误差范围为 0.5 m，到达目标角度允许误差范围为 0.5 m。

3　结果与分析

3.1　避障路径跟踪有效性测试结果

3.1.1　DWA 路径跟踪效果　无人农机与障碍物距

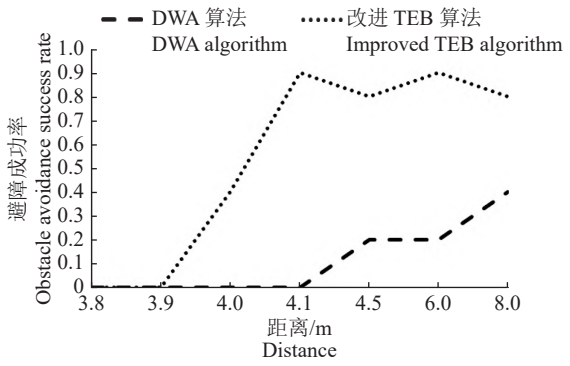

图 7　避障成功率

Fig. 7　Obstacle avoidance success rate

离为 3.8~8.0 m 区间内，分别进行了 10 次避障测试，测试结果如图 7 所示。改进 TEB 算法的最短有效避障距离达 4.1 m；DWA 算法，由于距离为 8.0 m 时，避障成功率尚未达到 0.5，因此最短有效避障距离大于 8.0 m。

在 DWA 算法避障的测试中，避障失败的主要表现有 2 种，一是由于缺少全局指引，在局部最小测试中陷入局部最优而无法脱离圆柱体障碍物；二是由于农机根据规划路径行驶时转弯半径过小，即转弯程度过大，绕开障碍物后偏航严重，无法回到全局路径中。

当农机与障碍物距离区间为 3.8~4.5 m 时，避障失败的原因均为无法绕过障碍物，DWA 算法在局部距离最短测试中陷入了局部最优而无法脱离圆柱体侧面的凹形障碍物；当距离为 6.0 m，避障失败情况中有 2 次是由于农机根据规划路径行驶时转弯半径过小，即转弯程度过大，绕开障碍物后偏航严重，局部路径规划无法将运动控制拉回至全局路径，农机无法回到向目标点行进的路径当中；当距离为 8.0 m 时，偏航情况出现 6 次。

3.1.2 阿克曼机械结构约束的 TEB 避障效果 采用基于阿克曼结构约束的改进 TEB 算法，最短可避障距离相较 DWA 算法提升至少 3.9 m。避障过程如图 8 所示，规划农机自起点至终点的全局路径；当靠近障碍物时，如 8b 所示，根据局部路径规划，修正全局路径以避障；如图 8c 所示，农机根据规划路径成功避障到达设定目标点，未偏离全局路径。因此，测试结果表明本文提出的基于阿克曼动力学约束的改进 TEB 局部路径规划算法的避障路径跟踪有效性良好。

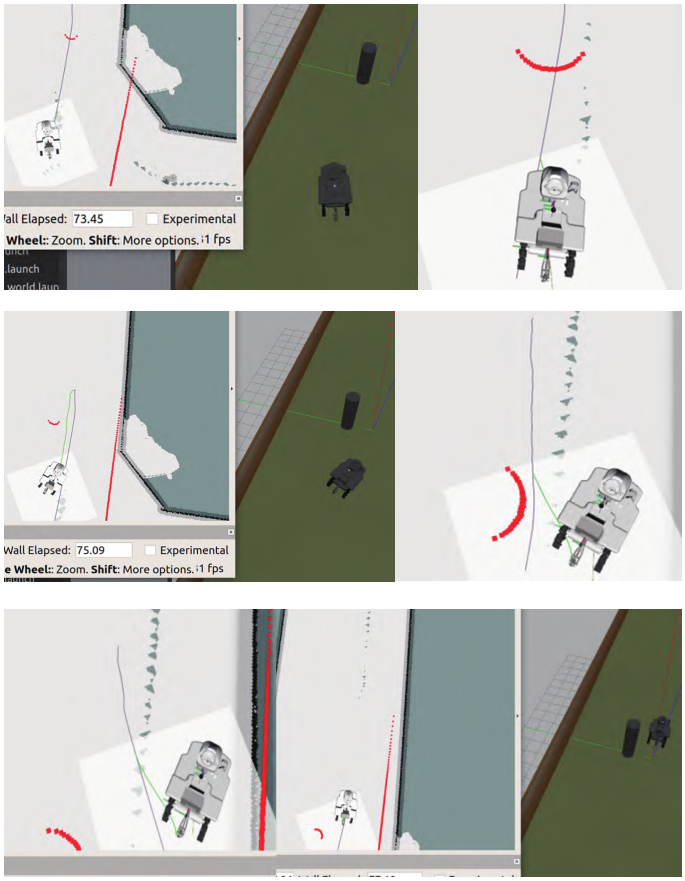

图中紫色曲线为农机自起点至终点的全局路径；绿色曲线为局部路径修正的全局路径

The purple curve in the figure is the global path planned from the starting point to the end point of the agricultural maehinery; The green curve is the global path corrected by the local path

图 8 避障路径规划

Fig. 8 Path planning of obstacle avoidance

3.2 避障路径平顺性测试结果

距离实时障碍物 4.5、5.0 m 时，农机实际行驶路径对规划路径的跟踪情况如图 9 所示。由图 9 可知实际路径和规划路径的相对误差随着时间推进逐渐逼近 0。由“3.1”可知本算法最短有效避障距离可达 4.1 m，因此图 9a 中实际行驶路径与规划路径的相对误差明显大于图 9b。图 9b 中农机图像尾端 *Y* 轴方向坐标相对误差稳定值约为 0.7 m；图 9a

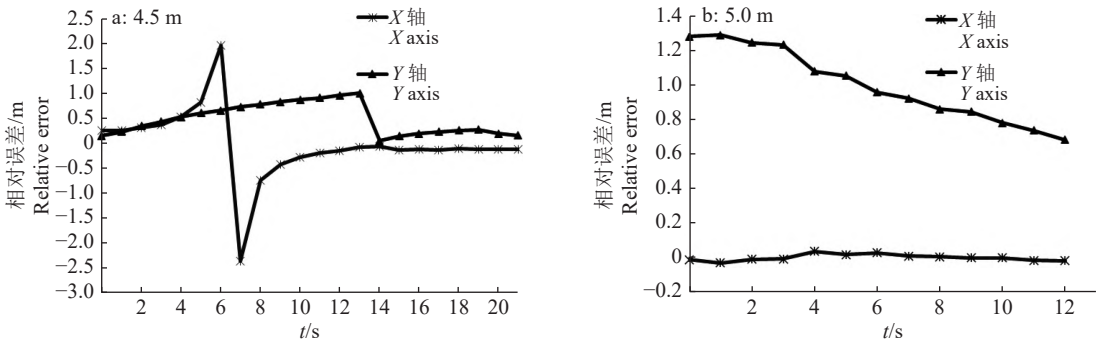

图 9　距障碍物不同距离时实际行驶路径与规划路径的相对误差

Fig. 9　Relative errors between the actual driving path and planned path of obstacles at different distances

中两轴方向坐标相对误差稳定值接近 0。距离障碍物 5.0 m 时，实际行驶路径与规划路径误差均值为 0.430 5 m，均方根误差为 0.315 1 m，均小于 0.45 m；距离障碍物 4.0 m 时，实际行驶路径与规划路径均方根误差为 1.353 8 m，误差均值为1.612 6 m，均小于 1.65 m，农机实际行驶路径对规划路径的跟踪状况良好、精度较高。

由上述试验结果可知，农机在田地仿真环境中导航作业时，若障碍物距离大于 5 .0 m 时，可控误差均值≤0.430 5 m，均方根误差≤0.315 1 m；若障碍物距离为 4.5~5.0 m 时，可控误差均值≤1.353 8 m，均方根误差≤1.612 6 m。上述结果表明基于阿克曼结构约束改进的 TEB 算法对局部路径的规划控制效果良好，满足农机自动导航系统对路径规划的精度要求，验证了算法的可行性。

4　结论

设计了一种无人驾驶农机避障路径跟踪仿真验证方法，集成真实复杂地形环境仿真、实际作业农机仿真、路径规划算法植入构建一个一体化仿真验证应用系统，该应用系统易于扩充，是一个通用的仿真验证应用系统，适用于各种地形地貌的作业环境。基于三维 SLAM 技术采集环境点云数据实现农田地形环境仿真建模，有利于体现测试算法下农机对复杂路面的适应性；适用于不同机械结构的农机，通过 ROS 系统话题转换实现农机模型模块化的通用移植与集成。

在仿真验证应用系统中，基于洋马 YR-10D 型无人驾驶直播机研究了阿克曼结构模型和无人驾驶农机动力学模型，测试结果及结论适用于具备相同阿克曼转向结构的农机。基于阿克曼结构和无人驾驶动力学约束，设计了改进型 TEB避障路径跟踪算法，验证了无人农机在农田环境中作业的路径规划效果。

避障路径跟踪有效性测试结果表明该算法规划下最短有效避障距离达 4.1 m，较传统 DWA 动态窗口法提升了 3.9 m，验证了其有效性。避障路径平顺性测试结果表明，在局部路径规划采用基于阿克曼结构动力学约束的改进 TEB 算法，农机自主导航行驶时可较好地跟踪规划路径，满足精度要求。障碍物距离大于 5.0 m 时，可控误差均值≤0.430 5 m，均方根误差≤0.315 1 m；障碍物距离小于 5.0 m 大于 4.5 m 时，可控误差均值≤1.353 8 m，均方根误差≤1.612 6 m。

各项测试结果表明，基于阿克曼结构动力学约束的 TEB 算法具有较强的作业能力以及较高的作业精度，满足无人驾驶农机避障路径跟踪仿真验证的需求，后续可应用该算法于无人农机在实际农田环境的避障路径跟踪。模型的惯性参数与碰撞参数未能很好地调试和校正，导致无人农机行驶在地势起伏不平的农田仿真环境中平稳性欠佳，后续研究应进一步调整校正。为无人农机模型配置的阿克曼前轮转向轮结构在实际运动时仍有缺陷，无人农机在仿真环境中行驶时出现震荡现象，该部分机械结构设计有待进一步完善。

参考文献：

[1] 罗锡文, 廖娟, 胡炼, 等. 我国智能农机的研究进展与无人农场的实践[J]. 华南农业大学学报, 2021, 42(6): 8-17.

[2] 尚业华, 王昊, 孟志军, 等. 基于激光雷达的稻麦收获边界检测与自动对齐系统研究[J]. 农业机械学报, 2023, 54(5): 19-28.

[3] 张朝宇, 董万静, 熊子庆, 等. 履带式油菜播种机模糊自适应纯追踪控制器设计与试验[J]. 农业机械学报, 2021, 52(12): 105-114.

[4] 丛佩超, 崔利营, 万现全, 等. 基于改进 ORB-SLAM2 的果园喷药机器人定位与稠密建图算法[J]. 农业机械学报, 2023, 54(7): 45-55.

[5] 刘慧, 段云鹏, 沈跃. 果园移动机器人激光雷达双源信息融合实时导航方法[J]. 农业机械学报, 2023, 54(8):

249-258.
[6] 齐咏生, 姚辰武, 刘利强, 等. 基于信息融合描述子的机器人复杂场景位姿估计算法[J]. 农业机械学报, 2022, 53(10): 293-305.
[7] 陈子文, 胡宗锐, 熊扬凡, 等. 树冠环绕式仿形对靶施药机设计与试验[J]. 农业工程学报, 2023, 39(3): 23-32.
[8] 刘慧, 张世义, 段云鹏, 等. 基于改进双向 RRT~*的果园机器人运动规划算法[J]. 农业机械学报, 2022, 53(11): 31-39.
[9] 胡炼, 王志敏, 汪沛, 等. 基于激光感知的农业机器人定位系统[J]. 农业工程学报, 2023, 39(5): 1-7.
[10] 郑路, 张啸, 王建国, 等. 基于宏微结合的田间作业机器人路径规划[J]. 农业机械学报, 2023, 54(9): 13-26.
[11] 郑凯林, 韩宝玲, 王新达. 基于改进 TEB 算法的阿克曼机器人运动规划系统[J]. 科学技术与工程, 2020, 20(10): 3997-4003.
[12] 王宾. 基于 RRT 的虚拟现实环境中 ROS 机器人路径规划研究[J]. 呼伦贝尔学院学报, 2023, 31(1): 112-116.
[13] 郑凯强. 基于软件定义的 VR 控制无人车架构研究[D]. 杭州: 浙江理工大学, 2022.
[14] 李献雯. 基于数字孪生的病害路面交通场景建模[D]. 西安: 西安工业大学, 2023.
[15] 王辉, 王桂民, 罗锡文, 等. 基于预瞄追踪模型的农机导航路径跟踪控制方法[J]. 农业工程学报, 2019, 35(4): 11-19.
[16] 胡子威. 基于多线激光雷达的室外移动机器人 SLAM 研究与实现[D]. 上海: 上海师范大学, 2023.
[17] FAN X, WANG Y, ZHANG Z. An evaluation of lidar-based 2D SLAM techniques with an exploration mode[J]. Journal of Physics: Conference Series, 2021, 1905(1): 012021. doi: 10.1088/1742-6596/1905/1/012021.
[18] SUPOD K, MONGKOL E, UKRIT T. High-accuracy position-aware robot for agricultural automation using low-cost IMU-coupled triple-laser-guided (TLG) system[J]. IEEE Access, 2021, 9: 54325-54337.
[19] 陆海英, 张成铭, 郭艳秋, 等. 基于阿克曼原理的三轴车辆全轮转向最优控制[J]. 广西大学学报(自然科学版), 2020, 45(3): 558-568.
[20] 宫金良, 马全坤, 张彦斐. 阿克曼转向农业机器人的多级模糊控制避障[J]. 农机化研究, 2021, 43(4): 196-201.
[21] 李萍, 杨晓辉, 房启飞, 等. 基于阿克曼理论的四轮转向汽车转向梯形优化设计[J]. 北京汽车, 2021(3): 16-20.
[22] YANG L G, CHI H F. SLAM self: Cruise vehicle based on ROS platform[C]//2021 IEEE International Conference on Consumer Electronics and Computer Engineering (ICCECE). Guangzhou, China: IEEE, 2021: 6-11. doi:10.1109/ICCECE51280.2021.9342204
[23] 张文玥, 娄小平, 陈福笛. 移动机器人多传感器融合定位仿真研究[J]. 计算机仿真, 2023, 40(3): 436-441.
[24] LIN Z N, YUE M, CHEN G Y , et al. Path planning of mobile robot with PSO-based APF and fuzzy-based DWA subject to moving obstacles[J]. Transactions of the Institute of Measurement and Control, 2022, 44(1): 121-132.

【责任编辑 霍 欢】

美国《工程索引》(Ei) 收录期刊
Scopus数据库收录期刊
中文核心期刊　中国科技核心期刊
中国科学引文数据库来源期刊

ISSN 1000-1298
CODEN NUYCA3

农业机械学报

Transactions of the Chinese Society for Agricultural Machinery

专栏主题: 智能农业动力装备关键技术
专栏主编: 宋正河 教授　徐立友 教授

中国农业机械学会
中国农业机械化科学研究院集团有限公司　主办

2025年
第 56 卷　12

农业机械学报
NONGYE JIXIE XUEBAO

2025 年　第 12 期(第 56 卷)

目　次

智能农业动力装备关键技术专栏

(专栏主编:宋正河　徐立友)

农业水土工程

农业生物环境与能源工程

农产品加工工程

车辆与动力工程

机械设计制造及其自动化

Transactions of the Chinese Society for Agricultural Machinery
Vol. 56 No. 12 2025

Contents

Agricultural Equipment and Mechanization Engineering

Agricultural Informatization Engineering

Agricultural Soil and Water Engineering

Agricultural Bio-environment and Energy Engineering

Agricultural Products Processing

Vehicle and Power Engineering

Mechanical Design & Manufacturing and Automation

doi:10.6041/j.issn.1000-1298.2025.12.059

双螺旋驱动式机器人全覆盖作业路径规划算法研究

汪　沛[1]　罗佳龙[1]　谢佳生[1]　王佳涛[1]　罗　皓[2]　宁锦泰[1]　胡　炼[1]　何　杰[1]
（1.华南农业大学工程学院，广州 510642；2.华南农业大学国际教育学院，广州 510642）

摘要：针对复杂农田环境下农业机器人在自主导航与作业路径规划方面的核心需求，特别是在不规则田块与软黏稻田场景中常见的路径覆盖率低、转弯冗余高以及路径连续性差等问题，本文提出一种面向多边形边界田块、适用于双螺旋驱动式农田机器人的全覆盖路径规划算法。该算法充分融合田块几何特征与机器人运动学约束，首先将作业区域划分为中心平行作业区与外围轮廓平行作业区，分别对应中心条带遍历路径与轮廓平行条带遍历路径。进一步将路径细分为作业路径与非作业路径，后者包括中心区域衔接路径、区域衔接路径、轮廓平行区域衔接路径以及进出田块路径等部分。本文阐述了各部分路径的生成原理，通过“长边作业”确定中心区域的最优作业方向，结合 Warnsdorff 规则优化条带遍历顺序，并引入 Dubins 路径与 Reeds－Shepp 路径模型，提升路径在转向过程中的连续性和可执行性。综合考虑作业路径长度、算法计算耗时与作业覆盖率等性能指标，选用双螺旋驱动式机器人作为平台载体，分别在矩形、梯形、不规则四边形、不规则多边形 4 类典型田块进行了仿真与实地对比测试。试验结果表明，本文算法在 4 种典型田块田间作业中可实现 96.69% ～97.80% 的覆盖率，路径重叠率控制在 1.77% ～2.30% 之间，路径整体连续、无越界转弯，表现出良好的执行稳定性与环境适应性。研究结果为复杂环境下农田作业机器人提供了高鲁棒性、高适应性的路径规划方案，具备良好的工程可行性与推广价值。

关键词：农业机器人；路径规划；双螺旋驱动；全覆盖；不规则田块
中图分类号：S224.1；TP242　　**文献标识码**：A　　**文章编号**：1000-1298(2025)12-0645-12　　**OSID**：

Full-coverage Path Planning Algorithm for Dual-helix Driven Robot in Convex Polygonal Farmlands

WANG Pei[1]　LUO Jialong[1]　XIE Jiasheng[1]　WANG Jiatao[1]　LUO Hao[2]　NING Jintai[1]　HU Lian[1]　HE Jie[1]
(1. *College of Engineering*, *South China Agricultural University*, *Guangzhou* 510642, *China*
2. *School of International Education*, *South China Agricultural University*, *Guangzhou* 510642, *China*)

Abstract: Aiming to address the core challenges faced by agricultural robots in autonomous navigation and path planning under complex farmland environments—particularly in irregular plots and soft, sticky paddy fields where common issues included low coverage rate, excessive turning redundancy, and poor path continuity, a full-coverage path planning algorithm tailored for convex polygonal farmlands and compatible with dual-helix driven agricultural robots was proposed. The algorithm integrated both the geometric characteristics of the farmland and the kinematic constraints of the robot. The working area was initially divided into a central parallel-working zone and a peripheral contour-following zone, corresponding respectively to strip-based traversal paths and boundary-parallel strip traversal paths. The complete path was further segmented into working and non-working paths, including center-region connection paths, inter-region transitions, contour-parallel region transitions, and entry/exit paths. The methodology for generating each type of path was detailed. An optimal working direction was determined via the “long-side-first” principle for the central region, and the Warnsdorff rule was applied to optimize the sequence of strip traversal. Dubins and Reeds－Shepp path models were introduced to enhance continuity and feasibility during turns. Considering metrics such as path length, computation time, and coverage rate, the algorithm was implemented on a dual-helix driven robot and tested in simulations and

收稿日期：2025－06－08　修回日期：2025－07－19
基金项目：国家重点研发计划项目(2021YFD2000605)、广东省自然科学基金面上项目(2025A1515011012)和广东省现代农业产业共性关键技术创新团队项目(2024CXTD28)
作者简介：汪沛(1983—)，女，副教授，博士，主要从事智能农机检测和农情信息采集研究，E-mail：wangpei@scau.edu.cn
通信作者：何杰(1985—)，男，副教授，博士，主要从事智能农机装备和无人化农场关键技术研究，E-mail：hooget@scau.edu.cn

field experiments across four typical farmland types: rectangular, trapezoidal, irregular quadrilateral, and irregular polygonal plots. Experimental results demonstrated that the proposed algorithm achieved a coverage rate between 96.69% and 97.80%, with a path overlap rate controlled within 1.77% ~ 2.30%. The generated paths were continuous and boundary-safe, indicating strong execution stability and environmental adaptability. The research result can provide a robust and adaptable path planning solution for agricultural robots operating in complex environments, with promising engineering feasibility and application potential.

Key words: agricultural robot; path planning; dual-helix drive; full-coverage; irregular farmland

0 引言

随着智慧农业的持续推进,小型农业机器人在高效、精准作业中的应用逐渐普及,路径规划作为其核心支撑技术,直接影响作业效率、燃油消耗和土地利用率[1-3]。特别是在边界不规则、地形起伏或设施密集的作业环境中,传统路径策略难以保障覆盖完整性与路径可执行性。研究表明,高精度农田边界识别对农机路径规划至关重要,直接影响作业效率和覆盖率[4],为此,面向复杂田块结构、满足作业连续性与机械转弯约束的全覆盖路径规划研究成为关键方向[5-8]。

现有覆盖路径规划方法主要包括等距条带的 Boustrophedon 算法和分区遍历算法、嵌套法和区域分解策略等,已广泛用于规则地块作业,但在不规则田块中存在路径断裂、覆盖不足、重叠率高等问题[9-11]。近年来,国外 HAMEED 等[12]与 HÖFFMANN 等[13]分别从三维投影与曲率约束角度优化覆盖路径,POUR 等[14-15]提出基于树搜索与改进 CCPP 算法,显著提升了蔬菜收获与复杂田块作业效率。SEYYEDHASANI 等[16]针对多机协同作业的优化,开发了一种可实现车辆路径动态、实时更新的全覆盖路径规划算法。PHAM 等[17]提出了基于旋转式策略的多边形区域覆盖路径生成方法,有效提升了田块边界贴合度。国内,在田块形状处理方面,文献[18-19]提出适用于四边形及凸多边形田块的全覆盖路径规划策略,显著减少了倒车与重播率,提高了播种覆盖率(95.14% ~98.54%)。刘国海等[20]结合改进粒子群算法,实现高地隙喷雾机在非规则凸田块中的路径最短优化。然而,这些研究多针对轮式或履带式机器人,难以满足特殊驱动平台在软黏农田中的运动特性需求。

双螺旋驱动式农田机器人相较于传统履带或轮式平台具有独特的推进机制和转向特性,其依靠螺旋叶片的轴向与径向复合力实现移动,在深泥脚水田等软黏环境中表现出更强的防陷能力[21-22],但无法实现零半径转向且存在显著滑移效应,导致最小转弯半径受限。这些特性使得现有路径规划方法难以直接应用:传统 Boustrophedon 路径因转弯半径不足易引发越界,Dubins 路径禁止倒退的特性难以适应狭窄轮廓平行区域,而纯 Reeds-Shepp 路径虽具灵活性,却易引入冗余倒车动作造成跨垄碾压。为此,本文提出融合 Warnsdorff 规则、Dubins 路径与 Reeds-Shepp 路径的混合算法,通过分区作业策略、条带序列优化及倒退转向机制,研究适用于双螺旋驱动特有的运动学约束问题,在保证覆盖率的同时显著降低转向冗余与滑移损耗,以期为特殊驱动结构农机提供针对性的路径规划方案。

1 双螺旋驱动农田机器人运动学模型与路径约束

在农田复杂环境下,作业机器人的运动性能直接决定了路径规划的可行性与路径跟踪执行质量。双螺旋驱动机器人通过双侧螺旋旋转产生推进力,以实现对称或差速式驱动控制,这种结构在复杂田间环境下具备优异的防陷性和越障性,但其运动模型相较传统轮式或履带式平台存在显著差异,给路径规划带来了新的约束与挑战。为实现高效、可行的路径规划,需首先建立机器人在典型农田环境中的运动学模型,并明确其路径设计所应满足的基本几何和运动学条件。

如图 1 所示,双螺旋轮的受力可分解为轴向牵引力 $F_{ly}(F_{ry})$和径向牵引力 $F_{lx}(F_{rx})$,机器人整体行驶状态取决于左右螺旋轮旋转方向及速度的匹配关系。若两侧螺旋轮以等速反向旋转,则机器人产生纯前进直线运动;若存在速度差异,则可实现转向运动[23]。然而,由于软土环境中径向阻力有限,机器人难以完成原地旋转,其转向过程往往伴随明显的滑移行为。因此,在路径设计中,需设定合理的最小转弯半径,以确保作业精度与农作物安全。

转弯半径 R 表达式为

$$R=\frac{B(\omega_r+\omega_l)}{2(\omega_r-\omega_l)} \tag{1}$$

式中 ω_l——左螺旋轮角速度,rad/s

ω_r——右螺旋轮角速度,rad/s

B——两螺旋轮间距,mm

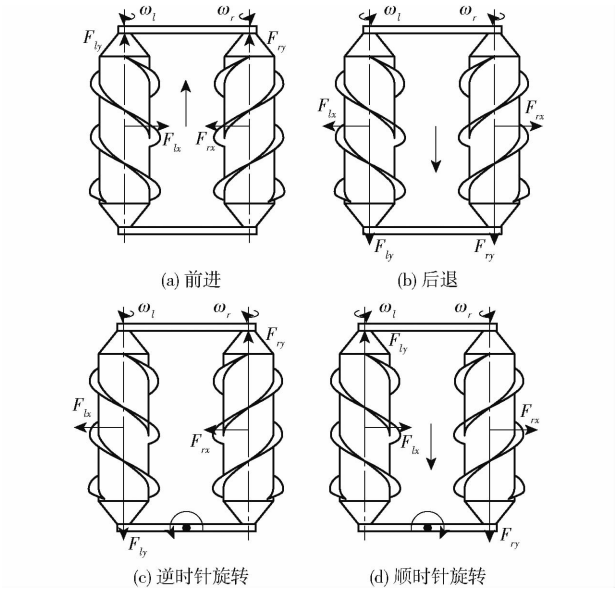

图 1　螺旋轮转向与机器人行驶方向的关系

Fig. 1　Correlation between helical wheel rotation and robot movement direction

式(1)表明转弯半径受差速比显著影响，极端差速情况下可能导致路径不可执行。因此在路径规划中，必须约束连续路径段之间的角度变化，避免产生超出最小转弯能力的剧烈转折。

此外，机具幅宽与路径条带排布密切相关。以软黏水田为例，移动平台搭载抬升式机具进行分区遍历，作业过程中田间条沿“长边界”方向布置，以减少作业轮次和转向成本[24]。考虑作业幅宽与车体幅宽差异，路径规划过程中常需将田块边界向内平移一定距离，形成中心作业区域。然而，若等距内缩宽度过大，会显著降低作业效率；若宽度过小，则可能导致转向失败或发生碰撞风险。因此，必须合理设定该转向缓冲区的宽度阈值。根据规划路径与地头边界存在夹角 α 关系，需分以下两种情况进行讨论。

当规划路径与地头边界存在夹角 α，$\alpha\in[0°,90°]$，如图 2a 所示，此时转向区域预留宽度 L_R 为

$$L_R=\begin{cases}(R+d)\cot\alpha+\dfrac{W+L_T}{2}+R & \text{(弓形)}\\ R\cot\alpha+\left(R+\dfrac{W}{2}\right)\cos\alpha+\dfrac{L_T}{2} & \text{(半圆形)}\\ \sqrt{(2R)^2-\left(R+\dfrac{W}{2}\right)^2}+\dfrac{L_T}{2}+\left(R+\dfrac{W}{2}\right)\cos\alpha+R\cot\alpha & \text{(梨形)}\end{cases}\tag{2}$$

式中　L_T——机器人总长，mm

W——机具幅宽，mm

d——横向直行行驶长度，mm

当规划路径与地头边界存在夹角 α，$\alpha\in[90°,180°]$，如图 2b 所示，此时转向区域预留宽度 L_R 为

$$L_R=\begin{cases}-(R+d)\cot\alpha+\dfrac{W+L_T}{2}+R & \text{(弓形)}\\ -R\cot\alpha-\left(R+\dfrac{W}{2}\right)\cos\alpha+\dfrac{L_T}{2} & \text{(半圆形)}\\ \sqrt{(2R)^2-\left(R+\dfrac{W}{2}\right)^2}+\dfrac{L_T}{2}-\left(R+\dfrac{W}{2}\right)\cos\alpha-R\cot\alpha & \text{(梨形)}\end{cases}\tag{3}$$

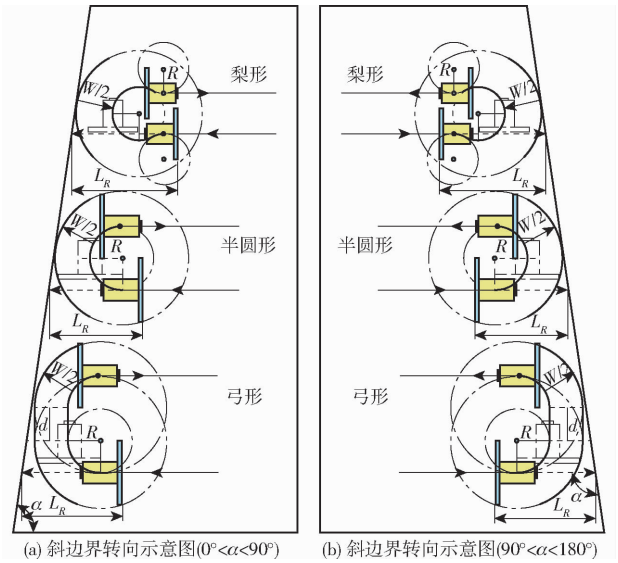

图 2　不同机具幅宽与边界关系对转弯方式影响示意图

Fig. 2　Illustration of influence of implement width and boundary relationship on turning patterns

在路径序列生成方面，由于相邻条带间的空间位置可能导致急剧的姿态切换，设路径条带编号集合 $S=\{s_0,s_1,\cdots,s_{N-1}\}$，则任意连续路径段编号差应满足

$$S_{\min}\leqslant|s_{i+1}-s_i|\leqslant S_{\max}\quad(\forall i\in[0,N-2])\tag{4}$$

其中

$$S_{\min}=\left\lceil\frac{2R_{\min}}{W}\right\rceil\tag{5}$$

式中　$S_{\min}$——最小条带跨度

$S_{\max}$——最大条带跨度

$\lceil\ \rceil$——向上取整

$R_{\min}$——最小转弯半径，mm

式(5)确保从当前路径段转向目标路径段时，所需的空间转弯圆弧在物理上可达；$S_{\max}$ 则用于限制路径跳跃造成的跨垄碾压，由于不同地块的形状和复杂度差异显著，$S_{\max}$ 通常通过经验或地块拓扑特征动态设定，而无固定数学模型。

2　全覆盖路径规划算法

2.1　路径规划流程

为实现双螺旋驱动式农田机器人在不规则田块中的高效率全覆盖作业，本文构建了包含田块边界

处理、中心区域路径生成、轮廓平行路径生成及整体路径合成在内的完整路径规划流程，如图 3 所示。流程考虑了机器人运动学约束、地块拓扑特征及农业作业需求，确保路径规划的可行性、覆盖性与连贯性。其中边界数据采集可由人工手持 Global Navigation Satellite System（GNSS）设备实地测量或通过农场高精度地图选取关键点，如图 4 所示。采集的 GNSS 坐标经通用横轴墨卡托投影（Universal transverse mercator，UTM）算法转换为平面坐标数据，选取特定边界点作为原点建立局部笛卡尔坐标系[25]。采用 Geospatial Data Abstraction Library（GDAL）库中的 OpenGIS Simple Features Reference Implementation（OGR）进行矢量数据读取与处理，选择某一边界点作为原点建立局部坐标系，确保后续路径生成具备一致性与可重构性。在路径规划过程中，先对田块边界实施多边形等距内缩，生成中心区域用于作业的平行条带。然后，采用 Warnsdorff 规则引导 Dubins 路径实现中心区域作业路径的高效连接。在此基础上，生成田块轮廓平行路径，最终通过 Reeds－Shepp 路径完成整体路径的合成，确保机器人可顺畅执行全场覆盖作业。

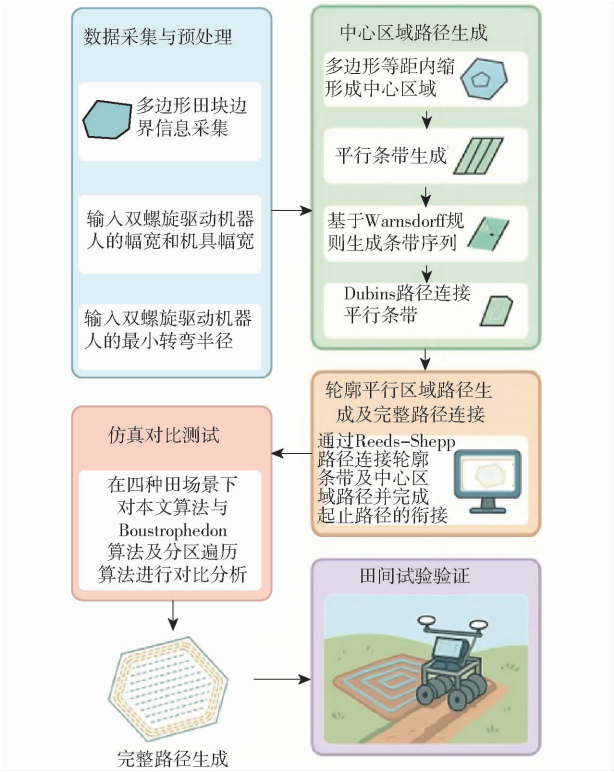

图 3 整体路径规划流程

Fig. 3 Overall path planning workflow

2.2 路径生成

2.2.1 中心区域路径生成

（1）多边形等距内缩

为预留中心区域内足够的转弯缓冲空间并保证

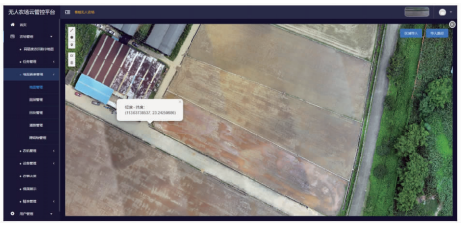

图 4 通过地理信息系统获取田块信息

Fig. 4 Acquisition of farmland information via geographic information system（GIS）

条带作业区的稳定生成，采用基于几何偏移的多边形等距内缩策略。该方法借鉴巩岩[26]提出的道路外扩线“几何法”思路，基于 GDAL/OGR 库读取矢量边界数据，并计算每条边的方向角，进而按单位法向量方向进行平移处理，从而构造内缩边界顶点。对于凹多边形区域，通过分解为多个凸多边形以避免形变退化问题[27]。多边形等距内缩示意图如图 5（a 田块中心区域；b 方向向量；c 法向量；d 沿着法向量 f 平移的边界线；e 方向向量；f 法向量；g 等距内缩距离 L_R；h 沿着法向量 c 平移的边界线；i 等距内缩顶点。绿色区域是地头）所示。内缩后多边形田块被分为轮廓平行区域及中心作业区域，内缩顶点集记为 $P_{in}=\{p_0',p_1',\cdots,p_{n-1}'\}$。

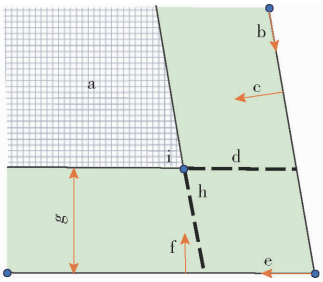

图 5 多边形等距内缩示意图

Fig. 5 Schematic of equidistant inward offset for a polygon

（2）平行条带生成

以“长边界”为作业方向，求取“长边界”垂线向量后，对每个多边形顶点在该垂线上求投影点，则最大投影宽度 L 和平行条带数 N 计算式为

$$L=\max_{(x,y)\in P_{in}}(x\boldsymbol{n}_x+y\boldsymbol{n}_y)-\min_{(x,y)\in P_{in}}(x\boldsymbol{n}_x+y\boldsymbol{n}_y) \tag{6}$$

$$N=\left\lfloor\frac{L}{W}\right\rfloor$$

式中 $\lfloor\ \rfloor$——向下取整

$\boldsymbol{n}$——“长边界”垂线向量

从最小投影起始点 p_0'开始，沿方向 $\boldsymbol{n}$ 以 W 生成每条条带的中心线。第 i 条条带中心线表达式为

$$L_i(t)=p_0'+iW\boldsymbol{n}+t\boldsymbol{d}\quad(t\in R) \tag{7}$$

式中 $\boldsymbol{d}$——“长边界”方向向量

由于每条中心线可能与作业区域存在多个交点，因此需将其与 P_{in}求交，仅保留实际可作业部分，

得到有限条带线段集S_i，如图 6（***a*** 单位法向量；***b*** 单位方向向量；c 最大投影宽度；S_i为条带线段集合；绿色区域为轮廓平行区域，黄色斜线区域为中心作业区域）所示。

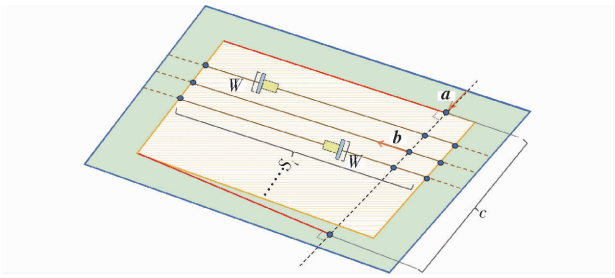

图 6　平行条带生成示意图

Fig. 6　Schematic of parallel strip generation

其中S_i可能为空、一段或多段。通常，若P_{in}为凸或类矩形区域，则每条S_i仅为一条连续线段。

（3）Warnsdorff 规则引导的条带排序

在农业作业路径规划中，作业机械的物理约束，特别是最小转弯半径，显著影响路径的可行性与连续性。在完成作业区域内平行条带的生成后，算法将条带集合按照其法线方向投影，并依据空间位置进行排序，形成编号集合 $S=\{s_0,s_1,\cdots,s_{N-1}\}$。若直接依序遍历该编号集合，部分条带由于边界曲率或区域拓扑的局部复杂性，可能在连接相邻路径段时引发剧烈转向，超出平台最小转弯半径 R_{min}所能承受的范围，导致路径不可执行。为规避此类问题，需要在 S_{min}和 S_{max}跨度区间构造一条覆盖所有条带编号且不重复的路径序列。

贪心算法作为一种在每一步选择中都采取当前最优策略以期获得全局最优解的算法，能够在一定程度上提升排序效率。然而，其仅关注局部最优选择，容易导致后续遍历出现条带跨度过大的问题，尤其在不规则田块中，可能引发跨垄碾压等现象，影响作业安全与质量。如图 7 所示，在复杂地块环境中，贪心策略的局限性尤为突出。基于此，本文算法引入 Warnsdorff 启发式规则，在每一步路径扩展时优先选择在剩余未访问节点中邻接度最小的节点作为下一个访问节点候选，从而有效避免搜索过程中陷入“路径死角”或导致后续节点无解的局部最优陷阱。此外，算法还辅以剪枝机制，当出现剩余条带数量不足以完成遍历、编号跨度超出允许范围、当前路径无法连接至任一未访问节点时立即回溯。通过以上策略，本文算法可在指数级搜索空间中高效构建一条满足物理约束的遍历路径，并显著提升路径连贯性与整体可执行性。

路径序列生成完成后，按照该序列编号依次为条带分配作业方向，即对相邻条带的方向进行交替

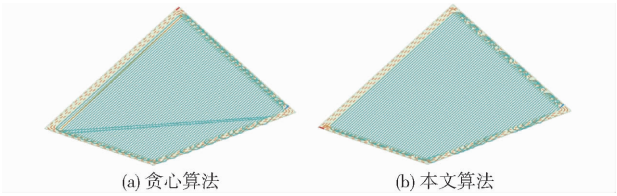

图 7　贪心算法与本文算法在不规则田块下仿真结果

Fig. 7　Simulation results of greedy algorithm and proposed algorithm in irregular fields

翻转处理，使相邻路径方向相反，从而构建出一组具有明确方向性且相互平行的路径段，如图 8（a 最小条带跨度 S_{min}；b 最大条带跨度 S_{max}；S：条带编号集合；虚线为被跨条带；绿色区域为轮廓平行区域，黄色斜线区域为中心作业区域；橙色和绿色箭头为当前条带方向；红色虚线为转弯行进路线）所示。

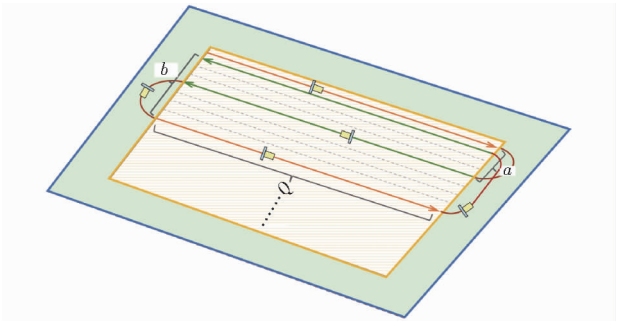

图 8　Warnsdorff 启发式条带排序生成示意图

Fig. 8　Schematic of strip sequencing using Warnsdorff heuristic

（4）Dubins 路径连接

最终生成的中心作业区域覆盖路径，其形成过程基于对前面生成的平行条带的几何排序与连接策略。几何排序已由回溯搜索算法在满足路径连续性、可达性与转弯半径约束的前提下完成。

采用“先作业中心区域，后封圈轮廓区域”的作业顺序策略，若单纯以路径最短为目标，容易在复杂田块中出现跨垄连接，导致机器人倒车进入已作业区域。如图 9 所示，这不仅造成作物碾压，也违背了作业路径的逻辑合理性，此时尚未作业的轮廓区域是理想的转弯缓冲区。考虑到 Dubins 路径与 Reeds－Shepp 路径在前向行驶情况下具有相同的解析解，在中心区域路径连接时优先采用 Dubins 路径，以生成连续、可行且满足机器人运动学约束的作业轨迹；而 Reeds－Shepp 路径则仅用于轮廓封圈等需灵活转向的特殊场景，以兼顾执行灵活性与作业规范性。

Dubins 路径是指在固定最小转弯半径 R_{min}条件下，从初始状态到目标状态，且只能前进行驶的最短路径。该路径由 3 段基本元素构成：左圆弧（L）、直线段（S）与右圆弧（R），其组合最多为 3 段。Dubins

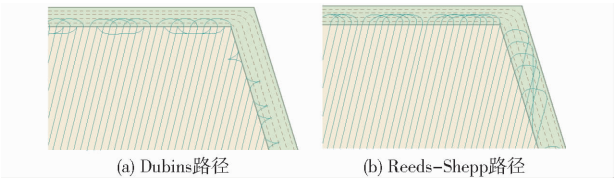

图 9 中心区域采用不同路径连接方式对比示意图

Fig. 9 Comparison of path connection methods in central working area

(1957 年)证明机器人的最短路径必然属于 LSL、RSR、LSR、RSL、RLR 或 LRL 6 种序列之一[28]。

在实际计算中,当机器人走圆弧时,记机器人转弯角度为 ψ,将转弯半径归一化为 1,则走过的弧长 $L_\psi=\psi*1$,此时不论是走过的圆弧还是直线长度均为 L,因此机器人左转、右转、直行的坐标变换经归一化后表达式为

$$\begin{cases} L_L(x,y,\phi)=(x+\sin(\phi+L)-\sin\phi, \\ \qquad y-\cos(\phi+L)+\cos\phi,\phi+L) \\ R_L(x,y,\phi)=(x-\sin(\phi-L)+\sin\phi, \\ \qquad y+\cos(\phi-L)-\cos\phi,\phi-L) \\ S_L(x,y,\phi)=(x+L\cos\phi,y+L\sin\phi,\phi) \end{cases} \tag{8}$$

式中 (x,y,ϕ)——机器人当前位姿

(x,y)——初始坐标 ϕ——航向角

以 LSL 路径为例,其连接由 1 段左圆弧、1 段直线和 1 段左圆弧构成。如图 10(θ 初始航向角、t、q 转弯弧长;p 直行距离;d 最终位置横坐标;橙色线为机器行进路线,蓝色方框表示机器)所示,结合归一化公式,存在 $L_q(S_p(L_t(0,0,\theta)))=(d,0,\beta)$,展开得

$$\begin{cases} p\cos(\theta+t)-\sin\alpha+\sin\beta=d \\ p\sin(\theta+t)+\cos\theta-\cos\beta=0 \\ \alpha+t+q=\beta(\mathrm{mod}2\pi) \end{cases} \tag{9}$$

式中 $(0,0,\theta)$——机器人初始坐标

$(d,0,\beta)$——机器人终点坐标

t——机器人第 1 个左转弧长,mm

p——机器人直线距离,mm

q——机器人第 2 个左转弧长,mm

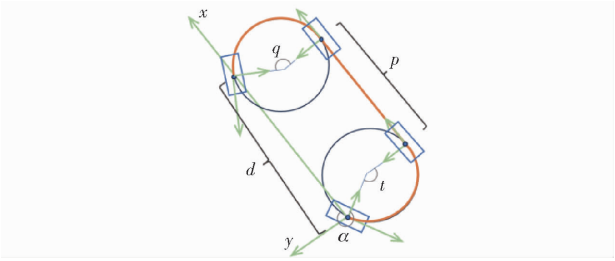

图 10 Dubins 路径建模示意图

Fig. 10 Schematic of Dubins path modeling

依据起、终点几何约束和方向夹角,联立求解各路径组合的总长度。对所有路径组合总长度进行比较,选取最短长度作为实际路径。

2.2.2 轮廓平行区域路径规划

轮廓平行区域路径规划在农业机器人全覆盖作业中具有关键作用,尤其对于不规则多边形田块,其边界区域往往呈现复杂的环状结构,直接影响整体覆盖率和作业效率。为高效地规划这些区域的作业路径,本文提出一种结合环状区域分割策略和 Reeds-Shepp 路径的规划方法,以适应农业机器人的运动约束及环境要求。

通过连接原始田块外边界与内缩边界上的对应顶点形成一系列四边形区域,每个四边形区域再通过进一步内缩处理,构成一组与中心作业区域相似的局部作业子区域,从而使得条带生成在每个局部区域内具备较为简单的几何形状。在生成各个子区域的平行条带后,需要对条带进行高效连接,以形成完整的作业路径。然而,由于轮廓平行区域具有狭窄、弯折频繁的特性,传统的 Dubins 路径仅支持前进运动且转弯方式受限,因此无法有效处理此类复杂环境,容易导致路径中断或严重的姿态误差,如图 11 所示。为解决这一问题,引入适用于允许倒退操作的 Reeds-Shepp 路径,以满足农业机器人在复杂狭窄区域内的灵活转向需求。

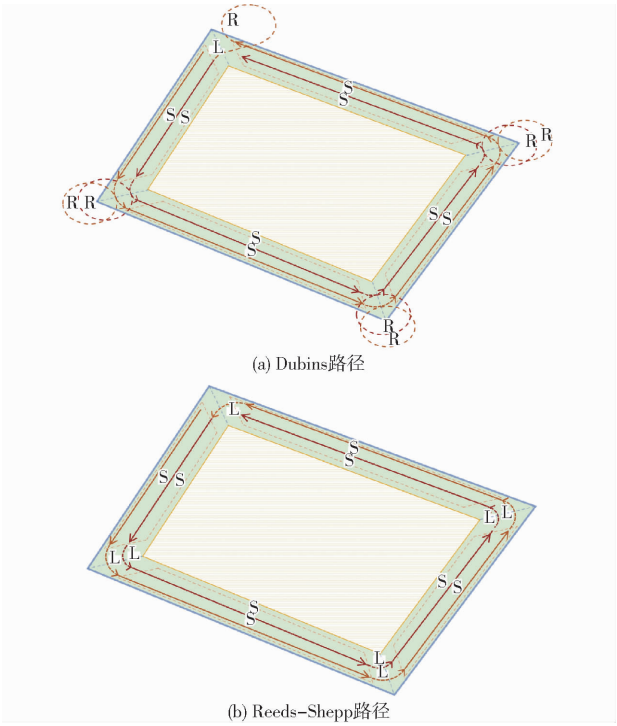

图 11 轮廓平行路径 Dubins 路径与 Reeds-Shepp 路径仿真

Fig. 11 Comparative simulation of Dubins and Reeds-Shepp paths for contour-parallel trajectories

文献[28]证明了 Reeds-Shepp 路径从起点到终点的最短路径一定为表 1 中 Base word 其中之一[29]。

表 1　Reeds－Shepp 基本类型

Tab.1　Basic types of Reeds－Shepp

Base word	运动序列组合
C|C|C	$(L^+R^-L^+)(L^-R^+L^-)(R^+L^-R^+)(R^-L^+R^-)$
CC|C	$(L^+R^+L^-)(L^-R^-L^+)(R^+L^+R^-)(R^-L^-R^+)$
C|CC	$(L^+R^-L^-)(L^-R^+L^+)(R^+L^-R^-)(R^-L^+R^+)$
CSC	$(L^+S^+L^+)(L^-S^-L^-)(R^+S^+R^+)(R^-S^-R^-)(L^+S^+R^+)(L^-S^-R^-)(R^+S^+L^+)(R^-S^-L^-)$
$CC_\beta\|C_\beta C$	$(L^+R_\beta^+L_\beta^-R^-)(L^-R_\beta^-L_\beta^+R^+)(R^+L_\beta^+R_\beta^-L^-)(R^-L_\beta^-R_\beta^+L^+)$
$C\|C_\beta C_\beta\|C$	$(L^+R_\beta^-L_\beta^-R^+)(L^-R_\beta^+L_\beta^+R^-)(R^+L_\beta^-R_\beta^-L^+)(R^-L_\beta^+R_\beta^+L^-)$
$C\|C_{\frac{\pi}{2}}SC$	$(L^+R_{\frac{\pi}{2}}^-S^-R^-)(L^-R_{\frac{\pi}{2}}^+S^+R^+)(R^+L_{\frac{\pi}{2}}^-S^-L^-)(R^-L_{\frac{\pi}{2}}^+S^+L^+)(L^+R_{\frac{\pi}{2}}^-S^-L^-)(L^-R_{\frac{\pi}{2}}^+S^+L^+)(R^+L_{\frac{\pi}{2}}^-S^-R^-)(R^-L_{\frac{\pi}{2}}^+S^+R^+)$
$CS\,C_{\frac{\pi}{2}}\|C$	$(L^+S^+L_{\frac{\pi}{2}}^+R^-)(L^-S^-L_{\frac{\pi}{2}}^-R^+)(R^+S^+R_{\frac{\pi}{2}}^+L^-)(R^-S^-R_{\frac{\pi}{2}}^-L^+)(R^+S^+L_{\frac{\pi}{2}}^+R^-)(R^-S^-L_{\frac{\pi}{2}}^-R^+)(L^+S^+R_{\frac{\pi}{2}}^+L^-)(L^-S^-R_{\frac{\pi}{2}}^-L^+)$
$C\|C_{\frac{\pi}{2}}S\,C_{\frac{\pi}{2}}\|C$	$(L^+R_{\frac{\pi}{2}}^-S^-L_{\frac{\pi}{2}}^-R^+)(L^-R_{\frac{\pi}{2}}^+S^+L_{\frac{\pi}{2}}^+R^-)(R^+L_{\frac{\pi}{2}}^-S^-R_{\frac{\pi}{2}}^-L^+)(R^-L_{\frac{\pi}{2}}^+S^+R_{\frac{\pi}{2}}^+L^-)$

其中 β 表示沿曲线运动角度，$\beta\in[0,\pi]$，L、R 和 S 含义与 Dubins 路径中定义一致；上标 +、－表示机器前进和后退，下标 β 和 $\pi/2$ 表示沿曲线运动角度。虽然 Reeds－Shepp 路径的 48 种情况需要每一组都进行求解，但通过时间变换、反射变换和逆向变换可以只求解其中 12 种情况，其余情况均可由 3 种变换得到。此外，为了规避 Reeds－Shepp 规划较长的倒车路径、较多的倒车动作等问题，需给予 Reeds－Shepp 进一步约束，并改进求解方法，避免 Reeds－Shepp 为了获取最短路径而产生不可用解。最终保留的路径运动序列组合为 $(L^+R^-)(L^+S^-)(R^+L^-)(R^+S^-)$、$(L^+R^-L^+)(R^+L^-R^+)$、$(L^+R^+L^-)(R^+L^+R^-)$、$(L^+S^+L^+)(R^+S^+R^+)$ 和 $(L^+S^+R^+)(R^+S^+L^+)$。由于前面 Dubins 路径部分已经给出前进时，左转右转和直行的坐标变换，后退的坐标变换归一化为

$$\begin{cases} L_L^-(x,y,\phi)=(x-\sin(\phi-L)+\sin\phi,\\ \qquad y+\cos(\phi-L)-\cos\phi,\phi-L)\\ R_L^-(x,y,\phi)=(x+\sin(\phi+L)-\sin\phi,\\ \qquad y-\cos(\phi+L)+\cos\phi,\phi+L)\\ S_L^-(x,y,\phi)=(x-L\cos\phi,y-L\sin\phi,\phi) \end{cases} \tag{10}$$

设定初始位姿为 (x_1,y_1,ψ_1)，目标位姿为 (x_2,y_2,ψ_2)，转弯半径为 R，归一化后初始位姿为 $(0,0,0)$，目标位姿为 $\left(\dfrac{(x_2-x_1)\cos\psi_1+(y_2-y_1)\sin\psi_1}{R},\dfrac{-(x_2-x_1)\sin\psi_1)+(y_2-y_1)\cos\psi_1)}{R},\psi_2-\psi_1\right)$。

仍以 $L_oS_uL_v$ 为例，在单位圆归一化后，存在

$$\begin{cases} u\cos o+\sin(o+v)=x\\ u\sin o-\cos(o+v)+1=y\\ o+v=\psi \end{cases} \tag{11}$$

式中　o——归一化后第 1 段左转行进长度，mm

u——归一化后直线行进长度，mm

v——归一化后第 2 段左转行进长度，mm

(x,y,ψ)——终点位姿

与归一化公式联立后求解可得路径总长度，对所有路径组合总长度进行比较，选取最短长度作为实际路径。

2.2.3　起止点（下田口）与整体路径合成

在完成中心区域与轮廓平行区域路径的规划后，为构建一条连续、可执行的完整作业路径，还需解决路径起点与终点的确定，以及中心路径与轮廓平行路径之间的合理衔接问题。在实际农田作业场景中，农业机器人往往依赖既定的下田口（即路径起点与终点）完成进出作业区域的导航，该位置通常位于田块边缘的一处可通行开口，并受制于农田排水沟、田埂宽度及作业路径布置等客观条件。因此，在路径规划过程中，合理设置下田口并将其纳入整体路径生成流程，对于保障路径的可达性与执行效率具有重要意义。

采用预设下田口位置的方法，先求中心区域条带与边界相交的各点中离起点最近的点，并将该点与中心区域路径的第 1 个作业条带起点进行连接路径起点确定后，机器人按照中心区域路径的排序顺序依次完成条带作业，最终到达中心路径的终端点。

中心作业完成后，算法将自动调度机器人转入轮廓平行区域进行封圈作业。为实现两区域之间的平滑过渡，设计中心终点与轮廓平行路径起始点之间的衔接路径，同样基于 Reeds－Shepp 路径生成，以支持复杂姿态变化及狭窄路径转接。在规划过程中，算法首先搜索距离中心路径终点最近的轮廓平行条带起点作为连接目标，然后求解二者之间最短可行路径，并将其拼接至整体作业路径中。

此外，为形成完整的闭环路径结构，机器人在完成轮廓平行路径最后一段作业后，还需规划一段返回路径，引导其从轮廓平行区域终点驶回下田口或作业出口。根据田块实际情况在规划层面构建一条

通往田块边缘的短路径,实现路径的闭合与作业流程的完整收束,整体路径如图 12(a 中心作业区域;b 路径起点;c 轮廓平行区域衔接路径;d 田块;e 外围轮廓作业区域;f 中心区域衔接路径;g 区域衔接路径;h 路径终点;i 轮廓平行路径;j 中心路径)所示。

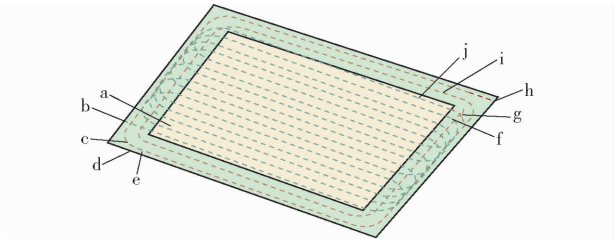

图 12 完整生成路径示意图

Fig. 12 Schematic of fully generated coverage path

2.3 作业覆盖率与重叠率计算函数构建

为客观评估路径规划方案作业有效性与空间利用效率,构建基于空间几何布尔运算的作业覆盖率与路径重叠率计算函数。考虑到平台搭载抬升式机具,路径转弯段处于非作业状态,实际作业区域由路径的作业条带决定。为模拟机具影响范围,针对每条作业条带,依据机具幅宽 W,构建与路径方向平行、宽度为 $W/2$ 向两侧扩展的矩形缓冲区,表示实际作业影响区域的几何对象。

为实现高效、稳定的空间计算,集成使用 Geometry Engine - Open Source(GEOS)库,对每条作业条带对象与田块边界进行空间交集分析,并完成有效区域的布尔求并操作。作业覆盖率为合并区域与田块总面积比值,表达式为

$$\eta_{cov} = \frac{A_{cov}}{A_f} \times 100\% \tag{12}$$

其中 $$A_{cov} = \cup (A_i \cap A_f)$$

式中 η_{cov}——作业覆盖率,%

A_{cov}——有效作业面积,m^2

A_f——田块总面积,m^2

A_i——第 i 条矩形缓冲区面积,m^2

路径重叠率计算基于作业条带集合的两两空间交集,通过设定面积阈值滤除边界贴合造成的微小重叠,得到总重叠面积,路径重叠率表达式为

$$\eta_{rep} = \frac{A_{over}}{\sum A_i} \times 100\% \tag{13}$$

式中 η_{rep}——路径重叠率,%

A_{over}——所有矩形缓冲区重叠面积之和,m^2

3 仿真试验

3.1 仿真设置

为全面验证所提出路径规划算法在多种田块几何形状下的适应性与执行效果,本文构建了包含仿真建模、算法运行与性能评估在内的完整仿真试验框架。仿真系统基于 Ubuntu 操作系统,采用 C++语言开发,同时借助 PyQt 设计图形用户界面,如图 13 所示,用于田块数据导入、参数设定与路径可视化输出。仿真平台运行环境为第 10 代 Intel Core i7 - 10510U(1.80 GHz)处理器,具备良好的运算性能与实时响应能力,满足路径规划算法在多样化测试场景的高效运行需求。

图 13 PyQt 图形用户界面

Fig. 13 Schematic of PyQt graphical user interface (GUI)

构建 4 类典型农田地块仿真模型,包括规则矩形、梯形、不规则四边形以及不规则多边形,分别代表常规田块、边界倾斜田块、边界夹角不规则田块及高度复杂的自由形状田块。每类地块均通过设定不同边界点坐标进行仿真建模,边界坐标通过实际田块采样数据进行缩放或理想化处理,以确保仿真结果的工程可比性。所有田块均采用相同的规划参数进行测试,保证结果之间具有统一的评估基础。

仿真中机器人几何参数包括最小转弯半径 R_{min} 为 0.6 m 与机具幅宽 W 为 0.3 m。路径条带方向设定为沿地块“长边”方向展开,以最大化直线作业段长度、减少转弯频率,提高作业效率并降低能耗。

在仿真运行过程中,系统首先加载预设田块边界数据,并依次执行多边形等距内缩、平行条带生成及排序、轮廓平行区域构建及连接处理等算法模块,最终输出完整路径。为确保路径的物理可执行性,每一连接段均在满足运动学约束的前提下,以 Dubins 路径或 Reeds - Shepp 路径进行解析求解。路径输出结果以矢量图形式呈现,包含方向、转弯段位置与路径段属性信息,支持后续误差分析与评估。

为系统性评估所提算法的性能并验证其工程实用性,仿真时在每类典型田块测试中均引入 2 种代表性路径规划方法作为与本文算法的对比基准,包括传统的 Boustrophedon 算法和分区遍历算法,传统 Boustrophedon 算法通过平行条带往复遍历实现覆盖而分区遍历算法因轨迹呈螺旋状得名。为避免整体螺旋遍历导致过长的非作业路径,将每 8 条平行条带分组实施局部螺旋遍历,以提升路径连贯性与作业效率。在统一的测试参数与边界条件下,对各

算法所生成的路径规划结果分析 5 项核心性能指标，包括非作业路径长度、有效作业路径长度、算法运行耗时、封圈前后覆盖率以及路径条带的重叠率，以考察不同算法在不同性能指标方面的表现差异。

3.2　仿真结果

在统一的仿真平台与输入参数下，对比本文算法与 2 类经典路径规划算法在 4 种典型田块中的表现。完整路径仿真结果如图 14 所示。

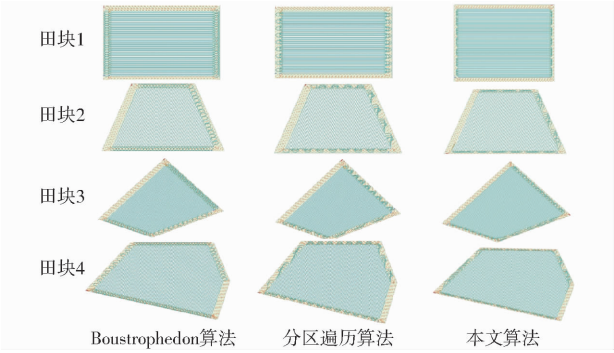

图 14　不同田块下完整路径仿真结果

Fig. 14　Simulation results of complete paths under different fields

仿真结果如表 2 所示，本文算法在各类地块中均实现了高覆盖率（封圈后不小于 97.14%）与低重叠率（不大于 0.17%）。与传统 Boustrophedon 算法和分区遍历算法相比，本文算法通过合理控制条带序列与路径连接方式，在作业路径长度略有增加的基础上，显著降低了非作业路径长度，展现出更高的路径连贯性与可执行性。

尽管在复杂多边形地块中路径计算耗时略高（最大 4.406 s），但仍在工程可接受范围内，验证了算法的实时计算能力。特别地，封圈策略有效补偿了边角区域覆盖盲区，使覆盖率平均提升近 20%，进一步提升作业完整性。

4　田间试验

4.1　试验设置

为验证本文算法在农业环境多样化地形下的适应性与鲁棒性，在华南农业大学增城试验基地开展了 4 种典型农田的路径规划田间试验，并以此真实田块进行了仿真。

表 2　不同田块下路径性能仿真结果

Tab. 2　Simulation results of path planning performance across different field types

田块编号	算法	非作业路径长度/m	作业路径长度/m	算法耗时/s	封圈前覆盖率/%	封圈后覆盖率/%	路径重叠率/%
1	Boustrophedon 算法	309.75	1 996.59	2.905	74.30	95.83	0.01
	分区遍历算法	219.32	2 003.95	2.951	74.65	96.19	0.01
	本文算法	176.99	2 059.48	2.848	81.36	98.54	0.17
2	Boustrophedon 算法	299.09	1 497.98	2.691	69.68	94.68	0.01
	分区遍历算法	239.37	1 514.05	2.585	70.68	95.62	0.01
	本文算法	228.13	1 567.59	3.438	78.70	98.33	0.08
3	Boustrophedon 算法	294.95	1 843.20	2.780	72.21	95.50	0.01
	分区遍历算法	250.03	1 846.61	2.727	72.38	95.68	0.01
	本文算法	249.66	1 874.85	2.632	78.22	97.14	0.01
4	Boustrophedon 算法	419.01	3 060.87	3.713	78.76	96.40	0.01
	分区遍历算法	377.33	3 079.22	3.693	79.33	96.98	0.01
	本文算法	365.75	3 121.03	4.406	84.02	98.22	0.02

田间试验采用自主研发的双螺旋驱动式机器人作为试验平台。该机器人机体质量为 23.00 kg，搭载内置驱动的低压直流无刷伺服电机（SDM8070JA1），额定功率为 211.52 W，输出转矩为 10.00 N·m，最大作业速度为 0.70 m/s。配备高精度 RTK－GNSS 定位系统，定位误差控制在 ±2 cm 以内，确保作业轨迹数据的空间精度。团队自研的导航系统具备路径导入、作业状态显示、速度控制、参数标定及数据导出等功能。控制指令通过 CAN 总线实时传输，支持精细化路径跟踪控制与姿态调整，整机系统具有较高集成度与工程可靠性，整机及控制流程如图 15 所示。

试验过程中，机器人在各测试地块内按规划路径依次完成中心区域与轮廓平行区域的作业任务。系统同步记录机器人当前位置坐标、航向角、横向偏差及当前路径段等动态运行数据。基于设定的作业幅宽，导航系统实时结合机器人当前位置与航向角，动态计算当前作业的覆盖率与重叠率，从而实现对作业质量的评估与反馈。

在试验准备阶段，使用 RTK 测量仪对各测试田块边界进行精确采集，并将边界坐标导入路径规划软件，完成中心作业路径与轮廓平行路径的全自动生成。所生成路径以标准格式导入至机器人导航系统，并进行路径可视化校验与坐标对齐，确保田间路

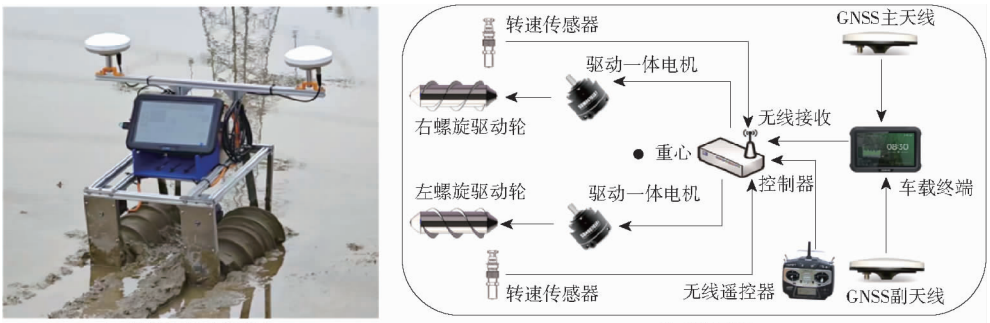

(a) 双螺旋驱动机器人 (b) 控制流程

图 15 双螺旋驱动机器人及控制流程

Fig. 15 Dual-helix driven robot and its control flow

径与仿真路径严格对应。每块田块的路径规划均采用统一参数设定,包括最小转弯半径 R_{min} 为 0.6 m 与机具幅宽 W 为 0.3 m,以保持试验一致性,路径生成结果如图 16 所示。

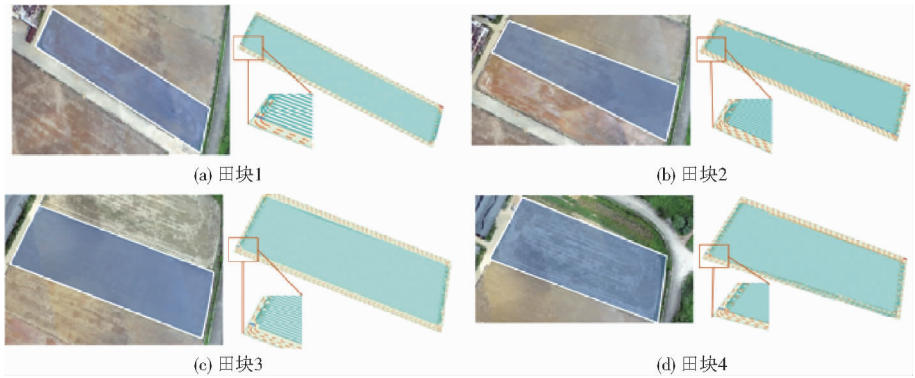

(a) 田块1 (b) 田块2

(c) 田块3 (d) 田块4

图 16 经算法处理后全覆盖路径生成结果

Fig. 16 Result of generating fully covered path after algorithm processing

4.2 试验结果与分析

真实田块仿真与田间试验结果如表 3 所示,实测路径封圈后覆盖率达 96.69% ~97.80%,与仿真结果(98.52% ~99.67%)基本一致,差异主要源于田间环境中地形起伏、水分分布不均以及机器人轨迹轻微漂移等因素。部分边缘区域因软土陷落或作物残留物干扰,影响了覆盖率的进一步提升。

在重叠率方面,典型田块仿真结果为 0.01% ~0.17%,真实田块几何的仿真重叠率略微上升至 0.01% ~0.37%,原因是边界不规则性引入的规划误差。而实际田间测试中重叠率进一步增至 1.77% ~2.30%,除规划误差外,主要归因于机器人在转向段的路径切入偏差及田间微小障碍物引发的姿态调整,二者共同导致实际轨迹偏离与重复作业。

实测作业路径长度略低于仿真值,主要由于实际行驶中机器人因控制响应延迟或地面滑动而对理想路径进行切割与简化,自动截弯取直,从而缩短总作业距离。

非作业路径长度在实测中略大于仿真,反映出实际操作中机器人需进行姿态修正与路径对齐,尤其在路径起始阶段与区域切换处,导航系统会预留缓冲距离以保证行驶稳定性。此外,因田间入口位

表 3 仿真与田间试验路径规划结果

Tab. 3 Comparison of path planning metrics between simulation and field experiments

田块编号	数据来源	非作业路径长度/m	作业路径长度/m	算法运行耗时/s	封圈前覆盖率/%	封圈后覆盖率/%	路径重叠率/%
1	仿真	428.27	9 255.94	9.521	90.83	99.39	0.23
	实测	442.96	9 245.27		88.73	97.53	2.30
2	仿真	625.44	10 282.80	9.609	88.04	98.52	0.01
	实测	644.14	10 269.95		86.37	96.69	1.77
3	仿真	261.83	11 823.10	9.014	93.43	99.67	0.37
	实测	281.09	11 807.90		90.84	97.80	2.30
4	仿真	737.60	11 083.00	9.041	89.87	98.75	0.01
	实测	765.17	11 062.55		88.10	96.84	1.79

置与理想规划入口位置存在偏差，导致连接段长度有所增加。

5　结论

（1）针对双螺旋驱动式农业机器人在多边形不规则田块中的全覆盖路径规划问题，设计了一种融合 Warnsdorff 规则、Dubins 路径与 Reeds－Shepp 路径的规划算法。构建了该算法路径生成与衔接机制，建立了基于机器人最小转弯半径和条带方向约束的路径优化模型，并设计了相应的规划流程与控制逻辑。

（2）仿真与田间试验结果表明，所提出的全覆盖路径规划算法在复杂田块环境中具备优异的覆盖完整性和路径可执行性。在典型多边形田块仿真中，算法实现了 97.14% 以上的覆盖率，路径重叠率低于 0.17%，且无转弯越界现象，验证了其规划的高效性与可靠性。同时，田间试验显示，对 4 种典型田块轮廓区域封圈后的覆盖率达到 96.69% ~97.80%，与仿真结果基本一致，证明了算法在实际环境中的有效性；路径重叠率为 1.77% ~2.30%，虽略高于仿真值，但仍在可接受范围。充分体现了该算法在优化路径冗余、保证作业质量方面的良好效果。

参　考　文　献

[1] 张漫，季宇寒，李世超，等. 农业机械导航技术研究进展[J]. 农业机械学报，2020，51(4)：1－18.
ZHANG Man, JI Yuhan, LI Shichao, et al. Research progress of agricultural machinery navigation technology[J]. Transactions of the Chinese Society for Agricultural Machinery，2020，51(4)：1－18. (in Chinese)

[2] 何勇，黄震宇，杨宁远，等. 设施农业机器人导航关键技术研究进展与展望[J]. 智慧农业(中英文)，2024，6(5)：1－19.
HE Yong, HUANG Zhenyu, YANG Ningyuan, et al. Research progress and prospects of key navigation technologies for facility agricultural robots[J]. Smart Agriculture，2024，6(5)：1－19. (in Chinese)

[3] 曹如月，张振乾，李世超，等. 基于改进 A* 算法和 Bezier 曲线的多机协同全局路径规划[J]. 农业机械学报，2021，52(增刊)：548－554.
CAO Ruyue, ZHANG Zhenqian, LI Shichao, et al. Multi-machine cooperation global path planning based on A-star algorithm and Bezier curve[J]. Transactions of the Chinese Society for Agricultural Machinery，2021，52(Supp.)：548－554. (in Chinese)

[4] 罗锡文，谷秀艳，胡炼，等. 大田无人化智慧农场农田边界识别技术研究现状与展望[J]. 农业机械学报，2025，56(2)：1－18.
LUO Xiwen, GU Xiuyan, HU Lian, et al. Research status and outlook of farmland boundary recognition technology in large-scale unmanned smart farms[J]. Transactions of the Chinese Society for Agricultural Machinery, 2025, 56(2): 1－18. (in Chinese)

[5] 周俊，何永强. 农业机械导航路径规划研究进展[J]. 农业机械学报，2021，52(9)：1－14.
ZHOU Jun, HE Yongqiang. Research progress on navigation path planning of agricultural machinery[J]. Transactions of the Chinese Society for Agricultural Machinery，2021，52(9)：1－14. (in Chinese)

[6] NØRREMARK M, NILSSON R S, SØRENSEN C A G. In-field route planning optimisation and performance indicators of grain harvest operations[J]. Agronomy, 2022, 12(5): 1151.

[7] VAHDANJOO M, SORENSEN C G. Novel route planning method to improve the operational efficiency of capacitated operations. case: application of organic fertilizer[J]. AgriEngineering, 2021, 3(3): 458－477.

[8] CHATZISAVVAS A, DOSSIS M, DASYGENIS M. Optimizing mobile robot navigation based on A-star algorithm for obstacle avoidance in smart agriculture[J]. Electronics, 2024, 13(11): 2057.

[9] PALMER R, WILD D, RUNTZ K. Improving the efficiency of field operations[J]. Biosystems Engineering, 2003, 84(3): 283－288.

[10] URVINA R P, GUEVARA C L, VÁSCONEZ JP, et al. An integrated route and path planning strategy for skid-steer mobile robots in assisted harvesting tasks with terrain traversability constraints[J]. Agriculture, 2024, 14(8): 1206.

[11] WANG N, JIN Z, WANG T, et al. Hybrid path planning methods for complete coverage in harvesting operation scenarios[J]. Computers and Electronics in Agriculture, 2025, 231: 109946.

[12] HAMEED I A, LA COUR-HARBO A, OSEN O L. Side-to-side 3D coverage path planning approach for agricultural robots to minimize skip/overlap areas between swaths[J]. Robotics and Autonomous Systems, 2016, 76: 36－45.

[13] HÖFFMANN M, PATEL S, BÜSKENS C. Optimal coverage path planning for agricultural vehicles with curvature constraints [J]. Agriculture, 2023, 13(11): 2112.

[14] POUR ARAB D, SPISSER M, ESSERT C. 3d hybrid path planning for optimized coverage of agricultural fields: a novel approach for wheeled robots[J]. Journal of Field Robotics, 2025, 42(2): 455－473.

[15] POUR ARAB D, SPISSER M, ESSERT C. Complete coverage path planning for wheeled agricultural robots[J]. Journal of Field Robotics, 2023, 40(6): 1460－1503.

[16] SEYYEDHASANI H, DVORAK J S. Dynamic rerouting of a fleet of vehicles in agricultural operations through a dynamic multiple depot vehicle routing problem representation[J]. Biosystems Engineering, 2018, 171: 63－77.

[17] PHAM T H, ICHALAL D, MAMMAR S. Complete coverage path planning for pests-ridden in precision agriculture using UAV [C]// Proceedings of the 2020 IEEE International Conference on Networking, Sensing and Control (ICNSC), 2020.

[18] 罗承铭,熊陈文,黄小毛,等. 四边形田块下油菜联合收获机全覆盖作业路径规划算法[J]. 农业工程学报,2021,37(9):140 - 148.
LUO Chengming, XIONG Chenwen, HUANG Xiaomao, et al. Coverage operation path planning algorithms for the rape combine harvester in quadrilateral fields[J]. Transactions of the CSAE,2021,37(9):140 - 148. (in Chinese)

[19] 黄小毛,张垒,王绍帅,等. 凸多边形田块下油菜联合直播机组作业路径规划[J]. 农业机械学报,2022,53(1):33 - 40,150.
HUANG Xiaomao, ZHANG Lei, WANG Shaoshuai, et al. Path planning of rapeseed combine seeder in field of convex boundary[J]. Transactions of the Chinese Society for Agricultural Machinery,2022,53(1):33 - 40,150. (in Chinese)

[20] 刘国海,万亚连,沈跃,等. 基于改进粒子群算法的高地隙无人喷雾机对不规则凸田块的全覆盖作业路径规划[J]. 华南农业大学学报,2025,46(3):390 - 398.
LIU Guohai, WAN Yalian, SHEN Yue, et al. Complete coverage path planning of irregular convex field for the high clearance unmanned sprayer based on improved particle swarm optimizer algorithm[J]. Journal of South China Agricultural University, 2025,46(3):390 - 398. (in Chinese)

[21] 陈行政,周浩,谢守勇,等. 双螺旋驱动式丘陵山区深泥脚水田插秧机设计与试验[J]. 农业机械学报,2025,56(3):247 - 255.
CHEN Xingzheng, ZHOU Hao, XIE Shouyong, et al. Rice transplanter with double helix drive for deep muddy paddy fields of hilly regions[J]. Transactions of the Chinese Society for Agricultural Machinery,2025,56(3):247 - 255. (in Chinese)

[22] 梁喜凤,陆鑫煜,郑立文,等. 螺旋推进式滩涂贝类采捕设备行走装置研制[J]. 农业工程学报,2024,40(24):11 - 19.
LIANG Xifeng, LU Xinyu, ZHENG Liwen, et al. Development of the walking system for spiral-propelled tidal flat shellfish harvesting device[J]. Transactions of the CSAE,2024,40(24):11 - 19. (in Chinese)

[23] 靳航嘉,吴文福,吴子丹,等. 螺旋驱动式粮仓机器人行走机构设计与试验[J]. 农业工程学报,2021,37(2):20 - 26.
JIN Hangjia, WU Wenfu, WU Zidan, et al. Design and experiment of screw drive granary robot running on the loose grain surface[J]. Transactions of the CSAE,2021,37(2):20 - 26. (in Chinese)

[24] HU L, HOU K, HE J, et al. Multi-constraint improved RS path planning method for unmanned rice direct seeding machine [J]. Computers and Electronics in Agriculture, 2024, 224: 109236.

[25] KUMAR M, SINGH R, SINGH A, et al. Referencing and coordinate systems in GIS[M]// Geographic information systems in urban planning and management. Springer. 2023.

[26] 巩岩. 利用 GDAL 实现导航道路的外扩线生成[J]. 测绘通报,2018(3):139 - 142.
GONG Yan. Realization of navigation road expanding based on GDAL API[J]. Bulletin of Surveying and Mapping,2018(3): 139 - 142. (in Chinese)

[27] KULP I, OCHANINE C, RICHARD L, et al. Decreasing paths of polygons[J]. arXiv preprint arXiv:240212643, 2024.

[28] HUANG X, YAN C B. Dubins curve based continuous-curvature trajectory planning for autonomous mobile robots[J]. arXiv preprint arXiv:230907565, 2023.

[29] LI H, ZHU D, CHEN M, et al. An improved Reeds - Shepp and distributed auction algorithm for task allocation in multi-AUV system with both specific positional and directional requirements[J]. Journal of Marine Science and Engineering, 2024, 12(3): 486.

《中文核心期刊要目总览》收录
Ei Compendex(核心版)收录
百种中国杰出学术期刊
RCCSE中国权威学术期刊

ISSN 1002-6819
CN 11-2047/S
CODEN NGOXEO
www.tcsae.org

农业工程学报

NONGYE GONGCHENG XUEBAO | TRANSACTIONS OF THE CHINESE SOCIETY OF AGRICULTURAL ENGINEERING

2023年 第39卷 VOL. 39 05

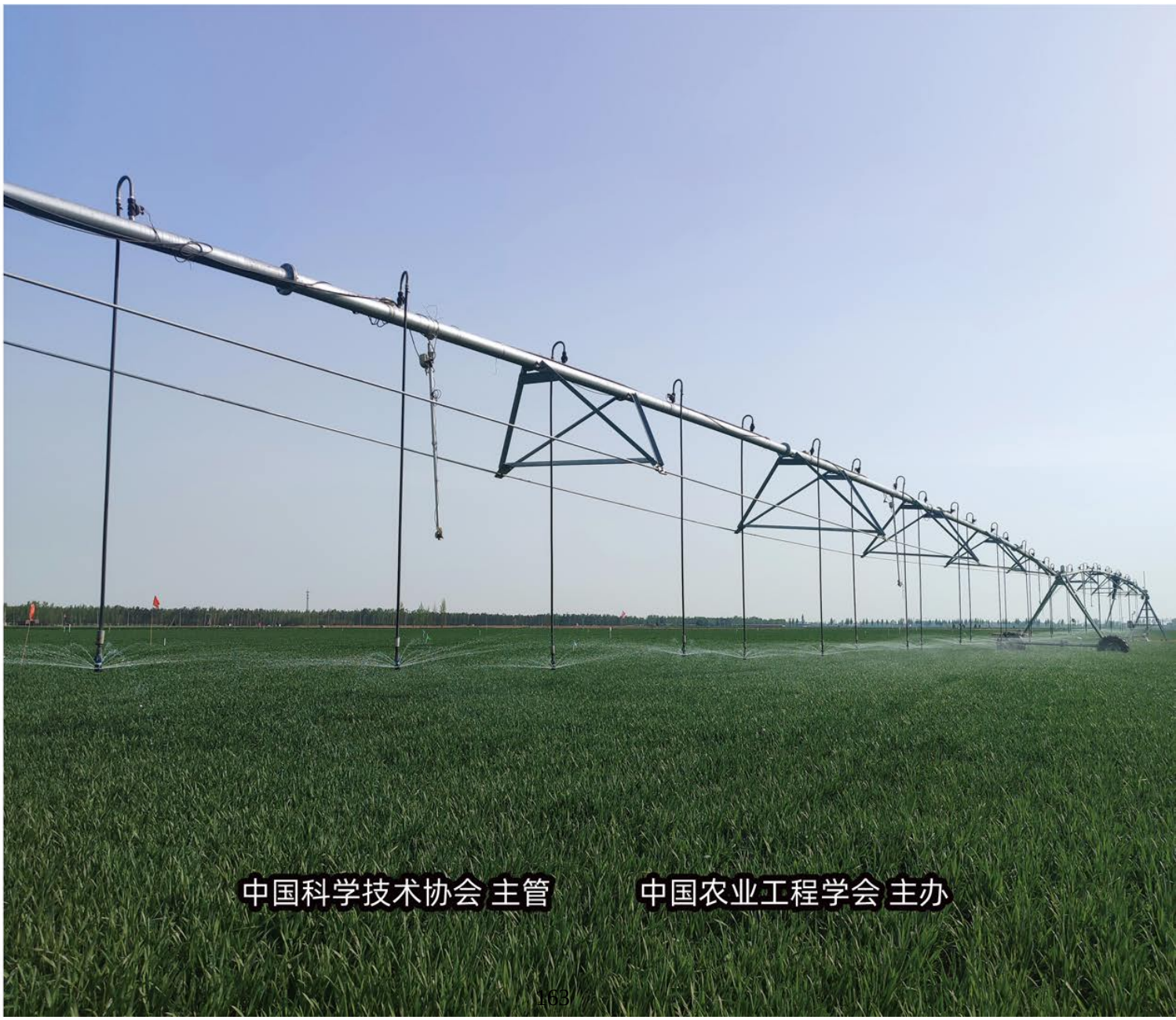

农业工程学报
TRANSACTIONS OF THE CHINESE SOCIETY OF AGRICULTURAL ENGINEERING
二〇二三年三月
第三十九卷
第五期
中国农业工程学会

农 业 工 程 学 报

2023 年 3 月第 5 期 （总第 454 期） 第 39 卷

目 次

·农业生物环境与能源工程·

·土地保障与生态安全·

·农产品加工工程·

·研究速报·

期刊基本参数：CN 11-2047/S*1985*s*16*270*zh*P*¥80.00*280*30*2023-03

✦✲✦✲✦✲✦✲✦✲✦✲✦✲✦✲✦✲✦✲✦✲✦✲✦

致谢：感谢中国水利水电科学研究院赵伟霞团队提供的封面图片“小麦地的水圆规”

Transactions
of the Chinese Society of Agricultural Engineering
Vol.39 No.5 (Total No.454) Mar. 2023

CONTENTS

• Agricultural Equipment Engineering and Mechanization •

• Soil and Water Engineering •

• Agricultural Information and Electrical Technologies •

• Research Letters •

·农业装备工程与机械化·

基于激光感知的农业机器人定位系统

胡 炼[1,2]，王志敏[1]，汪 沛[1,2※]，何 杰[1,2]，焦晋康[1]，王晨阳[1]，李明锦[1]

（1. 华南农业大学南方农业机械与装备关键技术教育部重点实验室，广州 510642；
2. 岭南现代农业科学与技术广东省实验室茂名分中心，茂名 525000）

摘 要：为解决基于全球导航卫星系统（global navigation satellite system，GNSS）的农业机器人和自动驾驶农机在机库、大棚等卫星信号弱或无环境下定位精度低甚至无法定位的问题，该研究提出了基于激光感知的农业机器人定位方法。采用二维激光雷达和激光接收器设计了基于激光感知的机器人定位系统，通过二维激光雷达发射扫描激光获取机器人上激光接收器的点云，同时激光接收器感应扫描激光，融合感应扫描激光时间差和激光接收器点云特征，得到移动激光接收器（即农业机器人）的定位。以全站仪测量为参照在大棚内开展验证试验，结果表明，在激光雷达扫描范围内，机器人行驶速度为 0.8 m/s 时，直线行驶时最大偏差绝对平均值为 4.1 cm，最大均方根误差为 1.5 cm；曲线行驶时最大偏差绝对平均值为 6.2 cm，最大均方根误差为 2.6 cm，满足农业机器人在农机库等环境中自动导航所需定位精度要求。

关键词：机器人；激光雷达；激光传感；定位；智能农机装备
doi：10.11975/j.issn.1002-6819.202211144
中图分类号：S24; TP273 **文献标志码**：A **文章编号**：1002-6819(2023)-05-0001-07

胡炼，王志敏，汪沛，等. 基于激光感知的农业机器人定位系统[J]. 农业工程学报，2023，39(5)：1-7.
doi：10.11975/j.issn.1002-6819.202211144 http://www.tcsae.org
HU Lian, WANG Zhimin, WANG Pei, et al. Agricultural robot positioning system based on laser sensing[J]. Transactions of the Chinese Society of Agricultural Engineering (Transactions of the CSAE), 2023, 39(5): 1-7. (in Chinese with English abstract)
doi：10.11975/j.issn.1002-6819.202211144 http://www.tcsae.org

0 引 言

农业机器人通常应用于结构化场景与随机的不确定场景，且作业任务日益复杂[1]，定位和导航是农业机器人的关键技术[2]。当前农机自动驾驶技术和农机辅助导航技术快速发展[3-7]，通过物联网、大数据和人工智能等先进信息技术的联合使用，农机自动驾驶和辅助导航技术已在无人化智慧农场开始实践应用[8]。

全球导航卫星系统（global navigation satellite system，GNSS）作为农业机械智能化技术中的一项关键技术，近年来已被广泛应用于农业生产各环节，其定位精度达到厘米级[9]，基于 GNSS 的农业机械导航系统旱地作业直线路径跟踪精度优于±2.5 cm[4]，水田作业直线路径跟踪横向偏差平均值为 4.3 cm[10]。因此，智能农机依靠 GNSS 定位实现了大田高精度智能化无人作业[11]，但在农机机库、农机转移行驶过程中经过树冠下和高架桥桥底以及温室大棚设施等场景时，存在 GNSS 卫星信号差或丢失的问题，难以实现导航定位，因此亟需其他定位方法融合补充。

Wi-fi、Zigbee、蓝牙和超宽带等无线通信技术[12]以及即时定位与地图构建（simultaneous localization and mapping，SLAM）技术是常用定位方法。无线通信技术中 Wi-fi、超宽带信号定位易受环境因素干扰[12-13]，Zigbee 和蓝牙定位需要铺设大量设备[14]。SLAM 指在没有环境先验信息下，通过使用各种传感器采集环境信息，在运动过程中构建环境地图，并估计机器人位置[15]，目前，已经有许多解决 SLAM 问题的数学模型与理论基础[16]。SLAM 技术包括视觉 SLAM 和激光 SLAM，可以提供载体的相对位置信息，定位精度较高，已在物流、工业、医疗、安防、服务和农业等移动机器人以及无人驾驶领域广泛应用[17-21]。在农业机器人出库入库时，因库内外光照强度差异大，易导致视觉 SLAM 定位误差增大甚至无法定位，而且图像处理的运算量大、实时性较差[2,22]。此外，当环境中有较多移动物体时，视觉 SLAM 的环境地图构建偏差增大，定位精度降低[23]。相比之下，激光 SLAM 技术较成熟、定位误差更小[24]，但激光 SLAM 构建的地图缺乏语义信息[25]，对于大场景非固定地图仍需进一步研究[26]，激光 SLAM 的地图构建可使用二维激光雷达和三维激光雷达，目前在物流和工业等领域主要使用成本较高的三维激光雷达[27]。

在无人化农场作业中，若每台无人驾驶农机均配备一套激光 SLAM 系统和高性能运算处理器实现小范围卫星信号被遮挡区域内的无人驾驶农机定位，不仅不能充分利用激光 SLAM 系统性能，而且增加了成本。因此，在保持现有农机无人驾驶系统定位解算算法等前提下，研究能够和 GNSS 系统融合补充的定位系统来解决无人驾

收稿日期：2022-11-14 修订日期：2023-01-16
基金项目：江苏大学农业装备学部项目（NZXB20210106）；广东省科技计划项目（2021B1212040009）；佛山市科技创新项目（2120001008424）；国家现代农业技术体系（CARS-13）
作者简介：胡炼，博士，研究员，研究方向为智能农机装备和无人农场。Email：lianhu@scau.edu.cn
※通信作者：汪沛，博士，讲师，研究方向为农业工程、精准农业研究。Email：wangpei@scau.edu.cn

驶农机出入库卫星信号弱或无的问题，对无人化农场的研究与建设具有重要意义。故本文设计了基于二维激光感知的农业机器人定位系统，并进行定位试验验证其定位精度。

1 基于激光感知的农业机器人定位方法

1.1 基于激光感知的农业机器人定位原理

基于激光感知的农业机器人定位系统由移动激光接收器、处理器、固定激光接收器和二维激光雷达组成，如图 1 所示，移动激光接收器和处理器安装在机器人上，固定激光接收器和二维激光雷达固定在已知大地坐标位置，根据大地坐标点及激光雷达坐标系与大地坐标系的位置关系，基于激光感知的定位算法计算得到机器人的大地坐标，因此现有农机无人驾驶系统的定位解算和控制算法均无需修改即可实现无 GNSS 信号时实现定位和导航，例如，机器人出库时，在既有基于激光感知的机器人定位系统定位信号又有 GNSS 信号的区域切换 GNSS 定位系统进行导航，而入库时，在该区域切换采用基于激光感知的机器人定位系统进行导航。

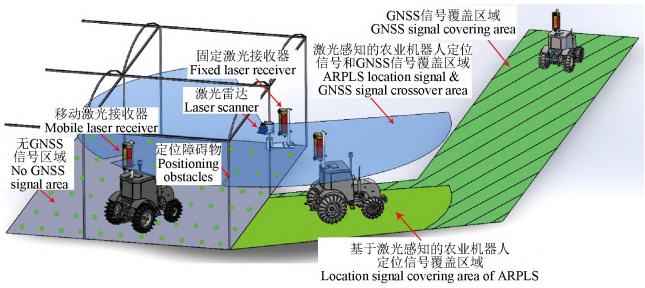

图 1 基于激光感知的农业机器人定位原理示意图

Fig.1 Schematic diagram of agricultural robot positioning principle based on laser sensing (ARPLS)

1.2 基于激光感知的农业机器人定位算法

激光雷达以一定周期扫描获得数量已知且排序固定的点云数据，固定激光接收器感应激光雷达周期性照射产生固定激光信号，且固定激光接收器位置已知，机器人运动过程中移动激光接收器感应激光雷达周期性照射产生移动激光信号，在一个扫描周期中，根据固定激光信号与移动激光信号得到两者的触发时间差，由此获得照射到移动激光接收器的激光射线与照射到固定激光接收器的激光射线夹角 $\Delta\theta$，以此快速准确找到移动激光接收器在激光雷达点云中的散点集，结合点云特征匹配算法获得移动激光接收器中心坐标，最后通过坐标转换得到移动激光接收器中心在大地坐标系中的位置，即农业机器人在大地坐标系中的位置。

在激光雷达扫描平面建立以激光雷达为圆心的极坐标系和直角坐标系，极坐标系中任意点（ρ，θ），其直角坐标系为（x，y），坐标转换关系如下：

$$\begin{cases} x = \rho \cdot \cos\theta \\ y = \rho \cdot \sin\theta \end{cases} \tag{1}$$

固定激光接收器光电转换模块的极坐标（ρ_g，θ_g）已知，同一扫描周期 T 内固定激光接收器的激光感应时间 t_1、移动激光接收器的激光感应时间 t_2，得到时间差为 $\Delta t = t_1 - t_2$，移动激光接收器与固定激光接收器之间的角度间隔为 $\Delta\theta = \dfrac{\Delta t}{T} \cdot 360°$，移动激光接收器光电转换模块的极坐标为（$\rho_y$，$\theta_y$），则 $\theta_y = \theta_g + \Delta\theta$。

设移动激光接收器感知激光照射的真实长度为 l_0，取激光照射到移动激光接收器产生的点云中间点，作该点与坐标原点连线的垂线段，此垂线段连接照射到移动激光接收器最左侧、最右侧的激光线束，激光线束为各点云与坐标原点的连线，垂线段长度即为激光接收器感知激光照射的真实长度。设 N 为移动激光接收器获得的点云数量，d 为点云距离坐标原点的平均长度，β 为激光雷达的角度分辨率，可得 N 与 d 的关系式为

$$N = \frac{2\arctan\dfrac{l_0}{2d}}{\beta} \tag{2}$$

激光接收器在激光雷达扫描平面的投影近视为长方形，如图 2 所示，移动激光接收器感光模块为图中长方形内的方形。激光接收器的位置状态在点云中主要有 3 种情况：激光接收器外壳有 1 个面被激光照射且该面上有激光雷达测量点云；激光接收器外壳有两个面被激光照射且 2 个面上都有激光雷达测量点云；激光接收器外壳有 2 个面被激光照射但只有 1 个面上有激光雷达测量点云。若激光接收器外壳有激光雷达测量点云，在直角坐标系 XOY 下，通过激光接收器外壳长边和短边的激光雷达点云分别拟合获得直线 l_1 和 l_3。

由几何关系可得 $k = \dfrac{\cos\theta_y}{\sin\theta_y}$、$k_1 k_3 = -1$、$k_2 = \tan(\arctan k_1 - \arctan\dfrac{D_0}{L_0})$。已知点 $p(x_p, y_p)$ 坐标，由直线 l_1 可求出 l_2 和 l_3，同样地，由直线 l_3 可求出 l_2 和 l_1。

若可从激光接收器外壳激光雷达的反馈点中提取出直线 l_1 与直线 l_3，则点 p 的坐标为

$$\begin{cases} x_p = \dfrac{b_2 - b_1}{k_1 - k_2} \\ y_p = k_1 x_p + b_1 \end{cases} \tag{3}$$

若只能提取出直线 l_1 或 l_3，则需要估计点 p 坐标。设已知拟合提取直线 l_1 的点云集合 dy 共有 i 个点，激光接收器长边上两端点分别为 dy_1 和 dy_i，若 $dy_1(x_0, y_0)$ 为靠近激光接收器光电转换模块中心的点，预测的点 p 介于点 dy_1 和射线 l_n 与直线 l_1 交点之间，则 l_n 为 $y = \tan(\theta_n - \dfrac{240}{682} \cdot \dfrac{\pi}{180})x$，射线 l_n 与直线 l_1 的交点 $t(x_t, y_t)$ 坐标为

$$\begin{cases} x_t = \dfrac{b_1}{\tan(\theta_n - \dfrac{240}{682} \cdot \dfrac{\pi}{180}) - k_1} \\ y_t = k_1 x_t + b_1 \end{cases} \tag{4}$$

取点 p 为点 dy_1 与点 t 的平均值，由此可得点 p 坐标为

$$\begin{cases} x_p = \left(\dfrac{b_1}{\tan\left(\theta_n - \dfrac{240}{682}\cdot\dfrac{\pi}{180}\right) - k_1} + x_0\right)/2 \\ y_p = (k_1 x_t + b_1 + y_0)/2 \end{cases} \tag{5}$$

可得直线 l_2 方程为

$$y = \tan\left(\arctan k_1 - \arctan\frac{D_0}{L_0}\right)x + (y_p - k_2 x_p) \tag{6}$$

激光接收器光电转换模块中心坐标 (x_c, y_c) 为直线 l_2 与直线 l 的交点，表达为

$$\begin{cases} x_c = \dfrac{k_2 x_p - y_p}{\tan\left(\arctan k_1 - \arctan\dfrac{D_0}{L_0}\right) - k} \\ y_c = k x_c \end{cases} \tag{7}$$

由激光接收器光电转换模块中心坐标推算出移动激光接收器中心坐标，再转换至大地坐标系下移动激光接收器中心坐标，即定位坐标。

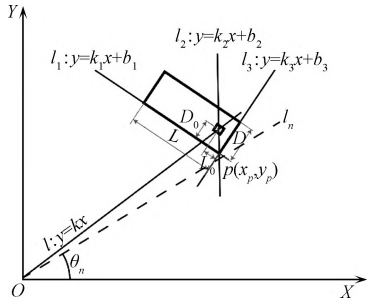

注：L 为接收器外壳长边长度，cm；D 为接收器外壳短边长度，cm；L_0 为接收器感光模块距外壳短边距离，cm；D_0 为接收器感光模块距外壳长边距离，cm；l 为接收器感光模块与坐标原点连线；l_1 为拟合出的接收器外壳长边所在直线；l_3 为拟合出的接收器外壳短边所在直线，点 P 为直线 l_1 和直线 l_3 的交点；l_2 为接收器感光模块与点 P 连线；k、k_1、k_2 和 k_3 分别为直线 l、l_1、l_2 和 l_3 的斜率；b_1、b_2 和 b_3 分别为直线 l_1、l_2 和 l_3 的截距。l_n 为离光电转换模块中心最近的激光雷达扫描射线，θ_n 为激光雷达射线 l_n 扫描线对应极坐标的角度值。

Note: L is the length of the long side of the mobile laser receiver housing, cm; D is the length of the short side of the mobile laser receiver housing, cm; L_0 is the distance from the photosensitive module of the mobile laser receiver to the short side of the housing, cm; D_0 is the distance from the photosensitive module of the mobile laser receiver to the long side of the housing, cm; the l is the connection line between the receiver photosensitive module and the coordinate origin, the l_1 is the fitting line of the receiver housing on long side , point P is the intersection of line l_1 and line l_3, l_2 is the connection line between the photosensitive module of the mobile laser receiver and point P, the l_3 is the fitting line of the receiver housing on short side, k, k_1, k_2 and k_3 is the slope of the straight line l, l_1, l_2 and l_3, respectively; b_1 is the intercept of the straight line l_1, b_1 is the intercept of the straight line l_2, b_3 is the intercept of the straight line l_3, the l_n is the closest laser radar scanning ray to the center of the photoelectric conversion module, θ_n is the angle value of the polar coordinate corresponding to the scanning line of the laser radar ray l_n.

图 2　激光接收器光电转换模块中心坐标几何关系示意图

Fig.2　Schematic diagram of the central coordinate geometric relationship of the photoelectric conversion module of the laser receiver

2　基于激光感知的农业机器人定位系统试验

2.1　系统介绍

基于激光感知的农业机器人定位（ARPLS）系统如图 3 所示，以东风井关 T954 拖拉机为试验平台。ARPLS 系统硬件部分主要由移动端和固定端组成，移动端包括移动激光接收器，固定端包括激光雷达和固定激光接收器。激光接收器通过滤光模块、光电转换模块、信号调制模块将激光雷达发射的光信号转换成电信号[28]，数据处理与通信传输模块将激光感应信号通过 CAN 总线进行传输，激光接收器外壳长边 11 cm，短边 6.5 cm。移动激光接收器安装在拖拉机顶部机体（沿机头方向）中心线上，离地高度 3 m，激光雷达和固定接收器固定在华南农业大学增城教学科研基地农机库支撑柱上，且移动激光接收器和固定激光接收器均能够接收到激光雷达发射的激光射线。移动激光接收器和固定激光接收器的 CAN 总线通过 PCAN-USB 传输到处理器，PCAN-USB 用于监听 CAN 网络消息，时间戳的分辨率为 42 μs。激光雷达的测量距离为 40～20 000 mm，扫描范围为 270°，角度分辨率为 0.117 2°，扫描频率为 10 Hz，误差为测量距离的 1%。

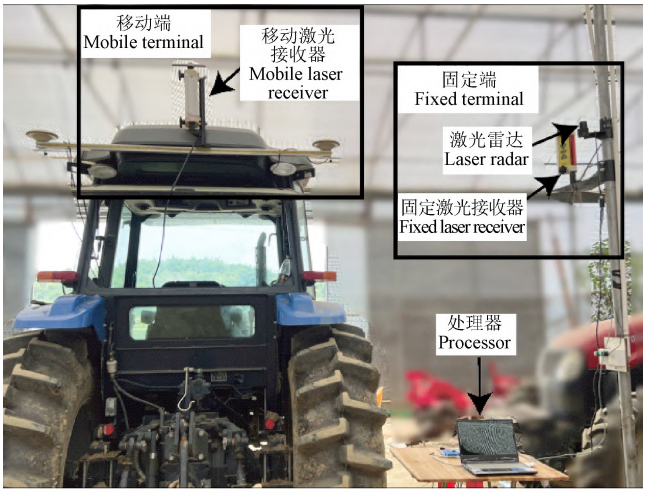

图 3　安装在拖拉机上的基于激光感知的农业机器人定位系统

Fig.3　Tractor mounted with ARPLS

使用 Visual studio 2022 通过 C#编程语言编写系统软件，采用多线程数据事件触发的方式进行数据处理与分析，得到准确的激光雷达、移动激光接收器和固定激光接收器的数据响应时间戳，固定端数据发送到移动端进行分析处理，从而实时获得定位数据。

试验以全站仪和 RTK GNSS 系统的测量轨迹作为参考对象，且均采用 WGS-84 坐标系。全站仪自动跟踪安装在移动激光接收器上的棱镜，进行动态跟踪测量，全站仪为 Leica Ms60，测量频率 10 Hz，100 m 范围内测量误差 1 mm；RTK GNSS 系统直接测量获取拖拉机定位，RTK GNSS 板卡为 K728，测量频率 10 Hz，平面定位精度 1 cm。

试验时拖拉机在激光雷达扫描范围内以 0.3、0.5 和 0.8 m/s 分别进行往复的直线运动和曲线运动，行驶距离 9～20 m，每组试验重复 5 次，ARPLS 系统、全站仪和 GNSS 三套定位系统同时采集定位数据，采集时长 3～5 min，其中激光感知定位系统每次试验获得定位点 2 000 个以上。

2.2 坐标系转换与机器人中心定位

为统一坐标系，试验将 ARPLS 系统的激光雷达坐标系转换至 WGS-84 坐标系。设 WGS-84 坐标系为 XOY，东向为 X 轴，北向为 Y 轴，激光雷达坐标系为 $X'O'Y'$，大地坐标原点为 O，激光雷达坐标为 O'，两个坐标系之间的夹角为 θ（逆时针为正）。在 $X'O'Y'$坐标系下 XOY 中坐标点转化关系如式（8）和式（9）所示，其中（x'，y'）为 $X'O'Y'$坐标系下激光雷达的坐标，（x_0，y_0）为 XOY 坐标系下激光雷达的坐标。

$$x' = (x - x_0)\cos\theta + (y - y_0)\sin\theta \tag{8}$$

$$y' = -(x - x_0)\sin\theta + (y - y_0)\cos\theta \tag{9}$$

激光雷达的中心点难以用全站仪直接进行测量，激光雷达坐标系与全站仪坐标系的夹角 θ 也难确定。因此，将激光雷达固定于标定板上。分别将棱镜固定于标定板上 2 个不同位置上，用全站仪进行测量，得到大地坐标系下点 1 (x_1, y_1) 和点 2 (x_2, y_2)，由点 1 和点 2 坐标计算得到大地坐标系下激光雷达中心坐标 (x_0, y_0)，过激光雷达中心做点 1 和点 2 连线的垂线，L 为激光雷达中心至垂足的距离，可得：

$$x_0 = \sqrt{\frac{L^2}{1 + \dfrac{(x_2 - x_1)^2}{(y_2 - y_1)^2}}} + \frac{x_2 + x_1}{2} \tag{10}$$

$$y_0 = -\frac{(x_2 - x_1)}{(y_2 - y_1)}\left(x_0 - \frac{x_2 + x_1}{2}\right) + \frac{y_2 + y_1}{2} \tag{11}$$

$$\theta = \arctan\frac{y_2 - y_1}{x_2 - x_1} \tag{12}$$

因此，激光感知定位系统得到的激光雷达坐标系下的定位点坐标 (x_d, y_d) 转换至 WGS-84 坐标系下坐标 (x_f, y_f) 为

$$x_f = x_d\cos\theta - y_d\sin\theta + x_0 \tag{13}$$

$$y_f = y_d\cos\theta + x_d\sin\theta + y_0 \tag{14}$$

3 结果与分析

ARPLS 系统、全站仪和 GNSS 测量的一组拖拉机以 0.8 m/s 速度直线行驶和曲线行驶的轨迹分别如图 4 和图 5 所示，其中直线行驶距离 10 m、曲线行驶距离 12 m。由图可知，ARPLS 系统测量的拖拉机轨迹与全站仪和 GNSS 测量的轨迹基本重合，表明在试验行驶距离范围内，ARPLS 系统提供了试验拖拉机在 WGS-84 坐标系下的定位。

ARPLS 系统动态测量拖拉机以 0.8 m/s 速度进行直线行驶和曲线行驶定位与全站仪测量定位的偏差绝对值曲线分别如图 6 和图 7 所示。在相同速度下，直线行驶定位的偏差绝对值明显小于曲线行驶定位的偏差绝对值，因此，ARPLS 系统动态测量直线运动定位精度高于曲线运动定位精度，测量直线运动定位偏差不大于 7 cm，测量曲线运动定位偏差小于 12 cm。

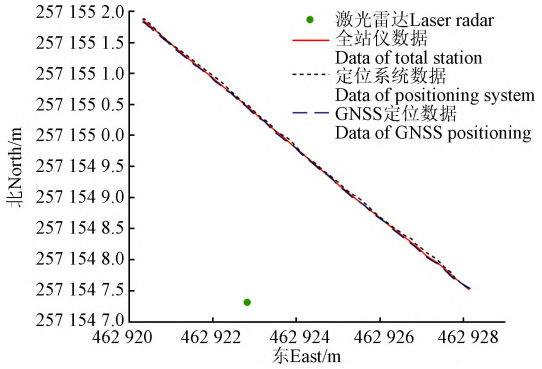

图 4 拖拉机直线行驶轨迹

Fig.4 Straight trajectory of the tractor

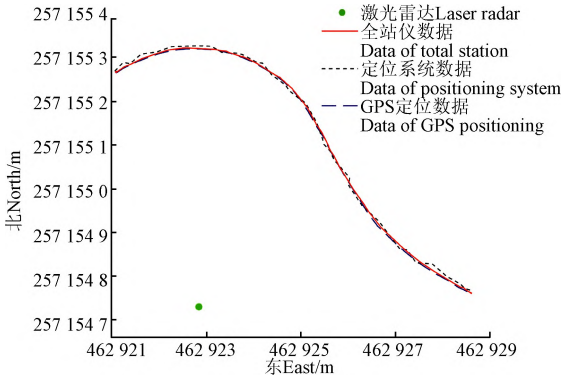

图 5 拖拉机曲线行驶轨迹

Fig.5 Curve trajectory of the tractor

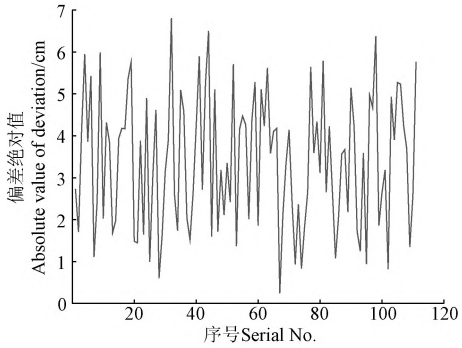

图 6 直线行驶的定位偏差绝对值曲线

Fig.6 Absolute value curve of positioning deviation for straight travel

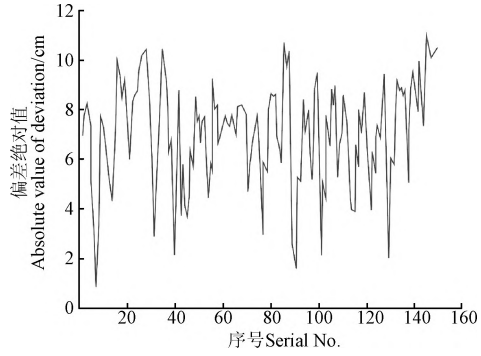

图 7 曲线行驶的定位偏差绝对值曲线

Fig.7 Absolute value curve of positioning deviation for curve travel

以全站仪测量定位为真值，各试验组次 ARPLS 系统相对全站仪测量定位的偏差绝对平均值和均方根误差如表 1 所示。表中试验数据表明，随着拖拉机速度越快，ARPLS 系统定位相对全站仪定位的误差随之增大；行驶速度相同时，曲线行驶比直线行驶定位的误差大。0.8 m/s 速度时，直线行驶时最大偏差绝对平均值为 4.1 cm，最大均方根误差为 1.5 cm；曲线行驶时最大偏差绝对平均值为 6.2 cm，最大均方根误差为 2.6 cm。

表 1　激光感知定位相比全站仪定位误差

Table 1　Positioning error between ARPLS and total station

行驶类型 Travel type	速度 Speed/(m·s^{-1})	序号 Serial No.	偏差绝对平均值 Absolute average of deviation/cm	均方根误差 Root mean square error/cm
直线行驶 Straight travel	0.3	1	2.4	1.0
		2	2.7	1.1
		3	2.3	1.1
		4	2.8	1.0
		5	2.3	1.1
	0.5	1	3.2	1.2
		2	2.7	1.1
		3	2.9	1.1
		4	3.0	1.1
		5	2.4	1.1
	0.8	1	3.6	1.4
		2	4.1	1.5
		3	3.3	1.4
		4	3.2	1.4
		5	2.8	1.4
曲线行驶 Curve travel	0.3	1	3.6	1.4
		2	3.8	1.5
		3	2.6	1.3
		4	3.5	1.5
		5	3.2	1.4
	0.5	1	4.8	1.8
		2	4.0	1.8
		3	3.5	1.8
		4	3.9	1.8
		5	4.3	1.9
	0.8	1	5.2	2.3
		2	5.6	2.5
		3	6.2	2.6
		4	5.2	2.5
		5	4.8	2.0

ARPLS 系统的误差主要源于移动激光接收器和固定激光接收器感知激光的时间差误差以及点云拟合误差。随着拖拉机速度增加而定位误差增大是由于激光雷达需要完成一圈扫描才能输出点云数据，导致定位系统数据输出与测量时刻存在延时。曲线行驶定位误差比直线行驶定位误差大主要是因为曲线运动导致激光接收器长方形外壳的长边或短边点云数量少甚至没有，从而降低了算法推算精度。

4　结　论

1）本文提出了基于激光感知的农业机器人定位方法，利用激光感知和激光雷达点云特征得到移动激光接收器相对固定激光雷达的位置，通过坐标转换获得机器人的实时大地定位坐标。

2）基于激光感知的定位算法解决了难以从二维激光雷达点云中确定目标对象点云的问题，通过固定激光信号与移动激光信号触发时间差快速准确找到移动激光接收器在激光雷达点云中的散点集，结合点云特征匹配算法实现了快速准确地获得目标对象定位。

3）设计了基于激光感知的农业机器人定位系统，大棚内试验结果表明，在激光雷达扫描范围内，机器人行驶速度为 0.8 m/s 时，直线行驶时最大偏差绝对平均值为 4.1 cm，最大均方根误差为 1.5 cm；曲线行驶时最大偏差绝对平均值为 6.2 cm，最大均方根误差为 2.6 cm。

移动接收器外形以及激光雷达扫描外壳获得的点云数量直接影响基于激光感知的农业机器人定位系统的定位精度，因此后续将从大尺寸圆形外壳激光接收器设计、高频率点云激光雷达选用以及与惯性传感器融合算法等方面开展研究，进一步提高定位精度和环境适应能力。

［参　考　文　献］

[1] 宫金良，王伟，张彦斐，等. 基于农田环境的农业机器人群协同作业策略[J]. 农业工程学报，2021，37(2)：11-19.
GONG Jinliang, WANG Wei, ZHANG Yanfei, et al. Cooperative working strategy for agricultural robot groups based on farmland environment[J]. Transactions of the Chinese Society of Agricultural Engineering (Transactions of the CSAE), 2021, 37(2): 11-19. (in Chinese with English abstract)

[2] 陈瑜，张铁民，孙道宗，等. 基于无线传感器网络的设施农业车辆定位系统设计与试验[J]. 农业工程学报，2015，31(10)：190-197.
CHEN Yu, ZHANG Tiemin, SUN Daozong, et al. Design and experiment of locating system for facilities agricultural vehicle based on wireless sensor network[J]. Transactions of the Chinese Society of Agricultural Engineering (Transactions of the CSAE), 2015, 31(10): 190-197. (in Chinese with English abstract)

[3] 何杰，朱金光，张智刚，等. 水稻插秧机自动作业系统设计与试验[J]. 农业机械学报，2019，50(3)：17-24.
HE Jie, ZHU Jinguang, ZHANG Zhigang, et al. Design and experiment of automatic operation systemfor rice transplanter[J]. Transactions of the Chinese Society for Agricultural Machinery, 2019, 50(3): 17-24. (in Chinese with English abstract)

[4] 何杰，高维炜，王辉，等. 基于 MEMS 陀螺仪的农机转向轮角测量方法[J]. 中国农机化学报，2020，41(4)：123-129.
HE Jie, GAO Weiwei, WANG Hui, et al. Steering wheel angle measurement method of agricultural machinery based on dual MEMS gyroscope[J]. Journal of Chinese Agricultural Mechanization, 2020, 41(4): 123-129. (in Chinese with English abstract)

[5] 张雁，李彦明，刘翔鹏，等. 水田环境下水稻直播机自动驾驶控制方法[J]. 农业机械学报，2018，49(11)：15-22.
ZHANG Yan, LI Yanming, LIU Xiangpeng, et al. An automatic drive control technique for rice drill seeder in uneven paddy fields[J]. Transactions of the Chinese Society for Agricultural Machinery, 49(11): 15-22. (in Chinese with English abstract)

[6] 钟银，薛梦琦，袁洪良. 智能农机 GNSS/INS 组合导航系统设计[J]. 农业工程学报，2021，37(9)：40-46.
ZHONG Yin, XUE Mengqi, YUAN Hongliang. Design of the GNSS/INS integrated navigation system for intelligent agricultural machinery[J]. Transactions of the Chinese

Society of Agricultural Engineering (Transactions of the CSAE), 2021, 37(9): 40-46. (in Chinese with English abstract)

[7] 潘新宇，赵英策，李建勋. GNSS/INS 组合导航的随机时延卡尔曼滤波[J]. 指挥控制与仿真，2022，44(1)：26-31.
PAN Xinyu, ZHAO Yingce, LI Jianxun. Random Delay Kalman Filtering of GNSS/INS integrated navigation[J]. Command Control & Simulation, 2022, 44(1): 26-31. (in Chinese with English abstract)

[8] 李道亮，李震. 无人农场系统分析与发展展望[J]. 农业机械学报，2020，51(7)：1-12.
LI Daoliang, LI Zhen. System analysis and development prospect of unmanned farming[J]. Transactions of the Chinese Society for Agricultural Machinery, 2020, 51(7): 1-12. (in Chinese with English abstract)

[9] 刘兆朋，张智刚，罗锡文，等. 雷沃 ZP9500 高地隙喷雾机的 GNSS 自动导航作业系统设计[J]. 农业工程学报，2018，34(1)：15-21.
LIU Zhaopeng, ZHANG Zhigang, LUO Xiwen, et al. Design of automatic navigation operation system for Lovol ZP9500 high clearance boom sprayer based on GNSS[J]. Transactions of the Chinese Society of Agricultural Engineering (Transactions of the CSAE), 2018, 34(1): 15-21. (in Chinese with English abstract)

[10] 张宜宝，孙经纬，石绍军，等. 自动驾驶插秧机控制系统的设计与试验[J]. 农机化研究，2023，45(7)：71-78.
ZHANG Yibao, SUN Jingwei, SHI Shaojun, et al. Design and experiment of control system for automatic driving transplanter[J]. Journal of Agricultural Mechanization Research, 2023, 45(7): 71-78. (in Chinese with English abstract)

[11] 罗锡文，廖娟，胡炼，等. 我国智能农机的研究进展与无人农场的实践[J]. 华南农业大学学报，2021，42(6)：8-17.
LUO Xiwen, LIAO Juan, HU Lian, et al. Research progress of intelligent agricultural machinery and practice of unmanned farm in China[J]. Journal of South China Agricultural University, 2021, 42(6): 8-17. (in Chinese with English abstract)

[12] 陈沛宇，袁勤政，戴鹏飞，等. 多技术融合的室内无线定位方法发展综述[J]. 导航定位学报，2022，10(3)：9-13.
CHEN Peiyu, YUAN Qinzheng, DAI Pengfei, et al. Overview of the development of indoor wireless positioning methods based onmulti-technology integration[J]. Journal of Navigation and Positioning, 2022, 10(3): 9-13. (in Chinese with English abstract)

[13] 闫大禹，宋伟，王旭丹，等. 国内室内定位技术发展现状综述[J]. 导航定位学报，2019，7(4)：5-12.
YAN Dayu, SONG Wei, WANG Xudan, et al. Review of development status of indoor location technology in China[J]. Journal of Navigation and Positioning, 2019, 7(4): 5-12. (in Chinese with English abstract)

[14] 姚立健，Santosh K Pitla，杨自栋，等. 基于超宽带无线定位的农业设施内移动平台路径跟踪研究[J]. 农业工程学报，2019，35(2)：17-24.
YAO Lijian, Santosh K Pitla, YANG Zidong, et al. Path tracking of mobile platform in agricultural facilities based on ultra wideband wireless positioning[J]. Transactions of the Chinese Society of Agricultural Engineering (Transactions of the CSAE), 2019, 35(2): 17-24. (in Chinese with English abstract)

[15] DONG F C, IENG S H, SAVATIER X, et al. Plenoptic cameras in real-time robotics[J]. International Journal of Robotics Research, 2013, 32(2): 206-217.

[16] GUALTIERI M, PLATT R. Robotic pick-and-place with uncertain object instance segmentation and shape completion[J]. IEEE Robotics and Automation Letters, 2021, 6(2): 1753-1760.

[17] KIM A, EUSTICE R M. Real-time visual SLAM for autonomous underwater hull inspection using visual saliency[J]. IEEE Transactions on Robotics, 2013, 29(3): 719-733.

[18] LU T T, YEH S C, CHEN C Y. A study of indoor positioning systems using iBeacons with different transmission power levels[J]. Journal of the Chinese Institute of Engineers, 2017, 40(6): 525-535.

[19] 王世峰，戴祥，徐宁，等. 无人驾驶汽车环境感知技术综述[J]. 长春理工大学学报（自然科学版），2017，40(1)：1-6.
WANG Shifeng, DAI Xiang, XU Ning, et al. Overview on environment perception technology for unmanned ground vehicle[J]. Journal of Changchun University of Science and Technology (Natural Science Edition), 2017, 40(1): 1-6. (in Chinese with English abstract)

[20] 胡广锐，孔微雨，齐闯，等. 果园环境下移动采摘机器人导航路径优化[J]. 农业工程学报，2021，37(9)：175-184.
HU Guangrui, KONG Weiyu, QI Chuang, et al. Optimization of the navigation path for a mobile harvesting robot in orchard environment[J]. Transactions of the Chinese Society of Agricultural Engineering (Transactions of the CSAE), 2021, 37(9): 175-184. (in Chinese with English abstract)

[21] 杨继之，乐毅，张加波，等. 移动机器人定位精度实时补偿策略研究[J]. 机械工程学报，2022，58(14)：44-53.
YANG Jizhi, LE Yi, ZHANG Jiabo, et al. Real-time compensation strategy of mobile robot positioning accuracy[J]. Journal of Mechanical Engineering, 2022, 58(14): 44-53. (in Chinese with English abstract)

[22] 陈艳，张漫，马文强，等. 基于 GPS 和机器视觉的组合导航定位方法[J]. 农业工程学报，2011，27(3)：126-130.
CHEN Yan, ZHANG Man, MA Wenqiang, et al. Positioning method of integrated navigation based on GPS and machine vision[J]. Transactions of the Chinese Society of Agricultural Engineering (Transactions of the CSAE), 2011, 27(3): 126-130. (in Chinese with English abstract)

[23] 王柯赛，姚锡凡，黄宇，等. 动态环境下的视觉 SLAM 研究评述[J]. 机器人，2021，43(6)：715-732.
WANG Kesai, YAO Xifan, HUANG Yu, et al. Review of visual SLAM in dynamic environment[J]. Robot, 2021, 43(6): 715-732. (in Chinese with English abstract)

[24] 李晨阳，彭程，张振乾，等. 融合里程计信息的农业机器人定位与地图构建方法[J]. 农业工程学报，2021，37(21)：16-23.
LI Chenyang, PENG Cheng, ZHANG Zhenqian, et al. Positioning and map construction for agricultural robots integrating odometer information[J]. Transactions of the

Chinese Society of Agricultural Engineering (Transactions of the CSAE), 2021, 37(21): 16-23. (in Chinese with English abstract)

[25] 刘凌云，蔡成林，吴芊. 室外光照易变场景下的回环检测方法[J]. 传感器与微系统，2022，41(4)：121-124.
LIU Lingyun, CAI Chenglin, WU Qian. Loop closure detection method in outdoor scene with variable illumination[J]. Transducer and Microsystem Technologies, 2022, 41(4): 121-124. (in Chinese with English abstract)

[26] 孙曼晖，杨绍武，易晓东，等. 基于 GIS 和 SLAM 的机器人大范围环境自主导航[J]. 仪器仪表学报，2017，38(3)：586-592.
SUN Manhui, YANG Shaowu, YI Xiaodong, et al. Autonomous navigation of robot in large-scale environments based on GIS and SLAM[J]. Chinese Journal of Scientific Instrument, 2017, 38(3): 586-592. (in Chinese with English abstract)

[27] 单吉超，李秀智，张祥银，等. 室内场景下实时地三维语义地图构建[J]. 仪器仪表学报，2019，40(5)：240-248.
SHAN Jichao, LI Xiuzhi, ZHANG Xiangyin, et al. Real-time 3D semantic map building in indoor scene[J]. Chinese Journal of Scientific Instrument, 2019, 40(5): 240-248. (in Chinese with English abstract)

[28] ZANG Y, MENG S, HU L, et al. Optimization design and experimental testing of a laser receiver for use in a laser levelling control system[J]. Electronics, 2020, 9(3): 536. (in Chinese with English abstract)

Agricultural robot positioning system based on laser sensing

HU Lian[1,2], WANG Zhimin[1], WANG Pei[1,2※], HE Jie[1,2], JIAO Jinkang[1], WANG Chenyang[1], LI Mingjin[1]

(1. *Key Laboratory of Key Technology on Agricultural Machine and Equipment*, *Ministry of Education*, *South China Agricultural University*, *Guangzhou* 510642, *China*; 2. *Maoming Branch*, *Guangdong Laboratory for Lingnan Modern Agriculture*, *Maoming* 525000, *China*)

Abstract: In order to solve the positioning problem of global navigation satellite system (GNSS) based robots and autonomous agricultural machinery, which is low accuracy or even unable to locate under the environment of weak or no satellite signals such as hangars and greenhouses. This research proposes an agricultural robot positioning system based on laser sensing. The system is designed by using two-dimensional laser scanner and laser receiver, which obtains the point cloud of the laser receiver on the robot through the scanning laser emitted by the two-dimensional laser scanner , and the laser receiver inductively scans by the laser scanner, the location of mobile laser receiver (i.e. agricultural robot) is obtained by fusing the time difference of laser scanning induction and the point cloud characteristics of mobile laser receiver. The agricultural robot positioning system based on laser sensing consists of mobile laser receiver, processor, fixed laser receiver and two-dimensional laser scanner. The mobile laser receiver and processor are installed on the robot, and the fixed laser receiver and two-dimensional laser radar are fixed at the known geodetic coordinate position. According to the position relationship between the laser scanner coordinate system and the known geodetic coordinate system. The laser scanner scanning at a certain period to obtain a known number of fixed-order point cloud data. The fixed laser receiver senses the periodic irradiation of the laser scanner to generate the base station laser signal, and the serial number of the fixed laser receiver shell in the point cloud is known. The mobile laser receiver senses the periodic irradiation of the laser radar to generate the mobile laser signal during the movement of the robot. According to the trigger time difference between the fixed laser signal and the mobile laser signal, the angle between the laser rays that are irradiated to the mobile laser receiver and the laser rays that are irradiated to the fixed laser receiver can be obtained in a scanning period of the laser scanner. And the scattered point set of the mobile laser receiver in the laser radar point cloud can be found, and the center coordinate of the mobile laser receiver can be obtained by combining the point cloud feature matching algorithm. The robot positioning can be calculated by combined with the geodetic coordinates of the laser scanner and the position relationship between the laser scanner coordinate system and the geodetic coordinate system, the central coordinates of the mobile laser receiver under the geodetic coordinate system. The geodetic coordinates of the robot are calculated by the positioning algorithm based on laser sensing, and the geodetic coordinates of the robot without GNSS signal are supplemented without changing the positioning solution and control algorithm of the existing robot unmanned system. For example, when the robot leaves the hangar, it switches to the GNSS positioning system for positioning and navigation in the area with both the positioning signals of the robot positioning system based on laser perception and the GNSS signal. When entering the hangar, switch to the robot positioning system based on laser sensing for positioning and navigation in the area cover with both the positioning signal of the robot positioning system based on laser perception and the GNSS signal. The verification test is carried out with the reference of total station which shows that within the scanning range of laser radar, when the robot is at a speed of 0.8 m/s, the absolute average value of the maximum deviation of the positioning error in a straight line is 4.1 cm, and the maximum root mean square error is 1.5 cm; when the robot driving on a curve, the absolute average value of the maximum deviation of positioning error is 6.2 cm , and the maximum root mean square error is 2.6 cm. The result shows that this method can achieve accurate robot positioning and meets the positioning accuracy requirements for automatic navigation of agricultural robots in agricultural machinery warehouses and other environments.

Keywords: robot; laser radar; laser sensing; positioning; intelligent agricultural machinery equipment

Computers and Electronics in Agriculture

Supports open access

15.1 CiteScore | 8.9 Impact Factor

Articles & Issues | About | Publish | Order journal ↗ | Search in this journal | Submit your article ↗ | Guide for authors

Volume 239, Part B

December 2025

< Previous vol/issue | Next vol/issue >

Download full issue

Actions for selected articles

Select all / Deselect all

Download PDFs

Export citations

Show all article previews

Contents

Full Length Articles

Review Articles

Short Communications

Receive an update when the latest issues in this journal are published

Sign in to set up alerts

Editorial board • Full text access

Editorial Board

Article 111100

View PDF

Full Length Articles

Research article • Full text access

Exploring the influence of coupling diverse spectral resolutions and feature selection approaches on the estimate of equivalent water thickness in fruit tree leaves

Jintao Cui, Mamat Sawut, Xin Hu, Areziguli Rouzi, ... Nijat Kasim

Article 110983

View PDF | Article preview

Research article • Full text access

A novel dual-polarization SAR vegetation index for crop phenology detection

Xin Bao, Rui Zhang, Xu He, Age Shama, ... Xianjian Shi

Article 110953

View PDF | Article preview

Research article • Full text access

SE-YOLO: A sobel-enhanced framework for high-accuracy, lightweight real-time tomato detection with edge deployment capability

Xiao Deng, Tianlun Huang, Weijun Wang, Wei Feng

Article 110973

View PDF | Article preview

Actions for selected articles

Select all / Deselect all

Download PDFs

Export citations

Show all article previews

Contents

Full Length Articles

Review Articles

Short Communications

Research article • Full text access

SE-YOLO: A sobel-enhanced framework for high-accuracy, lightweight real-time tomato detection with edge deployment capability

Xiao Deng, Tianlun Huang, Weijun Wang, Wei Feng

Article 110973

View PDF Article preview

Research article • Full text access

Caged broiler aggregation behavior recognition via target detection and label merging

Chao Yuan, Zikang Chen, Yurong Tang, Ruqian Zhao, ... Mingxia Shen

Article 110844

View PDF Article preview

Research article • Full text access

Vibratory threshing mechanism and multi-species threshing parameter testing of wine grapes based on discrete element method

Huineng Zhou, Haochao Tan, Congcong Shen, Junlong Ma, ... Shuai Ma

Article 110955

View PDF Article preview

Research article • Open access

Wheat yield forecasts with seasonal climate models and long short-term memory networks

Maximilian Zachow, Stella Ofori-Ampofo, Harald Kunstmann, Ridvan Salih Kuzu, ... Senthold Asseng

Article 110965

View PDF Article preview

Research article • Full text access

Detection of *Spodoptera litura* F. using an electronic nose: A novel approach for monitoring vegetable crop pests

Atirach Noosidum, Rattanawadee Onwong, Jarunee Phittayanivit, Chatchaloem Arkhan, ... Chatchawal Wongchaosuk

Article 110984

View PDF Article preview

Research article • Full text access

Nextv2-DETR: lightweight real-time classification model of potatoes based on improved RT-DETR for mobile deployment

Xiang Kong, Fei Liu, Yingsi Wu, Lihe Wang, ... Xuan Zhao

Article 110996

View PDF Article preview

Research article • Full text access

Automatic measurement method of sheep body size based on 3D reconstruction and point cloud

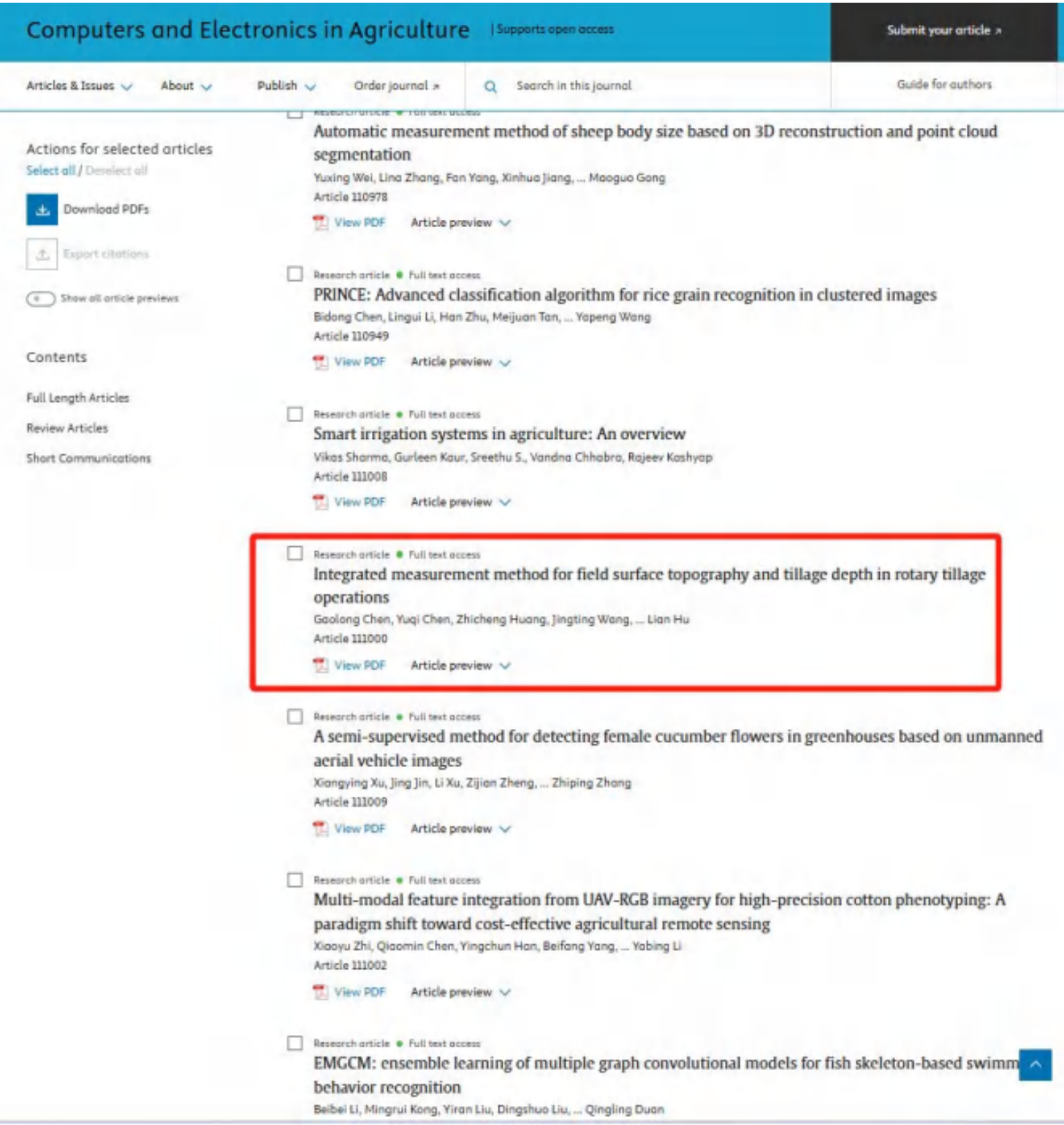
Computers and Electronics in Agriculture
| Supports open access
Submit your article
Articles & Issues
About
Publish
Order journal
Search in this journal
Guide for authors
Actions for selected articles
Select all / Deselect all
Download PDFs
Export citations
Show all article previews
Contents
Full Length Articles
Review Articles
Short Communications
Automatic measurement method of sheep body size based on 3D reconstruction and point cloud segmentation
Yuxing Wei, Lina Zhang, Fan Yang, Xinhua Jiang, ... Maoguo Gong
Article 110978
View PDF
Article preview
Research article
Full text access
PRINCE: Advanced classification algorithm for rice grain recognition in clustered images
Bidong Chen, Lingui Li, Han Zhu, Meijuan Tan, ... Yapeng Wang
Article 110949
View PDF
Article preview
Research article
Full text access
Smart irrigation systems in agriculture: An overview
Vikas Sharma, Gurleen Kaur, Sreethu S., Vandna Chhabra, Rajeev Kashyap
Article 111008
View PDF
Article preview
Research article
Full text access
Integrated measurement method for field surface topography and tillage depth in rotary tillage operations
Gaolong Chen, Yuqi Chen, Zhicheng Huang, Jingting Wang, ... Lian Hu
Article 111000
View PDF
Article preview
Research article
Full text access
A semi-supervised method for detecting female cucumber flowers in greenhouses based on unmanned aerial vehicle images
Xiangying Xu, Jing Jin, Li Xu, Zijian Zheng, ... Zhiping Zhang
Article 111009
View PDF
Article preview
Research article
Full text access
Multi-modal feature integration from UAV-RGB imagery for high-precision cotton phenotyping: A paradigm shift toward cost-effective agricultural remote sensing
Xiaoyu Zhi, Qiaomin Chen, Yingchun Han, Beifang Yang, ... Yabing Li
Article 111002
View PDF
Article preview
Research article
Full text access
EMGCM: ensemble learning of multiple graph convolutional models for fish skeleton-based swimm
behavior recognition
Beibei Li, Mingrui Kong, Yiran Liu, Dingshuo Liu, ... Qingling Duan

Computers and Electronics in Agriculture 239 (2025) 111000

Contents lists available at ScienceDirect

Computers and Electronics in Agriculture

journal homepage: www.elsevier.com/locate/compag

Original papers

Integrated measurement method for field surface topography and tillage depth in rotary tillage operations

Gaolong Chen, Yuqi Chen, Zhicheng Huang, Jingting Wang, Yufei Deng, Pei Wang *, Runmao Zhao, Lian Hu

Guangdong Laboratory for Lingnan Modern Agriculture, South China Agricultural University, Guangzhou 510642, China
Key Laboratory of Key Technology On Agricultural Machine and Equipment, Ministry of Education, South China Agricultural University, Guangzhou 510642, China
State Key Laboratory of Agricultural Equipment Technology, Guangzhou 510642, China

ARTICLE INFO

Keywords:
Field preparation
Rotary tillage
Field topography
Tillage depth

ABSTRACT

Field surface topography and tillage depth are crucial information for guiding crop production. However, the separate measurement of field surface topography and tillage depth increases production costs. To address issues, this study proposes an integrated measurement method for field surface topography and tillage depth in rotary tillage operations. Based on the operational characteristics of the rotary tiller, a simultaneous measurement method for field surface and the tillage bottom-layer topography (FS-TBLSM) was proposed. Building on this, a method was developed to arrange grid points, referred to as the directional adaptive gridding method in plane topography (DAG-PT), and a sample-approximated Gaussian process regression (SA-GPR) algorithm was used to estimate the field surface topography height and tillage depth at a given grid point. The accuracy of these methods was evaluated using verification and field tests. The verification results showed that the FS-TBLSM method achieved a static root mean square error (RMSE) of less than 15.00 mm along all three axes, with dynamic RMSEs below 20.00 mm, confirming the effectiveness of the FS-TBLSM method and its good dynamic tracking capability. Further field test results indicated that the field surface topography measured using the FS-TBLSM method aligned with the true topography. The measured field surface topography height exhibited an average absolute error (AAE) of 18.13 mm and an RMSE of 20.58 mm, validating the accuracy and reliability of this method for field surface topography measurement. Using true surface topographic height and tillage depth at 20 points as references, an AAE and RMSE of 17.13 and 17.95 mm, respectively, were obtained for surface topographic height estimation; estimated tillage depth exhibited an AAE and RMSE of 14.52 and 16.49 mm, respectively. These results demonstrate that the SA-GPR algorithm can accurately estimate the field surface topography height and tillage depth after rotary tillage operations. The integrated measurement method performs the measurement in a single operation, reducing the number of field operations by 50 %, saving an estimated 15.57 kg/ha in fuel consumption. Additionally, this study provides key inputs for leveling operations, including setting the base height, calculating earthwork volume, and planning paths. It also supports active control of seeding depth and provides references for yield assessment.

1. Introduction

1.1. Background

Field preparation plays a critical role in crop production and directly influences the subsequent planting and growth stages. Specifically, land tilling ensures the uniform incorporation of surface residues, weeds, and fertilizers, while contributing to soil loosening and restoring aggregate structure. In addition, it improves soil aeration and permeability (Zhou et al., 2016; Huang et al., 2023; Zhu et al., 2024). On the other hand, land leveling increases the effective area available for cultivation and enhances the efficiency of using irrigation water, crop uniformity, weed control, and crop yield, while reducing water and fertilizer usage (Jat et al., 2015; Rezaei-Moghaddam and Far, 2019; Miao et al., 2021; Nadimi et al., 2021; Chen et al., 2024).

Tillage depth substantially influences crop growth, particularly in

* Corresponding author.
E-mail address: wangpei@scau.edu.cn (P. Wang).

https://doi.org/10.1016/j.compag.2025.111000
Received 9 May 2025; Received in revised form 27 July 2025; Accepted 12 September 2025

terms of lodging resistance, yield, and quality (Arvidsson et al., 2013; Jia et al., 2016). Gong et al. (2023) reported that a tillage depth of 17 cm increased rice lodging resistance by 39.45–72.37 % and improved food quality by 12.33 %. The rice yield was 9.18 % higher for a tillage depth of 20 cm than for 14 cm. Topography plays a vital role in determining leveling heights, soil volumes, and planning pathways (Jing et al., 2021; Jing et al., 2022), particularly in rice production. Therefore, both tillage depth and topography are critical factors in crop production.

Currently, field surface topography and tillage depth are measured independently, as no integrated measurement methods are available. An integrated measurement approach can reduce the number of field operations by 50 %, saving an estimated 15.57 kg/ha in fuel consumption (Janulevičius et al., 2019). It can also reduce tractor rut depth by 5–10 % (Botta et al., 2009), effectively lowering the risk of soil compaction caused by repeated machinery passes. In land leveling operations for rice production, the cost and difficulty of independent topography measurements escalate as the field area expands. Furthermore, surface topography and tillage depth data provide key inputs for leveling operations, including base height design, earthwork calculation, and path planning, while also offering crucial inputs for seeding. Specifically, the seeding depth under varying tillage depth conditions can be actively controlled to provide an optimal growing environment.

1.2. Related work

Various methods have been developed for measuring tillage depth and field topography. Tillage-depth measurement methods can primarily be classified into two categories: contact and non-contact methods. Contact methods estimate tillage depth by relying on the movement of a vehicle across the ground and tracking the position of the ground wheels, lifting-arm or rocker angles, and the geometric relationships of these components. For example, Han et al. (2023) measured the lifting-arm angle using inclination sensors and used it with the geometric relationship of the suspension mechanism to estimate tillage depth. Similarly, Jia et al. (2016) measured the rotation angle of a ground wheel rocker using an encoder and employed it to estimate tillage depth based on the geometric relationship between the wheel and frame. By contrast, in non-contact methods, tillage depth is calculated by monitoring the height of the implement frame relative to the ground using sensors, such as ultrasonic (Lou et al., 2021) and optical sensors (Tao et al., 2025). However, factors such as soil moisture content, temperature, and surface residues can affect the accuracy of non-contact measurements (Jia et al., 2010). Furthermore, when measuring tillage depth, the bottom point of the profiling wheel in contact-based estimations and the surface monitoring point in non-contact measurements do not vertically align with the deepest cutting point where the tillage tool cuts into the soil, leading to inherent measurement errors. Existing contact/non-contact tillage depth measurement methods have vertical alignment errors of up to 500 mm, or even higher. Additionally, the distribution of tillage depth lacks coordinate information, hindering its effective integration with subsequent operations. Therefore, further studies are required to develop tillage-depth measurement methods that incorporate positioning information.

Field surface topography measurement methods are primarily classified into remote sensing and vehicle-based methods. Remote sensing methods estimate field topography using unmanned aerial vehicles (UAVs) equipped with non-contact sensors. For instance, Du et al. (2022) and Jin et al. (2021) used UAVs equipped with LiDAR systems to generate three-dimensional (3D) topographic data by integrating multi-source sensor data based on laser ranging. To measure field topography, DJI—a Chinese company—developed the Phantom 4 RTK aerial drone, which is a small multi-rotor UAV equipped with a 20-MP camera designed for low-altitude photogrammetry. However, remote sensing methods require extensive post-processing and frequent data transmission, which escalates time and labor costs. By contrast, vehicle-based methods use tractors and transplanters fitted with measurement devices to examine 3D field topography. For example, Jing et al. (2019) proposed a vehicle-based method for measuring field topography using dual-antenna global navigation satellite system (GNSS) and attitude and heading reference system (AHRS), which is suitable for pre- or post-leveling operations. Wang et al. (2023) developed a kinematic model for the land-leveling shovel and used coordinate transformation principles to calculate the coordinates of the bottom point of the supporting wheel in accordance with the topography. This method can be used to update topographic data in real time during leveling operations. Although both vehicle-based and remote sensing methods are applicable at different stages of leveling operations, measuring topography before leveling increases labor and energy costs as it delays or complicates earth-moving operations. Therefore, it is critical to develop efficient and cost-effective topographic measurement methods that can be used before leveling.

1.3. Research objectives

Existing measurement methods are constrained by several limitations, such as, high production costs, accuracy loss, and soil compaction issues due to the separate measurement of tillage depth and field surface topography.

This study aims to develop an integrated measurement method for field topography and tillage depth. To this end, the following objectives were adopted in this study.

(1) Develop a simultaneous measurement method for field surface and tillage bottom-layer topography (FS-TBLSM).
(2) Introduce a method that enables the construction of grid points required for subsequent operations, referred to as directional adaptive gridding for plane topography (DAG-PT) in this study.
(3) Propose the sample-approximated Gaussian process regression (SA-GPR) algorithm to estimate topographic height and tillage depth at a given grid point.

2. Materials and methods

2.1. Approach overview

Fig. 1 shows the operational components of a rotary tiller, which consists of a frame, rotating blade shaft, rotary blades, cover, and a tailboard. During the tilling operation, the rotating blades cut the soil and throw it backward. The soil then strikes the cover and tailboard, where it is finely broken. The soil eventually falls to the ground, forming a loose soil layer. The end of the tailboard is in contact with the field surface and moves along the topography. As shown in Fig. 1b, a dual-antenna GNSS and AHRS are mounted on the frame and tailboard, respectively. These systems were selected based on the operational characteristics of the rotary tiller. By establishing appropriate coordinate systems and performing coordinate transformations, the topography of the bottom layer of the tilled soil and field surface is acquired using FS-TBLSM. Subsequently, the DAG-PT method is employed to determine the long-edge direction of the field, extract boundary information, and perform raster processing of the plane topography. Finally, the topographic height and tillage depth are estimated at each grid point using the SA-GPR algorithm, enabling map generation.

2.2. Sensors and mounting

As shown in Fig. 2, a dual-antenna GNSS was installed on the frame to measure the heading and pitch angles of the implement. An AHRS was mounted on the tailboard to measure the roll angle of the implement and the rotation angle of the tailboard relative to the frame.

The technical specifications of the GNSS and AHRS are listed in Table 1.

An STM32F407ZGT6 development board was connected to the dual-

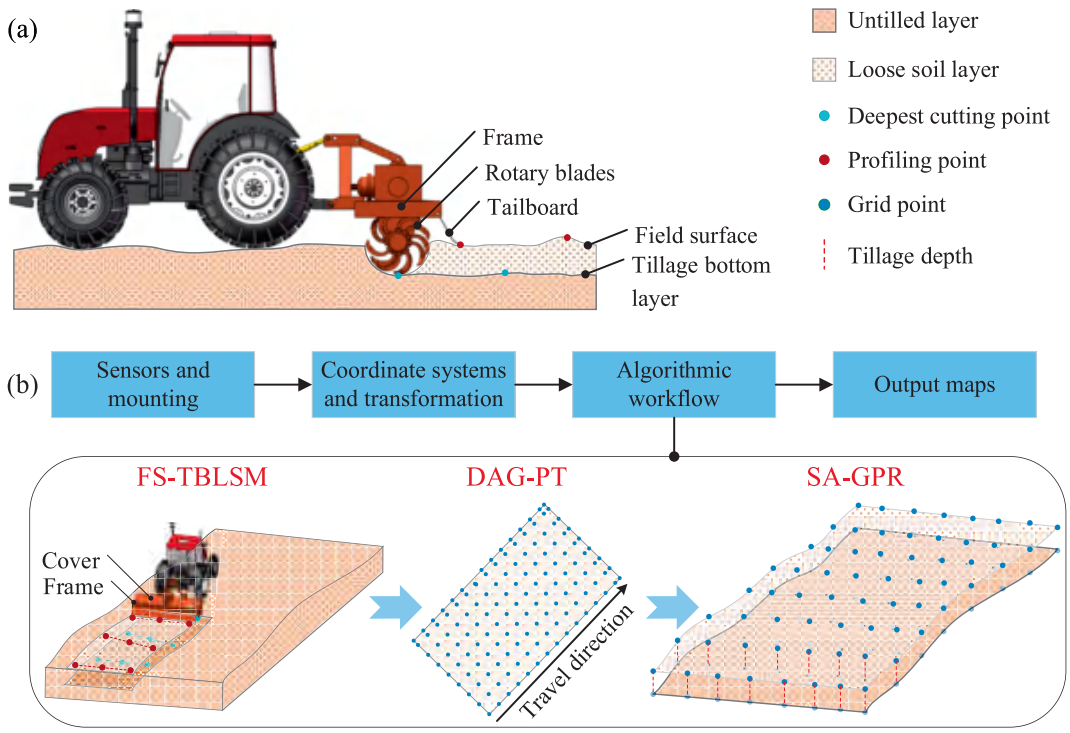

Fig. 1. Overview of the integrated measurement approach for field surface topography and tillage depth. (a) Operational characteristics of the rotary tiller; (b) overall workflow.

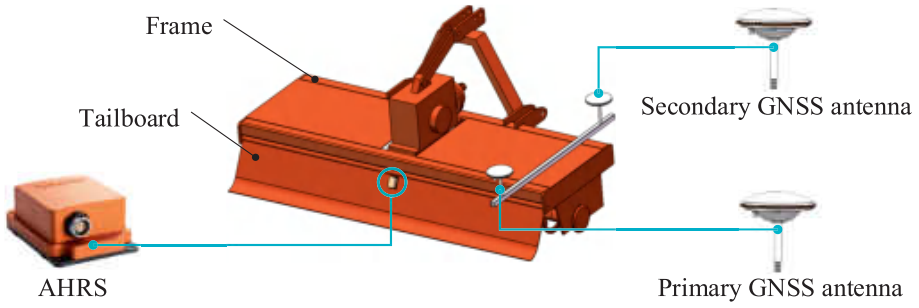

Fig. 2. Sensors and mounting.

Table 1
Technical specifications of sensors.

Sensor	Model	Serial number	Accuracy	Sampling rate	Synchronization method
GNSS	UNICORECOMM UM982	/	Horizontal (RTK): 0.8 cm + 1 ppm; Vertical (RTK): 1.5 cm + 1 ppm; Heading (RTK): 0.1°/1m	10 Hz	PPS signal
AHRS	XSENS MTi-300-2A5G4	0378268E	Roll/Pitch: 0.2°	10 Hz	Send latest (In)

antenna GNSS receiver and AHRS, which functioned as the data acquisition platform. The UM982 GNSS receiver outputs a 1-PPS signal and data packets. However, due to serial protocol parsing delays, the data packets become slightly delayed relative to the PPS signal. To synchronize the signals from the GNSS receiver and AHRS, the STM32F407ZGT6 development board activates a timer (triggered at 10 Hz) upon receiving the PPS signal, and the trigger source is transmitted to the "Sync in" synchronization pulse input port of the AHRS. Using XSENS MT Manager software, the AHRS data communication interface was configured to the RS232 protocol with a baud rate of 115,200 bps. The synchronization mode was set to the "Send Latest (In)" mode, implying that the latest value was sampled on the rising edge.

The STM32F407ZGT6 development board synchronously acquires the GNSS data packets and AHRS data, which are output via a serial channel to the host computer. Additionally, the STM32F407ZGT6 development board, dual-antenna GNSS, and AHRS are powered by a DC regulated power supply (YSN-12025000, 12 V, 0–10A). In field deployment, a 12 V battery from a power machine (tractor) can be used to power the system.

2.3. Coordinate systems and transformation

As shown in Fig. 3, this study used the earth-centered, earth-fixed (ECEF) coordinate system, the geodetic coordinate system (GCS), the

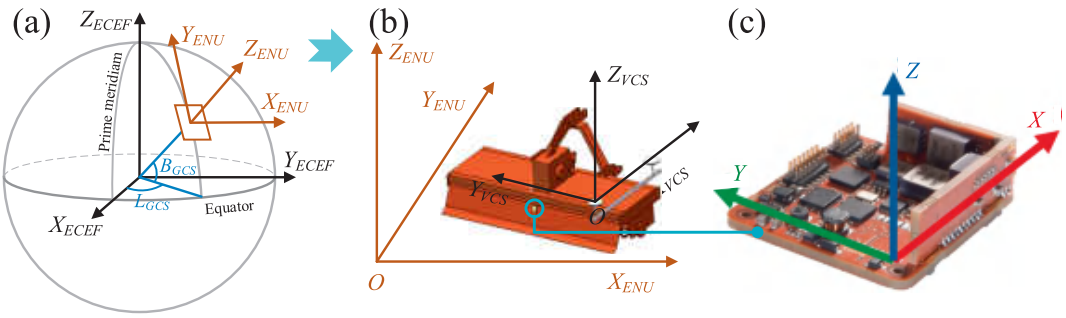

Fig. 3. Coordinate systems and transformation. (a) ECEF coordinate system, GCS, and ENU coordinate system; (b) Relationship between VCS and ENU coordinate system; (c) Sensor coordinate system.

east-north-up (ENU) coordinate system, the vehicle coordinate system (VCS), and the sensor coordinate system.

As shown in Fig. 3a, the three components of the GCS are geodetic latitude, geodetic longitude, and geodetic height, which represent the standard format of the positional information output by GNSS receivers. The transformation between the ECEF coordinate system and GCS is achieved using spatial geometric relationships. The X and Y axes of the ENU coordinate system align with the semi-major (eastward) and semi-minor (northward) axes of the Earth's ellipsoid, respectively, whereas the Z axis is aligned with the normal to the ellipsoid and points upward (skyward). The transformation between the GCS and ENU coordinate systems can be accomplished using projection methods (Tu et al., 2023). As shown in Fig. 3b, in the VCS, the position of the GNSS receiver is the origin. The X-axis is oriented toward the direction of the movement of the rotary tiller, the Y-axis points to the left of the travel direction, and the Z-axis is perpendicular to both the X and Y axes, forming a Cartesian coordinate system. The VCS can be transformed to the ENU coordinate system using homogeneous coordinate transformation. As shown in Fig. 3c, the sensor coordinate system is defined according to the manufacturer's specifications.

2.4. Algorithmic workflow

2.4.1. FS-TBLSM method

As shown in Fig. 4, the FS-TBLSM method is primarily used to obtain the field surface and tillage bottom-layer topography, which consists of four main steps. The angle and positioning data required for this process are obtained using sensors. This section provides a detailed analysis of these steps.

Based on the geometric relationships and kinematic analysis of the rotary tillage implement, the position vectors of the deepest cutting point B and the profiling point C are defined in the VCS. As shown in Fig. 5, the position vector of the center point T of the rotating blade shaft is denoted as ${}^{VCS}\boldsymbol{P}_T = [l_{TX}, l_{TY}, l_{TZ}]^T$, where l_{TY} can represent any length within the working width. As shown in Fig. 5a, when the rotation radius of the rotary blade is d_B, the position vector of point B in the horizontal state is ${}^{VCS}\boldsymbol{P}_B = [l_{TX}, l_{TY}, l_{TZ} + d_B]^T$. However, the position vector of point B changes as the pitch angle of the implement changes in real-time during the operation (Fig. 5b).

Therefore, when the pitch angle of the rotary tillage implement is θ_{GNSS}, the position vector of point B is updated as shown in Eq. (1).

$$ {}^{VCS}\boldsymbol{P}_B = \begin{bmatrix} l_{TX} - d_B \sin\theta_{GNSS} \\ l_{TY} \\ l_{TZ} + d_B \cos\theta_{GNSS} \end{bmatrix} \tag{1} $$

As shown in Fig. 6, the position vector of the rotation center R of the tailboard is denoted as ${}^{VCS}\boldsymbol{P}_R = [l_{RX}, l_{RY}, l_{RZ}]^T$, where l_{RY} can represent any length within the working width. During the operation, the tailboard rotates around point R, causing the position vector of the profiling point C to change in real-time.

The distance between the profiling point C and the rotation point R is denoted as d_{RC} When the pitch angle of the implement is θ_{GNSS}, and the angle between the tailboard and frame is θ_{AHRS}, the position vector of the profiling point C is given by Eq. (2).

$$ {}^{VCS}\boldsymbol{P}_C = \begin{bmatrix} l_{RX} - d_{RC} \cos(\theta_{AHRS} - \theta_{GNSS}) \\ l_{RY} \\ l_{RZ} - d_{RC} \sin(\theta_{AHRS} - \theta_{GNSS}) \end{bmatrix} \tag{2} $$

As shown in Fig. 7a, the vector from the primary antenna to the secondary antenna is the baseline vector. The angle between the baseline vector and the horizontal plane is the pitch angle of the implement (θ_{GNSS}), with a value in the range of $-90°$ $-90°$. As shown in Fig. 7b, the projection of the baseline vector onto the horizontal plane forms an angle with the north direction, which is the heading angle of the implement (φ_{GNSS}), with a value in the range of 0 $-360°$. Additionally, according to the coordinate system of the AHRS, the angle of rotation around the X-axis is the roll angle of the implement (ϕ_{AHRS}).

The rotation angles of the VCS relative to the ENU coordinate system along the X, Y, and Z axes are denoted as $\alpha, \beta,$ and γ, respectively. Based on the orientation of the installed sensors, the relationship between each rotation angle and the attitude of the implement is as follows.

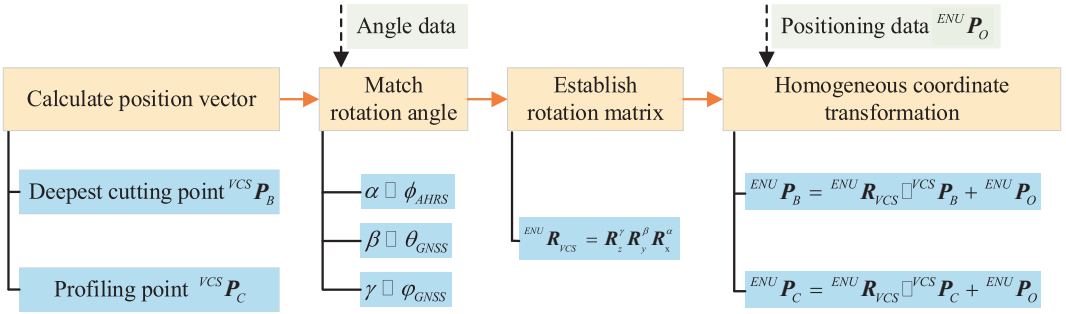

Fig. 4. Flowchart of FS-TBLSM method.

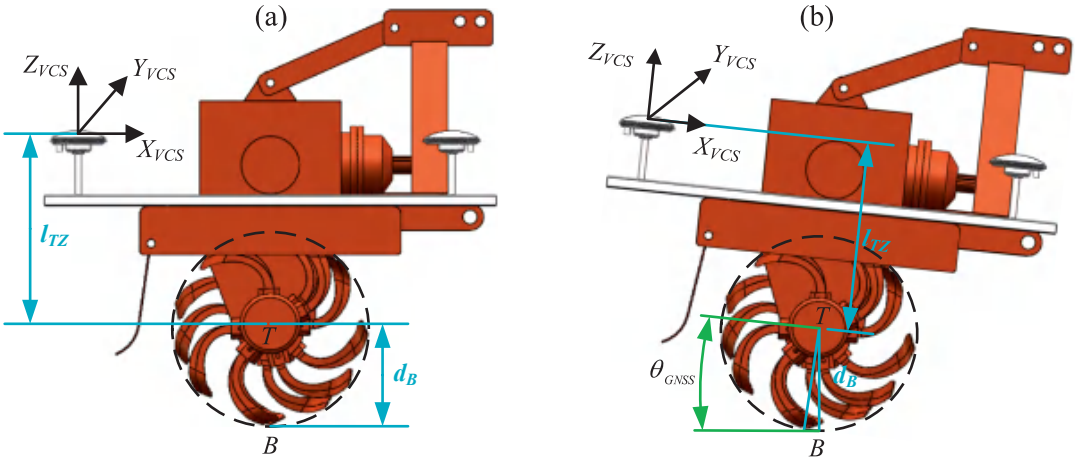

Fig. 5. Position vector of the deepest cutting point B. (a) Horizontal state; (b) Non-horizontal state.

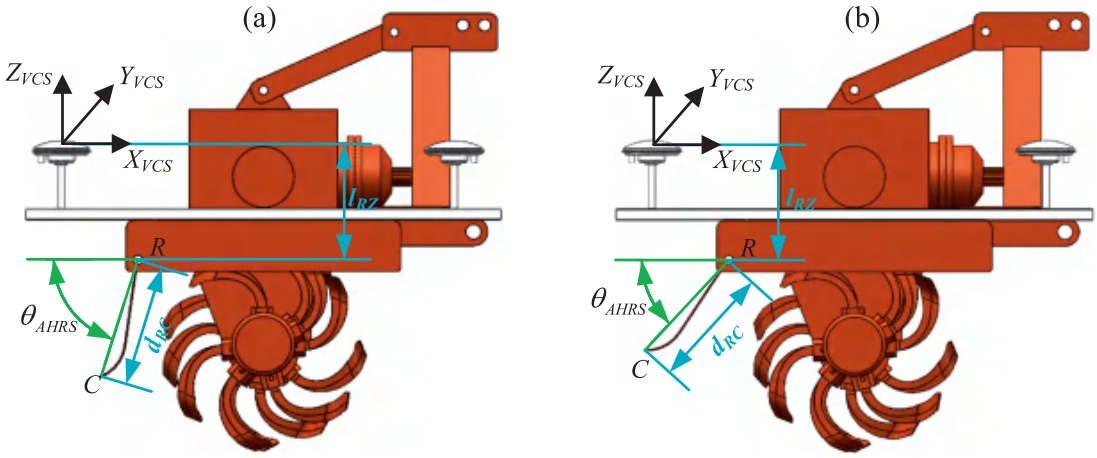

Fig. 6. Position of the profiling point *C*. (a) Initial state; (b) Operation state.

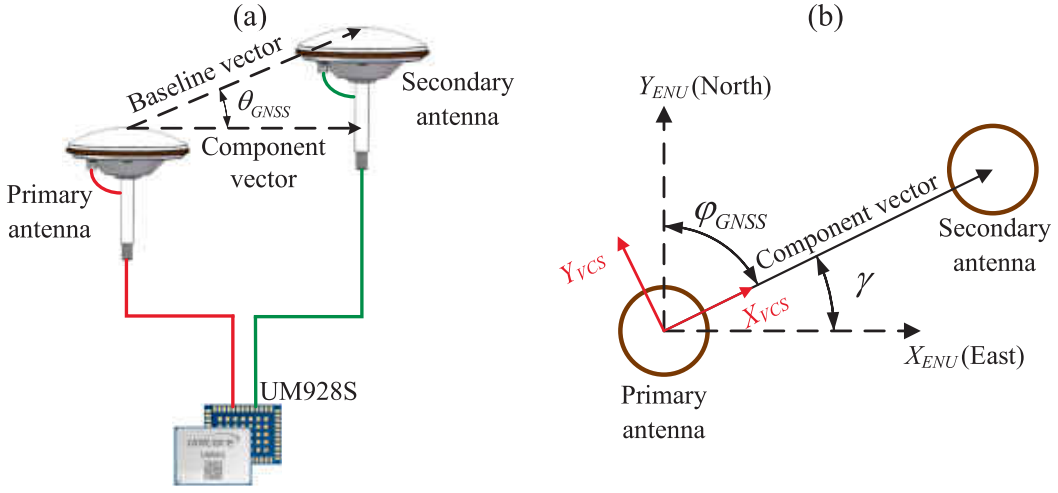

Fig. 7. Relationship between the GNSS receiver position and attitude angles. (a) Pitch angle θ_{GNSS}; (b) Heading angle φ_{GNSS}.

$$\begin{cases} \alpha = -\phi_{AHRS} \\ \beta = -\theta_{GNSS} \\ \gamma = 90^\circ - \varphi_{GNSS} \end{cases} \tag{3}$$

Based on the angle matching relationship, the rotation matrix is established as follow.

$$\begin{aligned} {}^{ENU}\boldsymbol{R}_{VCS} &= \boldsymbol{R}_z^{\gamma}\boldsymbol{R}_y^{\beta}\boldsymbol{R}_x^{\alpha} \\ &= \begin{bmatrix} \cos\gamma & -\sin\gamma & 0 \\ \sin\gamma & \cos\gamma & 0 \\ 0 & 0 & 1 \end{bmatrix} \begin{bmatrix} \cos\beta & 0 & \sin\beta \\ 0 & 1 & 0 \\ -\sin\beta & 0 & \cos\beta \end{bmatrix} \begin{bmatrix} 1 & 0 & 0 \\ 0 & \cos\alpha & -\sin\alpha \\ 0 & \sin\alpha & \cos\alpha \end{bmatrix} \end{aligned} \tag{4}$$

The coordinates of the VCS origin in the ENU coordinate system are denoted as ${}^{ENU}\boldsymbol{P}_O$, as measured using the GNSS receiver. Based on this information, the coordinates of the deepest cutting point B and the profiling point C in the ENU coordinate system are calculated using the homogeneous coordinate transformation method, as follows.

$$\begin{cases} {}^{ENU}\boldsymbol{P}_B = {}^{ENU}\boldsymbol{R}_{VCS} \cdot {}^{VCS}\boldsymbol{P}_B + {}^{ENU}\boldsymbol{P}_O \\ {}^{ENU}\boldsymbol{P}_C = {}^{ENU}\boldsymbol{R}_{VCS} \cdot {}^{VCS}\boldsymbol{P}_C + {}^{ENU}\boldsymbol{P}_O \end{cases} \tag{5}$$

The point cloud density of the deepest cutting point and the profiling point can be adjusted according to the requirements of subsequent operations. These point clouds serve as critical input for grid arrangement and the estimation of field surface topography and tillage depth.

2.4.2. DAG-PT method

Tillage depth refers to the vertical distance between the deepest cutting point and the field surface. However, at any given moment during the operations, the deepest cutting point and the profiling point are not vertically aligned, which prevents the direct calculation of the tillage depth. Therefore, a dataset consisting of the deepest cutting points and the profiling points was used as an input to construct a gridded field topography model. Subsequently, the surface height and the height of the tillage bottom layer were estimated at each grid point, thereby calculating the value of tillage depth without vertical alignment errors.

The gridding format is closely related to the direction and type of operation, as well as the width covered during the operation. The direction is typically aligned with the long side of the field. The interval between adjacent grid points in the direction of the short side and is determined by the width covered during the operation, whereas the interval along the long side is adjusted according to the operation type. Therefore, the field is gridded by identifying the direction of its long side. Grid points are distributed along both the long and short sides of the field, without exceeding the field boundaries. The specific implementation method is detailed below.

(1) Identifying the direction of the field's long side.

The plane point set obtained using the FS-TBLSM method is used as the input. Principal component analysis is used to analyze the correlation between the X and Y variables and identify the direction of maximum correlation. This direction corresponds to the largest eigenvalue of the covariance matrix (Gewers et al., 2022), which represents the long side of the field. The covariance matrix is calculated as shown below:

$$\boldsymbol{C} = \begin{pmatrix} cov(X,X) & cov(X,Y) \\ cov(Y,X) & cov(Y,Y) \end{pmatrix} \tag{6}$$

The singular value decomposition algorithm (Kühl et al., 2024) is used to calculate the eigenvalues and eigenvectors of the covariance matrix, as shown in Eq. (7).

$$\boldsymbol{C} = \boldsymbol{U}\cdot\boldsymbol{\Sigma}\cdot\boldsymbol{V}^T \tag{7}$$

where $\boldsymbol{U}$ represents the eigenvectors of the covariance matrix, arranged in the order of decreasing magnitude of their corresponding eigenvalues; $\boldsymbol{\Sigma}$ is a diagonal matrix, with its diagonal elements being the square roots of the eigenvalues of the covariance matrix; and $\boldsymbol{V}$ is an orthogonal matrix.

(2) Grid point arrangement.

The point set is rotated to align the long and short sides of the field with the ENU coordinate axes. The field boundary is established by calculating the maximum and minimum values ($X^R_{\min}, X^R_{\max}, Y^R_{\min}$ and $Y^R_{\max}$) along the X and Y axes of the rotated point set. The spacing between adjacent grid points along the X and Y axes is set as $\triangle x$ and $\triangle y$, respectively, and the grid points are arranged as shown below.

$$\begin{aligned} A^R = \Bigg\{ \left(X^R_{i'}, Y^R_{j'}\right) | X^R_{i'} = X^R_{\min} + i'\triangle x, Y^R_{i'} = Y^R_{\min} + j'\triangle y, i' \\ = 0, 1, ..., \left[\frac{X^R_{\max} - X^R_{\min}}{\triangle x}\right], j' = 0, 1, ..., \left[\frac{Y^R_{\max} - Y^R_{\min}}{\triangle y}\right] \Bigg\} \end{aligned} \tag{8}$$

Grid points are arranged along the local boundary of the field:

$$B^R = \left\{ \left(X^R_{\max}, Y^R_{j'}\right) | Y^R_{j'} = Y^R_{\min} + j'\triangle y, j' = 0, 1, ..., \left[\frac{Y^R_{\max} - Y^R_{\min}}{\triangle y}\right] \right\} \tag{9}$$

$$C^R = \left\{ \left(X^R_{i'}, Y^R_{\max}\right) | X^R_{i'} = X^R_{\min} + i'\triangle x, i' = 0, 1, ..., \left[\frac{X^R_{\max} - X^R_{\min}}{\triangle x}\right] \right\} \tag{10}$$

Grid points are merged as shown below.

$$G^R_{gri} = A^R \cup B^R \cup C^R \tag{11}$$

Subsequently, the grid point set is rotated to restore the long and short sides of the field to their original orientation.

$$\boldsymbol{G}_{gri} = \boldsymbol{G}^R_{gri}\cdot\boldsymbol{U} \tag{12}$$

2.4.3. SA-GPR algorithm

As shown in Fig. 8, this study proposes the SA-GPR algorithm to estimate the field topographic height and tillage depth for any grid point. Taking the profiling point cloud as an example, the first step is to define the region of interest (ROI) for each grid point. The ROI point set is then approximated to the grid points without any loss of accuracy. The optimized ROI point set is subsequently used as observation samples to estimate the surface topographic height and tillage depth for the grid points using GPR. This sub-section provides a details introduction to the SA-GPR algorithm.

According to the first law of geography, there is a strong correlation between the topographic height of a grid point and that of its neighboring region (Westlund, 2013). Rotary tillage operations can shape both the field surface and the tillage bottom-layer topography. For each grid point, the data within a circular region, with the machinery's working width as the radius, significantly influences the topographic height estimation. Therefore, this circular region is defined as the Region of Interest (ROI). Since both collinear and non-collinear points may exist within the ROI, a time variable is introduced to assess collinearity and eliminate non-collinear points. For collinear points, the closest point to the grid point is identified based on the collinearity relationship. If this point lies between collinear points, only the closest point is retained, and the corresponding collinear points are deleted. This method optimizes the point set within the ROI without compromising estimation accuracy.

Subsequently, the optimized ROI point set (P_{clo}) is used as the training sample, with the topographic height as the corresponding output. Assume that the topographic height $Z_{clo,i''}$ can be modeled using a Gaussian process $f\left(\boldsymbol{P}_{clo,i''}\right)$ and Gaussian noise.

$$Z_{clo,i''} = f\left(\boldsymbol{P}_{clo,i''}\right) + \varepsilon_{i''} i'' = 1, 2, 3\cdots n \tag{13}$$

Where, $f\left(\boldsymbol{P}_{clo,i''}\right)$ is the Gaussian process model, representing the true topographic height at the input point $P_{clo,i''}$; $\varepsilon_i \sim N(0, \sigma_n^2)$ epsilon is the independent and identically distributed Gaussian noise, with σ_n^2 as the noise variance.

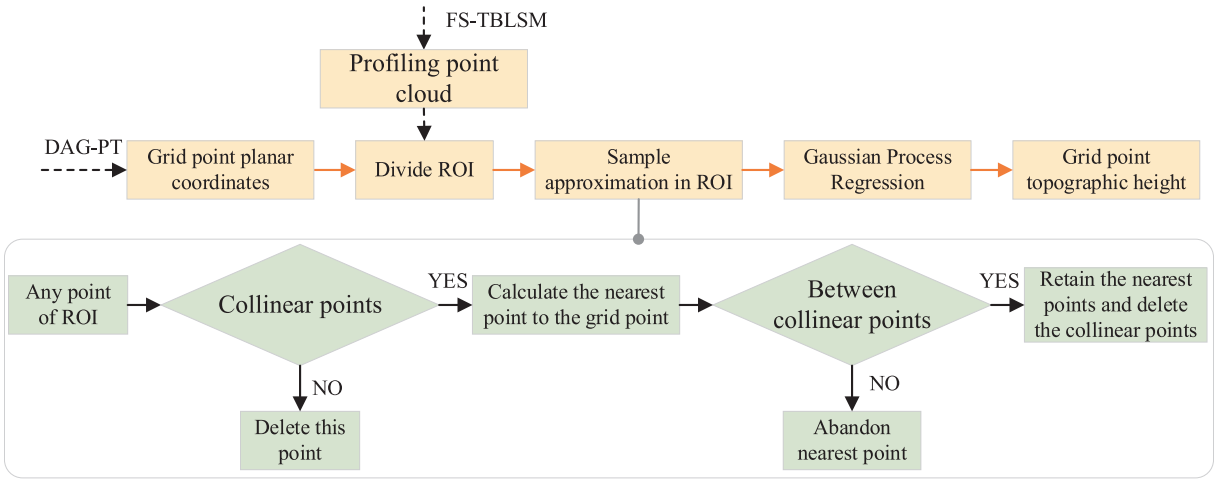

Fig. 8. SA-GPR algorithm flowchart.

From Eq. (13), it can be inferred that the output values $\boldsymbol{Z}_{clo}$ follow a multivariate Gaussian distribution.

$$\boldsymbol{Z}_{clo} \sim N\left(0, \boldsymbol{K}(\boldsymbol{P}_{clo}, \boldsymbol{P}_{clo}) + \sigma_n^2 \boldsymbol{I}\right) \tag{14}$$

where, $\boldsymbol{K}(\boldsymbol{P}_{clo}, \boldsymbol{P}_{clo})$ is the covariance matrix of the training samples, with its elements computed using the kernel function $k(\boldsymbol{P}_{clo,i''}, \boldsymbol{P}_{clo,j''})$; $\sigma_n^2 \boldsymbol{I}$ is the covariance matrix of the observation noise.

The radial basis function is well-suited for characterizing smooth and continuous topography (Hillier et al., 2014), which is consistent with the characteristics of the tillage bottom layer and field surface topography. The kernel function is defined as shown below.

$$k(\boldsymbol{P}_{clo,i''}, \boldsymbol{P}_{clo,j''}) = \sigma_f^2 \exp\left(-\frac{\left(X_{clo,i''} - X_{clo,j''}\right)^2 + \left(Y_{clo,i''} - Y_{clo,j''}\right)^2}{2l^2}\right) \tag{15}$$

where, σ_f^2 is the signal variance, and l is the length scale parameter.

This study optimizes the model parameters σ_f^2,σ_n^2 and l using maximum likelihood estimation.

For each grid point $G_{gri,t}(X_{gri,t}, Y_{gri,t})$, the function value $f(\boldsymbol{G}_{gri,t})$ and the topographic height of the training samples Z_{clo} follow a joint Gaussian distribution.

$$\begin{bmatrix} \boldsymbol{Z}_{clo} \\ f(\boldsymbol{G}_{gri,t}) \end{bmatrix} \sim N\left(0, \begin{bmatrix} \boldsymbol{K}(\boldsymbol{P}_{clo}, \boldsymbol{P}_{clo}) + \sigma_n^2 \boldsymbol{I} & \boldsymbol{k}(\boldsymbol{P}_{clo}, \boldsymbol{G}_{gri,t}) \\ \boldsymbol{k}(\boldsymbol{G}_{gri,t}, \boldsymbol{P}_{clo}) & k(\boldsymbol{G}_{gri,t}, \boldsymbol{G}_{gri,t}) \end{bmatrix}\right) \tag{16}$$

where, $\boldsymbol{k}(\boldsymbol{P}_{clo}, \boldsymbol{G}_{gri,t})$ and $\boldsymbol{k}(\boldsymbol{G}_{gri,t}, \boldsymbol{P}_{clo})$ are the covariance matrices between the training data and grid points; $k(\boldsymbol{G}_{gri,t}, \boldsymbol{G}_{gri,t})$ is the covariance scalar of the grid points.

According to the properties of the joint Gaussian distribution, the conditional distribution of the grid points is as shown below.

$$f(\boldsymbol{G}_{gri,t}) | \boldsymbol{P}_{clo}, \boldsymbol{Z}_{clo}, \boldsymbol{G}_{gri,t} \sim N\left(\mu(\boldsymbol{G}_{gri,t}), \sigma^2(\boldsymbol{G}_{gri,t})\right) \tag{17}$$

$$\mu(\boldsymbol{G}_{gri,t}) = \boldsymbol{k}(\boldsymbol{G}_{gri,t}, \boldsymbol{P}_{clo}) \left[\boldsymbol{K}(\boldsymbol{P}_{clo}, \boldsymbol{P}_{clo}) + \sigma_n^2 \boldsymbol{I}\right]^{-1} \boldsymbol{Z}_{clo} \tag{18}$$

$$\sigma^2(\boldsymbol{G}_{gri,t}) = k(\boldsymbol{G}_{gri,t}, \boldsymbol{G}_{gri,t}) - \boldsymbol{k}(\boldsymbol{G}_{gri,t}, \boldsymbol{P}_{clo}) \left[\boldsymbol{K}(\boldsymbol{P}_{clo}, \boldsymbol{P}_{clo}) + \sigma_n^2 \boldsymbol{I}\right]^{-1} \boldsymbol{k}(\boldsymbol{P}_{clo}, \boldsymbol{G}_{gri,t}) \tag{19}$$

Similarly, using the deepest tillage point from the optimized ROI as the observation sample, the SA-GPR algorithm estimates the topographic height (Z_{est}^B) of the tillage-bottom layer at each grid point. Let the estimated topographic height of the field surface be Z_{est}^C. The tillage depth is then given by the following equation.

Fig. 9. Test platform.

$$d_{til} = Z^C_{est} - Z^B_{est} \quad (20)$$

2.5. Accuracy verification test of the FS-TBLSM method

2.5.1. Test material

As shown in Fig. 9, the rotary tillage implement (Henan Haofeng Agricultural Equipment 230H) is powered by a tractor (Kubota M704KQ) and connected to the tractor via a three-point hitch. To adjust the pitch angle of the implement, a hydraulic cylinder is used instead of the traditional rigid upper link, and the cylinder is operated by controlling an electromagnetic valve using a display terminal. To install reflector prisms, two threaded rods are welded at the deepest tillage point and profiling point locations.

As shown in Fig. 10d, this study used a total station (Leica MS60, accuracy: 1 mm + 1.5 ppm) to measure the true coordinates of the deepest cutting point and profiling points (prism locations in Fig. 9) in the ENU. Prior to measurement, the total station was set up using proper procedures, including installation, atmospheric calibration, leveling, and stationing. During stationing, at least two high-precision control points are required.

2.5.2. Test method

As shown in Fig. 10, a validation test was conducted on a cement road at the Teaching and Research Base of South China Agricultural University. Five control points were placed within the test area (Fig. 10b). The coordinates of each control point were measured statically using a GNSS receiver (with 1-mi observation), and their average values were calculated (Fig. 10e). Notably, the height differences between the control points were rigorously calibrated. The coordinates of the control points are provided in Table 2. As shown in Fig. 10d, the total station sequentially targets the prisms, records the coordinates of each control point, and performs positioning based on the principle of rear intersection (position intersection), thereby completing the stationing.

Table 2
Coordinates of each control point.

Control point	Coordinate East (m)	North (m)	Height (m)
1	462986.7870	2571566.4891	25.1936
2	462976.4451	2571563.9702	25.1826
3	462944.9028	2571580.2009	25.3177
4	462934.6232	2571585.5347	25.3083
5	462926.3196	2571596.0860	25.3462

Table 3
The position vectors of the key points of the implement in the VCS.

Key point	Position vector X (m)	Y (m)	Z (m)
Primary antenna	0	0	0
Secondary antenna	1.1932	0.0000	−0.0008
Center point of rotating blade shaft	0.6735	\	−0.5754
Rotation point of tailboard	0.3953	\	−0.3755
Right deepest cutting point	\	−0.0202	\
Left deepest cutting point		1.9237	\
Right profiling point	\	−0.0051	\
Left profiling point	\	1.9948	\

Before the test, based on the geometric relationship of the rotary tillage implement, the motion radius d_B of the deepest cutting point was measured as 0.252 m, and the motion radius d_{RC} of the profiling point as 0.415 m. Table 3 lists the position vectors of the key points of the implement in the VCS.

The Y-axis value of the center point matches that of the deepest cutting point, and the Y-axis value of the rotation point matches that of the profiling point.

The tests were divided into two categories: static and dynamic.

(1) Static test.

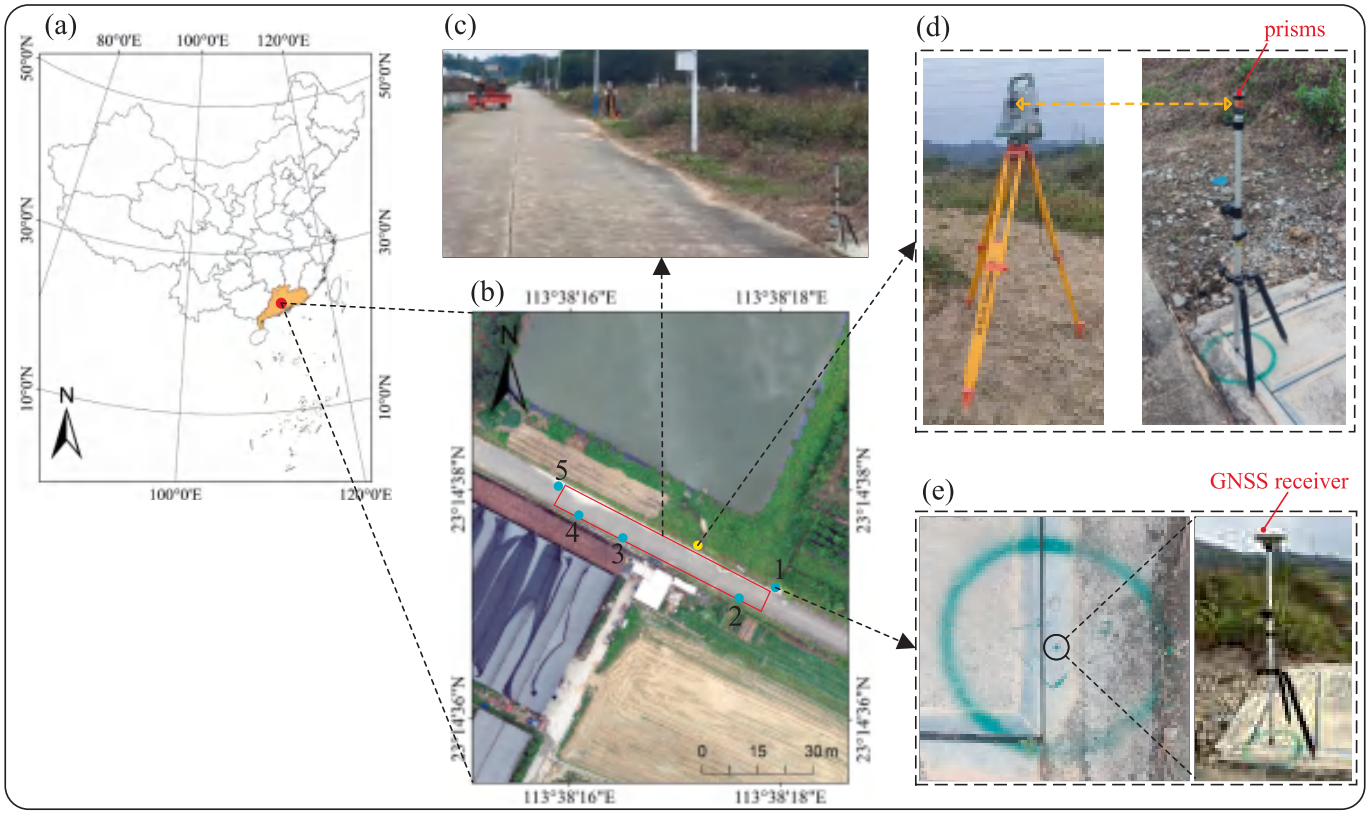

Fig. 10. Verification test site and method. (a) Test site; (b) Test area;(c) Test scenario; (d) Station; (e) Control point and its coordinate measurement method.

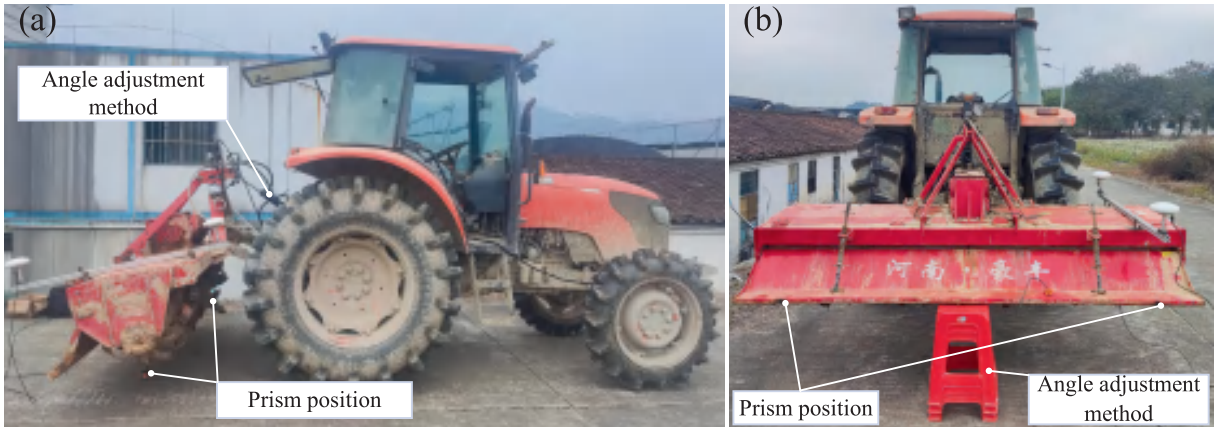

Fig. 11. Static test method. (a) Deepest cutting point; (b) profiling point.

As shown in Fig. 11, the measurement accuracy of the FS-TBLSM method was validated under different implement pitch angles and varying angles between the tailboard and frame. First, the pitch angle of the implement was adjusted by controlling the hydraulic cylinder via the display terminal, and the rotating blades were manually adjusted such that the threaded rod holding the prism was vertical (Fig. 11a). Similarly, the angle between the tailboard and frame was adjusted, and the prism was placed vertically at the profiling point (Fig. 11b). Subsequently, when the implement was completely stationary, its position and attitude information were collected. Finally, the coordinates of the prism were measured using a total station, representing the true coordinates of the deepest cutting point and the profiling point. During the test, five sets of implement pitch angles and tailboard–frame angles were used.

(2) Dynamic Test.

As shown in Fig. 12, the dynamic measurement accuracy of the FS-TBLSM method was validated. The prism was installed at either the deepest cutting point or the profiling point on the right side, and the true coordinates were obtained by dynamically tracking the prism using the total station. As the total station cannot track two prisms simultaneously, the true coordinates of only one point (either the deepest cutting point or the profiling point) were measured at a time. During the test, it was crucial to ensure that the line of sight between the prism and total station remained unobstructed by any objects.

Fig. 12. Dynamic test method.

2.6. Field test

2.6.1. Test material

The same test and data-acquisition platforms as those used in the validation test (Section 2.5.1) were employed for the field test.

2.6.2. Test method

As shown in Fig. 13c, according to the International System of Soil Texture Classification (ISSC), the soil in the test field is classified as sandy loam (Du et al., 2019). This is a rice soil formed by long-term seasonal rice cultivation. The test field is located in the subtropical monsoon climate zone, with an average annual temperature of 24 °C and average annual precipitation of 1891.9 mm. The field is heavily mechanized and typically subjected to rototilling rather than plowing. After several agricultural operations and wet-dry cycles, the soil became compacted. Prior to the test, the soil compaction was 1639.9 kPa, and the moisture content was 8.3 %. During the test, the rotary tiller operated at a speed of 1 m/s, and the position and attitude information of the implement was collected in real time.

After the operation, the true field surface topography height and tillage depth were measured. The method used for measuring the true topography is shown in Fig. 13d. The total station measured the true topography of the test area from two different positions, and the data from both measurements were combined. The method used for measuring the true tillage depth is shown in Fig. 13d and Fig. 13e. First, 20 measurement points were set up in the test area, and the field surface topography at each point was measured using the total station. Next, soil compaction at each measurement point was measured using a soil compaction meter (Spectrum Technologies SC 900), and the tillage depth at each point was roughly calculated using the Mann–Kendall test algorithm. Based on the calculated tillage depth, the tilled soil was removed until the untilled layer was reached, ensuring that the untilled layer remained undisturbed. Finally, the topographic height of the tillage bottom layer was measured using the total station, and the true tillage depth was calculated.

3. Results

3.1. Measurement accuracy of the FS-TBLSM method

3.1.1. Static measurement accuracy

The Wilcoxon signed-rank test was initially employed to analyze the errors in each axis and determine whether the measured values significantly deviate from the true values. Next, box plots of the errors in the X, Y, and Z axes were constructed to illustrate their distribution characteristics and reveal skewness and potential outliers. Finally, the maximum absolute error (MAE), average absolute error (AAE), and root

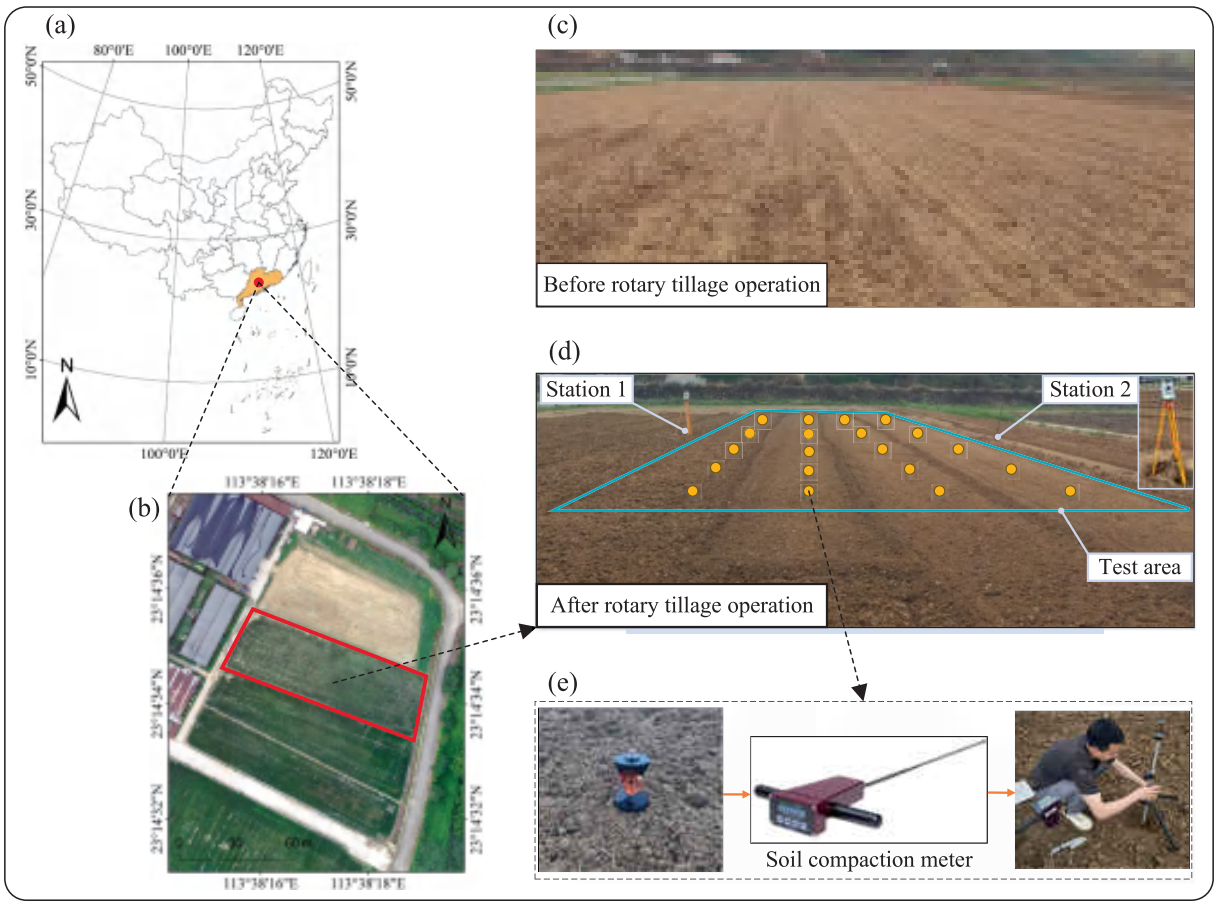

Fig. 13. Field test site and method. (a) Test site; (b) Test field;(c) Test scenario; (d) Topography measurement method and station setup; (e) Tillage depth measurement steps.

Table 4
Wilcoxon test results for static measurement.

Position	Axis	p-values
Right side of the deepest cutting point	X	1.000
	Y	0.125
	Z	0.313
Left side of the deepest cutting point	X	0.062
	Y	0.062
	Z	1.000
Right side of the profiling point	X	1.000
	Y	1.000
	Z	0.313
Left side of the profiling point	X	0.125
	Y	0.125
	Z	0.438

mean square error (RMSE) were used as precision evaluation metrics, and 95 % confidence intervals (CIs) were calculated for AAE and RMSE to quantify the variability of the measurement errors.

The results of the Wilcoxon test for the static measurement are presented in Table 4. The p-values in the X, Y, and Z axes exceed the 0.05 threshold for both the deepest cutting points and profiling points, indicating no significant differences between the measured and true values and that the measurement errors are within an acceptable range.

The distribution of measurement errors on the left and right sides of the deepest cutting points and profiling points is shown in Fig. 14. In the X-axis direction, the error distribution on the left is more concentrated and stable but exhibits a negative shift, with the median around −15 mm. On the right side, the error distribution is more symmetric, with most values concentrated between −10 and 10 mm. Additionally, the median is close to 0 mm, indicating higher measurement accuracy. In the Y-axis direction, the median error on the left is close to 10 mm, whereas the median on the right is slightly smaller. Errors on both sides are concentrated in the positive range, with no significant outliers. The error distribution along the Z axis has a broader range and exhibits more pronounced fluctuations than those along the X and Y axes. Overall, the errors on the left are significantly higher than those on the right, and the fluctuations in the Z-axis errors are slightly greater than those in the X and Y axes. This is primarily due to the misalignment between the X and Y axes of the VCS and the transverse and longitudinal directions of the equipment. The higher fluctuations are also attributed to the gaps between the components of the tillage equipment, which cause deviations in the mapping positions of the measurement points in the X–Z plane. Specifically, the left-side measurement points are farther from the VCS origin, making them more susceptible to error amplification during spatial transformation, resulting in larger errors on the left side. Additionally, the vertical accuracy of the GNSS receiver (1.5 cm + 1 ppm) is lower than its horizontal accuracy (0.8 cm + 1 ppm), which leads to higher measurement errors along the Z axis than along the X and Y axes.

Table 5 lists the measurement errors on both sides of the deepest cutting points and profiling points. For different positions and coordinate axes, the MAE for static measurements ranges from 6.3 mm to 25.6 mm, the AAE from 3.7 mm to 14.5 mm, and the RMSE from 4.1 mm to 15 mm. Due to differences in measurement accuracy between the vertical and horizontal directions of the GNSS sensor, the errors are slightly higher in the Z-axis direction than in the X- and Y-axis directions. Overall, the errors exhibit a narrow CI, indicating good measurement stability. In conclusion, the FS-TBLSM method demonstrates small measurement errors under static conditions, with reasonable CIs,

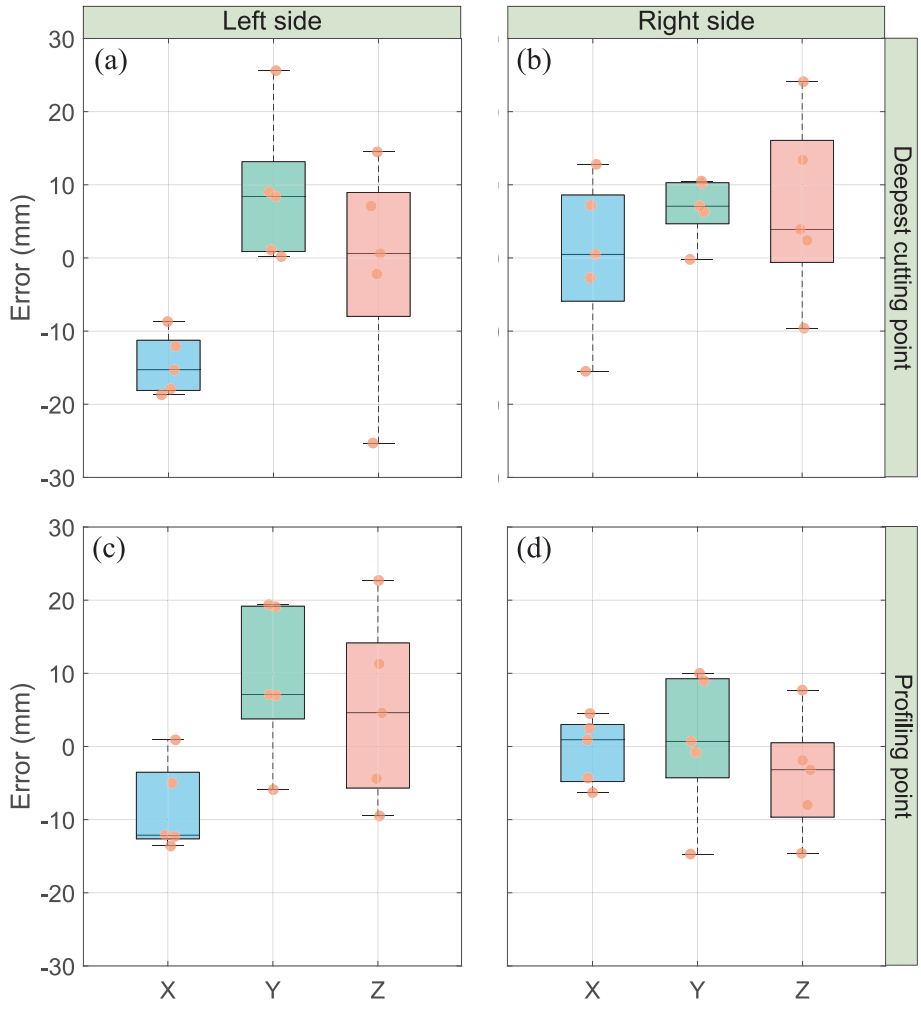

Fig. 14. Error distribution of static measurement. (a) Left side of the deepest cutting point; (b) Right side of the deepest cutting point; (c) Left side of the profiling point; (d) Right side of the profiling point.

Table 5
Static measurement error.

Position	Axis	MAE (mm)	AAE (mm, 95 %CI)	RMSE (mm, 95 %CI)
Right side of the deepest cutting point	X	15.5	7.7 (2.7, 12.7)	9.6 (3.7, 13.3)
	Y	10.5	6.8 (3.5, 9.7)	7.8 (5.1, 9.8)
	Z	24.1	10.7 (4.4, 18.1)	13.2 (5.2, 19.7)
Left side of the deepest cutting point	X	18.7	14.5 (11.3, 17.7)	15.0 (11.8, 17.7)
	Y	25.6	8.9 (2.0, 17.2)	12.7 (3.8, 20.2)
	Z	25.3	9.9 (2.5, 18.5)	13.5 (3.5, 20.4)
Right side of the profiling point	X	6.3	3.7 (1.9, 5.2)	4.1 (2.4, 5.6)
	Y	14.7	7.1 (2.4, 11.7)	8.9 (4.1, 12.2)
	Z	14.6	7.1 (3.4, 10.9)	8.4 (4.1, 11.9)
Left side of the profiling point	X	13.6	8.8 (4.0, 12.8)	10.1 (6.0, 12.8)
	Y	19.4	11.7 (6.6, 16.8)	13.2 (6.6, 17.6)
	Z	22.7	10.5 (5.5, 16.8)	12.4 (5.8, 18.4)

confirming its high measurement accuracy and reliability.

3.1.2. *Dynamic measurement accuracy*

Owing to the large sample size of the dynamic measurement data, hypothesis testing may amplify minor differences because of higher statistical power, potentially leading to conclusions that deviate from the actual situation. To accurately assess the deviation between the measured and true values, we plotted their trajectories across three dimensions—spatial, plane, and height—to analyze their trends. Next, box plots were constructed to illustrate the distribution characteristics of the errors. Finally, MAE, AAE, and RMSE were used as evaluation metrics for accuracy, and the 95 % CIs for AAE and RMSE were calculated to further quantify the stability and reliability of the measurement errors.

The collected data were processed using MATLAB R2023a. To enhance the readability of the results, the origin of the ENU coordinate system was shifted 462,900 m eastward and 2,571,500 m northward. The trajectories of the measured and true values for the deepest cutting points and profiling points in the spatial, plane, and height dimensions are shown in Fig. 15 and Fig. 16. The measured values of both the deepest cutting and profiling points are generally consistent with the true values in terms of the spatial motion trajectory. The measured values closely match the true values in terms of the plane trajectory, with their height trajectories also exhibiting consistent trends. However, the measured values of the deepest cutting points are consistently slightly higher than the true values, primarily due to centimeter-level fluctuations in the height data output by the GNSS receiver at different times.

The error distribution of the deepest cutting and profiling points along the X, Y, and Z coordinate axes is shown in Fig. 17. The error

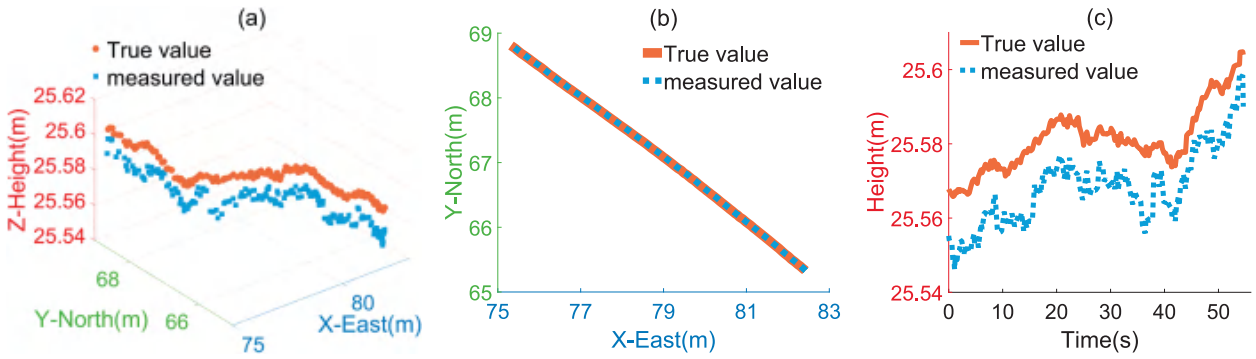

Fig. 15. Dynamic measurement results of the deepest cutting point; (a) Spatial trajectory; (b) Plane trajectory; (c) Height trajectory.

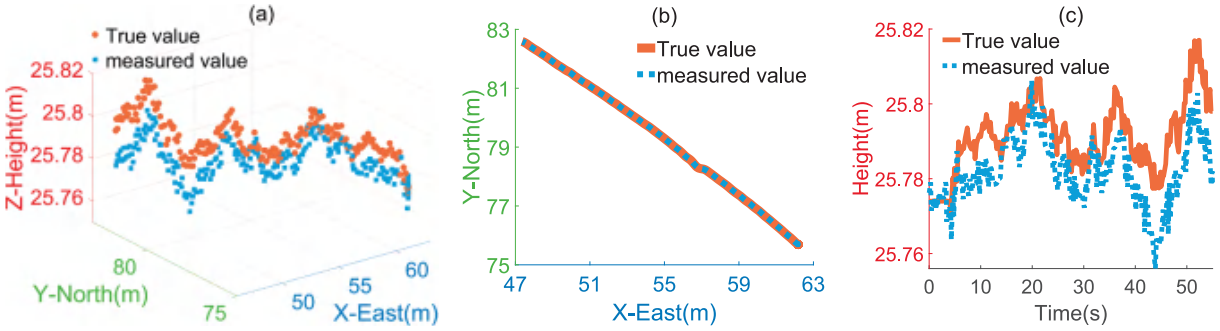

Fig. 16. Dynamic measurement results of the profiling point. (a) Spatial trajectory; (b) Plane trajectory; (c) Height trajectory.

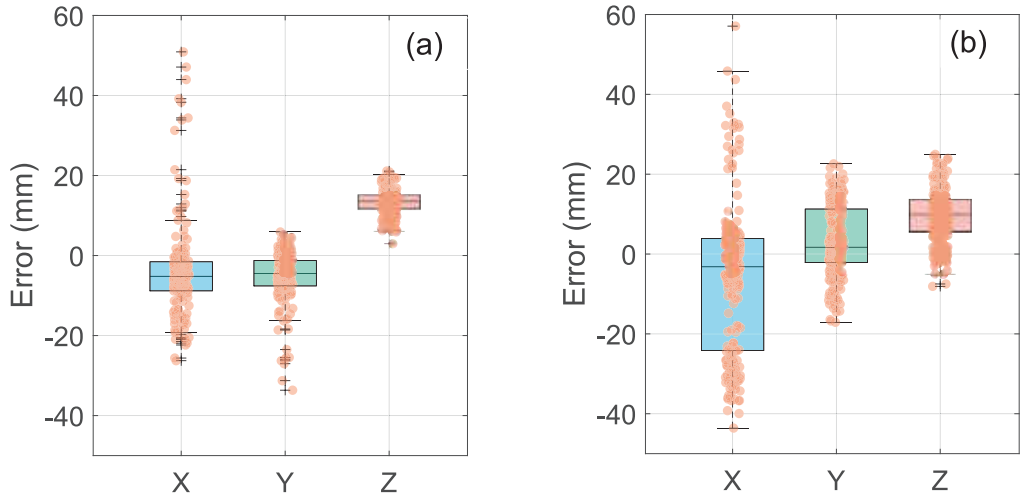

Fig. 17. Error distribution of dynamic measurement error. (a) Deepest cutting point; (b) Profiling point.

distribution in the X and Y directions is more symmetric and concentrated for the deepest cutting points than for the profiling points. Additionally, the errors primarily range from −10 mm to 0 mm, indicating minimal deviation between the measured and true values and high measurement accuracy. A narrow data-fluctuation range is observed in the Z direction, with the error distribution skewed toward positive values. The median is approximately + 15 mm, suggesting a systematic bias in the Z direction, though the overall measurement accuracy remains satisfactory. Compared to the deepest cutting points, the profiling points exhibit larger fluctuations in the X direction, with a negative error distribution and a wider range. However, most of the data points fall within the ±30 mm range. In the Y direction, the error distribution is more symmetric, with the median close to zero, and the box plot primarily concentrated between 0 and 15 mm. In the Z direction, the error distribution patterns are similar to that of the deepest cutting points, with both showing a positive bias and the median centered around +10 mm. Overall, the measurement accuracy meets the requirements for dynamic measurements. In summary, the error distribution for both the deepest cutting and profiling points is generally concentrated within the ±30 mm range, with medians below 20 mm. The medians for the X and Y directions are close to 0, while the median for the Z direction is approximately +15 mm, indicating good overall measurement accuracy.

To further quantify measurement accuracy, Table 6 provides a statistical analysis of the dynamic measurement errors for both points. Across different positions and coordinate axes, the AAE ranges from 6.1 mm to 14.5 mm, whereas the RMSE spans from 8.4 mm to 19.5 mm. As observed, all error values are below 20 mm. Moreover, the difference

Table 6
Dynamic measurement error.

Position	Axis	MAE (mm)	AAE (mm, 95 % CI)	RMSE (mm, 95 % CI)
The deepest cutting point	X	50.9	9.3 (8.09, 10.58)	12.8 (10.88, 14.63)
	Y	33.7	6.1 (5.24, 6.96)	8.4 (7.04, 9.74)
	Z	21.1	13.3 (12.87, 13.84)	13.7 (13.28, 14.23)
The profiling point	X	57.1	14.5 (12.72, 16.12)	19.5 (17.72, 21.01)
	Y	22.6	7.2 (6.49, 8.02)	9.3 (8.55, 10.10)
	Z	25.0	10.0 (9.25, 10.79)	11.7 (10.88, 12.39)

between the upper and lower limits of the CIs remains within approximately 2 mm. Therefore, the RMSEs for all measurement points in the X, Y, and Z directions remain low, with small fluctuations, indicating that the FS-TBLSM method ensures high dynamic tracking accuracy and provides reliable input for subsequent field topography and tillage-depth estimation.

3.1.3. Comparison of dynamic and static measurement errors

As shown in Fig. 18, an effect size analysis was performed to compare the differences between dynamic and static measurement errors and thereby assess the extent of the error differences under both measurement conditions.

The effect sizes of the errors in the X and Y axes are generally low for both dynamic and static measurements, indicating that accuracy values are consistent in the horizontal plane. However, at the deepest cutting point, a significantly larger negative effect size is observed in the Y-axis direction (Cohen's d = −1.89), suggesting that dynamic measurement errors are lower than the static errors. This phenomenon may be due to the specific operational procedures performed during static measurements: after measuring the coordinates of the deepest tillage point using the FS-TBLSM method, a prism was installed at the same position for true-value measurement. Due to the time gap between the two operations, the implement may experience slight lateral sway, introducing additional errors in the Y-axis direction. By contrast, during dynamic measurements, the positional changes of the implement are recorded during lateral swaying, with the measured and true values collected simultaneously. This approach ensures that a more accurate representation of lateral displacement is provided during actual operations, thereby demonstrating higher measurement stability and accuracy.

In addition, along the Z axis, both the deepest cutting and profiling points exhibited significant positive effect sizes (Cohen's d = 1.73 and 2.05, respectively), indicating that vertical dynamic measurement errors were considerably greater than static errors. This result aligns with the intrinsic limitations of the GNSS system, particularly its reduced vertical positioning accuracy under motion. Other possible contributing factors include multipath effects and signal instability.

3.2. Field test results

3.2.1. Field surface topography measurement accuracy

The true topography was compared with the FS-TBLSM-generated topography to evaluate their agreement. Next, the height of the profiling points predicted by FS-TBLSM was compared with the height of the nearest true points (reference points). Finally, the accuracy and stability of the FS-TBLSM-predicted topographic heights were assessed in terms of AAE and RMSE, along with their corresponding 95 % CIs.

As shown in Fig. 19, the origin of the ENU coordinate system was shifted 462,900 m eastward and 2,571,400 m northward. Subsequently, the true and measured topographic point clouds were color-rendered based on height and then merged for visual comparison. The topographic heights measured using the FS-TBLSM method are slightly lower than the true values. According to the color distribution, the variation patterns of the measured topographic height are consistent with those of the true values, with the areas of variation closely aligning with those of the true values.

The accurate measurement of topographic height is a primary concern in agricultural operations. As shown in Fig. 20, the topographic height of the measured points is compared with that of their nearest true points (reference points), with a horizontal distance of no more than 2 mm between them. The height variation trends in the two datasets are highly consistent, and most measurement errors are within 30 mm. Statistical analysis shows an AAE of 18.13 mm (95 % CI: 16.81–19.33 mm) and an RMSE of 20.58 mm (95 % CI: 19.41–21.60 mm), demonstrating that the FS-TBLSM method provides reliable measurement accuracy.

3.2.2. The impact of grid spacing on the accuracy of the SA-GPR algorithm

As the test site was a small-scale farmland and the main agricultural machinery used had an operational width of 2 m, a grid spacing of 2 m × 2 m was selected to provide more representative input data for subsequent processing. Subsequently, the grid-point heights estimated using the SA-GPR algorithm were compared with those of the nearest true

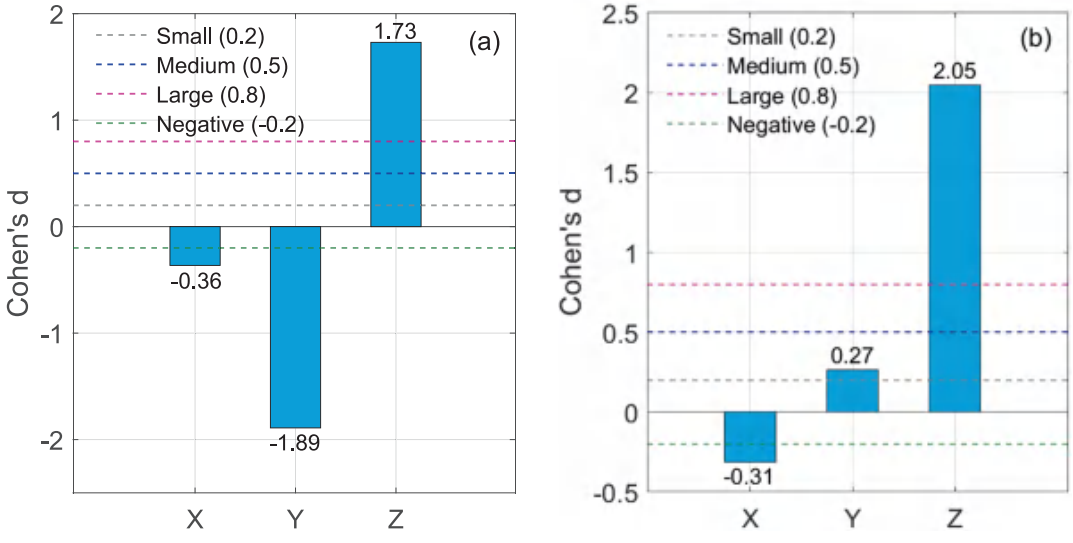

Fig. 18. Effect size of dynamic and static errors. (a) Deepest cutting point; (b) Profiling point.

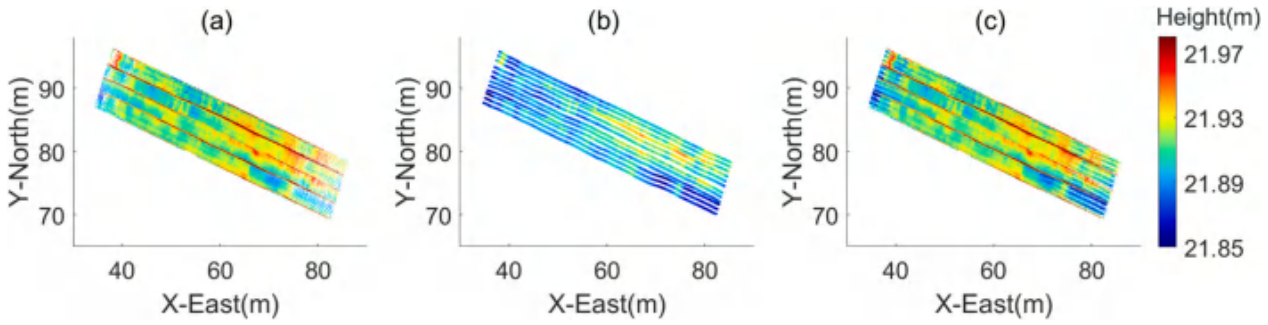

Fig. 19. Comparison of true and measured topography. (a) True topography; (b) Measured topography; (c) Merged topography.

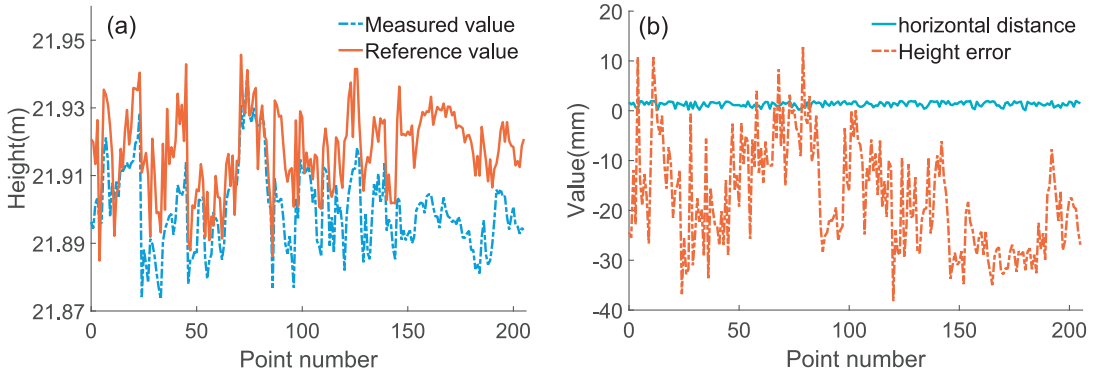

Fig. 20. Measurement accuracy of surface topographic height. (a) Measured and reference values; (b) Height measurement error.

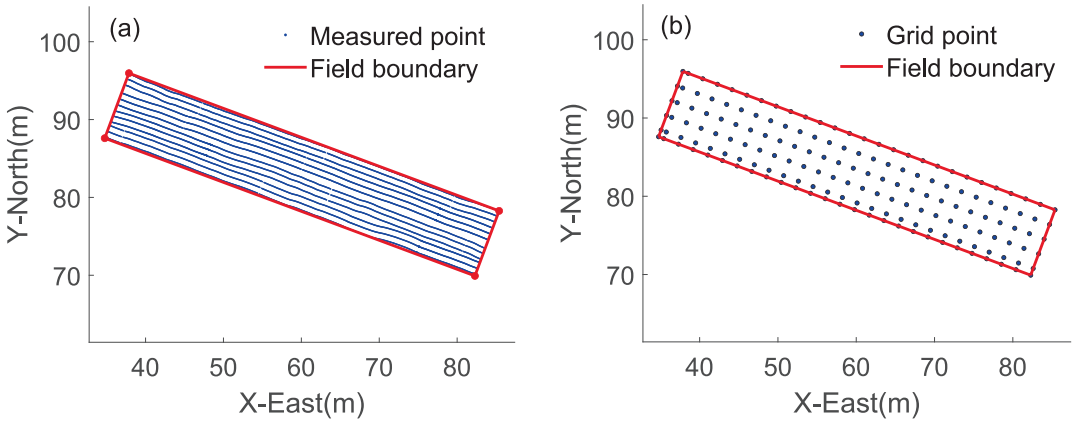

Fig. 21. Directional adaptive gridding method in plane topography; (a) Extraction of field boundary; (b) Grid point distribution.

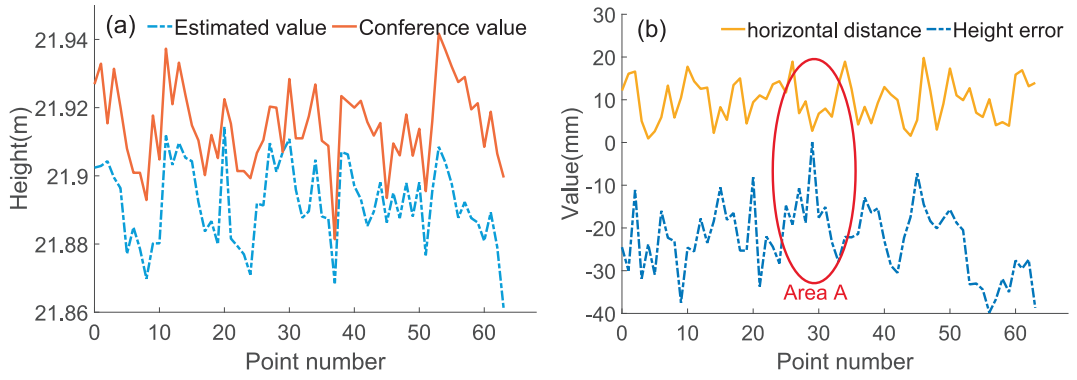

Fig. 22. Estimation results of the grid points surface topographic heights; (a) Estimated and reference values; (b) Height error.

points (reference points). Finally, three grid spacings—1 m × 1 m, 2 m × 2 m, and 3 m × 3 m—were used, and the corresponding AAE and RMSE were measured, along with their 95 % CIs, to evaluate the effect of grid resolution on the estimation accuracy of the SA-GPR algorithm.

As shown in Fig. 21, using the measured topographic points, the long-side direction of the field is determined, the field boundary extracted, and the field rasterized. Grid points are distributed along the long and short sides of the field, with the spacing between adjacent points (excluding boundary points) set to 2 m.

As shown in Fig. 22, with the known planar coordinates of the grid points, the SA-GPR algorithm was used to estimate their topographic heights. The estimated values were then compared with the topographic heights of their nearest true counterparts (reference points). As shown in Fig. 22a, the estimated height closely follows the trends of the reference curve, indicating a high degree of agreement. However, the horizontal distance between the grid and reference points can affect estimation accuracy. As illustrated in Area A of Fig. 22b, the estimation error decreases as this distance decreases, providing preliminary evidence supporting the accuracy of the SA-GPR algorithm in topographic height estimation.

As shown in Table 7, the estimation accuracy was statistically analyzed across different grid spacings. Although the error metrics (AAE and RMSE) exhibited slight variations across the 1 m × 1 m, 2 m × 2 m, and 3 m × 3 m grids, the overall differences were minimal, with substantial overlap in their 95 % CIs. For example, the maximum AAE was 22.71 mm (2 m × 2 m), whereas the minimum was 20.99 mm (1 m × 1 m), yielding a difference of approximately 1.7 mm. Similarly, the maximum difference in RMSE did not exceed 1.5 mm, and the CI ranges were also comparable for all grid spacings. These findings indicate that the estimation performance of the SA-GPR algorithm is largely insensitive to grid spacing. Even at a larger grid size (e.g., 3 m × 3 m), the SA-GPR algorithm exhibited consistent estimation accuracy and stability. Therefore, the SA-GPR method demonstrates strong adaptability for practical applications and allows the flexible adjustment of grid spacing based on operational requirements.

3.2.3. The estimation accuracy of topographic height and tillage depth

To further evaluate the accuracy of the SA-GPR algorithm, the known planar coordinates of 20 sampling points were used as inputs to estimate topographic height and tillage depth. First, the measured and true values of topographic height and tillage depth were visualized, along with their corresponding error variation curves. Subsequently, MAE, AAE, and RMSE were used as evaluation metrics. Additionally, the 95 % CIs of AAE and RMSE were calculated to quantify the accuracy and stability of the estimates under field conditions.

As shown in Fig. 23a, the estimated topographic height closely follows the trends of the true curve, with errors remaining within 30 mm. Similarly, as shown in Fig. 23b, the estimated tillage depth closely follows the trends of the true curve, with most errors within 20 mm.

Table 8 lists the estimation accuracy obtained for topographic height and tillage depth.

The results indicate that both the AAE and RMSE values are below 20 mm, confirming the high accuracy of the SA-GPR algorithm. The accuracy of topographic height and tillage depth is collectively affected by GNSS measurement errors, the FS-TBLSM method, and the SA-GPR algorithm. Notably, the estimation error is slightly lower for tillage depth than for topographic height, perhaps because tillage depth represents the relative vertical distance between the bottom of the tillage layer and the field surface, thereby mitigating the influence of GNSS errors. Moreover, the 95 % CIs of AAE and RMSE largely overlap for both variables, further confirming the applicability and stability of the algorithm across diverse surface parameters. Overall, the SA-GPR algorithm delivers reliable accuracy and robustness in estimating topographic height and tillage depth.

Table 7
Estimation accuracy under different grid spacings.

Grid spacing	AAE (mm, 95 %CI)	RMSE (mm, 95 %CI)
1 m × 1 *m*	20.99 (19.75, 22.20)	22.73 (21.54, 23.89)
2 m × 2 *m*	22.71 (20.84, 24.84)	24.13 (22.31, 26.18)
3 m × 3 *m*	21.14 (17.57, 25.21)	23.33 (19.74, 27.02)

4. Discussion

4.1. Comparison of measurement methods

Table 9 lists the main methods for field surface topography and tillage depth measurement are listed.

Field surface topography measurement methods are primarily classified into remote sensing and vehicle-based types. In terms of accuracy, remote sensing methods are susceptible to factors such as light, wind speed, and flight altitude, which typically result in lower measurement accuracy compared to vehicle-mounted methods. The RMSE of existing vehicle-mounted measurement methods is generally below 20 mm, while the RMSE of the method proposed in this study is 17.95 mm, demonstrating comparable accuracy. This method can be used to accurately calculate the base height and earthwork before leveling operations and to develop a reasonable leveling path, satisfying the requirement for leveling accuracy of less than 30 mm. Regarding cost, remote sensing methods typically require multiple sensors to be mounted on drone platforms, leading to higher hardware costs. High operational efficiency is achieved with such systems, making them suitable for large-scale farmland and contributing to a reduction in overall operational costs. In contrast, vehicle-mounted measurement methods are mostly integrated into land leveling machinery, with lower hardware costs but lower operational efficiency. Before leveling operations, it is necessary to traverse the entire field, increasing labor, energy, and time costs. By comparison, the method proposed in this study uses a rotary tiller as the platform, enabling topographic measurement to be performed simultaneously with tillage, incurring virtually no additional operational cost.

Tillage depth measurement methods are primarily divided into contact and non-contact types. In terms of accuracy, non-contact methods are influenced by factors such as soil moisture, temperature, field residue, and uneven field surface (Zhu et al., 2024), leading to lower and unstable measurement accuracy. In contrast, contact methods offer more stable and accurate results. However, tillage depth is defined as the vertical distance between the deepest cutting point and the field surface. Existing tillage depth measurement methods have vertical alignment errors. For instance, Lou et al. (2021) reported errors of up to 500 mm, with other methods potentially showing even larger errors. The tillage depth measurement accuracy based on the rotary tiller platform can reach 10.80 mm (Ma et al., 2024). This method uses GNSS receivers to measure the same location before and after tillage to obtain the true tillage depth. However, the measurement accuracy of GNSS equipment is limited, and changes in the field surface topography after tillage can also introduce measurement errors. Additionally, this method requires multiple sensors and adds a contour structure, making the operation complex and costly. The tillage depth measurement method proposed in this study has an RMSE of 16.49 mm, with no vertical alignment errors, and the true tillage depth is measured by a total station, ensuring the reliability of accuracy quantification. Furthermore, it is simple to operate and cost-effective. Supported by topographic height and tillage depth measurement accuracy, this method can provide guidance for active control of crop sowing depth. Traditional depth control relies on contour structures, but after tillage, the soil becomes loose, and the contour structure produces varying compression depths under different soil depths, preventing the sowing depth from reaching the expected value.

The method proposed in this study allows for the measurement of field surface topography and tillage depth in a single operation, while

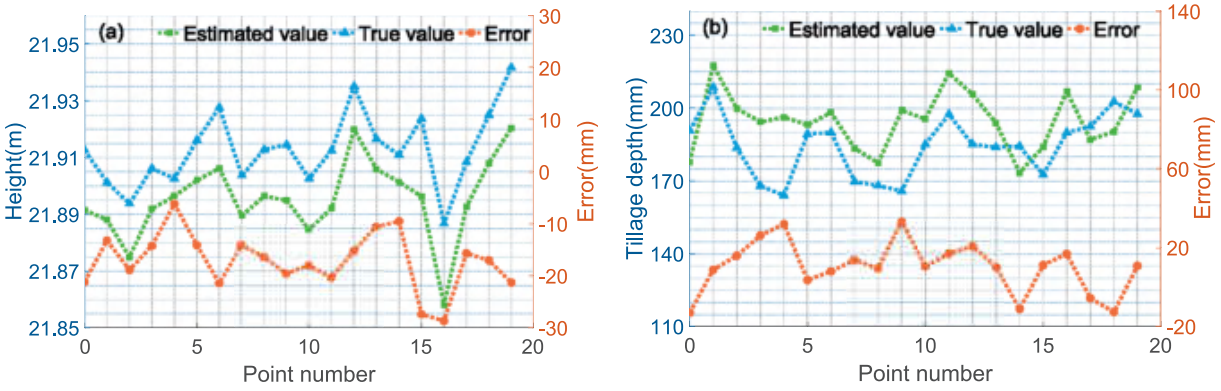

Fig. 23. Topographic height and tillage depth estimation results for 20 points; (a) Topographic height estimation error; (b) Tillage depth estimation error.

Table 8
Estimation accuracy of topographic height and tillage depth.

	AAE (mm, 95 %CI)	RMSE (mm, 95 %CI)
Topographic height	17.13 (15.12, 19.35)	17.95 (15.91, 20.11)
Tillage depth	14.52 (11.27, 17.99)	16.49 (12.26, 20.37)

existing measurement methods require separate operations. Completing mapping in one operation can reduce the number of field operations by 50 %, and save an estimated 15.57 kg/ha in fuel consumption. Additionally, it can reduce the depth of wheel tracks by 5–10 % (Botta et al., 2009), effectively reducing the risk of soil compaction caused by repeated machinery passes. Overall, the integrated measurement method proposed in this study offers accuracy comparable to existing methods, reduces redundant sensors and operational complexity, and maximizes data acquisition efficiency, providing good economic potential and prospects for wider application.

4.2. Advantages of integrated measurement method

4.2.1. Advantages of the FS-TBLSM method

The FS-TBLSM method uses GNSS and AHRS sensors, which are mounted on the frame and tailboard, respectively. Neither sensor comes into contact with the soil, ensuring that the devices remain unaffected by different soil textures and field conditions with residue cover. Additionally, this method considers the kinematic behaviors, such as sinking and posture changes, that may occur with rotary tillage machinery under varying soil conditions. Furthermore, the effects of the machinery's pitch angle and the angle between the frame and tailboard on the measurement of the deepest cutting point and profiling point are specifically analyzed. Static validation tests were conducted with varying pitch angles (–10.1° – 12.5°) and angles between the tailboard and frame (20.5° – 55.2°). The results show that this method offers good accuracy and is applicable to field environments with varying slopes. In summary, this method is theoretically suitable for field environments with different soil textures, moisture levels, and slopes.

4.2.2. Advantages of the DAG-PT method

Grid-based field operations, as the primary approach, enhance operational efficiency and quality, optimize resource utilization, and facilitate precision field management (Karunathilake et al., 2023). Compared to uniform gridding, the DAG-PTM method proposed in this study offers the following advantages:

(1) The grid distribution aligns with the long side of the field, ensuring consistency with the travel direction of the machinery. For instance, in leveling operations, after estimating the topographic height at grid points, the excavation and filling volumes for each grid can be calculated. During leveling, the cumulative volume of soil moved can be estimated to determine whether the implement is in an empty or full load state, providing precise information for intelligent planning of subsequent operations.
(2) The grid interval can be adjusted according to the type of subsequent operation. Specifically, the interval along the short side of the field is set based on the working width, while the interval along the long side is adjusted according to the operation type. For example, in leveling operations, the interval along the long side can be set according to the working width, as leveling operations often involve movement along the short side of the field. This facilitates the accurate calculation of the soil moved. For planting operations, the interval along the long side can be set

Table 9
Field surface topography and tillage depth measurement methods.

Object	method	Platform	Sensors	Height accuracy	References
Field surface topography	vehicle-based	Dry-land leveling machinery	GNSS, AHRS	Flatness improved by an average of 12.811 %	Jing et al. (2019)
		Dry-land leveling machinery	GNSS, IMU, displacement sensor	RMSE = 16.5 mm	Wang et al. (2023)
		Rice transplanter	GNSS, AHRS	RMSE = 14.9 mm	Tu et al. (2023)
	remote sensing	DJI M600 PRO UAV	LiDAR, GNSS, IMU	The average value of the flatness accuracy is 91.73 %	Jin et al. (2021)
		Six-rotor UAV	LiDAR, GNSS, MEMS	Average RMSE = 38.5 mm	Du et al. (2022)
Tillage depth	Non-contact type	Subsoiling shovel	Ultrasonic sensor	Standard deviation = 31.82 mm	Lou et al. (2021)
	Contact type	Subsoiling shovel with parallelogram and ground wheel	Ultrasonic sensor	Average RMSE = 7.7 mm	Niu et al. (2016)
		Rotary tiller with copying mechanism	Tilt sensors (4 units), GNSS	Average RMSE = 10.8 mm	Ma et al. (2024)
		Subsoiling shovel with swing arm and ground wheel	Optical encoder	RMSE = 10.38 mm	Jia et al. (2016)

based on plant spacing, enabling active control of sowing depth based on topographic height and tillage depth information.

In summary, the grid direction and interval settings are tailored to the operational characteristics, enabling more precise work. Compared to conventional grid methods, the DAG-PTM method provides greater flexibility and accuracy.

4.2.3. Advantages of the SA-GPR algorithm

Tillage operations can shape both field surface and tillage bottom-layer topography, with the topography exhibiting both linear and nonlinear characteristics. Kriging interpolation typically relies on large datasets, but its estimation accuracy decreases when the data is sparse or irregular. While the FS-TBLSM method can generate large datasets, it also increases computational load and complexity. Gaussian Process Regression (GPR), a non-parametric regression method based on Bayesian probability theory, is well-suited for handling complex data distributions. GPR offers significant advantages in addressing nonlinear relationships and small datasets (Zhang et al., 2024). This study proposes the SA-GPR algorithm, which defines a Region of Interest (ROI) and, based on spatial collinearity principles, approximates the point cloud within the ROI to the grid points to be estimated. This approach maximizes data reduction within the ROI while maintaining accuracy. By leveraging GPR's characteristics, the algorithm estimates the heights of grid points with high precision using minimal data. In summary, the SA-GPR algorithm reduces computational complexity while ensuring estimation accuracy.

4.3. Limitations and future work

This study has several limitations that need to be clearly defined, along with corresponding future research directions, as detailed below.

(1) The integrated measurement method proposed in this study relies on positioning information from GNSS receivers. The inherent characteristics of GNSS result in centimeter-level errors in height output. Additionally, GNSS signals may experience reduced accuracy due to interference from obstructions or multipath reflections, affecting measurement precision. Therefore, future research could incorporate V2X correction or local RTK differential stations and explore multi-sensor fusion methods in weak signal environments to ensure the stability and accuracy of the method in various scenarios.
(2) This study obtains the positioning and attitude information of the machinery by installing GNSS and AHRS sensors. However, sensor installation may involve deviations, and the coordinates of key points on the implement in the VCS must be manually measured, which could lead to a loss of measurement accuracy. Moreover, this study is based on a single model of rotary tillage implement and does not account for the differences in key point positions across different types of rotary tillage machines, limiting its reproducibility. Therefore, during agricultural machinery manufacturing, sensor installation positions should be precisely designed, and precision machining technologies should be used to provide high-accuracy coordinate information for key points, further improving measurement accuracy and applicability.
(3) Although the SA-GPR algorithm can reduce computational load and complexity to some extent, the computational requirements during its integrated deployment have not been quantified. Future research could clarify the hardware requirements necessary to support this algorithm.
(4) This method is theoretically suitable for different soil types and slope scenarios, but its applicability needs further validation in practical applications.

5. Conclusion

This study proposed the FS-TBLSM method, combined with the DAG-PT method and the SA-GPR algorithm, to achieve integrated measurement of field surface topography and tillage depth. The accuracy of these methods was evaluated through verification and field tests. The verification results showed that the FS-TBLSM method achieved static RMSEs of less than 15.00 mm along all three axes, with dynamic RMSEs below 20.00 mm, confirming the effectiveness of the FS-TBLSM method and its good dynamic tracking capability. Further field test results indicated that the field surface topography measured using the FS-TBLSM method aligned with the true topography. Using true surface topographic height and tillage depth at 20 points as references, an AAE and RMSE of 17.13 and 17.95 mm, respectively, were obtained for surface topographic height estimation; estimated tillage depth exhibited an AAE and RMSE of 14.52 and 16.49 mm, respectively. These results demonstrate that the SA-GPR algorithm can accurately estimate the field surface topography height and tillage depth after rotary tillage operations. The measurement accuracy of field surface topography and tillage depth in this study is comparable to existing methods, while reducing the number of field operations by 50 %, and saving an estimated 15.57 kg/ha in fuel consumption. This study provides key inputs for leveling operations, including setting the base height, calculating earthwork volume, and planning paths. It also offers inputs for the active control of seeding depth and references for yield assessment. In the future, GNSS positioning accuracy can be improved through signal enhancement and multisensor fusion technologies. Additionally, further testing of applicability under different rotary tillage machines, soil textures, and slope conditions can be conducted during implementation.

CRediT authorship contribution statement

Gaolong Chen: Writing – review & editing, Writing – original draft, Visualization, Validation, Methodology, Investigation, Formal analysis, Data curation, Conceptualization. **Yuqi Chen:** Visualization, Validation, Software, Investigation. **Zhicheng Huang:** Validation, Software, Investigation. **Jingting Wang:** Validation, Software, Investigation. **Yufei Deng:** Validation, Software, Investigation. **Pei Wang:** . **Runmao Zhao:** Writing – review & editing, Methodology, Formal analysis, Conceptualization. **Lian Hu:** Writing – review & editing, Supervision, Methodology, Formal analysis, Conceptualization.

Declaration of competing interest

The authors declare that they have no known competing financial interests or personal relationships that could have appeared to influence the work reported in this paper.

Acknowledgments

This study was financially supported by the National Natural Science Foundation of China (32472016, 32101623).

Appendix A. Supplementary data

Supplementary data to this article can be found online at https://doi.org/10.1016/j.compag.2025.111000.

Data availability

Data will be made available on request.

References

Arvidsson, J., Westlin, A., Sörensson, F., 2013. Working depth in non-inversion tillage—effects on soil physical properties and crop yield in swedish field

experiments. Soil Tillage Res. 126, 259–266. https://doi.org/10.1016/j.still.2012.08.010.
Botta, G.F., Becerra, A.T., Tourn, F.B., 2009. Effect of the number of tractor passes on soil rut depth and compaction in two tillage regimes. Soil Tillage Res. 103 (2), 381–386. https://doi.org/10.1016/j.still.2008.12.002.
Chen, G., Hu, L., Luo, X., Wang, P., He, J., Huang, P., Zhao, R., Feng, D., Tu, T., 2024. A review of global precision land-leveling technologies and implements: current status, challenges and future trends. Comput. Electron. Agric. 220, 108901. https://doi.org/10.1016/j.compag.2024.108901.
Du, M., Li, H., Roshanianfard, A., 2022. Design and experimental study on an innovative uav-lidar topographic mapping system for precision land levelling. Drones-Basel 6 (12), 403. https://doi.org/10.3390/drones6120403.
Du, P., Luo, H., He, J., Mao, T., Du, B., Hu, L., 2019. Different tillage induces regulation in 2-acetyl-1-pyrroline biosynthesis in direct-seeded fragrant rice. Bmc Plant Biol. 19 (1). https://doi.org/10.1186/s12870-019-1913-9.
Gewers, F.L., Ferreira, G.R., Arruda, H.F.D., Silva, F.N., Comin, C.H., Amancio, D.R., Costa, L.D.F., 2022. Principal component analysis. Acm Comput. Surv. 54 (4), 1–34. https://doi.org/10.1145/3447755.
Gong, D., Dai, G., Chen, Y., Yu, G., 2023. Optimal tillage depths for enhancing rice yield, quality and lodging resistance in the rice production systems of northeast China. PeerJ 11, e15739. https://doi.org/10.7717/peerj.15739.
Han, J., Yan, X., Tang, H., 2023. Method of controlling tillage depth for agricultural tractors considering engine load characteristics. Biosyst. Eng. 227, 95–106. https://doi.org/10.1016/j.biosystemseng.2023.01.011.
Hillier, M.J., Schetselaar, E.M., de Kemp, E.A., Perron, G., 2014. Three-dimensional modelling of geological surfaces using generalized interpolation with radial basis functions. Math. Geosci. 46 (8), 931–953. https://doi.org/10.1007/s11004-014-9540-3.
Huang, S., Islam, M.U., Jiang, F., 2023. The effect of deep-tillage depths on crop yield: a global meta-analysis. Plant Soil Environ. 69 (3), 105–117. https://doi.org/10.17221/373/2022-PSE.
Janulevičius, A., Šarauskis, E., Čiplienė, A., Juostas, A., 2019. Estimation of farm tractor performance as a function of time efficiency during ploughing in fields of different sizes. Biosyst. Eng. 179, 80–93. https://doi.org/10.1016/j.biosystemseng.2019.01.004.
Jat, M.L., Singh, Y., Gill, G., Sidhu, H., Aryal, J.P., Stirling, C., Gerard, B., 2015. Laser assisted precision land leveling: Impacts in irrigated intensive production systems of South Asia. Advances in soil science 323–352.
Jia, H., Guo, M., Yu, H., Li, Y., Feng, X., Zhao, J., Qi, J., 2016. An adaptable tillage depth monitoring system for tillage machine. Biosyst. Eng. 151, 187–199. https://doi.org/10.1016/j.biosystemseng.2016.08.022.
Jia, H., Wang, L., Li, C., Tan, H., Ma, C., 2010. Combined stalk–stubble breaking and mulching machine. Soil Tillage Res. 107 (1), 42–48. https://doi.org/10.1016/j.still.2010.02.002.
Jin, Z., Jing, Y., Liu, G., 2021. Farmland leveling topography measurement method based on uav lidar. Trans. Chinese Soc. Agric. Mach. 52 (S1), 51–57. https://doi.org/10.6041/j.issn.1000-1298.2021.S0.007.
Jing, Y., Liu, G., Jin, Z.K., 2019. Topographic survey of farmland based on GNSS dual antenna combined with ahrs. Trans. Chinese Soc. Agric. Eng. 35 (21), 166–174. https://doi.org/10.11975/j.issn.1002-6819.2019.21.020.
Jing, Y., Liu, G., Luo, C., 2021. Path tracking control with slip compensation of a global navigation satellite system based tractor-scraper land levelling system. Biosyst. Eng. 212, 360–377. https://doi.org/10.1016/j.biosystemseng.2021.11.010.
Jing, Y., Luo, C., Liu, G., 2022. Multiobjective path optimization for autonomous land levelling operations based on an improved Moea/d-aco. Comput. Electron. Agric. 197, 106995. https://doi.org/10.1016/j.compag.2022.106995.
Karunathilake, E.M.B.M., Le, A.T., Heo, S., Chung, Y.S., Mansoor, S., 2023. The path to smart farming: innovations and opportunities in precision agriculture. Agriculture 13 (8), 1593. https://doi.org/10.3390/agriculture13081593.
Kühl, N., Fischer, H., Hinze, M., Rung, T., 2024. An incremental singular value decomposition approach for large-scale spatially parallel & distributed but temporally serial data – applied to technical flows. Comput. Phys. Commun. 296, 109022. https://doi.org/10.1016/j.cpc.2023.109022.
Lou, S., He, J., Lu, C., Liu, P., Li, H., Zhang, Z., 2021. A tillage depth monitoring and control system for the independent adjustment of each subsoiling shovel. Actuators 10 (10), 250. https://doi.org/10.3390/act10100250.
Ma, R., Wei, L., Zhao, B., Zhou, L., Liu, Y., Xing, G., 2024. Research on rotary tillage depth detection based on multi-sensor data fusion. Trans. Chinese Soc. Agric. Machinery 55 (9), 52–64. https://doi.org/10.6041/j.issn.1000-1298.2024.09.004.
Miao, Q., Gonçalves, J.M., Li, R., Gonçalves, D., Levita, T., Shi, H., 2021. Assessment of precise land levelling on surface irrigation development. Impacts on maize water productivity and economics. Sustainability 13 (3), 1191. https://doi.org/10.3390/su13031191.
Nadimi, M., Sun, D., Paliwal, J., 2021. Recent applications of novel laser techniques for enhancing agricultural production. Laser Phys. 31 (5). https://doi.org/10.1088/1555-6611/abebda.
Niu, K., Yuan, Y., Zhang, J., Wang, F., Liu, Y., Fang, X., Cheng, H., 2016. Design Optimization and Performance Evaluation of a Tillage Depth Precision Measurement System. In: International Conference on Computer and Computing Technologies in Agriculture. Springer International Publishing, Cham, pp. 236–245. https://doi.org/10.1007/978-3-030-06155-5_23.
Rezaei-Moghaddam, K., Far, S.T., 2019. The impact assessment of technologies diffusion: a mixed methods analysis. Chem. Biol. Technol. Agric. 6 (1). https://doi.org/10.1186/s40538-019-0162-3.
Tao, W., Chen, B., Yang, X., Guo, B., Xu, W., Ke, S., Huang, S., 2025. Design and experimental study of tillage depth control system for electric rotary tiller based on ladrc. Sci. Rep. 15 (1). https://doi.org/10.1038/s41598-025-86283-6.
Tu, T., He, J., Luo, X., Hu, L., Wang, P., Chen, G., Tian, L., Feng, D., Wang, Z., Man, Z., Li, W., Wei, Z., Peng, J., Yi, Y., Wu, P., 2023. Methods and experiments for collecting information and constructing models of bottom-layer contours in paddy fields. Comput. Electron. Agric. 207, 107719. https://doi.org/10.1016/j.compag.2023.107719.
Wang, P., Feng, D., Chen, G., He, J., Hu, L., Peng, J., 2023. Real-time 3D terrain measurement method and experiment in farmland leveling. Trans. Chinese Soc. Agric. Mach. 54 (3), 42–48. https://doi.org/10.6041/j.issn.1000-1298.2023.03.004.
Westlund, H., 2013. A brief history of time, space, and growth: waldo Tobler's first law of geography revisited. Ann. Reg. Sci. 51 (3), 917–924. https://doi.org/10.1007/s00168-013-0571-3.
Zhang, W., Chen, X., Qi, J., Zhou, J., Li, N., Wang, S., 2024. Deep learning and gaussian process regression basedpath extraction for visual navigation under canopy. Trans. Chinese Soc. Agric. Mach. 55 (07), 15–26. https://doi.org/10.6041/j.issn.1000-1298.2024.07.002.
Zhou, H., Hu, L., Luo, X., Zhao, R., Xu, Y., Yang, W., 2016. Design and experiment on auto leveling system of rotary tiller. Trans. Chinese Soc. Agric. Mach 47 (S1), 117–123. https://doi.org/10.6041/j.issn.1000-1298.2016.S0.018.
Zhu, Y., Cui, B., Yu, Z., Gao, Y., Wei, X., 2024. Tillage depth detection and control based on attitude estimation and online calibration of model parameters. Agriculture 14 (12), 2130. https://doi.org/10.3390/agriculture14122130.

agriculture

Saved Queries

Sign In to use this feature.

Search Filter

Reset All

Years

Between: 1996 - 2026

Article Types

Select Article Types

Countries / Regions

Select Countries / Regions

Update Search

Search Results (1)

Search Parameters:
Keywords = Neural Network-Based SLAM/GNSS Fusion Localization Algorithm for Agricultural Robots in Orchard GNSS-Degraded or Denied Environments
Journal = Agriculture

Order results: Publication Date | Result details: Normal | Results per page: 50

Show export options

Open Access Article — 18 pages, 2469 KB

Neural Network-Based SLAM/GNSS Fusion Localization Algorithm for Agricultural Robots in Orchard GNSS-Degraded or Denied Environments

by Huixiang Zhou, Jingting Wang, Yuqi Chen, Lian Hu, Zihao Li, Fuming Xie, Jie He and Pei Wang

Agriculture 2025, *15*(15), 1612; https://doi.org/10.3390/agriculture15151612 - 25 Jul 2025

Cited by 4 | Viewed by 1465

Abstract To address the issue of agricultural robot loss of control caused by GNSS signal degradation or loss in complex agricultural environments such as farmland and orchards, this study proposes a neural network-based SLAM/GNSS fusion localization algorithm aiming to enhance the robot's localization accuracy [...] Read more.

(This article belongs to the Section Artificial Intelligence and Digital Agriculture)

► Show Figures

Show export options

Displaying article 1-50 on page 1 of 1.

agriculture

MDPI

Article

Neural Network-Based SLAM/GNSS Fusion Localization Algorithm for Agricultural Robots in Orchard GNSS-Degraded or Denied Environments

Huixiang Zhou [1,2], Jingting Wang [1], Yuqi Chen [1], Lian Hu [1], Zihao Li [1], Fuming Xie [1], Jie He [1,3,*] and Pei Wang [1,*]

[1] College of Engineering, South China Agricultural University, Guangzhou 510642, China; huixiangzhou@stu.scau.edu.cn (H.Z.); jingtingwang@stu.scau.edu.cn (J.W.); chenyuqi@stu.scau.edu.cn (Y.C.); lianhu@scau.edu.cn (L.H.);youyu@stu.scau.edu.cn (Z.L.); 2964330954@stu.scau.edu.cn (F.X.)
[2] State Key Laboratory of Agricultural Equipment Technology, Guangzhou 510642, China
[3] Huangpu Innovation Research Institute, South China Agricultural University, Guangzhou 510642, China
* Correspondence: hooget@scau.edu.cn (J.H.); wangpei@scau.edu.cn (P.W.)

Abstract

To address the issue of agricultural robot loss of control caused by GNSS signal degradation or loss in complex agricultural environments such as farmland and orchards, this study proposes a neural network-based SLAM/GNSS fusion localization algorithm aiming to enhance the robot's localization accuracy and stability in weak or GNSS-denied environments. It achieves multi-sensor observed pose coordinate system unification through coordinate system alignment preprocessing, optimizes SLAM poses via outlier filtering and drift correction, and dynamically adjusts the weights of poses from distinct coordinate systems via a neural network according to the GDOP. Experimental results on the robotic platform demonstrate that, compared to the SLAM algorithm without pose optimization, the proposed SLAM/GNSS fusion localization algorithm reduced the whole process average position deviation by 37%. Compared to the fixed-weight fusion localization algorithm, the proposed SLAM/GNSS fusion localization algorithm achieved a 74% reduction in average position deviation during transitional segments with GNSS signal degradation or recovery. These results validate the superior positioning accuracy and stability of the proposed SLAM/GNSS fusion localization algorithm in weak or GNSS-denied environments. Orchard experimental results demonstrate that, at an average speed of 0.55 m/s, the proposed SLAM/GNSS fusion localization algorithm achieves an overall average position deviation of 0.12 m, with average position deviation of 0.06 m in high GNSS signal quality zones, 0.11 m in transitional sections under signal degradation or recovery, and 0.14 m in fully GNSS-denied environments. These results validate that the proposed SLAM/GNSS fusion localization algorithm maintains high localization accuracy and stability even under conditions of low and highly fluctuating GNSS signal quality, meeting the operational requirements of most agricultural robots.

Keywords: agricultural robots; GNSS-degraded or denied environments; fusion localization; neural networks

Academic Editor: Suresh Neethirajan

Received: 7 June 2025
Revised: 9 July 2025
Accepted: 24 July 2025
Published: 25 July 2025

Citation: Zhou, H.; Wang, J.; Chen, Y.; Hu, L.; Li, Z.; Xie, F.; He, J.; Wang, P. Neural Network-Based SLAM/GNSS Fusion Localization Algorithm for Agricultural Robots in Orchard GNSS-Degraded or Denied Environments. *Agriculture* **2025**, *15*, 1612. https://doi.org/10.3390/agriculture15151612

1. Introduction

In recent years, China has faced intensifying population ageing, with rural labor shortages emerging as a critical constraint on rural revitalization. Agricultural automation and intelligentization represent an irreversible trend for the future of farming [1–3]. With

continuous advancements in technology, agricultural robots have emerged as a viable solution to replace human labor in repetitive agricultural tasks. These robots not only significantly enhance operational efficiency and quality but also inject new momentum into sustainable agricultural development. Their immense potential and promising prospects have garnered significant attention within the global agriculture technology sector [4–6]. Among the core technologies for agricultural robots, positioning systems play a pivotal role, serving as the fundamental enabler for autonomous navigation operations [7–9].

In open-field environments, RTK (Real-Time Kinematic)-enabled GNSSs (Global Navigation Satellite Systems) provide centimeter-level positioning accuracy, which has become the primary technical dependency for current agricultural robot navigation systems [10–15]. These works collectively demonstrate the critical role of high-precision GNSSs in enabling key functionalities such as autonomous navigation of agricultural vehicles, precise path management, and trajectory tracking. However, in occluded environments, GNSS signals suffer from degradation or even loss of fixed solutions, leading to drastic declines in positioning accuracy that severely compromise the reliability of autonomous navigation. Lidar (Light Detection and Ranging) systems, whether 2D or 3D configurations, provide autonomous machines with comprehensive environmental perception capabilities through active laser scanning. This environmental awareness compensates for GNSS limitations by enabling real-time ego-motion estimation during signal outages, thereby enhancing operational safety in agricultural scenarios. Given the critical need for reliable positioning in weak or GNSS-denied environments, achieving continuous and precise robot localization has emerged as a key research focus in agricultural robotics [16–22]. Cao et al. [23] proposed a neural network-based predictive MEMS-SINS error feedback correction method. This approach trains the neural network during GPS (Global Positioning System) availability and utilizes the trained model to predict MEMS-SINS errors during GPS outages. In four 50 s simulated GPS-denied experiments, the method achieved an average position error of 3.8 m. Shen et al. [24] proposed a Radial Basis Function-based Multilayer Perceptron-assisted Cubature Kalman Filter to compensate for position and velocity errors during GPS outages. In a 500 s GPS signal interruption test, the algorithm's mean square error was below 23.11 m. Liu et al. [25] addressed the challenge of cumulative errors in MEMS-INS during GPS signal loss by developing a neural network-aided GPS/MEMS-INS integrated navigation system. Experimental simulations under GPS-denied conditions demonstrated that this approach outperformed traditional frameworks using a Standard Kalman Filter and Unscented Kalman Filter, achieving approximately 65% improvement in velocity and positional accuracy. Zhang et al. [26] proposed a BDS (BeiDou Navigation Satellite System) outage endurance method for agricultural machinery navigation. By designing a Self-Calibrating Variable-Structure Kalman Filter for BDS/INS data fusion, this approach maintains straight-line tracking accuracy within limited durations. In robotic platform trials, during 20 s simulated BDS outages, the method achieved an average lateral deviation of 0.31 m on linear paths and an average positioning discrepancy of 0.77 m between the INS (Inertial Navigation System) and BDS on rectangular paths. However, cumulative errors inherent to the INS system limit its long-term operational viability. Wei et al. [27] addressed the challenge of GNSS signal occlusion in orchard environments by implementing a Kalman Filter-based fusion framework integrating GNSS and LiDAR data. To mitigate motion-induced distortion in LiDAR scans, an odometry-aided correction method was applied, enabling autonomous navigation for agricultural robots. Experimental results demonstrated a mean lateral deviation of less than 11 cm between actual and planned trajectories. However, the validity of GNSS signal availability during trials remains unverified, as the experiments did not isolate GNSS signals to quantify environmental signal degradation levels. Hu et al. [28] proposed a laser-based localization method for agricultural robots, which

achieves robot positioning by fusing ToF (time-of-flight) measurements from laser scanning with point cloud features acquired by a LiDAR receiver. Experimental results demonstrated that the average maximum deviations during straight-line and curvilinear motion were 4.1 cm and 6.2 cm, respectively. This method is primarily applicable to GNSS-denied indoor environments such as hangars and greenhouses, requiring unobstructed visibility between the LiDAR and receiver. However, its effectiveness is limited in outdoor scenarios due to potential occlusions. The aforementioned research studies provide valuable insights into achieving continuous and precise robot localization in weak or GNSS-denied environments. However, they still face limitations such as relatively low localization accuracy and suboptimal stability, which may cause trajectory deviations during autonomous navigation, operational failures in precision farming tasks, and potential safety hazards in complex agricultural environments.

To address the aforementioned issues, this study proposes a neural network-based SLAM/GNSS fusion localization algorithm. The algorithm integrates the local accuracy of LiDAR-inertial odometry with the global stability of a GNSS. It achieves multi-sensor observed pose coordinate system unification through coordinate system alignment preprocessing, optimizes SLAM (Simultaneous Localization and Mapping) poses via outlier filtering and drift correction, and dynamically adjusts the weights of poses from distinct coordinate systems via a neural network according to the GDOP (Geometric Dilution of Precision). These mechanisms collectively enhance the robot's localization accuracy and stability in weak or GNSS-denied environments. A wheeled differential-drive robotic platform was developed to preliminarily validate the algorithm's performance. Furthermore, field experiments were conducted in actual orchard environments to investigate the algorithm's effectiveness under orchard terrain conditions and tree-obstructed scenarios.

2. Materials and Methods

2.1. Algorithm Framework

The SLAM/GNSS fusion localization algorithm proposed in this study achieves continuous and precise positioning for robots in weak or GNSS-denied environments by integrating LIO-SAM (tightly-coupled lidar inertial odometry via smoothing and mapping) [29] and dual-antenna RTK-measured positioning and orientation data. This study adopts a loosely coupled approach where the SLAM and GNSS subsystems operate independently. A neural network-based dynamic weight adjustment fusion localization algorithm was designed to perform data integration. The overall framework is illustrated in Figure 1, with the corresponding nomenclature provided in Table 1. First, the point cloud data from LiDAR and the acceleration and angular velocity from the IMU (Inertial Measurement Unit) are coupled into LIO-SAM to obtain the observed pose of the center point of the drive wheel axis in the SLAM coordinate system. Subsequently, the real-time dynamically measured positioning orientation data from the dual antennas are subjected to Gauss–Kruger projection and coordinate transformation to obtain the observed pose of the center point of the drive wheel axis in the GNSS coordinate system. Then, coordinate system alignment preprocessing is implemented to unify the coordinate system of multi-sensor observed poses, followed by outlier filtering and drift correction to optimize the SLAM poses. Finally, the observed poses from two distinct coordinate systems and the GDOP are fed into the neural network model to dynamically adjust the optimization weights of each observed pose, thereby outputting the fused pose.

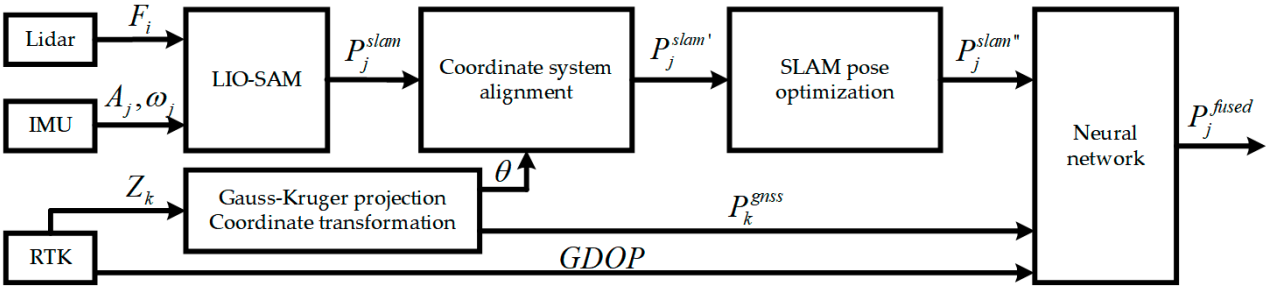

Figure 1. Framework of the SLAM/GNSS fusion localization algorithm.

Table 1. Nomenclature corresponding to Figure 1.

Symbol	Meaning
F_i	The point cloud data from LiDAR
A_j	The acceleration from IMU
ω_j	The angular velocity from IMU
Z_k	The positioning orientation data from the dual antennas
θ	The initial RTK heading angle
P_k^{gnss}	The observed pose in the GNSS coordinate system
P_j^{slam}	The observed pose in the SLAM coordinate system
$P_j^{slam'}$	The SLAM pose after preprocessing of coordinate system alignment
$P_j^{slam''}$	The optimized SLAM pose
P_j^{fused}	The fused pose
i, j, k	The time-series markers of the LiDAR, IMU, and RTK

2.2. SLAM/GNSS Fusion Localization Algorithm

2.2.1. LiDAR-Inertial Odometry

This research employs the LIO-SAM algorithm for state estimation. This algorithm constructs a factor graph optimization framework, as shown in Figure 2, incorporating four key factors: the IMU pre-integration factor, LiDAR odometry factor, GPS factor, and loop closure factor. By applying nonlinear optimization methods to optimize the factor graph, the system achieves globally consistent robot poses, enabling high-precision state estimation and map construction.

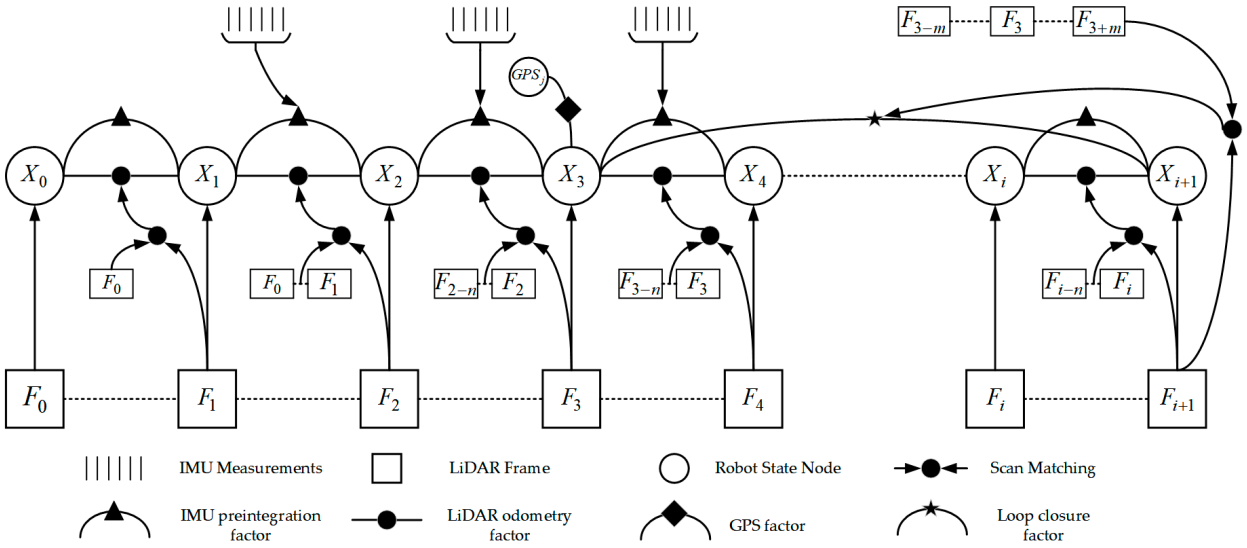

Figure 2. Factor graph optimization framework of LIO-SAM.

The IMU pre-integration factor efficiently computes the relative motion increments between consecutive LiDAR keyframes i and $i + 1$ by pre-integrating IMU data. These increments include positional increment $\Delta P_{i,i+1}$, velocity increment $\Delta V_{i,i+1}$, and rotational increment $\Delta R_{i,i+1}$, which are incorporated as constraints into the factor graph for optimization. The IMU pre-integration formulation is expressed as follows:

$$\begin{cases} \Delta V_{i,i+1} = R_i^T(V_{i+1} - V_i - g\Delta t_{i,i+1}) \\ \Delta P_{i,i+1} = R_i^T\left(P_{i+1} - P_i - V_i\Delta t_{i,i+1} - \frac{1}{2}g\Delta t_{i,i+1}^2\right) \\ \Delta R_{i,i+1} = R_i^T R_{i+1} \end{cases} \tag{1}$$

where g is the acceleration of gravity; $\Delta t_{i,i+1}$ is the time interval between two neighboring keyframes; V_i and V_{i+1} are the velocities at the moments i and $i + 1$; P_i and P_{i+1} are the positions at the moments i and $i + 1$; R_i^T is the rotation matrix transpose at the moment i; and R_{i+1} is the rotation matrix at the moment $i + 1$.

The LiDAR odometry factor first extracts features from preprocessed point cloud data using a curvature-based method, categorizing them into edge features and planar features, while introducing the concept of LiDAR keyframes. A sliding window approach is then employed to construct a point cloud map containing a fixed number of recent LiDAR scans. Finally, the point-to-edge distance d_{e_k} and point-to-plane distance d_{p_k} are utilized to formulate pose estimation equations.

$$\begin{cases} d_{e_k} = \frac{\left|\left(p_{i+1,k}^e - p_{i,u}^e\right) \times \left(p_{i+1,k}^e - p_{i,v}^e\right)\right|}{\left|p_{i,u}^e - p_{i,v}^e\right|} \\ d_{p_k} = \frac{\left|\left(p_{i+1,k}^p - p_{i,u}^p\right) \times \left(p_{i,u}^p - p_{i,v}^p\right) \times \left(p_{i,u}^p - p_{i,w}^p\right)\right|}{\left|\left(p_{i,u}^p - p_{i,v}^p\right) \times \left(p_{i,u}^p - p_{i,w}^p\right)\right|} \end{cases} \tag{2}$$

where k, u, v, and w are feature indices in the corresponding set; $p_{i+1,k}^e$, $p_{i,u}^e$, and $p_{i,v}^e$ are points on edge features; and $p_{i+1,k}^p$, $p_{i,u}^p$, $p_{i,v}^p$, and $p_{i,w}^p$ are points on planar features.

The Gauss–Newton method is used to solve for the optimal transformation by minimizing:

$$\min_{T_{i+1}} \left\{ \sum_{p_{i+1,k}^e \in {}'F_{i+1}^e} d_{e_k} + \sum_{p_{i+1,k}^p \in {}'F_{i+1}^p} d_{p_k} \right\} \tag{3}$$

where T_{i+1} is the pose at moment $i + 1$; ${}'F_{i+1}^e$ is the edge feature transformed to the world coordinate system; and ${}'F_{i+1}^p$ is the planar feature transformed to the world coordinate system.

The relative pose transformation between two adjacent keyframes is computed:

$$\Delta T_{i,i+1} = T_i^T T_{i+1} \tag{4}$$

where T_i is the pose at moment i.

The GPS factor provides global positional constraints to the system by integrating GPS measurement data. Upon receiving GPS observations, the data are transformed into a local Cartesian coordinate system. When new nodes are added to the factor graph, the corresponding GPS factor is associated with these nodes to establish spatial constraints.

The loop closure factor employs a simple yet effective Euclidean distance-based detection method. The algorithm first searches historical keyframes to identify candidate loop closure frames that are temporally distant but spatially proximate. Subsequently, scan-to-map optimization is performed to estimate the relative pose transformation between the current keyframe and the candidate frame. This transformation is then incorporated as a loop closure factor into the factor graph for global trajectory optimization.

2.2.2. Coordinate System Alignment

The SLAM coordinate system is defined with its origin at the initial position of the center point of the drive wheel axis. Its positive *X*-axis aligns with the robot's forward direction, while the positive *Y*-axis is oriented towards the robot's left side, following the right-hand rule. The GNSS coordinate system shares the same origin but adopts an ENU (East-North-Up) frame convention, with the positive *X*-axis pointing to geodetic east and the positive *Y*-axis to geodetic north. The arbitrary initial orientation of the robot typically results in a fixed angular deviation θ about the *Z*-axis between the SLAM and GNSS coordinate systems, as shown in Figure 3. To enable fusion of observed poses from these two distinct coordinate systems, coordinate system alignment is required.

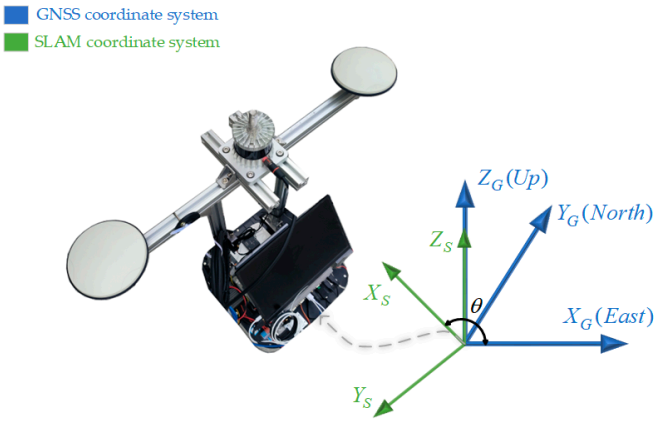

Figure 3. Coordinate system framework.

During the system initialization phase, the initial heading angle θ is obtained through dual-antenna RTK measurements. The SLAM coordinate system is then rotated about the *Z*-axis by $-\theta$ to align with the GNSS coordinate system, resulting in an intermediate coordinate system MID that serves as the base coordinate system for SLAM. By establishing the coordinate transformation relationship from the SLAM coordinate system to the MID coordinate system, positional coordinates in the SLAM coordinate system can be transformed into the MID coordinate system, thereby achieving unification of the coordinate system for multi-sensor observed poses. The transformation is formulated as follows:

$$\begin{bmatrix} x_{mid} \\ y_{mid} \\ z_{mid} \end{bmatrix} = R_{SLAM}^{MID} \begin{bmatrix} x_{slam} \\ y_{slam} \\ z_{slam} \end{bmatrix} = \begin{bmatrix} \cos(-\theta) & -\sin(-\theta) & 0 \\ \sin(-\theta) & \cos(-\theta) & 0 \\ 0 & 0 & 1 \end{bmatrix} \begin{bmatrix} x_{slam} \\ y_{slam} \\ z_{slam} \end{bmatrix} \quad (5)$$

where x_{slam}, y_{slam}, and z_{slam} are the position coordinates under the SLAM coordinate system; x_{mid}, y_{mid}, and z_{mid} are the position coordinates under the MID coordinate system; and R_{SLAM}^{MID} is the rotation matrix from the SLAM coordinate system to the MID coordinate system.

2.2.3. SLAM Pose Optimization

During the implementation of the LIO-SAM algorithm for simultaneous localization and mapping, sporadic localization outliers may emerge in the LiDAR-inertial odometry. These localization outliers, characterized by abrupt pose jumps at specific timestamps, often result from dynamic object interference, sensor noise, or feature matching errors. These localization outliers must be filtered out to enhance the system's temporal continuity and operational stability. The pose outlier detection proceeds by first computing the Euclidean displacement between the current and previous poses in the SLAM coordinate frame. If this displacement exceeds a predefined threshold, the current pose is identified as an outlier.

The system then substitutes the outlier with a linearly extrapolated pose derived from the previous pose data, as formalized below:

$$\begin{cases} x_t = x_{t-1} + k_x^{t-1}\Delta t \\ y_t = y_{t-1} + k_y^{t-1}\Delta t \\ \theta_t = \theta_{t-1} + k_\theta^{t-1}\Delta t \end{cases} \tag{6}$$

where x_t, y_t, and θ_t are the x, y coordinates and heading angle at the current moment; x_{t-1}, y_{t-1}, and θ_{t-1} are the x, y coordinates and heading angle at the previous moment; k_x^{t-1}, k_y^{t-1}, and k_θ^{t-1} are the rate of change of x, y coordinates and heading angle at the previous moment; and Δt is the time interval between the current moment and the previous moment.

GNSS data are not entered into the LIO-SAM framework because LIO-SAM does not fully utilize GNSS information [30]. The radar inertial odometers may have accumulated errors due to drift during long time operation of the system. When the quality of the GNSS signal is high, the drift of the radar inertial odometer can be suppressed by using the coordinate data under the GNSS coordinate system as a global position constraint, thus reducing the cumulative error and improving the stability of the system. When RTK has a fixed solution and the GNSS signal quality is high, the difference between the pose in the GNSS coordinate system and the pose in the SLAM coordinate system is calculated. When the difference exceeds the set distance threshold or angle threshold, the position coordinates are corrected in the SLAM coordinate system. Since this is designed for wheeled robots moving on a plane, we only consider distance deviations in the X and Y directions and heading angle deviation. The correction formula is as follows:

$$\begin{cases} x_{mix} = x + \Delta x \\ y_{mix} = y + \Delta y \\ \theta_{mix} = \theta + \Delta\theta \end{cases} \tag{7}$$

where x_{mix}, y_{mix}, and θ_{mix} are the x, y coordinates and heading angles after correction; x, y, and θ are the x, y coordinates and heading angles before correction; and Δx, Δy, and $\Delta\theta$ are the x, y coordinates and heading angle differences.

2.2.4. Neural Network-Based Dynamic Weight Adjustment

LIO-SAM assigns fixed observation weights to both GNSS and LiDAR odometry [30]. However, in practical scenarios, the signal quality of GNSS significantly differs between open and obstructed environments. The fixed-weight strategy fails to adequately account for the environmental sensitivity of GNSS signal quality, resulting in high-quality observations not being fully leveraged. Given the powerful adaptive and nonlinear mapping capabilities of neural networks, this study proposes a neural network model with dynamic weight adjustment. It adaptively adjusts the weights of poses from two distinct coordinate systems based on the magnitude of GDOP through end-to-end training, aiming to achieve the fusion of SLAM and GNSS poses.

The structure of the neural network model is shown in Figure 4. The input layer contains 5-dimensional features: the 2D SLAM position coordinates after preprocessing of coordinate system alignment, 2D GNSS position coordinates, and the GDOP. The first and second hidden layers are fully connected layers with 128 neurons each, using the ReLU (Rectified Linear Unit) as the activation function for feature extraction. The third hidden layer is also a fully connected layer with 64 neurons and ReLU activation, designed to further compress features. The fourth weight generation layer is a fully connected layer with 2 neurons, employing the Softmax function as the activation function to output normalized weights for GNSS and SLAM poses. The fifth fusion layer is a parameter-free mathe-

matical operation layer that performs weighted summation of SLAM and GNSS position coordinates to output the fused position coordinates. The fusion formula is as follows:

$$\begin{cases} x_{fused} = w_{gnss}x_{gnss} + w_{slam}x_{slam} \\ y_{fused} = w_{gnss}y_{gnss} + w_{slam}y_{slam} \\ w_{gnss} + w_{slam} = 1 \end{cases} \tag{8}$$

where w_{gnss} is the weight of the GNSS position; w_{slam} is the weight of the SLAM position; x_{gnss} and y_{gnss} are the position coordinates in the GNSS coordinate system; x_{slam} and y_{slam} are the position coordinates in the SLAM coordinate system; and x_{fused} and y_{fused} are the fused position coordinates.

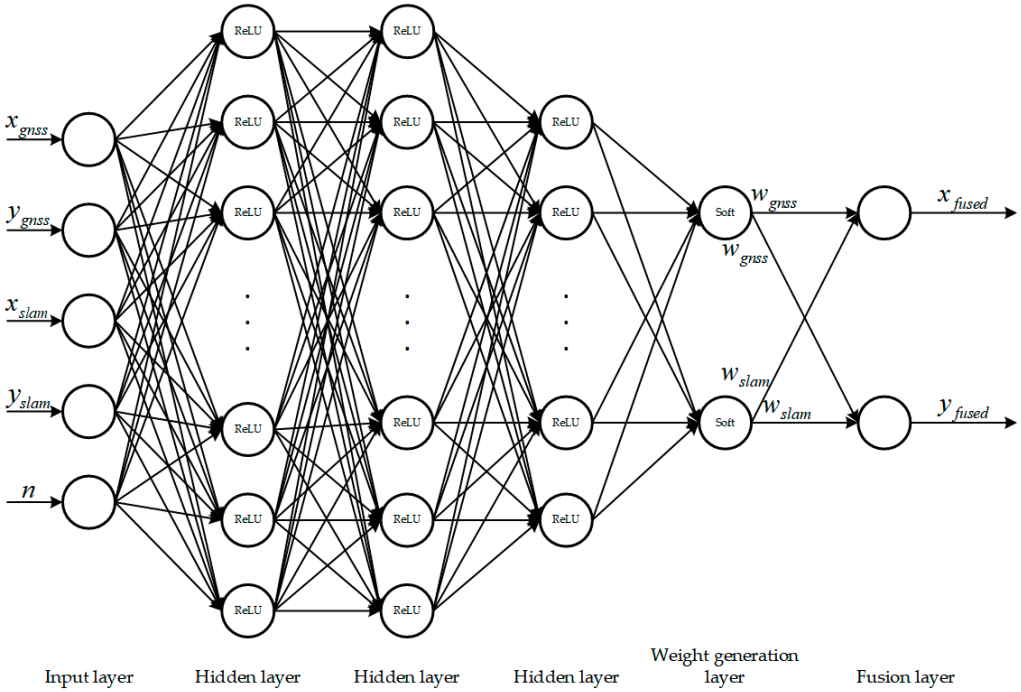

Figure 4. Architecture diagram of the neural network-based model.

The pseudocode for the neural network-based dynamic weight adjustment algorithm is shown in Algorithm 1. The raw GPS and SLAM coordinates as well as GDOP undergo normalization processing and then pass through three fully-connected layers with ReLU activation for feature extraction. A subsequent weight generation layer generates Softmax-normalized outputs that ensure weights sum to unity. The final fused position combines GPS and SLAM coordinates using these dynamically predicted weights. This architecture dynamically adjusts sensor contributions based on real-time GNSS signal quality while maintaining computational efficiency through compact design choices. The complete system operates within embedded platform constraints for dynamic sensor fusion in agricultural robotics.

This study adopts the MAE (mean absolute error) as the loss function, which computes the mean absolute error L_{MAE} between the fused position coordinates and the ground truth position coordinates. The mathematical formulation is defined as follows:

$$L_{MAE} = \frac{1}{N}\sum_{i=1}^{N}\left|p^{i}_{fused} - p^{i}_{true}\right| \tag{9}$$

where p^{i}_{fused} is the fusion position coordinate of the i-th sample; p^{i}_{true} is the ground truth position coordinate of the i-th sample; and N is the total number of samples.

Algorithm 1. The pseudocode for the neural network-based dynamic weight adjustment algorithm.

Input: M, μ, σ, gps_x, gps_y, $slam_x$, $slam_y$, $GDOP$
Output: W_{gps}, W_{slam}, $fused_x$, $fused_y$

function PREDICTWEIGHTS (M, μ, σ, gps_x, gps_y, $slam_x$, $slam_y$, $GDOP$)
  $x \leftarrow [gps_x, gps_y, slam_x, slam_y, GDOP]$
  if $\mu \neq \varnothing \wedge \sigma \neq \varnothing$ **then**
    $x \leftarrow (x - \mu) \oslash \sigma$
  end if
  $X \leftarrow \text{tensor}(x)$
  $(W_{gps}, W_{slam}) \leftarrow M(X)$
  return W_{gps}, W_{slam}
end function
function FUSEPOSITION (gps_x, gps_y, $slam_x$, $slam_y$, W_{gps}, W_{slam})
  $fused_x \leftarrow W_{gps} \times gps_x + W_{slam} \times slam_x$
  $fused_y \leftarrow W_{gps} \times gps_y + W_{slam} \times slam_y$
  return $fused_x$, $fused_y$
end function

The training dataset was collected in real-world environments by controlling the robot to maneuver repeatedly between open and obstructed areas. During this process, 5-dimensional input data were continuously recorded, while 2-dimensional ground truth output data were acquired using a total station. After temporal synchronization, the raw data were processed to create a custom dataset, which was then split into 70% for training, 20% for validation, and 10% for testing.

Finally, the fused heading angle is obtained by performing a weighted summation of the SLAM and GNSS heading angles. The fusion formula is defined as follows:

$$\theta_{fused} = w_{gnss}\theta_{gnss} + w_{slam}\theta_{slam} \tag{10}$$

where θ_{gnss} is the heading angle in the GNSS coordinate system; θ_{slam} is the heading angle in the SLAM coordinate system; and θ_{fused} is the fused heading angle.

2.3. Robotic Platform Experiments

2.3.1. Experimental Platform

To preliminarily validate the performance of the SLAM/GNSS fusion localization algorithm, a robotic platform was developed based on the wheeled differential chassis (AgileX TRACER MINI, Dongguan, China), with its physical prototype shown in Figure 5. The hardware components of the platform include a Yentek G3750F-P4 embedded industrial computer (Intel i9-13900 processor, 32GB RAM, Shenzhen, China); Unicorecomm UM982 satellite receiver (10 Hz output frequency, horizontal positioning accuracy: 0.8 cm + 1 ppm, heading accuracy: 0.1° per 1 m baseline, Yantai, China); WHEELTEC N100 IMU (400 Hz output frequency, accelerometer/gyroscope/magnetometer linearity < 0.1%, Dongguan, China); Ouster OS1 3D LiDAR (10 Hz point cloud output, 128 scan lines, San Francisco, CA, USA); display screen; and 24 V power supply. The software component consists of a localization system based on the SLAM/GNSS fusion localization algorithm. This system is developed within the ROS (Robot Operating System) framework using C++ and deployed on the embedded industrial computer. The satellite receiver's positioning and heading data, along with the IMU's inertial attitude data, are input to the localization system via serial port, while the LiDAR's point cloud data are streamed via ethernet. The localization system

employs neural networks to perform multi-sensor data fusion, continuously outputting the robot's fused pose.

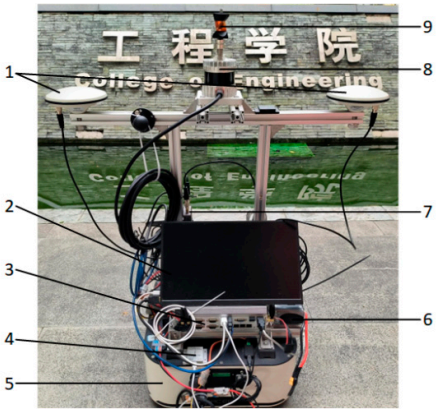

Figure 5. Physical prototype of robotic platform. 1. RTK dual antenna; 2. display screen; 3. embedded industrial computer; 4. IMU 5. wheeled differential chassis; 6. power supply; 7. satellite receiver; 8. LiDAR; 9. prism.

2.3.2. Experimental Protocol

The robotic platform experiments were conducted at the College of Engineering, South China Agricultural University, with the experimental scenario shown in Figure 6. A Leica MS60 total station in automated tracking mode was utilized to record the robot's ground truth position coordinates in real-time by tracking a prism mounted on the robot. The total station operates at a 10 Hz measurement frequency, achieving a positioning error of 1 mm within a 100 m range. A rectangular path was planned with the starting point set in an area of high GNSS signal quality to facilitate coordinate system alignment during the system initialization phase. The robot was remotely controlled to approximately follow the predefined path, transitioning from GNSS-available zones to GNSS-denied zones, then back to GNSS-available zones. During the robot's walking process, the position coordinates in the GNSS coordinate system, position coordinates in the SLAM coordinate system, and fused position coordinates output from the localization system were recorded in real-time. Three repeated trials were conducted under identical experimental conditions. Following temporal synchronization and uniform time sampling of the data, the following metrics were calculated: the average position deviation $\overline{d}$ throughout the whole process, the average position deviation $\overline{d}_1$ in areas of high GNSS signal quality, the average position deviation $\overline{d}_2$ in transitional zones experiencing signal degradation or recovery, the average position deviation $\overline{d}_3$ in GNSS-denied environments, and the average velocity $\overline{v}$. These metrics were used to evaluate the localization accuracy and stability of the SLAM/GNSS fusion localization algorithm.

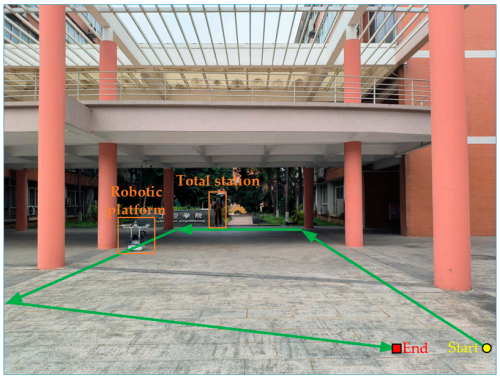

Figure 6. Experimental scenario of robotic platform.

2.4. Orchard Experiments

2.4.1. Experimental Platform

To investigate the operational performance of the SLAM/GNSS fusion localization algorithm in actual orchard terrains and tree-obstructed environments, the aforementioned software and hardware systems were ported to a tracked differential chassis (AgileX BUNKER, Dongguan, China). Its key technical specifications are summarized in Table 2, and the physical prototype is shown in Figure 7.

Table 2. Key technical specifications of tracked differential chassis.

Parameters	Value
Length ×Width ×Height/(mm × mm × mm)	1023 × 778 × 400
Total Mass/kg	130
Max Speed/$(m \cdot s^{-1})$	1.5
Min Turning Radius/mm	0
Max Gradeability/°	30
Ground Clearance/mm	560

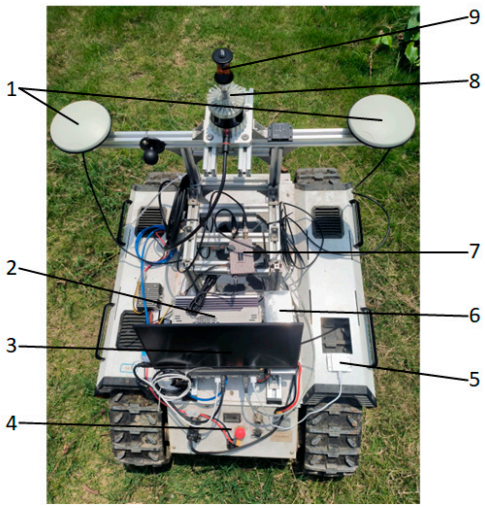

Figure 7. Physical prototype of orchard platform. 1. RTK dual antenna; 2. embedded industrial computer; 3. display screen; 4. tracked differential chassis; 5. IMU; 6. power supply; 7. satellite receiver; 8. LiDAR; 9. prism.

2.4.2. Experimental Protocol

The orchard experiments were conducted at the Horticultural Teaching and Research Base of South China Agricultural University, with the experimental scenario depicted in Figure 8. A rectangular path was planned with the starting point positioned in a GNSS high signal quality area to facilitate coordinate system alignment during initialization. The robot was remotely controlled to approximately follow the predefined path. Throughout the traversal, both the fused position coordinates from the localization system and the ground truth position coordinates from the total station were recorded in real-time. Three repeated trials were conducted under identical experimental conditions. Following temporal synchronization and uniform time sampling of the data, the following metrics were calculated: the average position deviation $\overline{d}$ throughout the whole process, the average position deviation $\overline{d}_1$ in areas of high GNSS signal quality, the average position deviation $\overline{d}_2$ in transitional zones experiencing signal degradation or recovery, the average position deviation $\overline{d}_3$ in GNSS-denied environments, and the average velocity $\overline{v}$. These metrics were utilized to evaluate the localization accuracy and stability of the SLAM/GNSS fusion localization algorithm in actual orchard terrains and tree-obstructed environments.

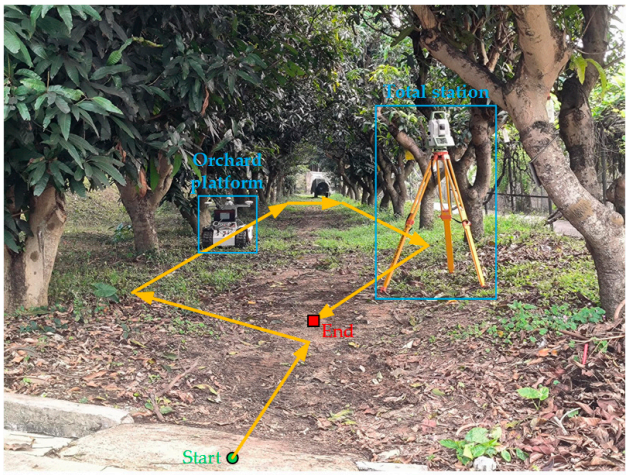

Figure 8. Orchard experimental scenario.

3. Results and Discussion

3.1. Analysis of Neural Network Model Training Results

The training and validation loss curves of the neural network model are shown in Figure 9. The model was trained using the Adam optimizer with a learning rate of 0.001, with a batch size of 32, and for 300 epochs. The curves demonstrate robust convergence characteristics: both losses decrease rapidly within the first 50 epochs, then plateau along near-parallel trajectories beyond epoch 50, indicating low overfitting risk. This efficient convergence is attributable to the optimized hyperparameter configuration, where the Adam optimizer coupled with ReduceLROnPlateau decay effectively balances convergence speed and stability.

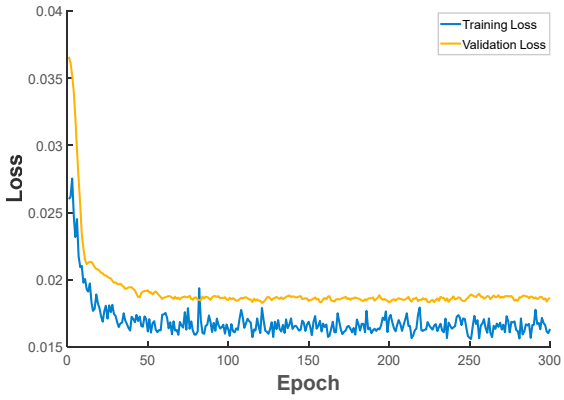

Figure 9. Training and validation loss curves of the neural network model.

3.2. Analysis of Robotic Platform Experimental Results

The fused trajectory versus the ground truth trajectory from the robotic platform experiment 1 is shown in Figure 10a. The position deviation over time for the localization system employing the SLAM/GNSS fusion localization algorithm is shown in Figure 10b. The position deviation over time for the SLAM localization subsystem without pose optimization is shown in Figure 10c. The position deviation over time for the fixed-weight fusion localization system is shown in Figure 10d. The GDOP over time is shown in Figure 10e, while the time-varying weights assigned to SLAM and GNSS poses are shown in Figure 10f.

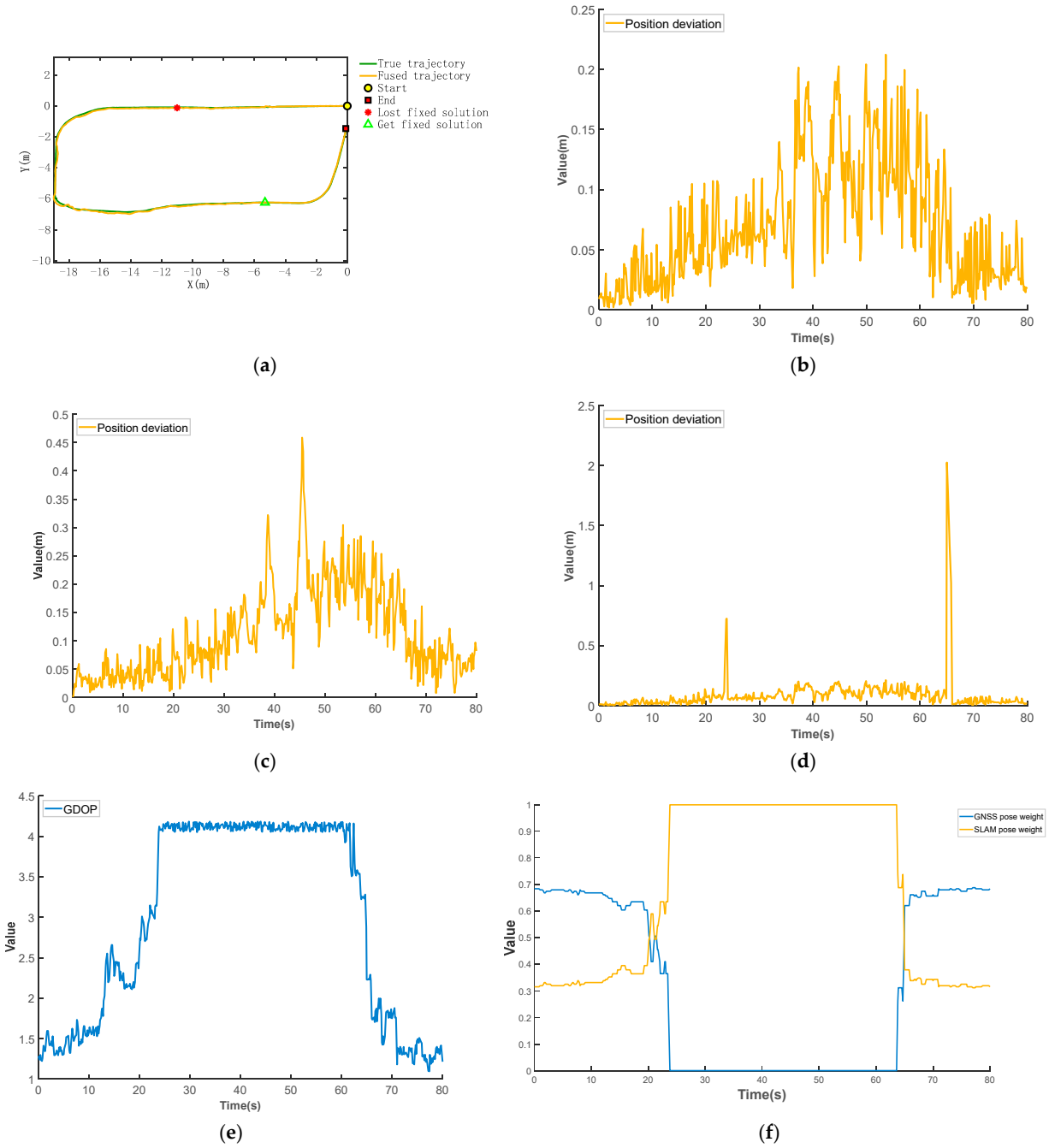

Figure 10. (**a**) Trajectory comparison from robotic platform experiment 1. (**b**) Position deviation variation curves of the positioning system using the SLAM/GNSS fusion localization algorithm from robotic platform experiment 1. (**c**) Position deviation variation curves of the SLAM localization subsystem without pose optimization from robotic platform experiment 1. (**d**) Position deviation variation curves of the fixed-weight fusion localization system from robotic platform experiment 1. (**e**) GDOP variation curve from robotic platform experiment 1. (**f**) Weight Variation Curve from robotic platform experiment 1.

During the intervals of 0–19.8 s and 65–80 s, the GDOP remained low, indicating high GNSS signal quality. The SLAM/GNSS fusion localization algorithm optimized the SLAM pose through outlier filtering and drift correction. The weights assigned to GNSS and SLAM poses showed not much difference and remained stable, resulting in an average positional deviation of 0.03 m in these segments. During the 19.9–23.5 s interval, the GDOP gradually increased, indicating a progressive degradation in GNSS signal quality.

The SLAM/GNSS fusion localization algorithm dynamically adjusted the weights via the neural network, with the GNSS pose weight continuously decreasing while the SLAM pose weight correspondingly increased. This resulted in an average positional deviation of 0.06 m for this segment. During the 60.7–64.9 s interval, the GDOP gradually decreased, indicating a progressive improvement in GNSS signal quality. The SLAM/GNSS fusion localization algorithm dynamically adjusted the weights via the neural network, with the SLAM pose weight continuously decreasing while the GNSS pose weight correspondingly increased. This resulted in an average positional deviation of 0.08 m for this segment. During the 23.8–60.5 s interval, the GDOP exceeded 4, indicating virtually no GNSS signals. The RTK fixed solution was lost and the GNSS pose weight was set to 0, while the SLAM pose weight was assigned a value of 1. The system thus relied solely on LiDAR odometry for localization. This segment exhibited an average positional deviation of 0.11 m with no significant dispersion in localization error, demonstrating stable performance over extended durations.

The results from three repeated trials are summarized in Table 3. The SLAM/GNSS fusion localization algorithm achieved the following metrics: $\bar{d}$ = 0.07 m, $\bar{d}_1$ = 0.04 m, $\bar{d}_2$ = 0.06 m, $\bar{d}_3$ = 0.10 m, and $\bar{v}$ = 0.57 m/s. Compared to the SLAM algorithm without pose optimization, the proposed SLAM/GNSS fusion localization algorithm reduced the whole process's average position deviation by 37%. Compared to the fixed-weight fusion localization algorithm, the proposed SLAM/GNSS fusion localization algorithm achieved a 74% reduction in average position deviation during transitional segments with GNSS signal degradation or recovery. Experimental results on the robotic platform demonstrate the superior positioning accuracy and stability of the proposed SLAM/GNSS fusion localization algorithm in weak or GNSS-denied environments.

Table 3. Experimental results of robotic platform.

Experiment NO.	$\bar{d}$/m	$\bar{d}_1$/m	$\bar{d}_2$/m	$\bar{d}_3$/m	$\bar{v}$/(m·s^{-1})
1	0.07	0.03	0.07	0.11	0.60
2	0.07	0.04	0.07	0.10	0.54
3	0.06	0.04	0.05	0.08	0.58
Average	0.07	0.04	0.06	0.10	0.57

3.3. Analysis of Orchard Experimental Results

The fused trajectory versus the ground truth trajectory from the orchard experiments 1 is shown in Figure 11a. The deviation d between the fused positions and ground truth positions over time is shown in Figure 11b. The GDOP over time is shown in Figure 11c, while the time-varying weights assigned to SLAM and GNSS poses are shown in Figure 11d.

During the 0–9.5 s interval, the robot transitioned from an open area to a tree-obstructed zone. The GDOP gradually increased, indicating a progressive degradation in GNSS signal quality. The SLAM/GNSS fusion localization algorithm dynamically adjusted the weights via the neural network, resulting in a continuous decrease in the GNSS pose weight and a corresponding increase in the SLAM pose weight. During the 9.8–107.3 s interval, the robot operated entirely within a tree-obstructed environment. The GDOP fluctuated between 2.8552 and 4.1664, indicating low and highly fluctuating GNSS signal quality. The SLAM/GNSS fusion localization algorithm dynamically adjusted the pose weights via the neural network, with both GNSS and SLAM weights continuously adapting to real-time GNSS signal quality variations.

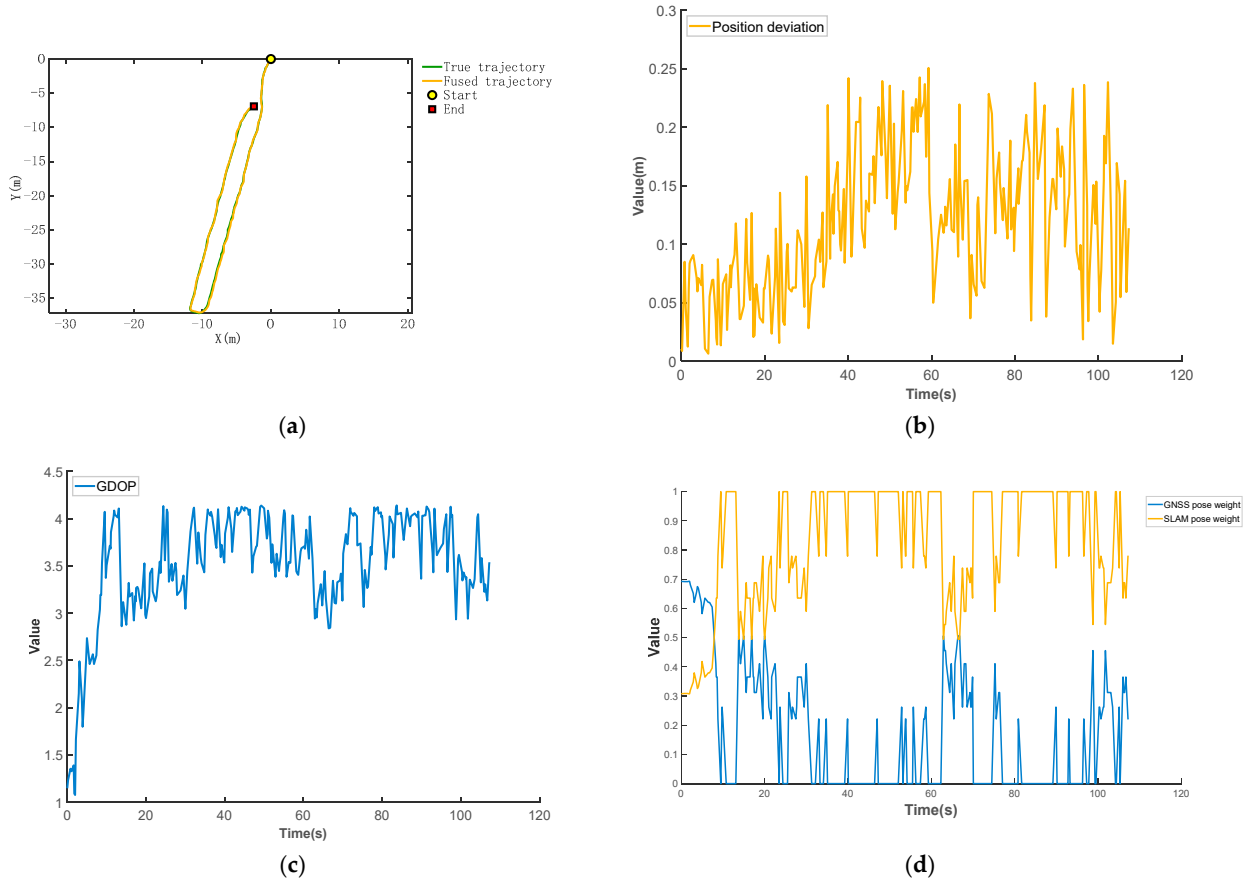

Figure 11. (**a**) Trajectory comparison from orchard experiment 1. (**b**) Position deviation variation curve from orchard experiment 1. (**c**) GDOP variation curve from orchard experiment 1. (**d**) Weight Variation Curve from orchard experiment 1.

The results from three repeated trials are summarized in Table 4. The SLAM/GNSS fusion localization algorithm achieved the following metrics: $\overline{d}$ = 0.12 m, $\overline{d}_1$ = 0.06 m, $\overline{d}_2$ = 0.11 m, $\overline{d}_3$ = 0.14 m, and $\overline{v}$ = 0.55 m/s. Experimental results in the orchard demonstrate that the proposed SLAM/GNSS fusion localization algorithm maintains high localization accuracy and stability even under conditions of low and highly fluctuating GNSS signal quality, meeting the operational requirements of most agricultural robots.

Table 4. Orchard experimental results.

Experiment NO.	$\overline{d}$/m	$\overline{d}_1$/m	$\overline{d}_2$/m	$\overline{d}_3$/m	$\overline{v}$/(m·s^{-1})
1	0.12	0.06	0.12	0.13	0.67
2	0.11	0.05	0.10	0.15	0.53
3	0.12	0.07	0.11	0.14	0.46
Average	0.12	0.06	0.11	0.14	0.55

3.4. Discussion

The requirement to position the robot's starting point in high GNSS signal quality areas for coordinate system alignment during initialization imposes limitations on the applicability of the proposed SLAM/GNSS fusion localization algorithm across diverse operational scenarios.

While this study achieved robust localization in GNSS-degraded or denied environments, atmospheric effects (particularly ionospheric delays) were not addressed. Future

work will characterize these impacts using the receiver's raw multi-frequency signals for real-time atmospheric error correction.

Since the total station cannot directly provide ground truth heading angles for tracked mobile devices, this study omitted heading angle deviation as an experimental metric. Future research could focus on acquiring accurate ground truth heading angles for robots in GNSS-denied environments to further analyze the heading angle accuracy of the proposed SLAM/GNSS fusion localization algorithm.

Typical agricultural machines operate at a speed of 1 to 1.5 m/s, but the experimental average speed described above was only about 0.5 m/s. At velocities exceeding 1 m/s, the algorithm may sacrifice positional precision to maintain real-time performance. Subsequent studies can add high-speed testing scenarios to verify the accuracy and stability of the algorithm at typical farm machine operating speeds.

In real agricultural scenarios, the dust generated during robotic operations and frequent precipitation during the rainy season can have an impact on the point cloud quality of the LiDAR. Suspended particulate matter in the dust scatters the laser light, resulting in noticeable noise. Raindrops reflect and absorb the laser light, resulting in anomalous increases or disappearances in the point cloud. The distortion of LiDAR point cloud data will affect the effectiveness of the algorithm to a certain extent, so in subsequent research we need to consider how to eliminate these effects as much as possible to improve the stability of the algorithm in harsh environments. For example, a waveform recognition algorithm could be used to analyze the reflectivity size and orientation of the noise and set an appropriate threshold to filter the noise, or a deep learning-based denoising method could be used to develop a noise filtering network based on semantic information.

Looking forward, the XAI-based SLAM and deep learning-based localization approaches will drive the development of next-generation agricultural positioning technologies [31]. For example, Tateno et al. [32] propose a method in which CNN-predicted dense depth maps are fused with depth measurements from direct monocular SLAM, resulting in semantically coherent scene reconstruction from a single view. Feng et al. [33] propose the 2D3D-MatchNet, an end-to-end deep network architecture that jointly learns descriptors for 2D and 3D keypoints from images and point clouds for visual pose estimation. While current computational constraints limit their real-time deployment on embedded platforms, emerging edge-compatible architectures and lightweight explainable AI models are rapidly closing this gap. Artificial intelligence-driven multi-modal perception will advance environmental adaptability, promising to further enhance the positioning accuracy and stability of agricultural robots in weak or GNSS-denied environments.

4. Conclusions

To address the issue of agricultural robot loss of control caused by GNSS signal degradation or loss in complex agricultural environments such as farmland and orchards, this study proposes a neural network-based SLAM/GNSS fusion localization algorithm. It achieves multi-sensor observed pose coordinate system unification through coordinate system alignment preprocessing, optimizes SLAM poses via outlier filtering and drift correction, and dynamically adjusts the weights of poses from distinct coordinate systems via a neural network according to the GDOP. These mechanisms collectively enhance the robot's localization accuracy and stability in weak or GNSS-denied environments.

To preliminarily validate the performance of the SLAM/GNSS fusion localization algorithm, robotic platform experiments were conducted. The experimental results demonstrate that, at an average speed of 0.57 m/s, the proposed SLAM/GNSS fusion localization algorithm achieves an overall average position deviation of 0.07 m, with average position deviation of 0.04 m in areas of high GNSS signal quality, 0.06 m in transitional zones expe-

riencing signal degradation or recovery, and 0.10 m in fully GNSS-denied environments. Compared to the SLAM algorithm without pose optimization, the proposed SLAM/GNSS fusion localization algorithm reduced the whole process average position deviation by 37%. Compared to the fixed-weight fusion localization algorithm, the proposed SLAM/GNSS fusion localization algorithm achieved a 74% reduction in average position deviation during transitional segments with GNSS signal degradation or recovery. These results validate the superior positioning accuracy and stability of the proposed SLAM/GNSS fusion localization algorithm in weak or GNSS-denied environments.

To investigate the operational performance of the SLAM/GNSS fusion localization algorithm in actual orchard terrains and tree-obstructed environments, orchard field experiments were conducted. The experimental results demonstrate that, at an average speed of 0.55 m/s, the proposed SLAM/GNSS fusion localization algorithm achieves an overall average position deviation of 0.12 m, with average position deviation of 0.06 m in high GNSS signal quality zones, 0.11 m in transitional sections under signal degradation or recovery, and 0.14 m in fully GNSS-denied environments. These results validate that the proposed SLAM/GNSS fusion localization algorithm maintains high localization accuracy and stability, even under conditions of low and highly fluctuating GNSS signal quality, meeting the operational requirements of most agricultural robots.

Author Contributions: Conceptualization, H.Z., J.H., J.W., and Y.C.; methodology, H.Z., J.H., J.W., and Y.C.; validation, H.Z., J.W., and Y.C.; formal analysis, H.Z., Y.C., J.W., and Z.L.; investigation, H.Z., J.W., and F.X.; resources, H.Z. and J.H.; data curation, H.Z., J.W., Y.C., Z.L., J.H., and L.H.; writing—original draft preparation, H.Z., J.W., Y.C., and F.X.; writing—review and editing, H.Z., J.W., and J.H.; visualization, H.Z., J.W., Y.C., and P.W.; supervision, J.H.; project administration, H.Z. and J.W.; funding acquisition, J.H. and L.H. All authors have read and agreed to the published version of the manuscript.

Funding: This research was funded by Special Fund for Hunan innovative province construction project (2023NK1020), Key R&D Plan Project of Shandong Province (2022SFGC0202).

Institutional Review Board Statement: Not applicable.

Data Availability Statement: Data are contained within this article.

Conflicts of Interest: The authors declare no conflicts of interest.

References

1. Luo, X.W.; Hu, L.; He, J.; Zhang, Z.G.; Zhou, Z.Y.; Zhang, W.Y.; Liao, J.; Huang, P.K. Key Technologies and Practice of Unmanned Farm in China. *Trans. Chin. Soc. Agric. Eng.* **2024**, *40*, 1–16. [CrossRef]
2. Liu, J.Z.; Jiang, Y.X. Industrialization Trends and Multi-arm Technology Direction of Harvesting Robots. *Trans. Chin. Soc. Agric. Mach.* **2024**, *55*, 1–17. [CrossRef]
3. Sun, Z.Q.; Tang, S.Y.; Luo, X.F.; Dong, J.W.; Xu, N. Research and Application Status of Path Planning for Agricultural Inspection Robots. *Agric. Equip. Veh. Eng.* **2025**, *63*, 18–24. [CrossRef]
4. Wang, N.; Han, Y.X.; Wang, Y.X.; Wang, T.H.; Zhang, M.; Li, H. Research Progress of Agricultural Robot Full Coverage Operation Planning. *Trans. Chin. Soc. Agric. Mach.* **2022**, *53*, 1–19. [CrossRef]
5. Zhang, M.; Ji, Y.H.; Li, S.C.; Cao, R.Y.; Xu, H.Z.; Zhang, Z.Q. Research Progress of Agricultural Machinery Navigation Technology. *Trans. Chin. Soc. Agric. Mach.* **2020**, *51*, 1–18. [CrossRef]
6. Xu, T.; Zhou, Z.Q. Current Status and Trends of Agricultural Robotics Development. *Agric. Equip. Technol.* **2024**, *2025*, 51.
7. Chen, Y.; Zhang, T.M.; Sun, D.Z.; Peng, X.D.; Liao, Y.Y. Design and experiment of locating system for facilities agricultural vehicle based on wireless sensor network. *Trans. Chin. Soc. Agric. Eng.* **2015**, *31*, 190–197. [CrossRef]
8. Ma, Q.; Tang, G.Y.; Fu, Z.Y.; Deng, H.G.; Fan, J.N.; Wu, C.C. Research progress on autonomous agricultural machinery technology and automatic parking methods in China. *Trans. Chin. Soc. Agric. Eng.* **2025**, *41*, 15–27. [CrossRef]
9. Liu, C.L.; Gong, L.; Yuan, J.; Li, Y.M. Development Trends of Agricultural Robots. *Trans. Chin. Soc. Agric. Mach.* **2022**, *53*, 1–22, 55. [CrossRef]

10. Liu, Z.P.; Zhang, Z.G.; Luo, X.W.; Wang, H.; Huang, P.K.; Zhang, J. Design of automatic navigation operation system for Lovol ZP9500 high clearance boom sprayer based on GNSS. *Trans. Chin. Soc. Agric. Eng.* **2018**, *34*, 15–21. [CrossRef]
11. Zhang, Z.G.; Luo, X.W.; Zhao, Z.X.; Huang, P.S. Trajectory Tracking Control Method Based on Kalman Filter and Pure Pursuit Model for Agricultural Vehicle. *Trans. Chin. Soc. Agric. Mach.* **2009**, *40*, 6–12.
12. Ding, Y.C.; He, Z.B.; Xia, Z.Z.; Peng, J.Y.; Wu, T.H. Design of navigation immune controller of small crawler-type rape seeder. *Trans. Chin. Soc. Agric. Eng.* **2019**, *35*, 12–20. [CrossRef]
13. Li, Q.T.; Liu, B. Design and Path Planning of Agricultural Machinery Automatic Navigation System Based on GNSS. *Test. Meas. Technol.* **2024**, *38*, 256–263. [CrossRef]
14. Hu, J.T.; Gao, L.; Bai, X.P.; Li, T.C.; Liu, X.G. Review of research on automatic guidance of agricultural vehicles. *Trans. Chin. Soc. Agric. Eng.* **2015**, *31*, 1–10. [CrossRef]
15. Ji, C.Y.; Zhou, J. Current Situation of Navigation Technologies for Agricultural Machinery. *Trans. Chin. Soc. Agric. Mach.* **2014**, *45*, 44–54. [CrossRef]
16. Luo, X.W.; Liao, J.; Hu, L.; Zhou, Z.Y.; Zhang, Z.G.; Zang, Y.; Wang, P.; He, J. Research progress of intelligent agricultural machinery and practice of unmanned farm in China. *J. South China Agric. Univ.* **2021**, *42*, 8–17. [CrossRef]
17. Wang, J.; Chen, Z.W.; Xu, Z.S.; Huang, Z.D.; Jing, J.S.; Niu, R.X. Inter-rows Navigation Method of Greenhouse Robot Based on Fusion of Camera and LiDAR. *Trans. Chin. Soc. Agric. Mach.* **2023**, *54*, 32–40. [CrossRef]
18. Yousuf, S.; Kadri, M.B. Information Fusion of GPS, INS and Odometer Sensors for Improving Localization Accuracy of Mobile Robots in Indoor and Outdoor Applications. *Robotica* **2021**, *39*, 250–276. [CrossRef]
19. Yin, X.; Wang, Y.X.; Chen, Y.L.; Jin, C.Q.; Du, J. Development of autonomous navigation controller for agricultural vehicles. *Int. J. Agric. Biol. Eng.* **2020**, *13*, 70–76. [CrossRef]
20. He, Y.; Huang, Z.Y.; Yang, N.Y.; Li, X.Y.; Wang, Y.W.; Feng, X.P. Research Progress and Prospects of Key Navigation Technologies for Facility Agricultural Robots. *Smart Agric.* **2024**, *6*, 1–19. [CrossRef]
21. Liu, Y.; Ji, J.; Pan, D.; Zhao, L.J.; Li, M.S. Localization Method for Agricultural Robots Based on Fusion of LiDAR and IMU. *Smart Agric.* **2024**, *6*, 94–106. [CrossRef]
22. Jin, B.; Li, J.X.; Zhu, D.K.; Guo, J.; Su, B.F. GPS/INS navigation based on adaptive finite impulse response-Kalman filter algorithm. *Trans. Chin. Soc. Agric. Eng.* **2019**, *35*, 75–81. [CrossRef]
23. Cao, J.J.; Fang, J.C.; Sheng, W.; Bai, H.X. Adaptive neural network prediction feedback for MEMS-SINS during GPS outage. *J. Astronaut.* **2009**, *30*, 2231–2236, 2264. [CrossRef]
24. Shen, C.; Zhang, Y.; Tang, J.; Cao, H.; Liu, J. Dual-optimization for a MEMS-INS/GPS system during GPS outages based on the cubature Kalman filter and neural networks. *Mech. Syst. Signal Process.* **2019**, *133*, 106222. [CrossRef]
25. Liu, Q.Y.; Hao, L.L.; Huang, S.J.; Zhu, S.Y. A New Study of Neural Network Aided GPS/MEMS-INS Integrated Navigation. *J. Geomat. Sci. Technol.* **2014**, *31*, 336–341. [CrossRef]
26. Zhang, W.Y.; Wang, J.; Zhang, Z.G.; He, J.; Hu, L.; Luo, X.W. Self-calibrating Variable Structure Kalman Filter for Tractor Navigation during BDS Outages. *Trans. Chin. Soc. Agric. Mach.* **2020**, *51*, 18–27. [CrossRef]
27. Wei, Y.F.; Li, Q.L.; Sun, Y.T.; Sun, Y.J.; Hou, J.L. Research on Orchard Robot Navigation System Based on GNSS and Lidar. *J. Agric. Mech. Res.* **2023**, *45*, 55–61+69. [CrossRef]
28. Hu, L.; Wang, Z.M.; Wang, P.; HE, J.; Jiao, J.K.; Wang, C.Y.; Li, M.J. Agricultural robot positioning system based on laser sensing. *Trans. Chin. Soc. Agric. Eng.* **2023**, *39*, 1–7. [CrossRef]
29. Shan, T.; Englot, B.; Meyers, D.; Wang, W.; Ratti, C.; Rus, D. LIO-SAM: Tightly-coupled Lidar Inertial Odometry via Smoothing and Mapping. In Proceedings of the 2020 IEEE/RSJ International Conference on Intelligent Robots and Systems, Las Vegas, NV, USA, 25–29 October 2020. [CrossRef]
30. Liu, H.; Pan, G.S.; Huang, F.X.; Wang, X.; Gao, W. LiDAR-IMU-RTK fusion SLAM method for large-scale environment. *J. Chin. Inert. Technol.* **2024**, *32*, 866–873. [CrossRef]
31. Jiang, L.; Xu, B.; Husnain, N.; Wang, Q. Overview of Agricultural Machinery Automation Technology for Sustainable Agriculture. *Agronomy* **2025**, *15*, 1471. [CrossRef]
32. Tateno, K.; Tombari, F.; Laina, I.; Navab, N. CNN-SLAM: Real-Time Dense Monocular SLAM with Learned Depth Prediction. In Proceedings of the 2017 IEEE Conference on Computer Vision and Pattern Recognition, Honolulu, HI, USA, 21–26 July 2017. [CrossRef]
33. Feng, M.; Hu, S.; Ang, M.; Lee, G.H. 2D3D-MatchNet: Learning to Match Keypoints Across 2D Image and 3D Point Cloud. *arXiv* **2019**, arXiv:1904.09742. [CrossRef]

《中文核心期刊要目总览》收录
Ei Compendex(核心版)收录
百种中国杰出学术期刊
RCCSE中国权威学术期刊

ISSN 1002-6819
CN 11-2047/S
CODEN NGOXEO
www.tcsae.org

农业工程学报

NONGYE GONGCHENG XUEBAO | TRANSACTIONS OF THE CHINESE SOCIETY OF AGRICULTURAL ENGINEERING

2025年 第41卷 VOL.41 24

农业工程学报
TRANSACTIONS OF THE CHINESE SOCIETY OF AGRICULTURAL ENGINEERING
二〇二五年十二月
第四十一卷
第二十四期
中国农业工程学会

农 业 工 程 学 报

2025 年 12 月第 24 期　（总第 521 期）　第 41 卷

目　次

·农业生物环境与能源工程·

·土地保障与生态安全·

·农产品加工工程·

期刊基本参数：CN 11-2047/S*1985*s*16*336*zh*P* ￥80.00*260*33*2025-12

✦✲✦✲✦✲✦✲✦✲✦✲✦✲✦✲✦✲✦✲✦✲✦✲✦

致谢：XXXXXXXX

Transactions
of the Chinese Society of Agricultural Engineering
Vol.41 No.24 (Total No.521) Dec. 2025

CONTENTS

• Special Topic on the 40th Anniversary of the Founding of the Transactions of the Chinese Society of Agricultural Engineering (Transactions of the CSAE) •

• Review and Special •

• Agricultural Mechanization and Equipment Engineering •

• Soil and Water Engineering •

• Agricultural Information and Electrical Technologies •

• Agricultural Bioenvironmental and Energy Engineering •

• Land Security and Ecological Safety •

• Agricultural Produce Processing Engineering •

· 农业水土工程 ·

疏松土层厚度及其压实量对灌水沉降的影响

陈高隆，陈禹琦，胡 炼，汪 沛※，罗锡文，赵润茂，黄志铖，王靖霆，贺子豪，邓宇飞

（1. 华南农业大学南方农业机械与装备关键技术教育部重点实验室，广州 510642；
2. 农业装备技术全国重点实验室，广州 510642）

摘 要：农田耕整是水稻生产的首要环节，其中稻田旱整作业的应用范围不断扩大。然而，稻田旱整灌后常产生差异性沉降，显著降低农田平整度，影响水稻生长管理效率与产量。为此，该研究通过田间试验探究土壤沉降差异的主要因素，并结合容器试验建立其与土壤沉降之间的关系。基于此，研究提出通过压实（定义为压实厚度）来控制土壤沉降，构建疏松土层、压实厚度与土壤沉降（膨胀）的非线性回归模型，并通过容器试验验证其预测准确性。结果表明，稻田旱耕整及灌后土壤沉降存在显著差异，同一田块内疏松土层厚度是影响沉降差异的主要因素，且与土壤沉降呈显著线性正相关。施加压实处理后，沉降量随压实厚度增加而减小，当压实厚度超过一定范围后，土壤出现膨胀现象。模型验证结果显示，预设沉降量与实测沉降量的绝对误差分别为 0.64 和 0.25 mm，均方根误差分别为 1.43 和 0.39 mm，表明回归关系模型具有较高的预测精度与可靠性。该研究构建的关系模型可为智能耕整技术提供理论依据，实现灌溉后土壤沉降的精准控制，从而提高农田平整度。此外，土壤沉降的量化分析还可为起垄种植作物的时空精准管理提供科学支撑。

关键词：旱地平整；疏松土层；灌溉；土壤沉降；压实厚度

doi：10.11975/j.issn.1002-6819.202502024

中图分类号：S225.5+1 **文献标志码**：A **文章编号**：1002-6819(2025)-24-0095-10

陈高隆，陈禹琦，胡炼，等. 疏松土层厚度及其压实量对灌水沉降的影响[J]. **农业工程学报**，2025，41(24)：95-104. doi: 10.11975/j.issn.1002-6819.202502024 http://www.tcsae.org

CHEN Gaolong, CHEN Yuqi, HU Lian, et al. Effects of loose soil layer thickness and compaction on soil subsidence after irrigation[J]. Transactions of the Chinese Society of Agricultural Engineering (Transactions of the CSAE), 2025, 41(24): 95-104. (in Chinese with English abstract) doi: 10.11975/j.issn.1002-6819.202502024 http://www.tcsae.org

0 引 言

水稻是三大粮食作物之一，为全球超过 50% 的人口提供粮食保障[1]。水稻生产以漫灌和淹灌为主，提高农田平整度可节约水稻生产用水，提高灌溉效率与均匀度[2-3]。此外，农田平整作业还可提高土地利用率、秧苗和稻种的成活率、杂草防治率、作物成熟均匀度和产量，并减少肥药施用量[4-7]。

在水稻整个生产周期，大部分生长期处于水田环境。根据耕整作业前的农田含水量差异，稻田耕整方式可分为水田耕整和旱田耕整[8-9]。水田耕整方式在华南地区应用广泛[10-11]，其工序包括灌溉、旋耕、打浆、沉淀、平整和再沉淀，随后进行插秧或直播。旱田耕整方式工序包括碎土和旱平整，再进行泡水插秧或直播。水田平整方式因泥浆流动性大、硬底层地形复杂以及工序繁多等因素，导致作业效率低、成本高和周期长。相比之下，旱田平整方式因土壤流动性小、单程土方搬运量大、耕整工序少，具有效率高、成本低和周期短的优势，使旱田平整方式在全球范围内广泛应用，包括东南亚和南亚等国家在内[12]。随着水稻生产国积极推行“小田并大田”和“高标准农田建设”等土地整治政策[13-15]，田块面积逐步增大。同时，稻田旱平免打浆技术与水稻旱直播技术的推广应用，进一步扩大了旱田平整方式的应用范围和需求。

农田精准平整技术主要有激光控制平整技术和 GNSS 控制平整技术，平整精度均可达±3 cm 以内[16-19]。旱田经旋耕、精准平整和灌溉后可形成适宜水稻种植的环境。研究表明，耕整作业可改善耕层土壤的物理特性，如孔隙度、容重和紧实度，使表层土壤结构更加疏松[20-21]。疏松土壤结构有利于植物生长过程中液体和气体的交换。然而，在实际生产中，农田灌溉后会产生局部低洼且积水区域，导致稻种和秧苗存活率下降，其主要原因是疏松土壤在灌溉（降雨）后发生了沉降。已有研究从干湿循环与土壤固结过程探讨了其对土壤物理特性及侵蚀性能的影响[22-23]，并揭示了团聚体破坏、颗粒沉积与孔隙演变等机制。研究表明，水分入渗会引起团聚体解体和细颗粒下移，改变孔径分布与孔隙结构[24-28]；同时，水分表面张力增强颗粒间结合力，在湿润条件下有效应力趋于零，使土壤颗粒因自身重力发生重新排列与压密[29-30]。综上，灌溉后疏松土壤的颗粒沉积与结构重构是导致孔隙度降低和密实度增加的主要原因，从而

收稿日期：2025-02-10 修订日期：2025-10-31
基金项目：农业装备技术全国重点实验室（华南农业大学）开放课题（SKLAET - 202404）、国家自然科学基金项目（32472016、32101623）
作者简介：陈高隆，博士后，主要研究方向为智能农机装备。
Email：gl.chen@scau.edu.cn
※通信作者：汪沛，博士，副教授，主要研究方向为无人农场和精准作业。
Email：wangpei@scau.edu.cn

引发区域性沉降与局部积水。然而，关于农田疏松土壤灌溉后的沉降差异性的研究报道比较少。

针对上述稻田旱整方式存在的问题，本研究旨在探究影响土壤沉降差异的主要因素，建立其与土壤沉降间的关系，并提出减少沉降差异的方案。具体而言，首先，通过田间试验，系统研究稻田旱耕整及灌后的土壤沉降特性，重点从地形变化、土壤物理性质变化与生产实际 3 个方面进行分析；其次，通过容器试验，建立主要因素与土壤沉降间的关系；最后，提出采用压实来控制土壤沉降，构建主要因素、压实量与土壤沉降的关系模型，并进行验证试验，以期为精准化稻田旱整作业提供指导参考。

1 材料与方法

1.1 试验地概况

如图 1 所示，试验地位于广州市华南农业大学教研基地水稻田（23°14′N，113°38′E）。根据国际制土壤质地分级标准，试验田的土壤为砂质壤土[31]，是长期双季稻种植形成的典型水稻土。该地区属亚热带季风气候带，年平均温度为 24 ℃，年平均降水量为 1 891.9 mm。试验田全年采用旋耕方式耕作，耕层浅薄。

图 1 试验地点

Fig.1 Test site

1.2 土壤沉降差异探究试验

1.2.1 农田地形变化监测

为探究农田疏松土层在灌水后的土壤沉降差异，试验于 2023 年 3 月在 2 号试验田进行。考虑到土壤耕整方式多样（如犁耕、旋耕等），本研究选择旋耕方式构建农田疏松土层环境。试验前，田块经历了水稻收获、多次干湿循环和农机碾压，导致土壤出现明显固结。试验过程分为 3 个阶段：旋耕前、旋耕后（即二次旋耕）和灌水后。在各阶段，均采用全站仪（Leica MS60，测量精度为 1.5 mm/50 m）对农田三维地形进行高精度测量。其中，依据水稻插秧对田间水层的要求，灌水定额设定为保持 20 ～ 30 mm 水层。在灌水后阶段，试验田蓄水 3 d 后排水，随后进行地形测量。

由于全站仪的测量范围有限，距离全站仪较远处的点云密度较低，因此本研究采用多站布设的测量方式，并将各测站的数据进行合并，以获取完整的试验区域三维地形信息。在旋耕前和旋耕后阶段，在试验区域内布设 2 个测量点；在灌水后阶段，考虑到水田环境下全站仪架设操作难度大且易破坏田面，改为在试验田周边布设 6 个测量站点。为确保测量稳定性，将全站仪三脚架固定于田块硬底层上。全站仪建立坐标系后可自动生成质量报告，3 个阶段的架设平均标准误差如表 1 所示。在 X、Y 轴方向的平均标准误差不超过 15 mm，在 Z 轴方向的平均标准误差不超过 1 mm，为准确反映土壤沉降差异提供了可靠的测量保障。

表 1 全站仪建站的平均标准误差

Table 1 The average standard error of the total station setup in the three stages mm

阶段 Stages	坐标方向		
	X	Y	Z
旋耕前 Pre-tillage	11.00	12.55	0.65
旋耕后 Post-tillage	8.10	8.75	0.15
灌水后 Post-irrigation	7.48	6.33	0.58

1.2.2 土壤物理参数采集

耕整作业改变了土壤的紧实度与容重等物理参数，使压实的土壤变为松散。土壤紧实度和容重是表征土壤压实和疏松程度的重要指标[32-34]。然而，由于容重测量需取样，易破坏田面且垂向取样间距较大，从而限制了其在分析土壤沉降差异时的应用[35]。相比之下，土壤穿透阻力的空间分辨率较高，是分析土壤物理差异空间分布的优选指标[36]。因此，本研究以土壤穿透阻力来分析旋耕前后土层结构的变化特征。为确保旋耕前后穿透阻力测量位置的一致性，在 2 号试验田（85 m×35 m）内划定长 65 m 和宽 25 m 的观测区，并按 5 m 间隔进行网格化布设。采用土壤紧实度仪（SC900型）在 84 个网格交点处测定土壤穿透阻力。考虑到各测点含水率存在差异，为提高数据准确性，同时使用土壤含水率仪（山东优云谱光电科技有限公司，YP-SWY 型）测定各测点的含水率，并对穿透阻力进行标准化处理。

根据 AKSAKAL 等[37] 提出的计算式，对不同土壤含水率的土壤穿透阻力进行标准化：

$$r_s = r_m \exp((m_m - 0.1)/0.716) \quad (1)$$

式中 r_s 为标准化的穿透阻力，MPa；r_m 为测量的穿透阻力，MPa；m_m 为测量点的含水率，kg/kg。

1.3 疏松土层及其压实灌后沉降试验

1.3.1 疏松土层及其压实对灌后沉降的影响

为研究不同疏松土层厚度经灌水后的土壤沉降量，本研究以二次旋耕作业后的疏松土壤为研究对象，参照农田耕层深度设置 50、100、150、200、250 和 300 mm 共 6 个土层厚度开展沉降试验，各土层厚度重复 3 次。

同时，本研究提出通过压实疏松土层来减少土壤沉降差异，并以压实厚度作为压实程度的评价指标。压实结构疏松的土壤可以提高土壤紧密性和稳定性[38]。诸多因素可使土壤发生压实，如农机的接地比压、轴载、压

实次数以及行驶速度[39-41]。通过建立各因素和土壤沉降的关系，可为压实作业提供理论依据。然而，土壤压实是由垂直应力引起的土壤压缩形变和水平应力引起的土壤剪切形变共同作用的结果。其中，垂直方向的压缩形变（压实厚度）对农田平整度影响显著。为研究不同疏松土层厚度经不同程度压实的沉降情况，设置 100、150、200、250 和 300 mm 共 5 个疏松土层厚度，并对每个厚度进行 4 个压实水平处理，其中 4 个压实水平分别代表轻度、中度、重度及超重度，各处理重复 3 次。

试验于 2023 年 7 月在 1 号试验田内进行，选取二次旋耕作业后的疏松土壤作为试验土样。采用土壤含水率仪和土壤紧实度仪分别测定土样的平均含水率和土壤穿透阻力。结果表明，平均土壤含水率为 6.25%，与田间试验条件下的土壤基本一致。标准化土壤穿透阻力随疏松土层厚度的增加而升高，最大值未超过 120 KPa。以内尺寸为 250 mm×250 mm×320 mm 的透明箱体为土壤容器，容器外侧面粘贴刚性刻度尺（精度 1 mm）。试验步骤如下：首先，将疏松土壤均匀铺入容器内，直至土层达到预设厚度，并由铲平板整平表面；其次，在容器口标记 9 个固定测量点，采用钢直尺（精度 1 mm）测定土层实际平均厚度；再次，为避免注水速度过快造成表层扰动，沿容器内壁缓慢注水，直至水位稳定并高出土层表面一定高度；最后，浸泡 24 h 后，当土层厚度变化趋于稳定，再次测定 9 个固定测点的土层厚度，计算平均沉降量。对于压实土壤试验组，在整平土层和灌水步骤之间增加压实土壤的步骤，以模拟压实作用对土壤沉降的影响。试验过程如图 2 所示。

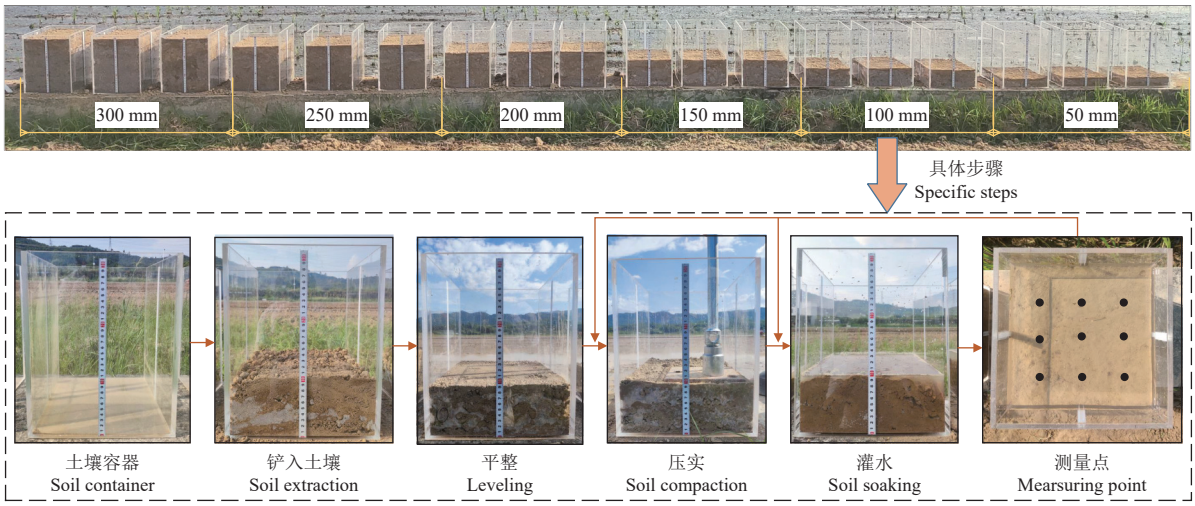

图 2　试验过程及具体步骤

Fig.2　Test process and specific steps

1.3.2　回归关系建立与验证

通过压实疏松土层减少土壤沉降差异，该过程需综合考虑压实厚度和土壤沉降量的共同作用。因此，建立疏松土层厚度、压实厚度与土壤沉降量之间的定量关系是实现精准压实作业的关键。依据疏松土层及其压实灌后沉降试验结果，拟建立三者之间的回归方程，以定量揭示压实条件下的土壤沉降规律。

为验证所建回归方程的预测准确性，本研究开展容器验证试验。根据回归方程与预设目标沉降量，对不同疏松土层厚度进行相应压实与灌水处理。试验结束后，比较实测沉降量与目标沉降量的差异，并以绝对偏差与均方根误差为评价指标，对回归方程的预测准确性进行评估，具体试验步骤如图 2 所示。

1.4　数据处理

对于农田地形变化的监测，本研究采用 Lei Infinity 软件导出全站仪在各阶段测得的地形点云数据，并采用 MATLAB 软件对 3 个阶段观测区的农田地形按照高度值进行可视化渲染。为进一步分析地形变化特征，采用 ArcGIS 软件先对 3 个阶段的地形数据进行栅格化处理，生成数字高程模型，并将旋耕后（灌水前）阶段的数字高程模型分别与旋耕前和灌水后作差值处理，以获取各阶段地形变化的空间分布特征。

对于采集的土壤物理参数数据，在 84 个测量点中均匀选取 6 个代表性测点，对比旋耕前后的标准化穿透阻力。随后，采用 Mann-Kendall 突变检测法来确认疏松土层的厚度。该方法是一种非参数检验方法，可用于检测变量的趋势变化并确定数据序列中发生突变的位置[42]。其主要优点是无需对数据序列进行特定的分布检验，广泛用于分析水文、气象等数据变化趋势[43-44]。根据各采样点穿透阻力在土壤剖面中的变化特征，可将其视为在空间序列上的变化。因此，采用 Mann-Kendall 突变检验法可判断土壤穿透阻力发生突变的位置，从而确定疏松土层的厚度。考虑到垂直序列中穿透阻力数据间的相关性会影响检验结果[45]，在应用该方法前，采用去趋势预置白法对数据进行预处理。采用的具体方法为一阶差分法[46]，具体计算式为

$$Y_{s,t} = R_{s,t+1} - R_{s,t} \tag{2}$$

$$T_{s,t} = R_{s,t} - Y_{s,t}\ (t = 1,2,...,n-1) \tag{3}$$

式中$Y_{s,t}$为不含趋势的新数据序列；$R_{s,t}$为标准化土壤穿透阻力原始数据序列；$T_{s,t}$为标准化土壤穿透阻力原始数据序列的趋势序列；n为序列长度；t为序列中每个数据

对应的次序。

在 Mann-Kendall 检验中，对于有 n-1 个样本的空间序列，构造一个样本统计量 s_k：

$$s_k = \sum_{i=1}^{k} p_i \quad k = 1,2,...,n-1 \tag{4}$$

$$p_i = \begin{cases} 1, \text{ if } Y_{s,i} > Y_{s,j} \\ 0, \text{ if } Y_{s,i} \leqslant Y_{s,j} \end{cases} \quad i = 1,2,...,n-1 \text{ 且 } j = 1,2,...,i \tag{5}$$

式中 k 为当前累积样本数；p_i 为比较符号函数。

在原序列独立的假设下，样本统计量 s_k 定义为

$$u(k) = \frac{s_k - E(s_k)}{\sqrt{var(s_k)}} \tag{6}$$

$$\begin{cases} E(s_k) = \dfrac{k(k-1)}{4} \\ var(s_k) = \dfrac{k(k-1)(2k+5)}{72} \end{cases} \tag{7}$$

式中 $u(k)$ 为正向统计序列；$u'(k)$为反向统计序列；$E(s_k)$ 为样本统计量 s_k 的均值；var(s_k) 为样本统计量 s_k 的方差。

$u(k)$ 的值是从序列的开始到结束计算，而从反序列计算可得$u'(k)$。如果 $u(k)$ 和$u'(k)$两条曲线的交点在置信区间（±1.96）内，则该点在本数据序列中突变显著。将确定发生突变点的序列顺序转换为相应的深度，即疏松土层厚度。

疏松土层及其压实灌后沉降试验数据采用 Excel 2019 进行基本处理，并采用 SPSS26.0 软件对疏松土层厚度、压实厚度和沉降量进行回归分析。

2 结果与分析

2.1 土壤沉降差异主要因素

2.1.1 农田地形变化结果与分析

3 个阶段的观测区地形高度可视化结果如图 3 所示。经旋耕作业后的田块地形高度明显升高，经过灌水后的地形高度下降。数据统计结果显示，旋耕前、旋耕后和灌水后 3 个阶段的地形平均高度分别为 15.813、15.858 和 15.844 m。旋耕作业使地形平均升高 47 mm，而灌水后农田地形平均降低 14 mm，这验证了农田疏松土层经灌水后存在沉降现象。

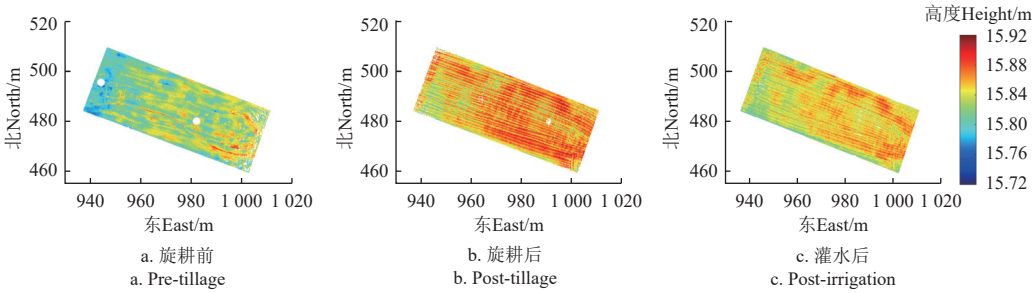

a. 旋耕前
a. Pre-tillage

b. 旋耕后
b. Post-tillage

c. 灌水后
c. Post-irrigation

图 3 三个阶段的农田地形变化

Fig.3 Height of farmland topography in three phases

旋耕前后与灌水前后的地形变化空间分布特征如图 4 所示。以旋耕前的农田地形为基准，旋耕后田块各区域的地形高度变化差异明显；同样，以旋耕后的地形为基准，灌水后农田各区域的地形高度变化也存在差异。因此，农田经旋耕和灌水作业后，不同区域间的沉降表现出明显的空间差异性。此外，通过对比图 4a 和图 4b 可知，旋耕后地形高度变化较大区域（红色区域），灌水后所产生的沉降量也随之变大（红色区域），说明旋耕作业形成的疏松土层较厚区域在灌水后更易发生显著沉降。

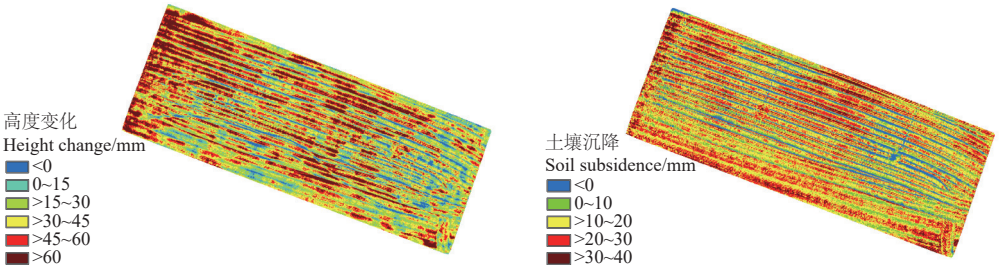

a. 旋耕前后
a. Before and after rotary tillage

b. 灌水前后
b. Before and after irrigation

图 4 地形变化空间分布特征

Fig.4 Spatial distribution characteristics of topographic height changes

2.1.2 土壤物理参数表征分析

土壤穿透阻力很大程度上受土壤含水率的影响[47]。旱作区土壤含水率普遍较低，且旋耕作业对其影响较小。图 5 为旋耕前后两个阶段各个测点的土壤含水率情况。通过数据统计，土壤含水率平均值为 6.21%，标准差为 0.56%，表明各区域间的土壤含水率差异性不显著。

旋耕前后 6 个测量点位置的标准化穿透阻力对比结果如图 6 所示。旋耕前土壤穿透阻力在浅土层呈快速上

升趋势，且随着深度增加持续保持在较高水平，表明其处于较强固结状态。相比之下，旋耕后土壤穿透阻力在一定范围内显著降低，并在超过一定深度后逐渐升高。这表明旋耕后农田土壤在一定深度内的土壤较松散，超过一定深度后的土壤松散程度与旋耕前的农田基本一致。因此，旋耕前后土壤穿透阻力的差异性主要体现在疏松土层厚度上。此外，根据旋耕后的土壤穿透阻力曲线，不同测点的疏松土层厚度也存在一定差异。采用 Mann-Kendall 突变检验可确定土壤穿透阻力曲线中突变点的位置，从而判定疏松土层厚度，判定结果如图 7 所示。

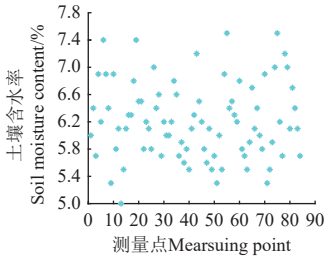

图 5　各测点位置的含水率情况

Fig.5　Soil moisture content at measuring points

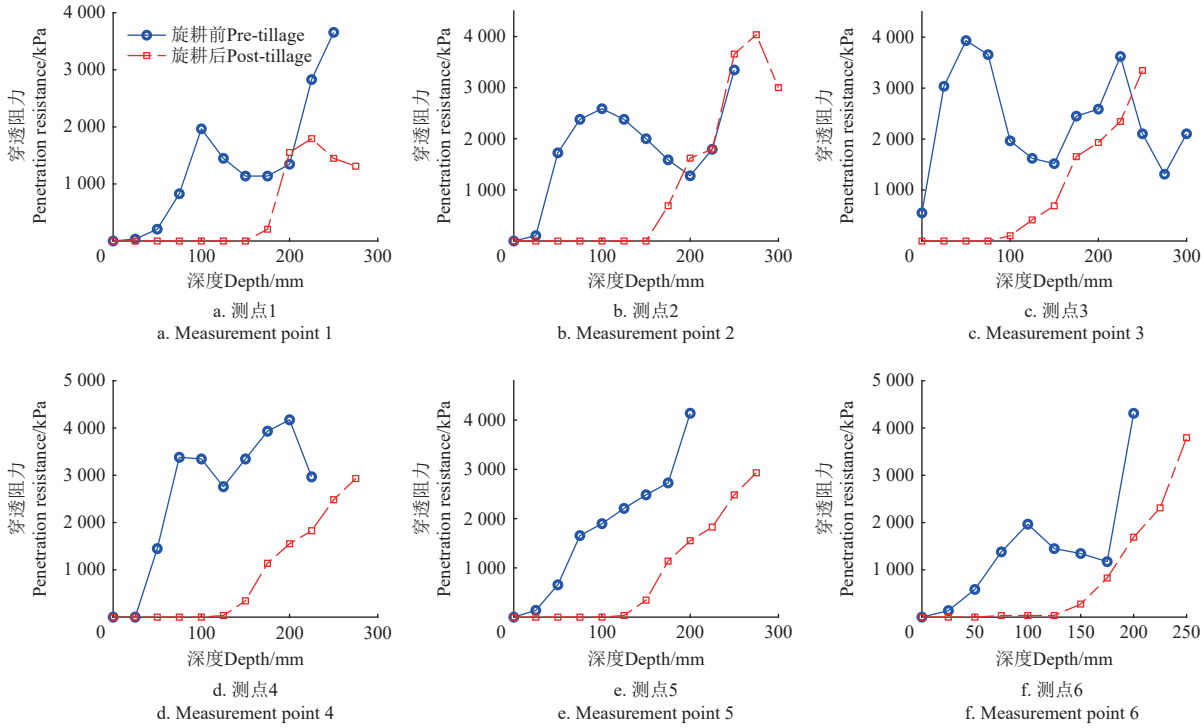

图 6　旋耕前后 6 个测点位置的穿透阻力对比

Fig.6　Comparison of penetration resistance at six measurement points before and after rotary tillage

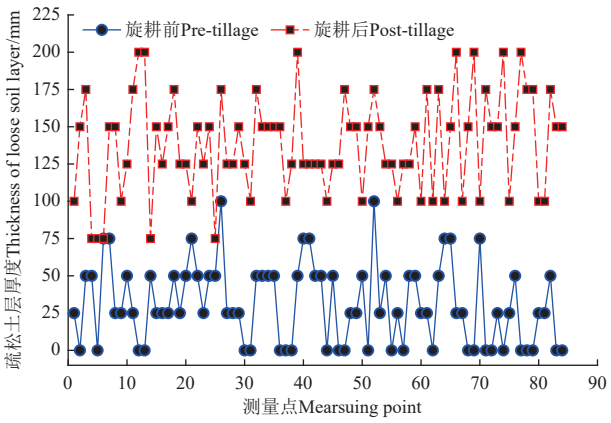

图 7　疏松土层厚度的判断结果

Fig.7　Judgment results of the thickness of loose soil layer

由图 7 可知，旋耕前的疏松土层厚度主要分布在 0~50 mm，而旋耕后增至 125~175 mm。已有研究表明，旋耕前田块灌水后的沉降可忽略不计，而旋耕后则出现明显沉降现象[23,48]。因此，同一田块内当疏松土层厚度较小时，灌水后沉降不显著；随着疏松土层厚度的增加，沉降现象愈加明显，且沉降量随厚度增加而增大。

2.1.3　生产应用可行性分析

综上所述，从农田地形与土壤物理参数两个方面的分析可知，导致土壤沉降差异的主要因素是疏松土层厚度。实际生产中，由于田面高低起伏，农机在旋耕作业过程中姿态变化会造成各区域耕作深度差异。旋耕形成的疏松土层在随后的“挖高填低”平整作业中，其厚度将发生显著变化，如图 8 所示。目前，土壤紧实度和容重的获取主要依赖定点取样测定，该方法效率低且难以实现实时监测，因此难以用于推测农田各区域沉降量和指导耕整作业。相比之下，利用多源传感技术可实现对农田疏松土层厚度的实时、快速获取[49-50]。基于此，本研究选取疏松土层厚度作为影响土壤沉降差异的主要因素，并进一步量化其与土壤沉降量之间的定量关系。

2.2　疏松土层厚度与土壤沉降关系

图 9 展示了不同疏松土层厚度灌水后的沉降情况。当疏松土层厚度为 50 mm 时，土壤沉降几乎可以忽略不计。由图 7 可知，未旋耕农田的疏松土层厚度主要分布在 0~50 mm 范围内，处于不发生显著沉降的厚度区间。

这一结果与 WANG 等[23]、MOREIRA 等[48]提出的研究结论一致，均认为未旋耕农田在经历干湿循环后沉降量可忽略不计。随着疏松土层厚度增加，土壤沉降量呈显著上升趋势。二者之间表现出良好的线性相关性，线性回归建立二者关系为：$y=0.15x-8.846(x\geqslant 50)$，$R^2$=0.970。因此，农田经旋耕和平整作业后各区域疏松土层厚度不一，会导致灌水后呈现不同程度的沉降现象。此外，沉降差异的程度主要受未耕整农田原始地形起伏的影响。对于地形起伏大的农田，经平整作业后各区域形成的疏松土层厚度差异更为显著，尤其低洼区域经过耕整作业后会出现较厚的疏松土层。根据线性关系可推算，当疏松土层厚度达到 300 mm 时，土壤沉降量可达 36.15 mm，这值已超过高标准农田建设对农田平整度（±30 mm）的规范要求。

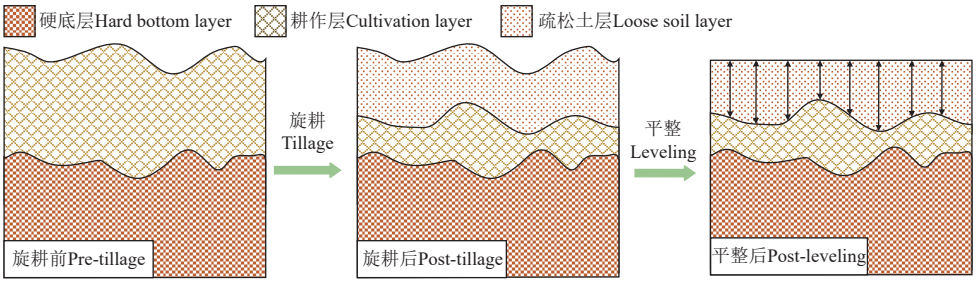

图 8 疏松土层厚度差异示意图

Fig.8 Schematic diagram of thickness differences in loose soil layers

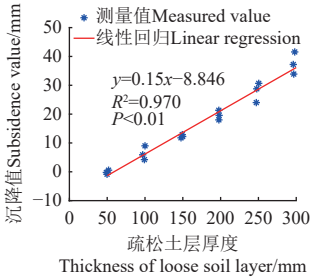

图 9 不同疏松土层厚度的沉降情况

Fig.9 Subsidence for different thicknesses of loose soil layers

2.3 压实疏松土层对土壤沉降的影响

图 10 展示了疏松土层经不同压实的沉降情况。图中负沉降值表示土壤在灌水后发生膨胀，即土层厚度增加。如图 10a 所示，随着压实厚度增加，疏松土层沉降量逐渐减小；当压实厚度超过一定阈值后，疏松土层发生膨胀，且膨胀程度随压实厚度增加而增强。分别对 5 个疏松土层厚度与沉降量关系进行拟合分析，各土层厚度的拟合结果均表现出较高的相关性（R^2>0.90）。由拟合曲线可知，各疏松土层厚度的沉降变化趋势基本一致。

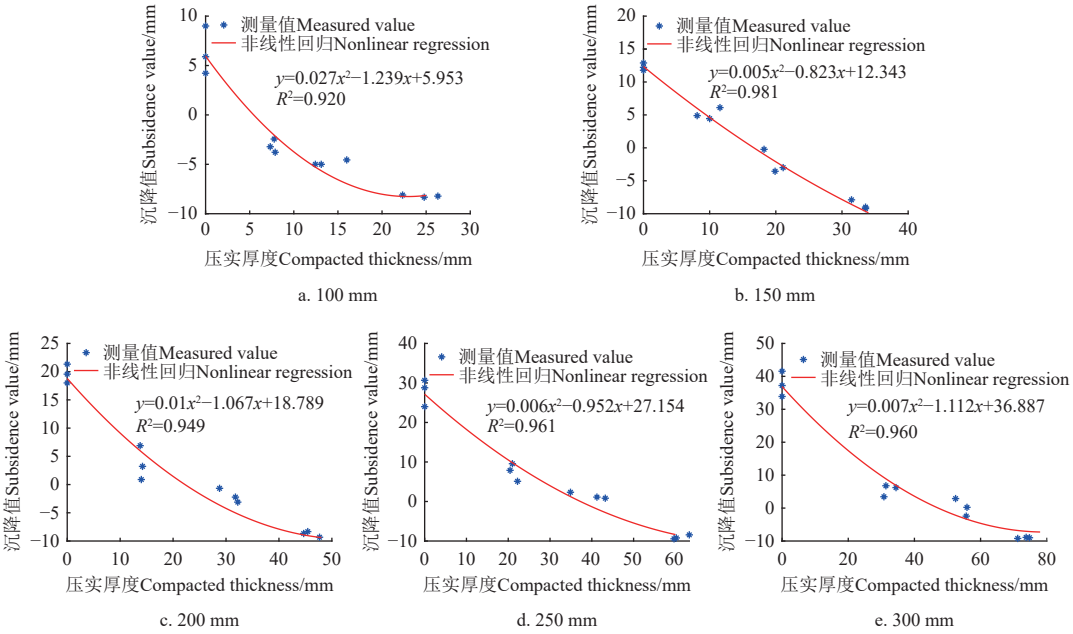

图 10 疏松土层（100~300mm 厚度）经不同压实的沉降情况

Fig.10 Subsidence of five loose soil layers (100–300 mm in thickness) subjected to different compaction

通过二次拟合曲线可计算出上述 5 个疏松土层厚度经不同压实的沉降量。在实际生产中，旋耕和平整作业后会形成不同厚度的疏松土层。因此，有必要建立不同疏松土层厚度经不同压实后的沉降关系。由试验结果可知，土壤沉降量和疏松土层厚度呈线性关系，但疏松土层厚度与压实厚度间同时影响沉降量，因此，建立如下非线性回归方程：

$$s_s=0.0002s_t^2+0.007s_c^2+0.075s_t-0.524s_c-0.002s_ts_c-4.605 \quad (8)$$

式中s_s为沉降量，mm；s_t为疏松土层厚度，mm；s_c为压

实厚度，mm。

非线性回归方程的 R^2=0.964，均方根误差为 2.4 mm，表明拟合度较好。因此，可以利用式（8）关系来描述土壤沉降。

2.4　回归关系检验结果

如表 2 所示，回归关系验证试验中预设的土壤沉降量分别为 5 和 –9 mm，依据式（8）计算可得各土层对应的压实厚度。

表 2　沉降一致时各土层厚度所需的压实厚度

Table 2　Compaction thickness required for each soil thickness under uniform subsidence　　mm

沉降值 Subsidence	土层厚度 Thickness of the soil layer	压实厚度 Compaction thickness	沉降值 Subsidence	土层厚度 Thickness of the soil layer	压实厚度 Compaction thickness
5	98.7	−0.35	−9	96.40	24.83
	147.87	7.65		145.50	33.78
	198.73	16.36		195.93	44.07
	247.70	25.20		247.10	56.31
	296.73	34.56		297.53	73.28

注：当压实厚度为负数时，不进行压实处理。

Note: No compaction shall be performed if the compaction thickness is a negative value.

如图 11 所示，实际压实厚度能与计算值基本一致，均方根误差为 3.2 mm。

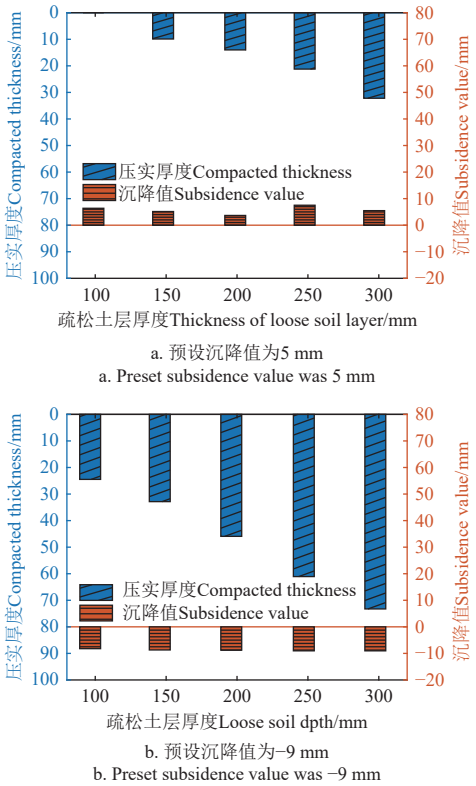

图 11　疏松土层经可控压实后的沉降情况

Fig.11　Subsidence of loose soil layers after controlled compaction

从图 11 可知，在相同预设沉降值下，不同疏松土层经压实后的土壤沉降基本一致。统计分析结果显示，两个预设沉降试验的平均实测沉降值分别为 5.64 和 −8.75 mm，与预设沉降值的绝对误差分别为 0.64 和 0.25 mm，均方根误差分别为 1.43 和 0.39 mm。结果表明实测沉降值与预设沉降值吻合度高，说明本研究提出的以疏松土层厚度为主要因素，并通过回归关系计算压实量，可以准确控制沉降量。

3　讨　论

本研究以疏松土层厚度为主要因素建立了土壤沉降关系，提出了对疏松土层实施压实以控制土壤沉降量，建立了土壤沉降、疏松土层厚度和压实厚度间的定量关系。在同一农田中，农田各区域的土壤类型、土壤含水率以及旋耕次数基本保持一致。本研究的土壤质地为砂质壤土，土壤含水率为 6.25%，旋耕次数为两次。在多地域农田尺度上，可进一步考虑土壤质地、农田含水率以及旋耕次数等因素，对上述关系进行修正与优化。土壤质地是以黏粒、粉砂和砂砾所占比值不同来划分的。在土壤质地方面，适宜水稻生长的土壤质地主要有壤土和砂壤土[51]，两者土壤颗粒组成差异小；在土壤含水率方面，旱地平整作业需保证土壤含水率不宜过高，决定了适宜旱地平整的土壤含水率适宜范围小；在旋耕次数方面，现有研究表明，两次旋耕可达到理想耕整效果[52]，进一步增加旋耕次数对土壤物理性质影响较小，这可认为旋耕次数对土壤沉降的影响小。因此，本研究提出的土壤沉降关系与疏松土层、压实厚度和土壤沉降的关系模型主要适用于砂质壤土，后续可对不同土壤质地、土壤含水率以及旋耕次数来优化本研究提出的关系模型，并开展田间试验验证其适用性。

根据疏松土层、压实厚度与土壤沉降（膨胀）的关系模型，可提出一种智能平整方案。具体步骤如下：首先，以农田三维地形和疏松土层厚度为基础数据，结合土方分布、土壤沉降、适度压实为约束条件，构建压实作业前的地形设计面；其次，根据地形设计面信息制定平整策略；最后，以土层-压实-沉降关系制定可控压实策略，并开展农田平整压实作业。通过该方案，在灌水后可保证农田表面平整度，从而解决稻田旱平方式在灌水后平整度不能满足农业生产的问题。

未经压实的疏松土层与土壤沉降关系不仅可用于水稻生产，也可用于起垄种植作物（如马铃薯、玉米、花生与红薯等）生产提供科学指导。农田经旋耕和起垄作业后形成田垄，其具有较厚的疏松土层。然而，田垄经降雨后易产生土壤沉降现象，导致种子覆土厚度产生变化。对于起垄种植作物，中耕培土既能优化土壤环境、抑制杂草，又有助于促进作物生长。尤其在马铃薯生产中，中耕培土是关键农艺环节，合理的培土次数与厚度可显著提升产量和品质[53]。结合播种深度、土壤沉降和气象信息，可以实时监测种子覆土厚度，并在时空尺度实现精准管理。因此，研究和应用土壤沉降规律可显著提高农情信息颗粒度，为田间作物的精准管理提供科学支撑与技术保障。

4　结　论

本研究通过田间试验和容器试验，研究了疏松土层厚度是影响土壤沉降差异的主要因素，建立了其与土壤沉降间的关系，并提出了减少沉降差异的方案。主要结论如下：

1）通过田间试验系统探究了稻田旱耕整及灌后的土壤沉降特性。结果表明，稻田旱耕整及灌后土壤沉降存在显著差异，疏松土层厚度是其主要因素，且以疏松土层厚度为主要因素满足实际生产需要。

2）通过开展容器试验建立了疏松土层厚度与土壤沉降量间的关系。疏松土层厚度与土壤沉降呈显著线性正相关。当疏松土层厚度较小时，土壤沉降不显著；随着厚度增加，沉降量逐渐增大。

3）研究提出了通过对疏松土层实施压实（定义为压实厚度）可有效控制土壤沉降。容器试验表明，疏松土层灌后沉降量随压实厚度增加而减小，且压实厚度达到一定数值后，土壤出现膨胀现象。通过非线性回归，构建了疏松土层、压实厚度与土壤沉降（膨胀）的关系模型。模型验证结果显示，预设沉降量与实测沉降量的绝对误差分别为 0.64 和 0.25 mm，均方根误差分别为 1.43 和 0.39 mm，表明回归关系模型具有较高的预测精度与可靠性。该关系模型可用于智能耕整技术的实施，精准控制灌水后土壤沉降量，从而保证农田平整度。

［参 考 文 献］

[1] NAWAZ A, REHMAN A U, REHMAN A, et al. Increasing sustainability for rice production systems[J]. Journal of Cereal Science, 2022, 103: 103400.

[2] 景云鹏，刘刚，金志坤. GNSS 双天线结合 AHRS 测量农田地形[J]. 农业工程学报，2019，35(21)：166-174.
JING Yunpeng, LIU Gang, JIN Zhikun. Topographic survey of farmland based on GNSS dualantenna combined with AHRS[J]. Transactions of the Chinese Society of Agricultural Engineering (Transactions of the CSAE), 2019, 35(21): 166-174. (in Chinese with English abstract)

[3] SHEIKH A T, MUGERA A, PANDIT R, et al. The adoption of laser land leveler technology and its impact on groundwater use by irrigated farmland in Punjab, Pakistan[J]. Land Degradation & Development, 2022, 33(12): 2026-2038.

[4] CHEN G L, HU L, LUO X W, et al. A review of global precision land-leveling technologies and implements: Current status, challenges and future trends[J]. Computers and Electronics in Agriculture, 2024, 220: 108901.

[5] KHATRI-CHHETRI A, ARYAL J P, SAPKOTA T B, et al. Economic benefits of climate-smart agricultural practices to smallholder farmers in the Indo-Gangetic Plains of India[J]. Current Science (Bangalore), 2016, 110(7): 1251-1256.

[6] BHATT R, SINGH P, HOSSAIN A, et al. Rice–wheat system in the northwest Indo-Gangetic plains of South Asia: issues and technological interventions for increasing productivity and sustainability[J]. Paddy and Water Environment, 2021, 19(3): 345-365.

[7] NGUYEN-VAN-HUNG, BALINGBING C, SANDRO J, et al. Precision land leveling for sustainable rice production: Case studies in Cambodia, Thailand, Philippines, Vietnam, and India[J]. Precision Agriculture, 2022, 23(5): 1633-1652.

[8] İRSEL G, ALTINBALIK M T. Adaptation of tilt adjustment and tracking force automation system on a laser-controlled land leveling machine[J]. Computers and Electronics in Agriculture, 2018, 150: 374-386.

[9] 胡炼，杜攀，罗锡文，等. 悬挂式多轮支撑旱地激光平地机设计与试验[J]. 农业机械学报，2019，50(8)：15-21.
HU Lian, DU Pan, LUO Xinwen, et al. Design and experiment on multi-wheel support laser land leveler hanging on tractor[J]. Transactions of the Chinese Society for Agricultural Machinery, 2019, 50(8): 15-21. (in Chinese with English abstract)

[10] HU L, XU, HE J, et al. Design and test of tractor-attached laser-controlled rotary scraper land leveler for paddy fields[J]. Journal of Irrigation and Drainage Engineering, 2020, 146(4): 04020002.

[11] 罗锡文，胡炼，何杰，等. 中国大田无人农场关键技术研究与建设实践[J]. 农业工程学报，2024，40(1)：1-16.
LUO Xiwen, HU Lian, HE Jie, et al. Key technologies and practice of unmanned farm in China[J]. Transactions of the Chinese Society of Agricultural Engineering (Transactions of the CSAE), 2024, 40(1): 1-16. (in Chinese with English abstract)

[12] TOMAR S, SINGH Y, NARESH R, et al. Impacts of laser land levelling technology on yield, water productivity, soil health and profitability under arable cropping in alluvial soil of north Madhya Pradesh[J]. Journal of Pharmacognosy and Phytochemistry, 2020, 9(4): 1889-1898.

[13] SHARIFI A, GORJI M, ASADI H, et al. Land leveling and changes in soil properties in paddy fields of Guilan province, Iran[J]. Paddy and Water Environment, 2014, 12(1): 139-145.

[14] BARUAH S, MOHANTY S, ROLA A C. Small Farmers Large Field (SFLF): A synchronized collective action model for improving the livelihood of small farmers in India[J]. Food Security, 2022, 14(2): 323-336.

[15] 杨斌，郭维红，谭青媛，等. 高标准农田建设对耕地系统韧性的影响及其机制[J]. 农业工程学报，2025，41(4)：269-278.
YANG Bin, GUO Weihong, TAN Qingyuan, et al. Impacts of high-standard farmland construction policy on cultivated land system resilience[J]. Transactions of the Chinese Society of Agricultural Engineering (Transactions of the CSAE), 2025, 41(4): 269-278. (in Chinese with English abstract)

[16] 李笑，李宏鹏，牛东岭，等. 基于全球导航卫星系统的智能化精细平地系统优化与试验[J]. 农业工程学报，2015，31(3)：48-55.
LI Xiao, LI Hongpeng, NIU Dongling, et al. Optimization of GNSS-controlled land leveling system and related experiments[J]. Transactions of the Chinese Society of Agricultural Engineering (Transactions of the CSAE), 2015, 31(3): 48-55. (in Chinese with English abstract)

[17] HU L, YANG W, HE J, et al. Roll angle estimation using low cost MEMS sensors for paddy field machine[J]. Computers and Electronics in Agriculture, 2019, 158: 183-188.

[18] ZHAO R, HU L, LUO X, et al. Method for estimating vertical kinematic states of working implements based on laser receivers and accelerometers[J]. Biosystems Engineering, 2021, 203: 9-21.

[19] 汪沛，冯达文，陈高隆，等. 农田精准平整过程中三维地形实时测量方法研究[J]. 农业机械学报，2023，54(3)：41-48.
WANG Pei, FENG Dawen, CHEN Gaolong, et al. Real-time 3d terrain measurement method and experiment in farmland leveling[J]. Transactions of the Chinese Society for Agricultural Machinery, 2023, 54(3): 41-48. (in Chinese with English abstract)

[20] GREEN T R, AHUJA L R, BENJAMIN J G, et al. Advances and challenges in predicting agricultural management effects on soil hydraulic properties[J]. Geoderma, 2003, 116(1-2): 3-27.

[21] MORET-FERNÁNDEZ D, PEÑA-SANCHO C, LÓPEZ M V. Influence of the wetting process on estimation of the water-retention curve of tilled soils[J]. Soil Research, 2016, 54(7): 840.

[22] WILSON G V, ZHANG T, WELLS R R, et al. Consolidation effects on relationships among soil erosion properties and soil

physical quality indicators[J]. Soil and Tillage Research, 2020, 198: 104550.
[23] WANG Y, ZHANG Z, GUO Z, et al. In-situ measuring and predicting dynamics of soil bulk density in a non-rigid soil as affected by tillage practices: Effects of soil subsidence and shrinkage[J]. Soil and Tillage Research, 2023, 234: 105818.
[24] SHIEL R S, ADEY M A, LODDER M. The effect of successive wet/dry cycles on aggregate size distribution in a clay texture soil[J]. Journal of Soil Science, 1988, 39(1): 71-80.
[25] COLLIS-GEORGE N, GREENE R S B. The effect of aggregate size on the infiltration behavior of slaking soil and its relevance to ponded irrigation[J]. Australian Journal of Soil Research, 1979, 17: 65-73.
[26] KEMPER W D, TROUT T, HUMPHERYS A, et al. Mechanisms by which surge irrigation reduces furrow infiltration rates in a silty loam soil[J]. Transactions of the ASAE, 1988, 31: 821-829.
[27] ASSOULINE S. Rainfall-induced soil surface sealing: a critical review of observations, conceptual models, and solutions[J]. Vadose Zone Journal, 2004, 3(2): 570-591.
[28] AUGEARD B, BRESSON L M, ASSOULINE S, et al. Dynamics of soil surface bulk density: Role of water table elevation and rainfall duration[J]. Soil Science Society of America Journal, 2008, 72(2): 412-423.
[29] JIM C Y. Soil compactions as a constraint to tree growth in tropical & subtropical urban habitats[J]. Environmental Conservation, 1993, 20(1): 35-49.
[30] ZHANG M, LU Y, HEITMAN J, et al. Temporal changes of soil water retention behavior as affected by wetting and drying following tillage[J]. Soil Science Society of America Journal, 2017, 81(6): 1288-1295.
[31] DU P, LUO H, HE J, et al. Different tillage induces regulation in 2-acetyl-1-pyrroline biosynthesis in direct-seeded fragrant rice[J]. BMC Plant Biology, 2019, 19(1): 308.
[32] 高晨，李晓鹏，张红霞，等. 初始含水量和容重对黑土压缩特性的影响[J]. 农业工程学报，2023，39(9)：102-111.
GAO Chen, LI Xiaopeng, ZHANG Hongxia, et al. Effects of initial moisture and bulk density on the soil compression characteristics of black soil[J]. Transactions of the Chinese Society of Agricultural Engineering (Transactions of the CSAE), 2023, 39(9): 102-111. (in Chinese with English abstract)
[33] 丁启朔，孙浩田，李毅念，等. 集约化生产条件下稻田土壤机械压实预测模型构建与验证[J]. 农业工程学报，2023，39(3)：42-51.
DING Qishuo, SUN Haotian, LI Yinian, et al. Establishment and verification of soil mechanical compaction prediction model in paddy field under intensive production conditions[J]. Transactions of the Chinese Society of Agricultural Engineering (Transactions of the CSAE), 2023, 39(3): 42-51. (in Chinese with English abstract)
[34] 刘湘君，乔冠宇，郭丰浩，等. 基于最小数据集的黄淮海旱作区耕层土壤质量评价及障碍分析[J]. 农业工程学报，2023，39(12)：104-113.
LIU Xiangjun, QIAO Guanyu, GUO Fenghao, et al. Evaluation and obstacle analysis of cultivated horizon soil quality based on MDS in the dry farming areas of Huang-Huai-Hai Region[J]. Transactions of the Chinese Society of Agricultural Engineering (Transactions of the CSAE), 2023, 39(12): 104-113. (in Chinese with English abstract)
[35] 李勇，赵云泽，勾宇轩，等. 黄淮海旱作区农田耕层土壤结构特征与其影响因素[J]. 农业机械学报，2022，53(3)：321-330.
LI Yong, ZHAO Yunze, GOU Yuxuan, et al. Characteristics and influencing factors of topsoil structure of farmland in dry farming region of Huang-Huai-Hai[J]. Transactions of the Chinese Society for Agricultural Machinery, 2022, 53(3): 321-330. (in Chinese with English abstract)
[36] BÖLENIUS E, WETTERLIND J, KELLER T, et al. Can within field yield variation be explained using horizontal penetrometer resistance and electrical conductivity measurements? Results from three Swedish fields[J]. Acta Agriculturae Scandinavica. Section B, Soil and Plant Science, 2018, 68(8): 690-700.
[37] AKSAKAL E L, ÖZTAŞ T, ÖZGÜL M. Time-dependent changes in distribution patterns of soil bulk density and penetration resistance in a rangeland under overgrazing[J]. Turkish Journal of Agriculture and Forestry, 2011, 35(2): 195-204.
[38] 付娟，马仁明，贾燕锋，等. 机械压实对农田土壤性质及土壤侵蚀的影响研究进展[J]. 农业工程学报，2022，38(增刊 1)：27-36.
FU Juan, MA Renming, JIA Yanfeng, et al. Research progress in the effects of mechanical compaction on soil properties and soil erosion in farmland[J]. Transactions of the Chinese Society of Agricultural Engineering(Transactions of the CSAE), 2022, 38(Supp 1): 27-36. (in Chinese with English abstract)
[39] HAMZA M A, ANDERSON W K. Soil compaction in cropping systems[J]. Soil and Tillage Research, 2005, 82(2): 121-145.
[40] 张兴义，隋跃宇. 农田土壤机械压实研究进展[J]. 农业机械学报，2005,36(6)：122-125.
ZHANG Xingyi, SUI Yueyu. International research trends of soil compaction induced by moving machine during field operations[J]. Transactions of the Chinese Society for Agricultural Machinery, 2005,36(6): 122-125. (in Chinese with English abstract)
[41] KELLER T, LAMANDÉ M. Challenges in the development of analytical soil compaction models[J]. Soil and Tillage Research, 2010, 111(1): 54-64.
[42] ZHUO Z, XING A, CAO M, et al. Identifying the position of the compacted layer by measuring soil penetration resistance in a dryland farming region in northeast China[J]. Soil Use and Management, 2020, 36(3): 494-506.
[43] DU L, RAJIB A, MERWADE V. Large scale spatially explicit modeling of blue and green water dynamics in a temperate mid-latitude basin[J]. Journal of Hydrology (Amsterdam), 2018, 562: 84-102.
[44] ULLAH S, YOU Q, ULLAH W, et al. Observed changes in precipitation in China-Pakistan economic corridor during 1980–2016[J]. Atmospheric Research, 2018, 210: 1-14.
[45] HAN L, ZHU H, ZHAO Y, et al. Analysis of variation in river sediment characteristics and influential factors in Yan'an city, China[J]. Environmental Earth Sciences, 2018, 77(13): 479.
[46] ZHAO Y, ZOU X, CAO L, et al. Spatiotemporal variations of potential evapotranspiration and aridity index in relation to influencing factors over southwest China during 1960–2013[J]. Theoretical and Applied Climatology, 2018, 133(3/4): 711-726.
[47] 杨金玲，张甘霖，赵玉国，等. 土壤压实指标在城市土壤评价中的应用与比较[J]. 农业工程学报，2005，21(5)：51-55.
YANG Jinling, ZHANG Ganlin, ZHAO Yuguo, et al. Application and comparison of soil compaction indexes in the evaluation of urban soils[J]. Transactions of the Chinese Society of Agricultural Engineering (Transactions of the CSAE), 2005, 21(5): 51-55. (in Chinese with English abstract)

[48] MOREIRA W H, TORMENA C A, KARLEN D L, et al. Seasonal changes in soil physical properties under long-term no-tillage[J]. Soil and Tillage Research, 2016, 160: 53-64.
[49] CHEN G, CHEN Y, HUANG Z, et al. Integrated measurement method for field surface topography and tillage depth in rotary tillage operations[J]. Computers and Electronics in Agriculture, 2025, 239: 111000.
[50] KIM Y S, KIM T J, KIM Y J, et al. Development of a real-time tillage depth measurement system for agricultural tractors: application to the effect analysis of tillage depth on draft force during plow tillage[J]. Sensors, 2020, 20(3): 912.
[51] DOU F, SORIANO J, TABIEN R E, et al. Soil texture and cultivar effects on rice (*Oyza sativa*, L.) Grain yield, yield components and water productivity in three water regimes[J]. Plos One, 2016, 11(3): e0150549.
[52] 孙永健，郑洪帧，徐徽，等. 机械旱直播方式促进水稻生长发育提高产量[J]. 农业工程学报，2014，30(20)：10-18.
SUN Yongjian, ZHENG Hongzhen, XU Hui, et al. Mechanical dry direct-sowing modes improving growth, development and yield of rice[J]. Transactions of the Chinese Society of Agricultural Engineering (Transactions of the CSAE), 2014, 30(20): 10-18. (in Chinese with English abstract)
[53] 高中超，刘峰，王秋菊，等. 马铃薯专用中耕培土犁的应用及增产效果[J]. 农业工程学报，2016，32(20)：49-54.
GAO Zhongchao, LIU Feng, WANG Qiuju, et al. Application and yield increasing effect on potato using special-designed ridging cultivator[J]. Transactions of the Chinese Society of Agricultural Engineering (Transactions of the CSAE), 2016, 32(20): 49-54. (in Chinese with English abstract)

Effects of loose soil layer thickness and compaction on soil subsidence after irrigation

CHEN Gaolong , CHEN Yuqi , HU Lian , WANG Pei※ , LUO Xiwen , ZHAO Runmao , HUANG Zhicheng , WANG Jingting , HE Zihao , DENG Yufei

(1. *Key Laboratory of Key Technology on Agricultural Machine and Equipment*, *Ministry of Education*, *South China Agricultural University*, *Guangzhou* 510642, *China*; 2. *National Key Laboratory of Agricultural Equipment Technology*, *Guangzhou* 510642, *China*)

Abstract: Soil preparation is one of the most critical steps in rice production. The dry-land leveling operations have also been continuously expanding in paddy fields. However, the differential soil subsidence can often occur during irrigation after dry tillage. Field levelness can be significantly reduced on the efficiency of the rice growth and yield. In this study, a systematic investigation was implemented on the influencing factors on the differential soil subsidence. A series of the field tests were carried out to determine the effects of the loos soil layer thickness and compaction on the soil subsidence after irrigation. The relationship was then established between these factors and soil subsidence. The soil subsidence was controlled using moderate compaction (defined as compaction thickness). A nonlinear regression model was constructed between loose soil layer thickness, compaction thickness, and soil subsidence (or expansion). A container test was finally conducted to validate the feasibility. Field tests revealed that there was the significant differential soil subsidence that caused by dry tillage and subsequent irrigation. In terms of the terrain changes, the rotary tillage increased the average terrain height of the field by 47 mm, whereas, the post-irrigation decreased 14 mm. Additionally, the areas with the greater height after rotary tillage also exhibited the significantly higher subsidence after irrigation. In the soil physical properties, the Mann-Kendall test was used to locate the abrupt variations in the soil penetration resistance, indicating the thickness of the loose soil layer. The field tests showed that the loose soil layer was typically 0–50 mm thick before rotary tillage, thus increasing to 125–175 mm afterward. There was the negligible subsidence after irrigation before tillage. But there was the significant subsidence after tillage and irrigation. As such, the thickness of the loose soil layer was the primary factor on the differential soil subsidence. The thickness of the loose soil layer was taken as the key variable with the real-world needs from the perspective of the practical production. Furthermore, the agricultural machinery that equipped with sensors was utilized to real-time measure the thickness of the loose soil layer for the soil subsidence. The container tests show that there was the relationship between loose soil layer thickness and soil subsidence. There was the significant positive linear correlation between them, with a determination coefficient of 0.970. Once the loose soil layer thickness was 50 mm, the subsidence was nearly negligible; When the thickness increased to 300 mm, the soil subsidence reached 36.15 mm, thus exceeding the requirement of the high-standard farmland leveling (±30 mm). Additionally, the soil subsidence was controlled after moderate compaction, defined as the compaction thickness. Container test results showed that the post-irrigation subsidence of the loose soil layer decreased gradually, as the compaction thickness increased. Once the compaction thickness exceeded the critical value, the soil expansion began to occur. A nonlinear regression analysis was conducted for the relationship between loose soil layer thickness, compaction thickness, and soil subsidence (or expansion). A determination coefficient of 0.964 and a root mean square error of 2.4 mm were achieved for the excellent accuracy. According to the principle of subsidence uniformity, the model validation tests demonstrated that there were the absolute errors between calculated and measured subsidence of 0.64 and 0.25 mm, respectively, with the root mean square errors of 1.43 and 0.39 mm, respectively, indicating the high precision and reliability. The findings can provide a scientific basis to develop and apply the soil preparation using intelligent technologies. The precise control of the post-irrigation soil subsidence and field levelness can be expected to enhance the production efficiency and profitability. Moreover, the quantification of the soil subsidence can also offer the spatial and temporal guidance for the precision field of the ridge-planted crops.

Keywords: dry-land leveling; loose soil layer; irrigation; soil subsidence; compacted thickness

国家出版基金项目
“十四五”时期国家重点出版物出版专项规划项目
智慧农业关键技术集成与应用系列丛书

大田无人化智慧农场

Unmanned Smart Farm for Field Crops Production

罗锡文　胡　炼◎主编

中国农业大学出版社
China Agricultural University Press

内 容 简 介

无人化智慧农场是智慧农业的主要实现方式，是一个多学科交叉的应用领域，涉及农业工程、车辆工程、控制工程、计算机科学与技术、机器人工程等，并融合了自动驾驶、机器视觉、深度学习、遥感信息和农机-农艺融合等前沿技术。

本书的作者为高校从事智慧农业方向的教师、科研人员和研究生，依托“无人化智慧农场”团队的教研与推广实践，全面详细地介绍了大田无人化智慧农场的技术体系，内容涵盖了从农场规划建设至运行维护所涉及的各个环节，重点阐述支撑农场高效生产的智能农机装备的相关理论与方法，特别是线控底盘、卫星定位、路径规划、导航控制、自动避障和多机协同等。本书适合作为现代农业研究人员和应用技术人员的参考资料，也可作为农业工程、智慧农业和车辆工程等相关专业研究生、本科生和专科生的学习资料。

图书在版编目(CIP)数据

大田无人化智慧农场/罗锡文，胡炼主编. --北京：中国农业大学出版社，2024. 12.
ISBN 978-7-5655-3346-4

Ⅰ. S126

中国国家版本馆 CIP 数据核字第 2024JS6117 号

书　　名　大田无人化智慧农场
　　Datian Wurenhua Zhihui Nongchang
作　　者　罗锡文　胡　炼　主编

总 策 划　王笃利　丛晓红　张秀环
策划编辑　刘　聪　石　华
责任编辑　刘　聪　石　华　蔡恩嘉
封面设计　中通世奥图文设计中心

出版发行　中国农业大学出版社
社　　址　北京市海淀区圆明园西路 2 号
邮政编码　100193
电　　话　发行部 010-62733489，1190
　　读者服务部 010-62732336
　　编辑部 010-62732617，2618
　　出　版　部 010-62733440
网　　址　http://www.caupress.cn
E-mail cbsszs@cau.edu.cn
经　　销　新华书店
印　　刷　涿州市星河印刷有限公司
版　　次　2024 年 12 月第 1 版　2024 年 12 月第 1 次印刷
规　　格　185 mm×260 mm　16 开本　23.5 印张　509 千字
定　　价　128.00 元

编委会

目录

“十四五”时期国家重点出版物出版专项规划项目（重大出版工程）
中国工程院重大咨询项目
中国农业发展战略研究（2050）丛书

第三卷

至2050年中国农业生产方式和产业体系发展战略研究

中国工程院“至2050年中国现代农业生产方式与生产体系发展战略研究”课题组
罗锡文　主编
赵春江　罗必良　臧　英　副主编

科学出版社

国家科学技术学术著作出版基金资助出版

“十四五”时期国家重点出版物出版专项规划项目（重大出版工程）

中国工程院重大咨询项目

中国农业发展战略研究（2050）丛书

第三卷

至2050年
中国农业生产方式和产业体系发展战略研究

中国工程院“至2050年中国现代农业生产方式与生产体系发展战略研究”课题组

罗锡文　主编

赵春江　罗必良　臧　英　副主编

科学出版社

北　京

内 容 简 介

本书是中国工程院重大咨询项目“中国农业发展战略研究（2050）”的课题“至 2050 年中国现代农业生产方式与生产体系发展战略研究”的研究成果。全书分为课题综合报告和专题研究两个部分。课题综合报告部分论述了过去 40 年中国农业发展趋势和新时代面临的机遇与挑战，至 2050 年中国农业生产方式和产业体系的演变趋势及其发展战略和政策建议；专题研究部分阐述了至 2050 年中国农业生产方式与技术装备发展趋势战略研究、经营体系及其转型战略研究、融合创新发展战略研究。

本书适合从事农业发展战略研究、农业及其相关产业生产的相关人员阅读，可供从事农林研究的科研院所、高等院校的科技工作者参考，也适合关心国家农业发展的其他读者收藏和阅读。

图书在版编目（CIP）数据

至 2050 年中国农业生产方式和产业体系发展战略研究 / 罗锡文主编. 北京 : 科学出版社, 2025. 11. -- (中国农业发展战略研究(2050)丛书). -- ISBN 978-7-03-083906-0

Ⅰ. F325

中国国家版本馆 CIP 数据核字第 20255RN186 号

责任编辑：马 俊 岳漫宇 闫小敏 / 责任校对：严 娜

责任印制：肖 兴 / 封面设计：无极书装

科学出版社出版

北京东黄城根北街 16 号

邮政编码：100717

http://www.sciencep.com

北京建宏印刷有限公司印刷

科学出版社发行 各地新华书店经销

*

2025 年 11 月第 一 版 开本：787×1092 1/16

2025 年 11 月第一次印刷 印张：20 1/4

字数：477 000

定价：268.00 元

（如有印装质量问题，我社负责调换）

“中国农业发展战略研究（2050）”项目组成员名单

顾　问

宋　健　徐匡迪　周　济　李晓红　潘云鹤　沈国舫

组　长

刘　旭　邓秀新

副组长

罗锡文　唐华俊　李德发

成　员

孙宝国　王　浩　陈君石　尹伟伦　盖钧镒　陈温福
李　玉　李　坚　康绍忠　戴景瑞　汪懋华　武维华
傅廷栋　颜龙安　官春云　桂建芳　陈焕春　陈剑平
山　仑　李佩成　南志标　陈学庚　荣廷昭　向仲怀
朱有勇　麦康森　黄季焜　青　平　王济民　王金霞
盛　誉　高中琪　左家和　王晓兵　侯玲玲　解　伟
黄海涛　鞠光伟　杨　波　王　波　王　庆　梁真真
缴　旭　宝明涛　吕　彤　侯晓云

“至2050年中国现代农业生产方式与生产体系发展战略研究”课题组成员名单

组　长：罗锡文　华南农业大学，院士

成　员（按姓氏拼音排序）：

曹冰雪　北京市农林科学院信息技术研究中心，助理研究员

常　倩　北京市农林科学院信息技术研究中心，博士后

陈小知　华南农业大学，博士

冯　献　北京市农林科学院信息技术研究中心，副研究员

郭美荣　北京市农林科学院信息技术研究中心，副研究员

何　杰　华南农业大学，副教授

洪炜杰　华南农业大学，副教授

胡　炼　华南农业大学，研究员

胡新艳　华南农业大学，教授

李　瑾　北京市农林科学院信息技术研究中心，研究员

李尚蒲　华南农业大学，教授

梁菲菲　华南农业大学，博士

廖　娟　华南农业大学，助理研究员

罗必良　华南农业大学，教授

罗明忠　华南农业大学，教授

马　晨　北京市农林科学院信息技术研究中心，副研究员

米运生　华南农业大学，教授

区颖刚　华南农业大学，教授

任雅欣　北京市农林科学院信息技术研究中心，助理研究员

汪　沛　华南农业大学，副教授

王艾萌　北京市农林科学院信息技术研究中心，助理研究员

王在满　华南农业大学，研究员
夏　薇　华南农业大学，副教授
谢　琳　华南农业大学，副教授
杨文武　华南农业大学，副教授
臧　英　华南农业大学，教授
曾　山　华南农业大学，研究员
张　彤　华南农业大学，教授
张怀波　北京市农林科学院信息技术研究中心，助理研究员
张沁岚　华南农业大学，副教授
张智刚　华南农业大学，副教授
赵春江　北京市农林科学院信息技术研究中心，院士
钟文晶　华南农业大学，教授
周志艳　华南农业大学，教授
朱文珏　华南农业大学，博士

专题一组长：罗锡文　华南农业大学，院士
成　员：臧　英　华南农业大学，教授
廖　娟　华南农业大学，助理研究员
区颖刚　华南农业大学，教授
王在满　华南农业大学，研究员
汪　沛　华南农业大学，副教授
胡　炼　华南农业大学，研究员
周志艳　华南农业大学，教授
曾　山　华南农业大学，研究员
张智刚　华南农业大学，副教授
何　杰　华南农业大学，副教授
杨文武　华南农业大学，副教授

专题二组长：罗必良　华南农业大学，教授
成　员：米运生　华南农业大学，教授
胡新艳　华南农业大学，教授
罗明忠　华南农业大学，教授
李尚蒲　华南农业大学，教授

高等学校科学研究优秀成果奖
（科学技术）

证　书

项目名称：农田精准平整技术与机具

奖励类别：科学技术进步奖

奖励等级：一等奖

获 奖 者：汪沛

中华人民共和国教育部

2023年6月6日

证书编号：2022-408-R011

中华人民共和国国家版权局
计算机软件著作权登记证书

证书号： 软著登字第15995442号

软 件 名 称： 基于嵌入式工控机的组合导航系统
1.0

著 作 权 人： 华南农业大学

权利取得方式： 原始取得

权 利 范 围： 全部权利

登 记 号： 2025SR1339244

根据《计算机软件保护条例》和《计算机软件著作权登记办法》的规定，经中国版权保护中心审核，对以上事项予以登记。

2025年07月23日

中华人民共和国国家版权局
计算机软件著作权登记证书

证书号： 软著登字第13405211号

软 件 名 称： YOLOV8缺秧检测系统 1.0

著 作 权 人： 华南农业大学

权利取得方式： 原始取得

权 利 范 围： 全部权利

登 记 号： 2024SR1001338

根据《计算机软件保护条例》和《计算机软件著作权登记办法》的规定，经中国版权保护中心审核，对以上事项予以登记。

2024年07月15日

证书号第6240737号

发明专利证书

发明名称：一种无人驾驶农机作业速度自主决策方法

发明人：何杰;汪沛;胡炼;黄培奎;李明锦;黄钰峰;丁帅奇
曾思晓

专利号：ZL 2023 1 0293891.3

专利申请日：2023年03月24日

专利权人：华南农业大学

地址：510642 广东省广州市天河区五山路483号

授权公告日：2023年08月15日　　授权公告号：CN 116069043 B

国家知识产权局依照中华人民共和国专利法进行审查，决定授予专利权，颁发发明专利证书并在专利登记簿上予以登记。专利权自授权公告之日起生效。专利权期限为二十年，自申请日起算。

专利证书记载专利权登记时的法律状况。专利权的转移、质押、无效、终止、恢复和专利权人的姓名或名称、国籍、地址变更等事项记载在专利登记簿上。

局长
申长雨

国家知识产权局
2023年08月15日

其他事项参见续页

证书号第6240737号

专利权人应当依照专利法及其实施细则规定缴纳年费。本专利的年费应当在每年03月24日前缴纳。未按照规定缴纳年费的，专利权自应当缴纳年费期满之日起终止。

申请日时本专利记载的申请人、发明人信息如下：

申请人：

华南农业大学

发明人：

何杰;汪沛;胡炼;黄培奎;李明锦;黄钰峰;丁帅奇;曾思晓

证书号第7150646号

专利公告信息

发明专利证书

发明名称：水稻直播机手自一体化设计方法、水稻直播机及作业方法

专利权人：华南农业大学;华南农业大学黄埔创新研究院

地　　址：510642 广东省广州市天河区五山路483号

发 明 人：何杰;胡炼;汪沛;黄钰峰;李明锦;杨文武;丁帅奇

专　利　号：ZL 2023 1 0240833.4　　授权公告号：CN 116267109 B

专利申请日：2023年03月14日　　授权公告日：2024年06月28日

申请日时申请人：华南农业大学;华南农业大学黄埔创新研究院

申请日时发明人：何杰;胡炼;汪沛;黄钰峰;李明锦;杨文武;丁帅奇

国家知识产权局依照中华人民共和国专利法进行审查，决定授予专利权，并予以公告。

专利权自授权公告之日起生效。专利权有效性及专利权人变更等法律信息以专利登记簿记载为准。

局长
申长雨

国家知识产权局
2024年06月28日

证书号第8170539号

专利公告信息

发明专利证书

发明名称：水田硬底层轮廓感知与数字化建模方法

专利权人：华南农业大学

地　　址：510642 广东省广州市天河区五山路483号

发 明 人：胡炼;涂团鹏;罗锡文;汪沛;何杰;黄培奎;王晨阳;李明锦
田力

专 利 号：ZL 2023 1 0001415.X　　授权公告号：CN 116090206 B

专利申请日：2023年01月03日　　授权公告日：2025年08月19日

申请日时申请人：华南农业大学

申请日时发明人：胡炼;涂团鹏;罗锡文;汪沛;何杰;黄培奎;王晨阳;李明锦
田力

国家知识产权局依照中华人民共和国专利法进行审查，决定授予专利权，并予以公告。

专利权自授权公告之日起生效。专利权有效性及专利权人变更等法律信息以专利登记簿记载为准。

局长
申长雨

国家知识产权局
2025年08月19日

证书号第6096802号

发明专利证书

发 明 名 称：一种曲形农田边界的路径规划方法

发　明　人：何杰;李媛媛;胡炼;侯康;汪沛;黄培奎;李明锦;资乐

专　利　号：ZL 2023 1 0153495.0

专利申请日：2023年02月23日

专 利 权 人：华南农业大学

地　　址：510642 广东省广州市天河区五山路483号

授权公告日：2023年06月27日　　授权公告号：CN 115855067 B

国家知识产权局依照中华人民共和国专利法进行审查，决定授予专利权，颁发发明专利证书并在专利登记簿上予以登记。专利权自授权公告之日起生效。专利权期限为二十年，自申请日起算。

专利证书记载专利权登记时的法律状况。专利权的转移、质押、无效、终止、恢复和专利权人的姓名或名称、国籍、地址变更等事项记载在专利登记簿上。

局长
申长雨

国家知识产权局
2023年06月27日

其他事项参见续页

证书号第6096802号

专利权人应当依照专利法及其实施细则规定缴纳年费。本专利的年费应当在每年02月23日前缴纳。未按照规定缴纳年费的，专利权自应当缴纳年费期满之日起终止。

申请日时本专利记载的申请人、发明人信息如下：

申请人：

华南农业大学

发明人：

何杰;李媛媛;胡炼;侯康;汪沛;黄培奎;李明锦;资乐

华南农业大学重点科研平台负责人变更申请表

平台名称	广东省农业航空应用工程技术研究中心					
现任负责人	职务	出生年月	职称	学科专长	联系电话	签名
罗锡文	主任		教授	农业工程		罗锡文
兰玉彬	副主任		教授	农业工程		兰玉彬
周志艳	副主任		教授	农业工程		周志艳
拟变更负责人	职务	出生年月	职称	学科专长	联系电话	签名
周志艳	主任		教授	农业工程		周志艳
汪沛	副主任		副教授	农业工程		汪沛
姜锐	副主任		副教授	农业工程		姜锐
变更理由	根据《华南农业大学重点科研平台管理办法》的要求进行变更。 现任工程技术研究中心主任罗锡文院士科研重点聚焦智慧农场，申请将该平台负责人变更为本校顶级知名专家周志艳教授负责平台的建设和管理。					
依托单位审核意见	同意！ 负责人签字（加盖公章）： 2024年10月11日					
科研平台学术（或技术）委员会审议意见	学术（或技术）委员会主任（签名）：罗锡文 2024年10月11日					

填表说明：

1. 科研平台负责人包括正职和副职；

2. 变更平台正职，需附拟任正职简介（包括基本情况、研究方向、学术水平、组织管理和协调能力等，300字左右）；

3. 无组建科研平台学术（或技术）委员会可不填写意见。

广东省科学技术厅

粤科函政字〔2013〕1589号

广东省科学技术厅关于同意广州中船黄埔造船有限公司等472家单位组建广东省工程技术研究中心的通知

各有关地级以上市科技局（委）、省直有关部门、顺德区经济和科技促进局，各有关单位:

按照《广东省科学技术厅关于省工程技术研究中心建设的管理办法》（粤科函政字〔2013〕1513号）的要求，我厅已组织专家对申请组建广东省工程技术研究中心的可行性方案进行了评审。经研究，同意广州中船黄埔造船有限公司等472家单位组建广东省工程技术研究中心（名单附后）。

请各组建单位认真落实省工程技术研究开发中心的组建任务和目标，进一步加强本单位研发体系建设，充分发挥省工程研究中心在促进技术创新、推动科技成果转化及产业化的示范和带动作用。

附件：1. 2013 年第一批新组建广东省工程技术研究中心名单

2. 2013 年第二批新组建广东省工程技术研究中心名单

广东省科学技术厅

2013 年 12 月 5 日

公开方式：主动公开

抄送：广东省发展改革委、广东省经济和信息化委。

附件：2013 年第一批新组建广东省工程技术研究中心名单（省属）

序号	单位名称	项目名称
1	广东工业大学材料与能源学院	广东省金属成形与模具新技术工程技术研究中心
2	广东工业大学计算机学院	广东省物联网与控制专用芯片及系统智能化工程技术研究中心
3	广东工业大学轻工化工学院	广东省药食两用资源综合利用工程技术研究中心
4	广东工业大学土木与交通工程学院	广东省建筑业土木工程技术研究中心
5	广东工业大学信息工程学院	广东省集成电路高端芯片应用工程技术研究中心
6	广东海洋大学	广东省珍珠养殖与加工工程技术研究中心
7	广东省工业技术研究院金属加工与成型技术研究所	广东省金属复合材料加工与成型工程技术研究中心
8	广东省建筑科学研究院	广东省南亚热带绿色建筑共性技术工程技术研究中心
9	广东石油化工学院	广东省石油化工资源清洁利用工程技术研究中心
10	华南理工大学材料科学与工程学院	广东省建筑材料低碳技术工程技术研究中心
11	华南理工大学计算机科学与工程学院	广东省大数据分析与处理工程技术研究中心
12	华南理工大学环境与能源学院	广东省环境风险防控与应急处置工程技术研究中心
13	华南理工大学机械与汽车工程学院	广东省节能与新能源绿色制造工程技术研究中心
14	华南理工大学轻工与食品学院	广东省食品绿色加工与营养调控工程技术研究中心
15	华南农业大学工程学院	广东省农业航空应用工程技术研究中心
16	华南农业大学食品学院	广东省食品安全检测与风险控制工程技术研究中心
17	华南师范大学教育信息学院	广东省教育云服务工程技术研究中心
18	南方医科大学生物医学工程学院	广东省放射诊断治疗设备工程技术研究中心

广东省科学技术厅

粤科函产字〔2025〕272号

广东省科学技术厅关于认定2024年度广东省工程技术研究中心的通知

各地级以上市科技局，各有关单位:

根据《广东省工程技术研究中心管理办法》（粤科规范字〔2022〕12号）和《广东省科学技术厅关于组织申报2024年度广东省工程技术研究中心的通知》（粤科函产字〔2024〕1096号），经组织申报、专家评审和网上公示及复核，现认定广东省智慧能源技术与应用工程技术研究中心等554家单位为2024年度广东省工程技术研究中心（简称“工程中心”，名单见附件）。有关事项通知如下:

一、工程中心是构建以企业为主体、市场为导向、产学研用深度融合的技术创新体系的重要科研平台。各工程中心要加大科研投入和条件建设，加强技术攻关和协同合作，加速成果转化和人才培养，在推进现代化产业体系建设、促进产业科技互促双强中发挥支撑作用。

二、鼓励各地市科技管理部门积极研究并制定配套支持政

策，指导和服务工程中心进一步提高自主创新能力，推动工程中心高质量发展。

三、工程中心实行网络化管理，相关信息发布及过程管理依托“广东省工程技术研究中心创新服务平台”（www.gdetrc.net）实施，请2024年度认定通过的工程中心于2025年3月15日前登录该平台进行注册备案。后续工程中心如发生依托单位更名、所属地或工程中心主任变更及资格撤销等情况，请通过服务平台进行相关操作。

附件：2024年度广东省工程技术研究中心认定名单

广东省科学技术厅

2025年2月21日

公开方式：主动公开

附件

2024年度广东省工程技术研究中心认定名单

序号	工程中心名称	依托单位	所在地市
1	广东省Mini LED新型显示工程技术研究中心	广州市鸿利显示电子有限公司	广州市
2	广东省新能源汽车充电设备及管理系统（万城万充）工程技术研究中心	广州万城万充新能源科技有限公司	广州市
3	广东省智慧能源技术与应用工程技术研究中心	广东电网能源投资有限公司	广州市
4	广东省综合智慧能源工程技术研究中心	广州发展集团股份有限公司	广州市
5	广东省生物质能复合应用工程技术研究中心	广州环峰能源科技股份有限公司	广州市
6	广东省光伏电站AI智慧运维工程技术研究中心	广东省电力开发有限公司	广州市
7	广东省户用储能及其控制系统工程技术研究中心	广州疆海科技有限公司	广州市
8	广东省高效燃气输配工程技术研究中心	广州东部发展燃气有限公司	广州市
9	广东省汽车座椅舒适系统线束工程技术研究中心	广州市信征汽车零件有限公司	广州市
10	广东省新能源汽车动力总成自动化成套装备工程技术研究中心	广州市创智机电设备有限公司	广州市
11	广东省汽车电器分配系统（整车线束）工程技术研究中心	广州新李汽车零部件有限公司	广州市
12	广东省智能大屏应用工程技术研究中心	广州欢网科技有限责任公司	广州市
13	广东省新一代信息技术与数字化应用（科城数科）工程技术研究中心	科学城（广州）数字科技集团有限公司	广州市
14	广东省民航数字经济工程技术研究中心	广州民航信息技术有限公司	广州市
15	广东省效果营销工程技术研究中心	省广营销集团有限公司	广州市

序号	工程中心名称	依托单位	所在地市
118	广东省节能建筑工程质量检测工程技术研究中心	广东惠和工程检测有限公司	广州市
119	广东省公路数智化养护工程技术研究中心	广东和立交通养护科技有限公司	广州市
120	广东省智能认知与行为决策工程技术研究中心	华南理工大学	广州市
121	广东省集成电路设计自动化工程技术研究中心	广东工业大学	广州市
122	广东省无人系统群体智能应用工程技术研究中心	中山大学	广州市
123	广东省毫米波太赫兹器件与系统工程技术研究中心	广东大湾区空天信息研究院	广州市
124	广东省人工智能赋能智慧物流工程技术研究中心	暨南大学	广州市
125	广东省新型显示工程技术研究中心	广东聚华新型显示研究院	广州市
126	广东省空天飞行器工程技术研究中心	广东空天科技研究院（南沙）	广州市
127	广东省近海基础设施韧性提升工程技术研究中心	广州航海学院	广州市
128	广东省无人化智慧农场工程技术研究中心	华南农业大学	广州市
129	广东省聚集诱导发光工程技术研究中心	广东省大湾区华南理工大学 聚集诱导发光高等研究院	广州市
130	广东省智慧设施农业工程技术研究中心	广东省农业科学院设施农业研究所	广州市
131	广东省未来植源性化妆品创制工程技术研究中心	中新国际联合研究院	广州市
132	广东省粤北地方家禽健康养殖工程技术研究中心	广东科贸职业学院	广州市
133	广东省高性能纸用功能材料工程技术研究中心	广东轻工职业技术大学	广州市

广东省工程技术研究中心认定申请书

中心名称： 广东省无人化智慧农场工程技术研究中心

研究开发方向： 农业技术

所属领域： 农业装备(农业机械、设备及材料等)

依托单位： 华南农业大学

联合共建单位：

通信地址： 广东省广州市天河区五山路483号

邮政编码： 510642

联 系 人： 胡炼

联系电话： 915767370

申报日期： 2024-09-17

广 东 省 科 学 技 术 厅

2024年7月制

一、申报单位基本情况

依托单位	华南农业大学			
法人代表	薛红卫		法人代码	124400004554165634
主管部门				
通信地址	广东省广州市天河区五山路483号			
邮政编码	510642		传真	020-85281885
单位性质	高等院校		申报单位类型	高校/科研院所/医院
联系人	胡炼		联系电话	15915767370
电子邮件	lianhu@scau.edu.cn			
经济类型	高等院校			
成立时间	1952-07-01			
注册资本	311733.00万人民币			
职工总数	3380			
工程技术人员数	2360			
市（区）级科研平台建设情况	否	批准成立名称		
		批准成立时间		
		获得资助金额	（万元）	
其他研发机构建设情况：	市（区）级科研平台：	否		
	省级科研平台：	是	成立名称：南方农业机械与装备关键技术教育部重点实验室 成立时间：2006-05-01	
	国家级科研平台：	是	成立名称：农业装备技术全国重点实验室 成立时间：2022-11-30	
	其他			
“专精特新”企业建设情况：	省级专精特新中小企业：	否		
	国家级专精特新“小巨人”企业：	否		
是否上市公司：	否			

依托单位和联合共建单位分工

序号	单位名称	分工

中心主要研究人员										
序号	姓名	性别	年龄	职称	职务	学历	现从事专业	在中心承担的任务	所在单位	签名
1	胡炼	男	40	研究员	工程学院副院长	博士研究生	农业电气化与自动化	中心副主任作大田物无人化智慧农场首席科学家	华南农业大学工程学院	
2	李君	男	45	教授	工程学院院长	博士研究生	农业机械化工程	中心副主任无人化智慧果园首席专家	华南农业大学工程学院	
3	何杰	男	39	副教授	无	博士研究生	农业电气化与自动化	中心副主任智能装备共性技术首席专家	华南农业大学工程学院	
4	肖德琴	女	52	教授	无	博士研究生	农业电气化与自动化	智慧养殖场首席专家	华南农业大学数学与信息学院	
5	汪沛	女	41	副教授	无	博士研究生	农业电气化与自动化	无人农场管控平台	华南农业大学工程学院	
6	黄培奎	男	34	高级工程师	无	博士研究生	农业电气化与自动化	农业机械智能导航及自动作业	华南农业大学工程学院	
7	赵润茂	男	34	副教授	无	博士研究生	农业电气化与自动化	农田土壤信息感知智能及决策	华南农业大学工程学院	
8	臧英	女	51	教授	重点实验室常务副主任	博士研究生	农业机械化工程	农情信息感知及精准管控	华南农业大学工程学院	
9	张智刚	男	47	副教授	无	博士研究生	农业电气化与自动化	农业机械智能导航及自动作业	华南农业大学工程学院	

广东省科学技术厅文件

粤科资字〔2021〕51号

广东省科学技术厅关于下达2021年省科技创新战略专项资金（省重点实验室新立项与运行评估）项目计划的通知

各有关单位:

2021年度省重点实验室（新立项）、省重点实验室评估运行项目已按程序完成立项工作，现按规定下达给你们，并就有关事项通知如下:

一、本批项目共计115项，2021年拨付财政资金16100万元。其中，省重点实验室（新立项）项目34项，项目资金6400万元；省重点实验室运行评估项目81项，项目资金9700万元。

二、省重点实验室（新立项）项目须按有关规定尽快完成任务书签订工作。省重点实验室评估运行项目按原任务书（合同

书）继续执行，不再签订新的任务书（合同书）。

三、各级主管部门和项目承担单位收到本通知后，应尽快协助下达省级财政资金（资金计划由省财政厅另文下达）。

四、各级主管部门应履行项目的日常监管职责，督促项目承担单位做好项目的组织实施，并配合省有关部门及专业机构组织开展的中期评估、绩效评价、验收结题、项目审计等相关工作。

五、各项目承担单位要抓紧项目的组织实施，严格按照科技经费的使用范围和有关规定管好用好财政资金，履行好项目实施和资金使用的主体责任。项目在研过程中每年4月10日前须在省科技业务管理阳光政务平台填报上年度执行情况报告。

附件：1.2021年度广东省科技创新战略专项资金（省重点实验室认定）项目计划安排表

2.2021年度广东省科技创新战略专项资金（省重点实验室运行评估）项目计划安排表

广东省科学技术厅

省科技厅

2021年3月27日

公开方式：依申请公开

附件1

2021年度广东省科技创新战略专项资金（省重点实验室认定）项目计划安排表

单位：万元

序号	项目编号	项目名称	申报单位	负责人	2021年拨付金额
合计（34项）					6400
专题一： 学科类省重点实验室建设					
1	2021B1212040005	广东省光电信息处理芯片与系统重点实验室（2021年度）	中山大学	李朝晖	300
2	2021B1212040006	广东省消化系统恶性肿瘤防治研究重点实验室（2021年度）	中山大学	何裕隆	300
3	2021B1212040016	广东省医学大动物模型重点实验室（2021年度省市共建）	五邑大学	金南衡	200
4	2021B1212040013	广东省岭南特色食品科学与技术重点实验室（2021年度）	仲恺农业工程学院	肖更生	300
5	2021B1212040008	广东省农业农村污染治理与环境安全重点实验室（2021年度）	华南农业大学	仇荣亮	300
6	2021B1212040009	广东省农业人工智能重点实验室（2021年度）	华南农业大学	罗锡文	300
7	2021B1212040010	广东省芯片与集成技术重点实验室（2021年度）	华南师范大学	李京波	300
8	2021B1212040003	广东省现代土木工程技术重点实验室（2021年度）	华南理工大学	吴波	300
9	2021B1212040001	广东省信息功能氧化物材料与器件重点实验室（2021年度）	南方科技大学	李江宇	300
10	2021B1212040011	广东省植物资源生物炼制重点实验室（2021年度）	广东工业大学	王铁军	300
11	2021B1212040012	广东省微创手术器械设计与精密制造重点实验室（2021年度）	广东工业大学	王成勇	300
12	2021B1212040014	广东省运动与健康重点实验室（2021年度）	广州体育学院	胡敏	300
13	2021B1212040007	广东省中医药信息化重点实验室（2021年度）	暨南大学	张荣华	300
14	2021B1212040004	广东省肿瘤介入诊治研究重点实验室（2021年度）	珠海市人民医院	陆骊工	300
15	2021B1212040015	广东省粤东药食资源功能物质与治未病研究重点实验室（2021年度省市共建）	韩山师范学院	程永现	200

受理编号：c2133250100012

项目编号：2021B1212040009

项目下达文号：粤科资字〔2021〕51号

广东省科技计划项目
合同书

（科技创新平台类）

项目名称：	广东省农业人工智能重点实验室（2021年度）		
专项名称：	重点实验室认定		
项目起止时间：	2021年 01月 01日　至　2023年 12月 31日		
管理单位(甲方)：	广东省科学技术厅		
项目承担单位（乙方）：	华南农业大学		
项目推荐（主管）单位（丙方）：	华南农业大学		
通讯地址：	广东省-广州市-天河区五山路483号		
邮政编码：	510642	单位电话：	020-85283435
项目负责人：	罗锡文	联系电话：	020-85280158
项目联系人：	周志艳	联系电话：	02038676975
电子邮箱：	zyzhou@scau.edu.cn		

广东省科学技术厅
二〇一九年九月制

（广东科技微信公众号）　　（受理纸质材料二维码）

一、项目基本情况表

<table>
<tr><td>项目名称</td><td colspan="4">广东省农业人工智能重点实验室（2021年度）</td></tr>
<tr><td>项目起止时间</td><td colspan="4">2021-01-01　至　2023-12-31</td></tr>
<tr><td>项目总经费预算</td><td>1636.00 万元</td><td colspan="2">申请经费资助</td><td>300.00 万元</td></tr>
<tr><td>社会经济目标</td><td colspan="4">农林牧渔业体系支撑</td></tr>
<tr><td>项目摘要</td><td colspan="4">定位在农业人工智能领域，开展农情信息感知、农业大数据、农业机械智能作业及无人农场等基础理论及关键技术研究和应用推广，解决中国特别是广东省农业人工智能产业发展中的“共性”、“瓶颈”技术，将实验室建设成为高水平的农业人工智能研究、推广和应用示范的基地，聚集和培养优秀农业人工智能专家的基地，促进农业人工智能专家学术交流的平台，为中国现代农业的“可持续发展”提供“可持续的支撑”。</td></tr>
<tr><td>关键字</td><td colspan="4">人工智能 ； 无人农场 ； 农业大数据 ； 农情信息感知 ； 精准管控</td></tr>
<tr><td rowspan="3">平台情况</td><td>技术领域</td><td>软件开发,数据库系统及数据处理,自动化与智能控制技术,智能制造装备,农业装备(农业机械、设备及材料等),农业信息(农业信息技术、农业网络建设等)</td><td>学科</td><td>农业信息学,农业系统工程,机器智能基础理论与方法,模式识别基础,生物特征识别,人工智能基础,知识的表示、发现与获取,数据挖掘与机器学习,逻辑、推理与问题求解,神经网络基础及应用,人机交互与人机系统,智能系统及应用,智能与自主机器人,光谱诊断技术</td></tr>
<tr><td>研究活动类型</td><td>应用研究,研究与实验发展成果应用</td><td>项目研究阶段</td><td>小试</td></tr>
<tr><td>技术来源</td><td>自有技术</td><td>行业领域</td><td>稻谷种植,农业科学研究和试验发展</td></tr>
<tr><td>预期成果形式</td><td colspan="4">新产品，新装置，技术标准(国际标准、国家标准、行业标准、企业标准)，专利，计算机软件 ，论文论著，研究报告
简要说明：无</td></tr>
<tr><td>项目已受财政资金资助情况</td><td colspan="4">国家(部委)财政资金资助
简要说明：“南方水稻生产全程机械化科研基地”，农业部全国农业科技创新能力条件建设规划项目，1136万元，2016.01-2017.12，负责人：罗锡文。</td></tr>
<tr><td colspan="5">其它需要说明的问题</td></tr>
<tr><td colspan="5">无</td></tr>
</table>

本项目是否涉及实验动物：□是 ■否

新增经费预算（单位：万元）				
	新增经费总额		省科技厅经费	
支出经费	经费额	用途说明	经费额	用途说明
基建费			------	------
1、直接费用	455.00		260.00	
（1）设备费	95.00	人工智能研究相关仪器设备	50.00	人工智能研究相关仪器设备
（2）材料费	130.00	开展技术研发试验及样机制作等消耗材料	90.00	开展技术研发试验及样机制作等消耗材料
（3）测试化验加工外协费	25.00	科学试验等测试费、化验及 加工等	10.00	科学试验等测试费、化验及 加工等
（4）燃料动力费	5.00	田间试验及实验室动力能源消耗	4.00	田间试验及实验室动力能源消耗
（5）差旅费/会议费/国际合作与交流费	55.00	项目调研、考察、田间试验、学术交流等差旅支出	25.00	项目调研、考察、田间试验、学术交流等差旅支出
（6）出版/文献/信息传播/知识产权事务费	30.00	资料复印、装订、论文发表、知识产权申请维护等费用	10.00	资料复印、装订、论文发表、知识产权申请维护等费用
（7）劳务费	110.00	研究生、临时用工劳务补助	66.00	研究生、临时用工劳务补助
（8）人员费				
（9）专家咨询费	5.00	课题专家咨询	5.00	课题专家咨询
（10）直接费用其他支出				
（11）科技金融服务体系其他费用	0.00	无	0.00	无
①信用评级补贴				
②大赛场租				
③特派员奖励与补贴				
2、间接费用	45.00	无	40.00	无
（1）间接成本				
（2）管理成本	15.00	科研管理部门提取5%管理费	15.00	科研管理部门提取5%管理费
（3）绩效支出	30.00	实验室成员绩效奖励	25.00	实验室成员绩效奖励
合计	500.00		300.00	

六 、项目组人员情况

项目负责人

序号	姓名	职称	职务	学位/学历	现从事专业	所在单位	证件类型	证件号码	在本项目中承担的工作任务	签名
1	罗锡文	教授	教育部重点实验室主任	硕士/硕士研究生	农业工程	华南农业大学	身份证		实验室主任	
2	王海林	教授	院长	博士/博士研究生	智能农机装备	华南农业大学	身份证		实验室副主任	
3	周志艳	教授	副主任	博士/博士研究生	农业电气化与自动化	华南农业大学	身份证		实验室副主任	

主要参与人员

序号	姓名	职称	职务	学位/学历	现从事专业	所在单位	证件类型	证件号码	在本项目中承担的工作任务	签名
1	胡炼	教授	副主任	博士/博士研究生	农业电气化与自动化	华南农业大学	身份证		实验室副主任兼学术委员会秘书	
2	臧英	教授	副主任	博士/博士研究生	农业机械化工程	华南农业大学	身份证		农情信息感知及精准管控首席专家	
3	李君	教授	副院长	博士/博士研究生	农业电气化与自动化	华南农业大学	身份证		果园信息化系统与智能装备	
4	闫国琦	副教授	副院长	博士/博士研究生	智能农机装备	华南农业大学	身份证		南药智能作业装备	
5	张智刚	副教授	无	博士/博士研究生	智能农机装备	华南农业大学	身份证		农业机械智能作业首席专家	
6	肖德琴	教授	无	博士/博士研究生	计算机应用	华南农业大学	身份证		农业大数据及云平台首席专家	
7	张波	高级工程师	主任	博士/博士研究生	计算机科学与技术	华南农业大学	身份证		农业大数据及云平台	
8	汪沛	讲师	无	博士/博士研究生	农业电气化与自动化	华南农业大学	身份证		作物长势信息感知	
9	何杰	实验师	无	硕士/硕士研究生	智能农机装备	华南农业大学	身份证		水田作业机械智能导航及自动作业	

合成时间：2025 年 12 月 12 日 16 时 25 分 20 秒

全国重点实验室人员信息表

全国重点实验室名称：农业装备技术全国重点实验室

1. 固定人员

序号	姓名	性别	国籍	证件号码	工作单位	实验室职务	职称	学历	学术荣誉	研究领域及科研方向	联系方式
1	苑严伟	男	中华人民共和国		中国农业机械化科学研究院集团有限公司	主任	正高级	博士研究生	国家高层次人才特殊支持计划	制造	
2	韩亚芬	女	中华人民共和国		中国农业机械化科学研究院集团有限公司	其他	副高级	博士研究生	无	制造	
3	陈志	男	中华人民共和国		中国农业机械化科学研究院集团有限公司	其他	正高级	博士研究生	无	制造	

95	夏红梅	女	中华人民共和国		华南农业大学	其他	正高级	博士研究生	无	制造	
96	张智刚	男	中华人民共和国		华南农业大学	其他	副高级	博士研究生	无	制造	
97	王春桃	男	中华人民共和国		华南农业大学	其他	副高级	博士研究生	无	制造	
98	何杰	男	中华人民共和国		华南农业大学	其他	副高级	博士研究生	无	制造	
99	汪沛	女	中华人民共和国		华南农业大学	其他	副高级	博士研究生	无	制造	
100	张闻宇	男	中华人民共和国		华南农业大学	其他	中级	博士研究生	无	制造	
101	马旭	男	中华人民共和国		华南农业大学	其他	正高级	博士研究生	无	制造	

2025中国机器人大赛暨RoboCup机器人世界杯中国赛

河北·石家庄 2025.10.17-10.19

获奖证书

Y2509T1498742

华南农业大学

西园战队

农业机器人-节水灌溉机器人(总决赛)

一等奖

指导教师：汪沛

队　　员：林炳钿 罗东宇 黄展鸿

中国自动化学会

2025年10月31日

荣誉证书

2024 年第 21 届全国大学生信息安全与对抗技术竞赛

（智能安全赛-全国总决赛-药房机器人）

竞赛奖项：　一等奖

获奖成员：　周惠祥　李子豪　周煜峰

获奖单位：　华南农业大学

指导教师：　汪沛

中国兵工学会　北京理工大学

中国兵工学会信息安全与对抗专业委员会

NO.ISCC-USC-ZNAQ-NF-2024-1-56R　　0699　　2024 年 12 月 19 日

荣誉证书

2025 年第 22 届全国大学生信息安全与对抗技术竞赛

（智能安全赛-全国总决赛-采收机器人）

竞赛奖项：　二等奖

获奖成员：　林炳钿　李菀莹　苏怡

获奖单位：　华南农业大学

指导教师：　汪沛

中国兵工学会　北京理工大学

中国兵工学会信息安全与对抗专业委员会

NO.ISCC-USC-ZNAQ-NF-2025-2-58Q　　0657　　2025 年 11 月 20 日

荣誉证书

CERTIFICATE OF AWARD

在第八届国际大学生智能农业装备创新大赛中，经评审，

荣获

一 等 奖

特发此证，以资鼓励

单位名称：华南农业大学

作品名称：果实采摘分选机器人

获奖学生：翁宗标,李煜东,冯国健,黄泽凯,王景榕

指导教师：汪沛,何杰

国际农业和生物系统工程委员会　中国农业机械学会　中国农业工程学会　省部共建现代农业装备与技术协同创新中心　农业工程大学国际联盟

证书编号：NZDS2023-B-001

二零二三年五月

CERTIFICATE
获 奖 证 书

ROBOMASTER UNIVERSITY SERIES

ROBOMASTER
机甲大师超级对抗赛

华南农业大学 Taurus 战队

在“**第二十四届全国大学生机器人大赛 RoboMaster 2025 机甲大师超级对抗赛**”的**步兵机器人组**中，荣获机器人竞技奖

一等奖

指导单位：
中国高等教育学会
中国工程院战略咨询中心

指导老师：汪沛、胡炼、何杰、赵润茂、黄培奎、陆永超、漆海霞、罗锡文

参赛队员：张冠豪、曾竟源、江威瑜、覃柏霖、连炜生、植正雄、余凯佳、马锐涛、陈利坤、潘智杰、张梓源、李浩岚

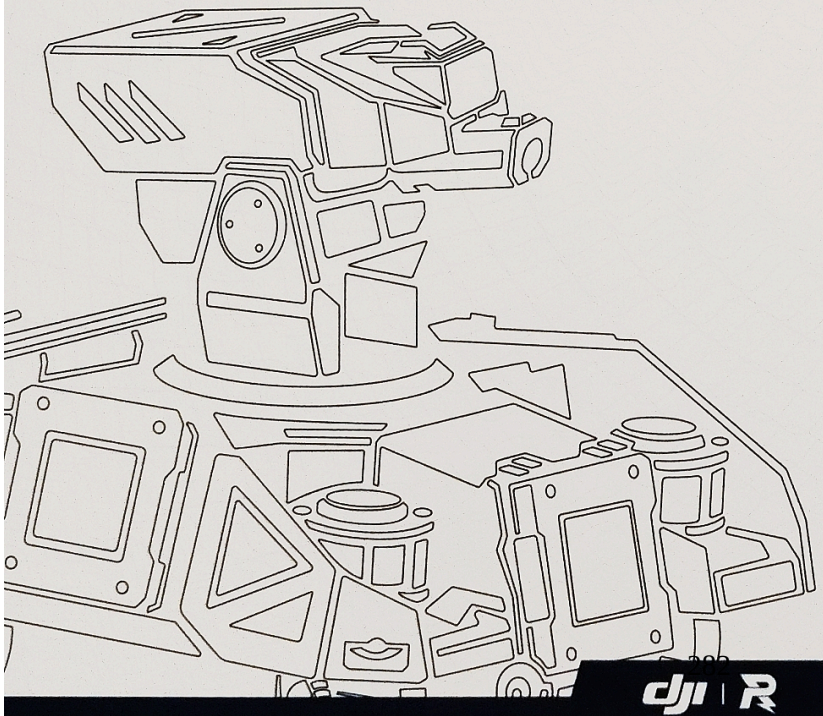

全国大学生机器人大赛组委会
2025 年 7 月

CHINA UNIVERSITY ROBOT COMPETITION 全国大学生机器人大赛 组委会 ORGANIZING COMMITTEE

证书编号：RMUC2025BBQCOUM

CERTIFICATE

获 奖 证 书

ROBOMASTER UNIVERSITY SERIES

ROBOMASTER
机甲大师超级对抗赛

华南农业大学 Taurus 战队

在“**第二十四届全国大学生机器人大赛 RoboMaster 2025 机甲大师超级对抗赛**”的**飞镖系统组**中，荣获机器人竞技奖

一等奖

指导单位：
中国高等教育学会
中国工程院战略咨询中心

指导老师：汪沛、胡炼、何杰、赵润茂、黄培奎、陆永超、漆海霞、罗锡文

参赛队员：许可岳、曹钺、李岳峰、李庆东、沈思予

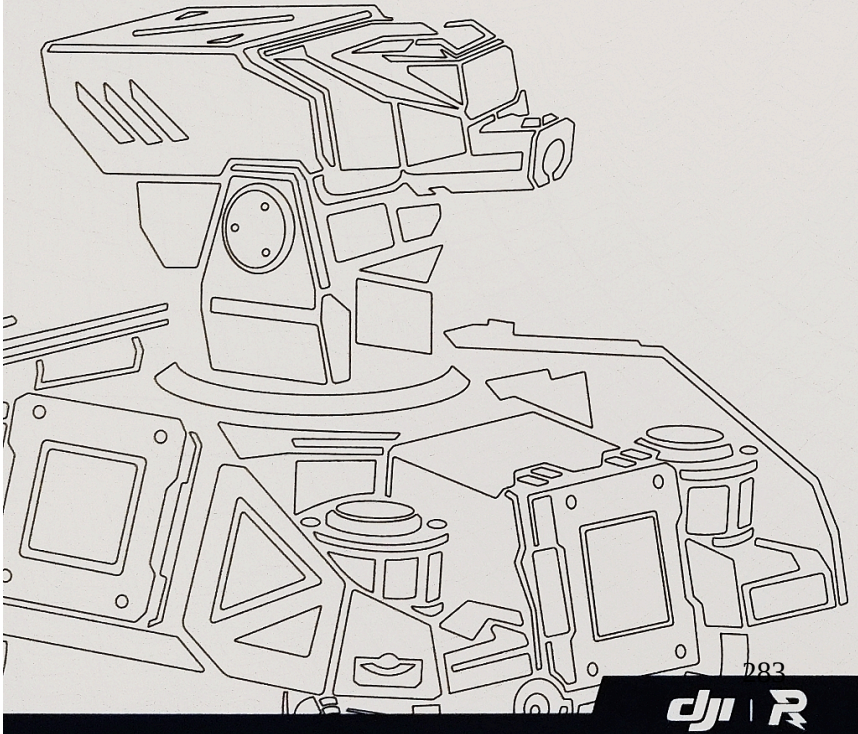

全国大学生机器人大赛组委会
2025 年 7 月

证书编号：RMUC2025FBQCOUM

证书编号：RMUC2024KHWJX105336

CERTIFICATE
获 奖 证 书

ROBOMASTER
机甲大师超级对抗赛

华南农业大学 Taurus 战队

汪沛 老师

您指导的队伍在**“第二十三届全国大学生机器人大赛 RoboMaster 2024 机甲大师超级对抗赛·全国赛”**中，荣获

一等奖

特发此状，以资鼓励。

指导单位：

中国高等教育学会

中国工程院战略咨询中心

全国大学生机器人大赛组委会

2024年8月

CERTIFICATE

获 奖 证 书

ROBOMASTER
机甲大师超级对抗赛

华南农业大学 Taurus 战队

汪沛 老师

您指导的队伍在“**第二十四届全国大学生机器人大赛 RoboMaster 2025 机甲大师超级对抗赛·区域赛（南部赛区）**”中，荣获

一等奖

特发此状，以资鼓励。

指导单位：中国高等教育学会

中国工程院战略咨询中心

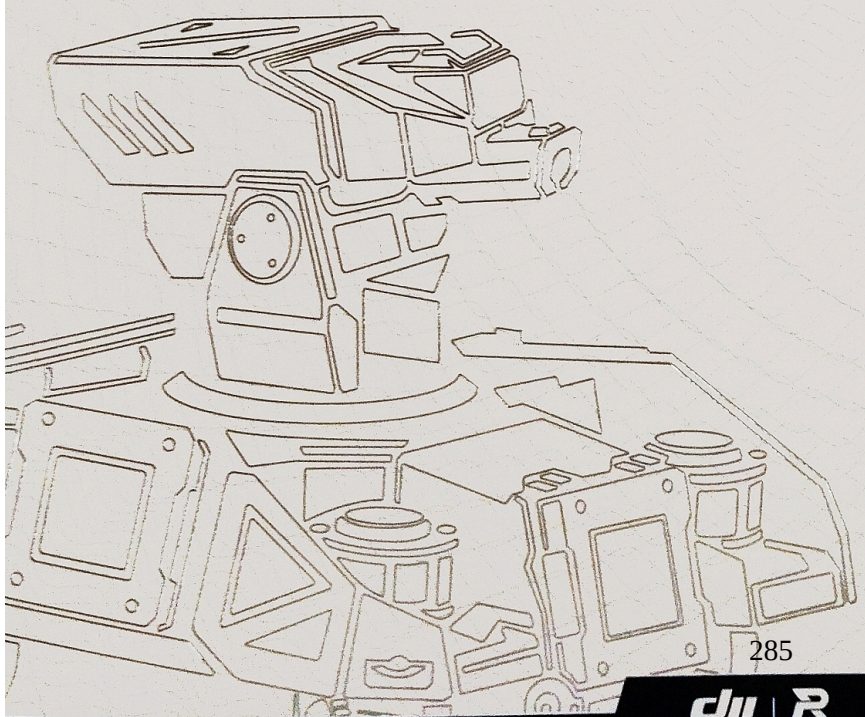

全国大学生机器人大赛
RoboMaster 组委会
2025 年 6 月

证书编号：RMUC2025QCOUM105336

证书编号：RMUC2024QYSKHWJX105336

CERTIFICATE
获 奖 证 书

ROBOMASTER
机甲大师超级对抗赛

华南农业大学 Taurus 战队

汪沛 老师

您指导的队伍在“**第二十三届全国大学生机器人大赛 RoboMaster 2024 机甲大师超级对抗赛·区域赛（南部赛区）**”中，荣获

一等奖

特发此状，以资鼓励。

指导单位：

中国高等教育学会

中国工程院战略咨询中心

全国大学生机器人大赛
RoboMaster 组委会
2024 年 6 月

荣誉证书

2025 年第 22 届全国大学生信息安全与对抗技术竞赛

（智能安全赛-区域赛-采收机器人）

竞赛奖项：　二等奖

获奖成员：　林炳钿　李菀莹　苏怡

获奖单位：　华南农业大学

指导教师：　汪沛

中国兵工学会　北京理工大学

中国兵工学会信息安全与对抗专业委员会

NO.ISCC-USC-ZNAQ-RC-14-2025-2-49B　　0057　　2025 年 11 月 20 日

获 奖 证 书

CERTIFICATE OF AWARD

华南农业大学 代表队：

在第二十七届中国机器人及人工智能大赛全国总决赛中，表现优异，成绩突出，荣获 机器人任务挑战赛（智慧药房）

一等奖

团队成员：蔡昭锐、何浩文、李子豪

指导老师：胡炼、汪沛

特发此证，以资鼓励。

中国机器人及人工智能大赛组委会

二〇二五年八月

证书编号： CRAIC2025-NF-JUAWWD

荣誉证书

CERTIFICATE OF HONOR

在“天鹅杯”第九届国际大学生智能农业装备创新大赛中，经评审，荣获

二等奖

特发此证，以资鼓励！

单位名称：华南农业大学

作品名称：棉花变量播种机器人

获奖学生：张冠豪，曾竟源，陈锡润，陈晓锋，翁宗标

指导教师：何杰，汪沛

国际农业和生物系统工程委员会　中国农业机械学会　中国农业工程学会　省部共建现代农业装备与技术协同创新中心　农业工程大学国际联盟

证书编号：NZDS2024-B-009

二〇二四年五月

荣誉证书

CERTIFICATE OF HONOR

在“天鹅杯”第十届国际大学生智能农业装备创新大赛中，经评审，荣获

二等奖

特发此证，以资鼓励！

单位名称：华南农业大学

作品名称：果树对靶变量施药机器人

获奖学生：张冠豪,曾竟源,马锐涛,连炜生,赖展鹏

指导教师：何杰,汪沛

国际农业和生物系统工程委员会　中国农业机械学会　中国农业工程学会　省部共建现代农业装备与技术协同创新中心　农业工程大学国际联盟

证书编号：NZDS2025-B-015

二〇二五年五月

获奖证书

参赛院校：华南农业大学

参赛学生：李思贤、周晓伟、耿双洋、马锐涛、刘梓瑶、袁闰祺

指导老师：何杰、汪沛

荣获"2024睿抗机器人开发者大赛（RAICOM）广东省"智能灌溉竞赛项目三等奖。

特发此证，以资鼓励！

工业和信息化部人才交流中心

2024年 07月 31日

证书编号： HJROBO202407006229

2025中国机器人大赛暨RoboCup机器人世界杯中国赛

河北·石家庄 2025.10.17-10.19

获奖证书

Y2509T1434800

华南农业大学

稻香园最好吃

自动分拣机器人-立体仓库赛项

三等奖

指导教师：何杰 汪沛

队　　员：林浩俊 谢卓 许凯泓 赖炜健 陈浩洋

中国自动化学会

2025年10月31日

广东青年大学生
百千万工程突击队

华南农业大学汪沛老师在2023年广东大中专学生志愿者暑期文化科技卫生“三下乡”社会实践活动暨广东青年大学生“百千万工程”突击队行动中荣获

优秀个人

特发此证，以资鼓励！

共青团广东省委员会　中共广东省委宣传部　广东省精神文明建设委员会办公室　广东省教育厅　广东省学生联合会

2023年12月20日

荣誉证书

汪　沛 同志：

荣获华南农业大学学生党支部书记素质能力大赛

三等奖

特发此证，以兹鼓励。

华南农业大学党委组织部

2025 年 5 月

获 奖 证 书

CERTIFICATE OF AWARD

华南农业大学汪沛老师 指导的团队在第二十七届中国机器人及人工智能大赛中取得了优异成绩，被评为

优秀指导教师

特发此证，以资鼓励。

中国机器人及人工智能大赛组委会

二〇二五年十一月

证书编号：CRAIC2025-EI-64K3AJ

CRAIC

获奖证书

HONORARY CERTIFICATE

汪沛 老师：

在第二十七届中国机器人及人工智能大赛广东省选拔赛中，指导学生完成比赛，表现优异，荣获

优秀指导教师

特颁此证，以资鼓励。

广东省产教融合促进会

中国机器人及人工智能大赛
广东赛区组委会（代章）

二零二五年七月

广东青年大学生
百千万工程突击队

华南农业大学《无人农场——机器代人助力乡村振兴》在2023年广东大中专学生志愿者暑期文化科技卫生“三下乡”社会实践活动暨广东青年大学生“百千万工程”突击队行动中荣获

优秀品牌项目

特发此证，以资鼓励！

指导老师：汪　沛、何　杰、陆永超

共青团广东省委员会　　中共广东省委宣传部　　广东省精神文明建设委员会办公室　　广东省教育厅　　广东省学生联合会

2023年12月20日

荣誉证书

工程学院重点实验室：

在华南农业大学2024年“三育人”评选中，被评为“先进集体”荣誉称号。

特发此证，以资鼓励。

中共华南农业大学委员会

华南农业大学

二〇二四年七月

授 予

华南农业大学南方农业机械与装备关键技术教育部重点实验室团队：

第二十五届“广东青年五四奖章集体”。

共青团广东省委员会　　广东省青年联合会

二〇二三年五月